Investigation of Epigenomic, Transcriptomic, and Metabolic Vulnerabilities in Rare Tumors of the Brain and Spine

by

Matthew Pun

A dissertation submitted in partial fulfillment
of the requirements for the degree of
Doctor of Philosophy
(Cellular and Molecular Biology)
in the University of Michigan
2023

Doctoral Committee:

Associate Professor Sriram Venneti, Chair
Professor Donna Martin
Professor Gary Hammer
Associate Professor Arvind Rao

Matthew J. Pun

punm@umich.edu

ORCID iD: 0000-0002-4766-4301

© Matthew J. Pun 2023

Dedication

This dissertation is dedicated to all the patients and families who have been impacted by brain and spine tumors and the patients and researchers who have laid the foundation for these studies.

Acknowledgements

I am incredibly grateful for my thesis advisor Dr. Sriram Venneti's mentorship. From our first meeting and throughout my time in the lab, his passion for science has been infectious and his deep care for his mentees is evident. Thank you Sriram for challenging me to think differently about scientific questions, giving me the guidance to develop in my science communication, and supporting me inside and outside of lab. Your mentorship means so much to me.

Thank you very much to my co-mentor Dr. Arvind Rao, who welcomed me as an advisee and a member of his lab. Arvind has provided me with guidance both on how to grow in my pursuit of developing my computational skills and on how to plan for a career in science. I am so grateful for your mentorship throughout my PhD.

In addition to Arvind and Sriram, I wish to thank Dr. Donna Martin and Dr. Gary Hammer who have served on my thesis committee. Your guidance and critical feedback have been extraordinarily helpful, and I am grateful for your advice and support as an aspiring physician-scientist.

The Venneti Lab has been an incredibly supportive and exciting place to work, and to Jill Bayliss, Chan Chung, Stefan Sweha, Siva Kumar Natarajan, Derek Dang, James Haggerty-Skeans, Mateus Mota, Joanna Lum, and Akash Deogharkar, I am incredibly thankful. I also am

grateful for my time with two Venneti Lab rotation students, Grace McIntyre and Jae Bucknor, who helped tremendously with several experiments in the past year. James, thank you for suggesting I rotate with the Venneti lab and letting me know how fantastic a place it is to train. Jill, Chan, and Stefan, thank you for helping me get started and oriented in the lab in a time of shift work and social distancing. Stefan, it has been fun to collaborate on so many projects throughout the years, and I look forward to doing so for many to come. Derek, thank you for creating a welcoming environment and for all of your advice. Lastly, thank you Siva for so graciously sharing a bench and a bay with me, for teaching me so much about metabolism, and for your help throughout my time in lab. I am excited to continue to discuss science and collaborate with you for decades to come.

The Rao lab has also provided me with a fantastic environment for learning how to approach biological questions from a computational perspective. Thank you especially to Viswes Ravikumar and Anand Shankar for providing valuable feedback and pointing me to helpful tools and tutorials.

The Medical Scientist Training Program (MSTP) has created a wonderful training environment, and I am grateful to Dr. Ronald Koenig, Dr. Kathy Collins, Justine Hein, Gretchen Aland, Elizabeth Bowman, Hilkka Ketola, and Laurie Koivupalo for all they have done to help me throughout both medical school and graduate school. My cohort of Bobby, Charles, Enze, James, Kristen, Michael, Mitra, Pha, and Suzie has been a constant source of support, and I am so fortunate to train with you. I am also thankful for the mentorship I have received from Cell and

Molecular Biology (CMB) directors Roberta Fuller and Manoj Puthenveedu and my CMB classmates.

I owe all I know about chordoma to the wonderful team I worked with as an undergraduate at the Chordoma Foundation. I am so grateful to Josh Sommer, Patty Cogswell, and Tammy Kutter. You welcomed me to the group and gave me incredible opportunities to see how rare disease research is supported and to learn from the community of patients and families who have faced chordoma.

Thank you to Drs. Kristin Scott and Hunt Willard who gave me my first opportunities in research and have continued to serve as mentors throughout my journey. Thank you also to Drs. Rinath Jeselsohn and Myles Brown who introduced me to cancer research, gave me a wonderful environment to grow as a scientist, and showed me the possibilities of a physician-scientist career.

Lastly, thank you to my fantastic family who have supported me on this journey. My parents, Karen and Manuel Pun fostered a love for science in me from a young age, encouraging me to learn about everything from the solar system to the depths of the sea. My brother Mike has always supported me in graduate school and has been my math and programming tutor. Thank you to my in-laws, Irene and Henry Kuo, who have been so supportive of my academic journey as well. Finally, thank you to my wife Molly for your love and support throughout this program. I could not have accomplished this without you.

Research Contributions: Collaborators within the Venneti lab, across the University of Michigan (UM), and at institutions throughout the world have contributed to the work presented in this dissertation. Chapter-by-chapter acknowledgements of these contributions are detailed below:

Chapter 2: DNA methylation datasets were curated and shared by Dr. Drew Pratt and. Dr. Kenneth Aldape at the National Cancer Institute. Posterior fossa datasets previously published by the Venneti lab have been processed and curated by Dr. Marcin Cieslik and Dr. Arul Chinnaiyan at UM. Pre-processed single-cell datasets were generously shared by: Drs. Li Jiang, Bernhard Englinger, and Mariella Filbin from the Dana Farber Cancer Institute (tumors); Drs. Patricia R. Nano and Aparna Bhaduri from the University of California, Los Angeles (developing hindbrain); and Drs. Piyush K. Joshi and Stefan Pfister of the German Cancer Research Center (developing cerebellum). Drs. Sriram Venneti and Arvind Rao provided input on the design and approaches.

Chapter 3: The work presented in Chapter 3 was a collaboration between the labs of Dr. Sriram Venneti and Dr. Carl Koschmann. The clinical trial data were collected and analyzed by the Koschmann lab and Dr. Sebastian Waszak at the University of Oslo. Mint-ChIP data were generated by Jasper Spitzer and Dr. Susanne Schmidt at the University Bonn, and initial processing was performed by Dr. Tingting Qin at the UM. I worked with Dr. Stefan Sweha to generate the RNA-seq and ChIP-seq samples in DIPG-007 cells, while Dr. Mateus Mota generated the ATAC-seq samples. I then performed analyses on the resulting sequencing data that had been preprocessed by either the UM Advanced Genomics (RNA) core or by Active

Motif (ChIP, ATAC). All metabolite samples were generated by Stefan Sweha and Yujie Ding and then processed by Dr. Costas Lyssiotis' lab.

Chapter 4: For reagent contributions, UM-Chor cell lines were donated by Dr. Mark Prince's lab at the University of Michigan. CH22 was provided by the Chordoma Foundation. I generated RNA-seq data in collaboration with Dr. Arul Chinnaiyan's lab in accordance with their standard pipeline. Reagents and study design input were provided by Dr. Abhijit Parolia; RNA-seq libraries were prepared by Rui Wang, sequencing was performed by Xuhong Cao; and read pseudoalignment was performed by Dr. Eleanor Young. Metabolite samples were collected with the help of rotation student Grace McIntyre. They were processed and analyzed by Anthony Andren in the lab of Costas Lyssiotis. Mouse xenograft studies were conducted primarily by Siva Kumar Natarajan with assistance from Grace McIntyre and me. Replicate N-acetyl cysteine rescue experiments and reduced/oxidized glutathione measurements were performed with assistance from Grace McIntryre and rotation student Jae Bucknor.

Chapter 5: The projects described in Chapter 5 are largely composed of projects under Sriram's mentorship that I was asked to contribute to that have been driven by fantastic postdoctoral fellows and graduate students in the lab. The diffuse midline glioma project was led by Mateus Mota; the H3G34R pediatric glioma project by Stefan Sweha, the mutant IDH1 glioma project by James Haggerty-Skeans; the supratentorial ependymoma project by Siva Kumar Natarajan; and the posterior fossa ependymoma project by Dr. Pooja Panwalkar, Derek Dang, Siva Kumar Natarajan, Dr. Chan Chung, and Stefan Sweha.

Table of Contents

Dedication ii

Acknowledgements iii

List of Tables xvii

List of Figures xviii

List of Abbreviations xxi

Abstract xxiii

Chapter 1 Introduction to Cancers of the Brain and Spine 1

1.1.1 Molecular classifications lay a foundation for understanding heterogeneity of brain tumor landscape 1

1.1.2 Pediatric brain tumors exhibit distinct biology from adult counterparts 3

1.1.3 Current treatment approaches to primary bone cancers are limited 3

1.2 Histones are critical regulatory molecules in cell biology and cancer 4

1.2.1 Histones enable packaging and transcriptional regulation of the genome 4

1.2.2 Variability in chromatin structure is also influenced by histone variant incorporation . 5

1.2.3 Studies of pediatric glioma genomes resulted in discovery of tumor-promoting histone mutations: “oncohistones” 5

1.3 Cancer cells reshape metabolism to meet tumorigenic needs 6

1.3.1 TCA-cycle derived oncometabolites reshape genomic regulatory landscapes 7

1.4 Biology of pediatric histone mutant histone mutant high-grade gliomas 8

1.4.1 Spatiotemporal patterns of histone mutant DMG incidence 10

1.4.2 H3K27M inhibits canonical PRC2 function 10

1.4.3 Current H3K27M biomarkers and therapeutic approaches 10

1.4.4 H3G34R/V mutations occur in distinct spatiotemporal profile 11

1.5 Biology of pediatric PFA ependymomas 11

1.5.1 Ependymomas arise throughout the CNS and comprise 9 molecular subgroups 11

1.5.2 Overexpression of EZHIP characterizes an aggressive subset of PF ependymomas ... 12

1.5.3 ZFTA fusions in ST ependymomas are associated with aggressive tumors 15

1.6 Biology of chordoma 15

1.6.1 Chordomas are one of the most common primary tumors of the spine 15

1.6.2 Chordomas are hypothesized to derive from vestiges of the embryological notochord 16

1.6.3 Limited treatment options are available for chordoma 17

1.6.4 Chromatin modifiers are among the most commonly mutated in chordoma 18

1.6.5 Preclinical data show brachyury is a critical vulnerability of chordomas 18

1.6.6 Maintenance of low H3K27me3 may be a prognostic marker and targetable vulnerability in chordoma 19

1.6.7 Chordoma cells display unique structural features 19

1.6.8 Studies of chordoma metabolism have been limited 20

1.7 Increasing understanding of the biology of rare bone and brain tumors lays the groundwork for needed therapeutic development 21

Chapter 2 Common Molecular Features of H3K27M DMGs and PFA Ependymomas Map to Hindbrain Developmental Pathways 22

2.1 Introduction 22

2.1.1 Group A posterior fossa ependymomas (PFAs) and diffuse midline gliomas (DMGs), H3K27-altered exhibit similar epigenetic landscapes of depleted H3K27me3 22

2.1.2 PFAs and DMGs rely on residual H3K27me3 methyltransferase activity 23

2.1.3 PFAs and DMGs likely arise in neighboring regions of the developing human hindbrain 24

2.2 Methods 24

2.2.1 Copy number alteration analyses 24

2.2.2 Gene expression analyses 25

2.2.3 Protein immunoblotting 25

2.2.4 Histone 3 lysine 27 trimethylation (H3K27me3) ChIP-seq analyses 26

2.2.5 H3K27ac and enhancer analyses 27

2.2.6 Single-cell RNA-seq analyses 28

2.2.7 Allen Brain Atlas analyses 28

2.2.8 Statistical analyses 29

2.3 Results 29

2.3.1 H3.1K27M and EZHIP-DMGs share key copy-number alterations with PFAs 29

2.3.2 The 1q gene MDM4 is commonly upregulated in 1q gain cohorts of PFAs and H3K27M DMGs and associated with PFA survival 32

2.3.3 Patterns in 1q gain highlight differences between subtypes of H3K27-altered DMGs 34

2.3.4 The recently identified PFA prognostic marker 6q loss recurs in DMGs and trends toward worse survival in DMGs 39

2.3.5 ACVR1 expression is prognostic in PFAs and is associated with transcriptomic signatures observed in ACVR1-mutant DMGs. 41

2.3.6 DMGs and PFAs share many genes with retained H3K27me3, but degrees of silencing vary within tumor subtypes 44

2.3.7 Differential expression patterns along H3K27me3-associated HOX loci correspond to anatomic origins 48

2.3.8 Enhancer signatures in PFAs and H3K27M DMGs show high expression in astrocyte-like tumor cells 52

2.3.9 H3K27me3-enriched CRABP1 is highly expressed in progenitor populations of both tumors 56

2.3.10 Integration of scRNA-seq datasets from PFAs and DMGs highlights potential role for CRABP1 in progenitor-type cells unique to PFA/DMGs 62

2.3.11 Common H3K27me3 signatures mirror human hindbrain brain developmental patterns 65

2.3.12 CRABP1 expression is seen in first trimester hindbrain and brainstem progenitor cells 67

2.3.13 CRABP1 demonstrates distinct positional expression patterns in human and mouse hindbrain consistent with prior studies in mice 70

2.4 Discussion 74

Chapter 3 Characterizing the Epigenomic and Transcriptomic Impact of the Clinically Promising Compound ONC201 in H3K27M-mutant Diffuse Midline Gliomas 83

3.1 Introduction 83

3.1.1 Patients with H3K27M-mutant gliomas have limited treatment options 83

3.1.2 Treatment with the investigative compound ONC201 is associated with unprecedented survival times in H3K27M DMG 84

3.1.3 The mechanism underlying efficacy in H3K27M DMGs remains unknown 87

3.2 Methods 87

3.2.1 In vitro modeling of H3K27M DMG ONC201 treatments 87

3.2.2 DIPG-007 (in vitro) RNA- and ChIP-seq sample preparation 88

3.2.3 RNA-seq processing 90

3.2.4 ChIP-seq processing 90

3.2.5 Super enhancers analysis 91

3.2.6 ATAC-seq analysis 91

3.2.7 Mint ChIP analysis 91

3.3 Results 92

3.3.1 ONC201 drives unfolded protein response in DIPG-007 cells 92

3.3.2 Integration of tumor and cell line transcriptome data highlights the role of metabolic pathways in ONC201 response 95

3.3.3 ONC201 restricts TCA cycle flux and drives production of 2-hydroxyglutarate (2HG) 98

3.3.4 ONC201 treatment drives 2HG production, alters the chromatin landscape of H3K27M DMGs, and reverses pathognomonic H3K27me3 depletion 99

3.3.5 ONC201 drives loss of H3K27ac and a subset of ONC201-driven transcriptional changes are associated with loss of chromatin accessibility. 103

3.4 Discussion 107

Chapter 4 Isocitrate Dehydrogenase 1 as a Therapeutic Vulnerability in Chordoma 110

4.1 Introduction 110

4.1.1 Chordomas are poorly understood, aggressive malignancies 110

4.1.2 Targeting chromatin modifiers in chordoma is a promising therapeutic avenue 110

4.1.3 We hypothesized chordomas may alter metabolism to maintain their epigenomic regulation 111

4.2 Methods 111

4.2.1 Microarray-based transcriptional analysis 111

4.2.2 Survival analysis 112

4.2.3 Cell culture 112

4.2.4 Short-hairpin RNA (shRNA) mediated knockdown of IDH1 112

4.2.5 Cell proliferation assays 114

4.2.6 Transcriptomic profiling of chordoma cell lines with IDH1 inhibition 115

4.2.7 Metabolite profiling of chordoma cell lines with IDH1 inhibition 115

4.2.8 Chromatin-immunoprecipitation followed by high-throughput sequencing of chordoma cell lines with IDH1 inhibition 118

4.2.9 N-Acetyl-Cysteine proliferation rescue experiments 119

4.2.10 Reduced-to-oxidized glutathione quantification 119

4.2.11 Summary of cell line models used 119

4.3 Results 121

4.3.1 Chordomas exhibit elevated TCA cycle gene expression compared to notochordal tissue 121

4.3.2 Elevated expression of the TCA cycle family enzyme IDH1 is associated with worse prognosis in chordomas 124

4.3.3 Addition of the IDH1 product alpha-ketoglutarate provides partial rescue of TCA cycle carbon source depletion 126

4.3.4 Cell culture models of chordoma rely on IDH1 for proliferation 128

4.3.5 Inhibition of a parallel α-KG-generating pathway has minimal effects in chordoma 131

4.3.6 Alpha ketoglutarate-to-succinate ratios drop with IDH1 inhibition..... 133

4.3.7 IDH1 inhibition increases H3K27me3 levels but has minimal effects at promoter regions 135

4.3.8 IDH1 inhibition significantly reduces brachyury expression in one model 138

4.3.9 Integrated analysis of changes in H3K27ac ChIP-seq and RNA-seq highlights stress response pathway activation..... 140

4.3.10 Glutathione synthesis pathway enzymes are among the highest overexpressed genes with IDH1 inhibitor treatment 143

4.3.11 Chordoma cell lines increase glutathione production in response to IDH1 inhibition 146

4.3.12 N-acetylcysteine rescues proliferation with IDH1 inhibition..... 148

4.3.13 IDH1 inhibitor treatment reduces tumor proliferation in a mouse xenograft model 150

4.4 Discussion 152

Chapter 5 Probing Transcriptomic and Epigenomic Alterations Lays the Groundwork for Therapeutic Interventions across Multiple Brain Tumors 154

5.1 Introduction 154

5.2 Methods..... 154

5.2.1 RNA sequencing analysis..... 154

5.2.2 ATAC sequencing analysis 155

5.2.3 Hi-C data analysis..... 160

5.2.4 DNA methylation 161

5.3 Targeting BAF complex dependencies in H3K27M DMGs..... 161

5.3.1 H3K27M DMGs show susceptibility to multiple epigenetically focused inhibitors in preclinical models..... 161

5.3.2 Mammalian SWI/SNF (BAF) complexes are frequently altered in cancer and represent a potential therapeutic target 163

5.3.3 The H3K27M mutation promotes sensitivity to mSWI/SNF complex inhibition in DMGs 164

5.3.4 SWI/SNF ATPase subunit and PBRM1 degradation targets enhancers, disrupting key developmental and structural pathways 166

5.3.5 Motif enrichment analyses identifies FOXO1 as a critical SWI/SNF-regulated transcriptional factor for H3K27M DMGs 171

5.3.6 Discussion 174

5.4 Redistribution of chromatin marks in H3G34-mutant pediatric gliomas reveals a therapeutic vulnerability to JAK/STAT pathway inhibition 176

5.4.1 Recurrent histone 3 glycine 34 mutations occur in cortical gliomas in adolescents and young adults 176

5.4.2 Consistent with prior work, H3.3G34R alters H3K36me3 distribution, increasing deposition in gene bodies. 178

5.4.3 Integration of H3K36me3 ChIP-seq with RNA-seq highlights elevated Lif levels 180

5.4.4 Discussion 182

5.5 *PTEN* haploinsufficiency may drive metabolic-epigenomic rewiring of mIDH1 astrocytomas to promote a more aggressive G-CIMP-low phenotype 183

5.5.1 Copy number loss of PTEN segregates with DNA methylation status in mIDH1 astrocytoma 183

5.5.2 PTEN is a critical regulator of growth signaling and its loss can shunt carbon away from the TCA cycle 184

5.5.3 Orthologous approaches across species demonstrate PTEN reduction enhances tumor growth and reduces D2HG levels 185

5.5.4 PTEN reduction results in durable transcriptional changes in both models 186

5.5.5 Reduction in PTEN results in upregulation of genes with H3K27me3-marked high-CpG promoters in neural progenitor cells 189

5.5.6 Transcriptional analysis further identifies dampened immune signatures as a critical consequence of PTEN modulation 191

5.5.7 Discussion 193

5.6 Dissecting the metabolic and transcriptional nodes of ZFTA-fusion positive supratentorial ependymomas 194

5.6.1 ZFTA fusion ependymomas are the major form of supratentorial ependymomas and lack effective therapies 194

5.6.2 ZFTA-RELA fusion upregulates glutamine metabolism via the Akt pathway 195

5.6.3 PTEN reduction in ZFTA-RELA fusion models occurs in part at the transcriptional level 196

5.6.4 The TCA cycle-derived metabolite itaconate is uniquely found in ZFTA fusion models 199

5.6.5 Multi-pronged approaches to dissect the impact of itaconate on ZFTA-RELA fusion driven biology in ST ependymomas 199

5.6.6 ZFTA-RELA fusion cells upregulate immune response and PI3K/Akt pathways 202

5.6.7 Discussion 211

5.7 Isogenic modeling of PFA ependymomas recapitulates tumor-informed super enhancer landscapes 212

5.7.1 Group A posterior fossa (PFA) ependymomas upregulate the TCA cycle 212

5.7.2 Generation of isogenic models to model PFA ependymoma metabolism 213

5.7.3 EZHIP overexpression drives a super enhancer profile that overlaps with PFA tumors 214

5.7.4 Discussion 216

Chapter 6 Conclusions and Future Directions 217

6.1 Summary 217

6.2 Summary of studies on diffuse midline gliomas and posterior fossa ependymomas 217

6.3 Outstanding questions for future research on DMGs and PFAs 221

6.4 Summary of studies on ONC201 treatment for DMGs 223

6.5 Outstanding questions for future research on ONC201 treatment of PFAs 224

6.6 Summary of studies on chordoma 227

6.7 Outstanding questions for future research on chordoma metabolism and IDH1 inhibition 228

6.8 Summary of studies on other brain tumors and outstanding questions 230

6.9 Concluding remarks 232

Bibliography 233

List of Tables

Table 2.1: Genes with retained H3K27me3, shared by H3K27M DMGs and PFA ependymomas. 79

Table 2.2: Enhancer-associated genes, shared by H3K27M DMGs and PFA ependymomas. 82

Table 5.1: Indices used for PCR amplification of ATAC-seq libraries. 159

Table 6.1: Summary of clinical and genomic features of H3K27-altered DMG subtypes and PFA ependymoma 220

List of Figures

Figure 1.1: Epigenomic alterations in brain cancers cluster in distinct anatomic regions. 9

Figure 1.2: Modes of H3K27me3 inhibition in pediatric brain tumors. 14

Figure 2.1 PFAs and DMGs share copy number alterations. 31

Figure 2.2 MDM4 is commonly upregulated in PFAs and DMGs. 33

Figure 2.3: H3.1K27M and EZHIP-DMGs share key copy-number alterations with PFAs. 37

Figure 2.4: 1q gain is not prognostic in other pediatric brain tumors. 38

Figure 2.5: The recently identified prognostic marker of 6q loss for PFA ependymomas may play a role in H3K27M DMG biology 40

Figure 2.6: ACVR1 expression is prognostic in PFAs and is associated with transcriptomic signatures observed in ACVR1-mutant DMGs. 43

Figure 2.7: Developmental patterning H3K27me3-enriched genes in PFAs and H3K27M DMGs display transcriptomic and epigenomic heterogeneity. 47

Figure 2.8: Heterogeneity in expression of commonly marked H3K27me3 genes is influenced by anatomic origin and not EZH2 inhibition. 50

Figure 2.9: Astrocyte-like cell types show the highest expression of enhancer signatures in both PFAs and H3K27M DMGs. 54

Figure 2.10: Heterogeneity in PFA and DMG H3K27me3-marked genes and CRABP1, in particular, is driven by expression in progenitor-like cells. 58

Figure 2.11: Differences in CRABP1 expression are associated with differences in HOX gene expression but progenitor cell type enrichment is unique to CRABP1. 60

Figure 2.12: Integrated scRNA-seq from DMG and PFA cohorts reveals CRABP1 is the top marker of a cluster of PFA and DMG cells with progenitor-like signatures. 63

Figure 2.13: H3K27me3-associated genes from DMGs and PFAs are most highly expressed along oligodendrocyte and ependymal development. 66

Figure 2.14: CRABP1 expression is associated with less differentiated cells of the hindbrain/brainstem. 69

Figure 2.15: CRABP1 maps to more caudal structures of developing human hindbrain in a similar manner as HOXA2 and HOXD3. 72

Figure 2.16: HOXD3 and HOXA2 are enriched in pontomedullary structures in mice..... 73

Figure 3.1: Patients treated with ONC201 demonstrate improved survival compared to available data from multiple historical cohorts 86

Figure 3.2: ONC201 treatment of DIPG-007 cells replicates observed upregulation of ER and metabolic stress response pathways. 94

Figure 3.3: Highly expressed TCA cycle genes in ONC201 responders are downregulated with treatment in vitro and reprogram metabolic pathways. 97

Figure 3.4: H3K27me3 levels are enriched in ONC201-treated tumors. 102

Figure 3.5: ONC201 treatment results in global loss of H3K27ac and downregulation of neural developmental pathways. 105

Figure 4.1: Pathway enrichment of tumor-upregulated centers on metabolism. 122

Figure 4.2: Elevated IDH1 but not IDH2 expression is associated with poor prognosis in chordoma..... 125

Figure 4.3: Chordoma cells rely on both glucose and glutamine for proliferation. 127

Figure 4.4: IDH1 inhibition through genetic and pharmacologic means reduces chordoma proliferation..... 129

Figure 4.5: Chordoma cell lines do not display strong sensitivity to glutamine pathway antagonists..... 132

Figure 4.6: IDH1 inhibitor treatment reduces downstream TCA cycle metabolites and lowers the demethylase-driving α-KG/Succinate ratios. 134

Figure 4.7: IDH1 inhibition raises H3K27me3 but drives minimal changes in transcription. ... 136

Figure 4.8: Preliminary studies suggested Brachyury may be regulated by IDH1 and alpha-ketoglutarate..... 139

Figure 4.9: Integration of H3K27ac ChIP-seq and RNA-seq demonstrates IDH1 inhibitor induces stress response pathways..... 141

Figure 4.10: Glutathione metabolism genes show increased promoter acetylation and expression. 144

Figure 4.11: IDH1 inhibition drives increased levels of oxidized glutathione. 147

Figure 4.12: N-acetylcysteine supplementation reverses IDH1 inhibitor toxicity. 149

Figure 4.13: IDH1 inhibitor treatment limits tumor growth in chordoma xenografts in mice. .. 151

Figure 5.1: H3K27M DMGs are highly sensitive to treatment with the SWI/SNF ATPase PROTAC AU-15330. 165

Figure 5.2: AU-15330 treatment decreased enhancer accessibility in DIPG-007. 167

Figure 5.3: AU-15330 decreases expression of genes associated with cell motility and development. 170

Figure 5.4: mSWI/SNF inhibition may disrupt FOXO1 expression through enhancer modulation. 173

Figure 5.5: The H3G34R mutation redistributes H3K36me3 deposition in an isogenic model. 179

Figure 5.6: Integrated epigenomic and transcriptomic profiling of H3G34R-expressing mNSCs support Lif activation as a potential targetable alteration. 181

Figure 5.7: PTEN knockdown in mIDH1 cell lines or mIDH1 tumor development in a PTEN heterozygous background produce strong transcriptional changes. 188

Figure 5.8: Upregulation of neural progenitor high-CpG island promoter gene sets with PTEN loss. 190

Figure 5.9: PTEN levels lead to dysregulation of immune response pathways. 192

Figure 5.10: ZFTA-RELA fusion results in small but significant reduction of the tumor suppressor Pten. 198

Figure 5.11: Experimental design investigating the transcriptional and epigenetic effects of the ZFTA-RELA fusion expression. 201

Figure 5.12: The ZFTA-RELA fusion isogenic model recapitulates known activation of NF-kB pathways and lends support for activation of PI3K-Akt pathway. 203

Figure 5.13: Irg1 knockdown reverses fusion-mediated silencing of neuron differentiation program and upregulation of PI3K-Akt signaling. 207

Figure 5.14: Citraconate treatment reverses downregulation of glycolysis and induces glutathione synthesis. 209

Figure 5.15: The super enhancer landscape of EZHIP-expressing mNSCs is similar to that of PFA tumors. 215

Figure 6.1: Proposed experiments to dissect the role of 2HG in DMG ONC201 response. 226

List of Abbreviations

α-KG: alpha-ketoglutarate
2HG: 2-hydroxyglutarate
5mC: 5-methyl cytosine
ACVR1: activin A receptor type I
ATAC-seq: assay for transposase-accessible chromatin with sequencing
ChIP-seq: chromatin immunoprecipitation followed by sequencing
BET: bromodomain and extra-terminal motif
cBAF: canonical BRG1/BRM-associated factor
CDKN2A: cyclin dependent kinase inhibitor 2A
CDKN2B: cyclin dependent kinase inhibitor 2B
CIMP: CpG Island Methylator Phenotype
ClpP: caseinolytic peptidase P
CNA: copy number alteration
CNS: central nervous system
CRABP1: cellular retinoic acid-binding protein 1
D2HG: D-2-hydroxyglutarate
DMG: diffuse midline glioma
DNA: deoxyribonucleic acid
EZH2: enhancer of zeste homolog 2
EZHIP: enhancer of zeste homologs inhibitory protein
FBS: fetal bovine serum
FDA: federal drug administration
G-CIMP: glioma CpG Island Methylator Phenotype
H3K4me1: histone H3 lysine 4 monomethylation
H3K4me3: histone H3 lysine 4 trimethylation
H3K27ac: histone H3 lysine 27 acetylation
H3K27M: histone H3 lysine 27-to-methionine substitution
H3K27me2: histone H3 lysine 27 dimethylation
H3K27me3: histone H3 lysine 27 trimethylation
H3K34R: histone H3 lysine 34-to-arginine substitution
H3K34V: histone H3 lysine 34-to-valine substitution
H3K36me3: histone H3 lysine 36 trimethylation
HDAC: histone deacetylase

HDACi: histone deacetylase inhibitor
HGG: high-grade glioma
IDH1: isocitrate dehydrogenase 1
IDH2: isocitrate dehydrogenase 2
KDM: histone lysine demethylase
L2HG: L-2-hydroxyglutarate
Mint-ChIP: multiplexed, indexed T7 chromatin immunoprecipitation followed by sequencing
mIDH1: mutant isocitrate dehydrogenase 1
mTOR: mammalian target of rapamycin
ncBAF: noncanonical BAF
OS: overall survival
PBAF: polybromo-associated BAF
PCA: principal component analysis
PF: posterior fossa
PFA: posterior fossa ependymoma, group A
PFS: progression-free survival
PI3K: phosphoinositide 3-kinase
PRC2: polycomb repressive complex 2
PROTAC: proteolysis-targeting chimera
PTEN: phosphatase and tensin homolog
PTM: post-translational modification
RIPA: radioimmunoprecipitation assay buffer
RELA: REL-Associated protein
RNA: ribonucleic acid
RNA-seq: RNA sequencing
scRNA-seq: single-cell RNA sequencing
SETD2: SET Domain Containing 2
SMARCA2: SWI/SNF related, matrix associated, actin dependent regulator of chromatin, subfamily a, member 2
SMARCA4: SWI/SNF related, matrix associated, actin dependent regulator of chromatin, subfamily a, member 4
SMARCB1: SWI/SNF related, matrix associated, actin dependent regulator of chromatin, subfamily a, member 1
ST: supratentorial
UMAP: uniform manifold approximation and projection
ZFTA: zinc-finger translocation associated

Abstract

Cancer is the second-leading cause of death in the United States and encompasses a heterogeneous group of diseases with distinct spatiotemporal incidence patterns and molecular alterations. Tumors of the brain and spine present substantial challenges to treatment due to their invasion into structures integral to the nervous system, resulting often in poor survival outcomes and substantial morbidity. These difficulties underscore the pressing need to develop effective medical therapies to control tumor growth and to complement surgical and radiotherapy approaches. To this aim, it is imperative to improve our understanding of the molecular drivers of these tumors, characterize clinically effective mechanisms of treatment, and investigate novel therapeutic avenues informed by our increasing access to patient-derived data and models. In this dissertation, I: (1) characterize common molecular alterations in two deadly pediatric brain tumors that share a distinct epigenomic phenotype, (2) demonstrate how an investigational compound disrupts integrated metabolic and epigenetic pathways in an extremely deadly pediatric brain tumor, (3) propose a novel metabolic vulnerability in a rare spinal tumor, and (4) leverage transcriptomic and epigenomic assays to inform therapeutic strategies for aggressive brain tumors.

In Chapter 2, I methodically evaluate genomic, transcriptomic, and epigenomic characteristics of two high-risk pediatric brain tumors: group A posterior fossa ependymomas (PFAs) and diffuse midline gliomas histone 3 lysine 27 (H3K27)-altered (DMGs). Both cancers harbor alterations

that inhibit canonical activity of the H3K27 methyltransferase, enhancer of zeste homolog 2 (EZH2). Moreover, both most commonly arise in neighboring structures of the developing hindbrain. For each tumor type, we aggregated available copy-number data, bulk and single cell RNA-sequencing, and H3K27 methylation and acetylation chromatin immunoprecipitation with sequencing (ChIP-seq). I then compared datasets between tumors and mapped findings to patterns in developmental expression atlases. Altogether, our analyses nominate potential biomarkers and demonstrate the impact of developmental origins on chromatin and gene expression.

In Chapter 3, I focus on DMGs with H3 lysine 27-to-methionine (H3K27M) mutations and characterize the transcriptional, epigenomic, and metabolic impacts of the small molecule inhibitor ONC201, an investigational drug that is associated with unprecedented extended survival in two early clinical trials. Integrating transcriptomic studies with radiographic response measurements and *in vitro* modeling of ONC201 treatment, I pinpoint tricarboxylic acid (TCA) cycle interruption as a critical mechanism. Complemented by metabolite analyses that discovered production of the oncometabolite 2HG, I then explore high-throughput profiling of chromatin to show how treatment with ONC201 influences cell state.

In Chapter 4, I explore sensitivity of the spine-associated tumor chordoma to inhibition of the TCA-cycle enzyme isocitrate dehydrogenase 1 (IDH1). I investigate the association between IDH1 expression and survival in the largest available cohort. Through genetic and pharmacologic approaches, I demonstrate that chordoma proliferation relies on IDH1. By

integrating metabolomic, transcriptomic, and epigenomic approaches, I characterize how IDH1 inhibition induces stress response pathways.

In Chapter 5, I investigate transcriptomic and epigenomic consequences of putative molecular drivers for five brain tumors: DMGs, PFAs, supratentorial ZFTA-RELA fusion ependymomas, H3G34R/V gliomas, and PTEN heterozygous IDH1-mutant adult gliomas. Exploiting transcriptome profiling and various high-throughput epigenomic assays, we characterize how molecular alterations associated with each tumor may sensitize them to potential therapeutic vulnerabilities.

Overall, the data presented here advance our knowledge of the biology underlying multiple brain and spine tumors and lays the groundwork for the development of several novel therapeutic approaches.

Chapter 1
Introduction to Cancers of the Brain and Spine

Cancer is the second-leading cause of death in the U.S. (R. L. Siegel et al., 2023). Broadly, cancer occurs when cells exhibit patterns of unrestrained growth and division, invading into the normal structures of multicellular organisms. Cancer cells derive from normal lineages but acquire evolutionary advantages such as hyperactivation of proliferative signaling, insensitivity to anti-growth signals, and altered metabolism, permitting survival and proliferation (Fouad & Aanei, 2017; D Hanahan & Weinberg, 2000; Douglas Hanahan & Weinberg, 2011).

1.1 Plateaued survival rates for brain and bone cancers in the last 30 years highlight the need for improved treatments

Cancer encompasses an extremely heterogenous class of distinct diseases, and while overall cancer mortality rates have decreased continuously since 1991, trends in survival rates vary considerably across tumors (R. L. Siegel et al., 2023). For example, brain and central nervous tumors have proven especially difficult to treat with an increase in 5-year survival rates of just 32% to 33% between 1995-97 and 2012-18. Similarly, bone tumors have had similarly stagnant survival rates, with overall tumor-specific survival rates holding around 69% between the 1990s and the 2010s (Hu et al., 2021).

1.1.1 Molecular classifications lay a foundation for understanding heterogeneity of brain tumor landscape

Malignant brain tumors are broadly classified histologically as gliomas and non-gliomas. Gliomas describe a class of tumors that demonstrate histological characteristics of glial cells, which are support cells for neurons in the brain, and glial precursors. Gliomas account for about three quarters of malignant CNS tumors (K. D. Miller et al., 2021) and encompass a large, heterogeneous mix of tumors that include high-grade diffuse gliomas, astrocytomas, and ependymomas (McNamara et al., 2022).

With improvements in biomedical technologies and greater availability of tumor samples, molecular profiling has shed light on the diversity of tumors under the glioma umbrella. Early approaches stratified tumors based on distinct copy number changes such as loss of Chr1p or 19q or mutations in tumor suppressors such as *TP53* and *CDKN2A* or oncogenes such as *EGFR* respectively (Barker II et al., 2001; Cairncross et al., 1998; Louis et al., 2001; Maintz et al., 1997). Advances in sequencing technology enabled high-throughput approaches to scan for additional recurrent mutations. In gliomas in particular, high-throughput sequencing uncovered novel oncogenic mutations. Exome sequencing of a cohort of glioblastomas, the most aggressive glioma, revealed mutations in the region encoding the substrate-binding site of isocitrate dehydrogenase 1 (IDH1) (Parsons et al., 2008). Further characterization of the genomic, transcriptomic, and epigenomic landscape has since provided the basis for a more comprehensive and detailed picture of the brain tumor landscape, with well-defined markers associated with prognostic stratification (Brat et al., 2015; Brennan et al., 2013; Ceccarelli et al., 2016; Frattini et al., 2013; Kim et al., 2015; H. Suzuki et al., 2015). These classifications and subclassifications have provided the framework for therapeutic strategies.

1.1.2 Pediatric brain tumors exhibit distinct biology from adult counterparts

In children and adolescents under 20 years old, the highest cancer mortality is due to brain and other nervous system tumors (R. L. Siegel et al., 2023). Pediatric brain tumors most frequently arise in infratentorial regions (I F Pollack, 1999) unlike their adult counterparts. Due to their relative rarity and shared histological features with the tumors found in adults, pediatric gliomas were traditionally classified and treated based on approaches developed for their adult counterparts (Jones & Baker, 2014). While some molecular characteristics apply to both adult and pediatric tumors such as mutations in the tumor suppressor *TP53* and the oncogene *PIK3CA* (Gallia et al., 2006; Ian F Pollack et al., 2001), pediatric cancers differ in other markers such as *EGFR* and *PTEN* status (Ian F Pollack et al., 2006). With the increasing availability of pediatric brain tumor samples, genomic and transcriptomic approaches have highlighted large, meaningful distinctions between pediatric and adult brain malignancies (Mackay et al., 2017; Kristian W Pajtler et al., 2015; Paugh et al., 2010; Rickert et al., 2001; Wong et al., 2006). These diverse molecular profiles of pediatric brain tumors that correlate with distinct patterns of incidence and survival outcomes underscore the needs for unique treatment approaches.

1.1.3 Current treatment approaches to primary bone cancers are limited

Bone tumors account for an estimated 0.2% of malignancies and 0.3% of deaths due to cancer (R. L. Siegel et al., 2023). These tumors are associated with significant morbidity to patients due to their anatomic locations. Due to the relative rarity of these cancers, studies of bone tumors have been far more limited. Additionally, surgery, radiation, and, for some tumors, chemotherapy, remain the only treatment options. Bone cancer incidence follows a distinct bimodal pattern with peak incidences observed in the second and eighth decades of life

(Dorfman & Czerniak, 1995). Furthermore, histological tumor subtypes display distinct distributional patterns across the skeleton. Tumors arising along the spine account for just 5% of all bone tumors and most commonly fall into one of four subtypes: chordomas, chondrosarcomas, osteosarcomas, and Ewing's sarcomas (Kerr et al., 2019; Sundaresan et al., 2009).

1.2 Histones are critical regulatory molecules in cell biology and cancer

1.2.1 Histones enable packaging and transcriptional regulation of the genome

Inside a cell's nucleus, DNA is packaged in an ordered structure called chromatin (Kornberg & Thomas, 1974). Histones are a class of conserved proteins with positive charge that form octamer units called nucleosomes and facilitate compaction of negatively charged DNA (DeLange et al., 1969). The canonical histone proteins in human nucleosomes are histones H2A, H2B, H3, and H4, with two of each composing the nucleosome (Kornberg & Thomas, 1974; Leffak et al., 1977; Weintraub et al., 1975; Worcel et al., 1978). Whereas the C-terminal domains of histone proteins mediate the octamer-forming interactions of the nucleosome, the N-termini are frequently subject to post-translational modification (PTMs) that influence nucleosomal interactions with DNA and other proteins (Allfrey, 1964; Johnson *et al.* 1990; Luger *et al.* 1998; Shrogen-Knaak *et al.* 2006; Reviewed in Millar and Grunstein 2006).

While the tails of all four canonical histones have been demonstrated to undergo PTMs, covalent modifications of histone H3 in particular have been associated with variation in transcriptional state. Most strikingly, regions of the genome that remain densely compacted throughout the cell cycle, termed heterochromatin (Heitz, 1928), exhibit global hypoacetylation of histones and

enrichment of histone H3 lysine 9 trimethylation (H3K9me3) and, to an extent, H3K27me3 (Saksouk et al., 2015). These regions are commonly, though not absolutely, associated with transcriptional silencing (Allis & Jenuwein, 2016; Bernstein et al., 2006; Young et al., 2011).

Acetylation of histones in general is associated with conditions more permissive of transcription. H3K27 acetylation (H3K27ac) in particular is a mark of active promoters and enhancers across the genome (Allis & Jenuwein, 2016; Raisner et al., 2018). Moreover, assessment of the relative distribution of H3K27ac across enhancers is tightly correlated to specific patterns of cell identity due to the role these regulatory elements play in transcriptional state (Hnisz et al., 2013; Pott & Lieb, 2015).

1.2.2 Variability in chromatin structure is also influenced by histone variant incorporation

While the canonical histones comprise the majority of nucleosomes, a variety of histone variants exist and are incorporated into chromatin. In humans in particular, there are six identified variants for histone H3 and eight for H2A (Buschbeck & Hake, 2017). In contrast to the replication-coupled H3.1 and H3.2 genes, the variant histone H3.3 (encoded by H3-3A) can be deposited independent of cell-cycle and is most commonly found in active promoters (Mito et al., 2005; Wirbelauer et al., 2005).

1.2.3 Studies of pediatric glioma genomes resulted in discovery of tumor-promoting histone mutations: "oncohistones"

The advent of affordable high-throughput sequencing revealed a landscape of mutations in epigenetic regulators across cancer types (Shen & Laird, 2013). Among these discoveries,

sequencing of pediatric gliomas demonstrated high frequencies of mutations in histone H3-encoding genes (Schwartzentruber et al., 2012; G. Wu et al., 2012). Specifically, H3-3A was found to have mutually exclusive mutations at two hotspots: lysine 27 (K27) and arginine 34 (R34). As will be discussed in greater detail below, these mutations result in aberrant modulation of chromatin modifying enzymes and reshaping of chromatin landscapes.

1.3 Cancer cells reshape metabolism to meet tumorigenic needs

Cellular metabolism describes the set of chemical reactions that generate energy sources, convert nutrients into building blocks necessary for cell function and growth, and eliminate harmful byproducts. Alterations in the ways cancer cells utilize nutrients were first observed a century ago when Otto Warburg described how cancer cells utilize glucose and meet energy needs differently from nonmalignant cells (Warburg et al., 1924; Warburg & Negelein, 1923). Although revolutionary advances in cancer genetics largely shifted the field's focus to the characterization of oncogenes, tumor suppressors, and, later, the genomic landscape of tumors, altered metabolism is now recognized as a hallmark of cancer (Douglas Hanahan & Weinberg, 2011). In fact, oncogenic alterations drive shifts in metabolism that support tumorigenicity (C. V Dang & Semenza, 1999).

Similar to physiologic cellular metabolism, cancer metabolism has traditionally been studied through three lenses: energetics, biosynthesis, and reduction of harmful products, which in the case of tumor cells, largely concerns oxidative stress species (DeBerardinis & Chandel, 2016). Furthermore, studies of tumor metabolism have expanded that perspective in multiple ways,

highlighting the critical ways that key metabolites are central to critical cellular processes including epigenetic regulation and immune modulation.

1.3.1 TCA-cycle derived oncometabolites reshape genomic regulatory landscapes

With regards to epigenetic regulation, the past two decades have led to the characterization of oncometabolites, species that accumulate in a cancer cell due to mutations in metabolic pathways that directly promote tumorigenesis (DeBerardinis & Chandel, 2016; Ward & Thompson, 2012). D-2-hydroxyglutarate (D2HG), a reduced form of the tricarboxylic acid (TCA) cycle metabolite alpha-ketoglutarate (α-KG), represents the best characterized of this class. Produced by a gain-of-function mutant form of IDH1 or IDH2 first discovered in gliomas, D2HG accumulates in cells expressing the mutant (L. Dang et al., 2009; Ward et al., 2010). D2HG levels are low physiologically, and outside of cancer, accumulation of D2HG is associated with rare neurometabolic disease (Kranendijk et al., 2012). It competitively inhibits a class of enzymes called α-KG-dependent dioxygenases, which includes the Jumanji family of histone lysine demethylases (KDMs) and the TET family of 5-methlycytosine (5mC) hydroxylases that facilitate DNA methylation (Xu et al., 2011). D2HG accumulation results in drastic reprogramming of the epigenome that restricts expression of differentiation programs (Lu et al., 2012).

Additionally, accumulation of two canonical TCA cycle products results in substantial epigenetic dysregulation in tumors. Loss-of-function mutations in fumarate hydratase (FH) and succinate dehydrogenase (SDH) occur in renal cell carcinoma, hereditary paragangliomas/pheochromocytomas, and hereditary leiomyomatosis (Baysal et al., 2000;

Tomlinson et al., 2002). Accumulation of fumarate and succinate, the substrates for FH and SDH also results in inhibition of α-KG-dependent dioxygenases and reshaping of epigenetic landscapes, highlighting the critical interplay between TCA cycle metabolites and chromatin regulation.

While inhibition of α-KG-dependent dioxygenases as described above represents a tumorigenic mechanism, metabolic regulation of their activity plays a pivotal role in nonmalignant regulation of potency, with embryonic stem cells requiring elevated α-KG/succinate ratios to maintain pluripotency (Carey et al., 2015). Recent findings in pediatric glioma demonstrate that some tumors also rely on α-KG-driven activity of KDMs to maintain their proliferative state (Chung et al., 2020).

1.4 Biology of pediatric histone mutant histone mutant high-grade gliomas

Epigenomic alterations are common and critical to the biology of gliomas. While adult gliomas are well-characterized for their incidence of *IDH1/2* mutations and production of the epigenome-reshaping oncometabolite D2HG that alters methylation deposition as discussed in Section 1.3.1, sequencing studies have demonstrated that pediatric tumors have high frequencies of mutations in histones themselves that alter chromatin landscapes (Figure 1.1).

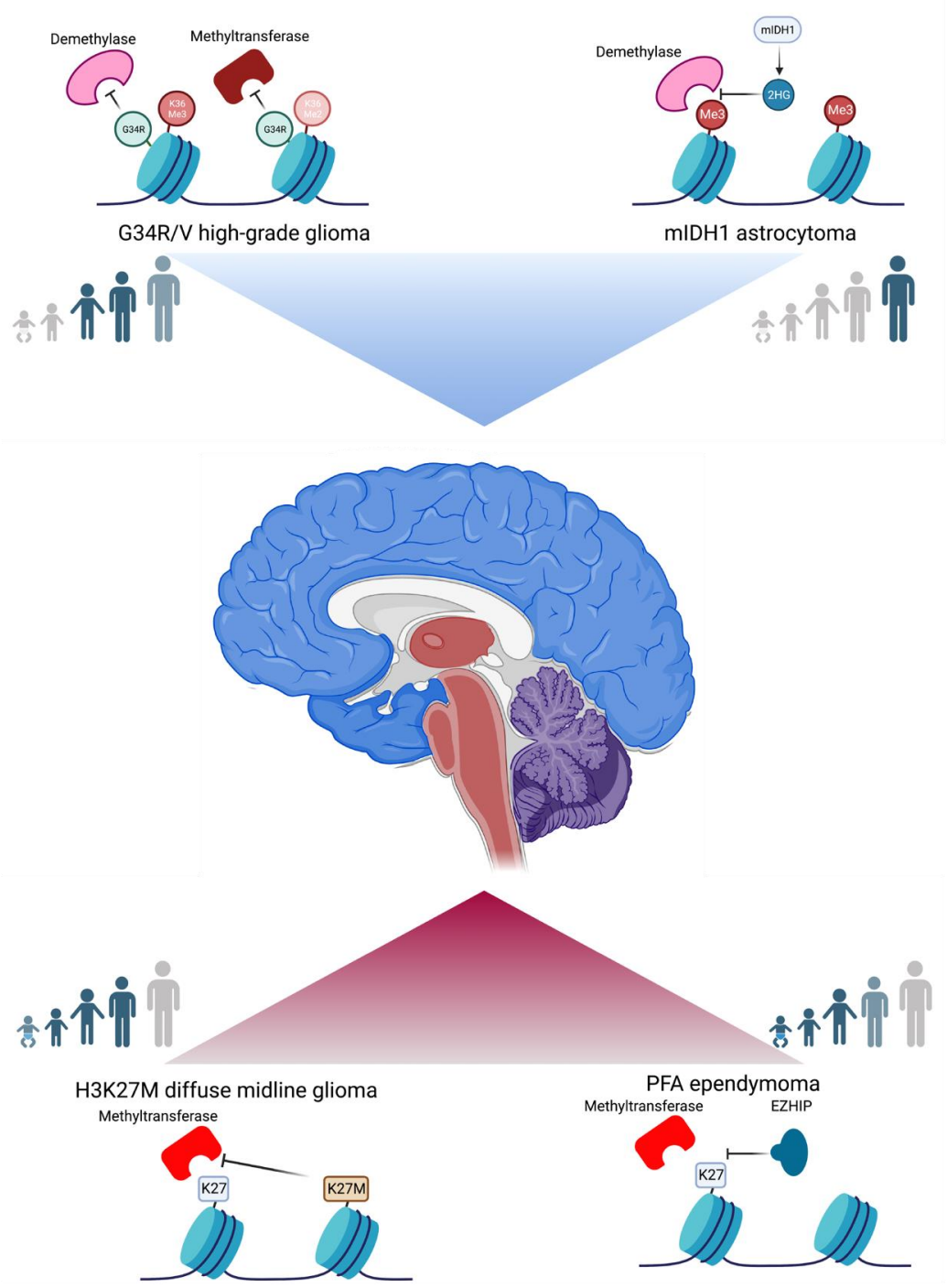

Figure 1.1: Epigenomic alterations in brain cancers cluster in distinct anatomic regions.

IDH-mutant gliomas largely occur in adults in cortical regions of the brain. H3G34-mutant pediatric gliomas also segregate in hemispheric regions but are associated with an adolescent and young-adult population. H3K27M mutations and EZHIP expression, which both inhibit methylation of histone H3 lysine 27 are found in inferior regions and in younger populations.

1.4.1 Spatiotemporal patterns of histone mutant DMG incidence

Approximately half of pediatric high-grade gliomas harbor histone mutations (Mackay et al., 2017). Mutations of histone H3 in pediatric brain cancer fall into two main classes: lysine-to-methionine mutations at residue 27 (H3K27M) and glycine to arginine or valine substitutions at residue 34 (H3G34R/V). Assessment of these alteration across large cohorts has revealed distinct spatial and temporal patterns of tumor occurrence for these two histone-mutant subtypes (Mackay et al., 2017). H3K27M gliomas in general are found in midline structures, primarily in the pons and thalamus whereas H3G34R/V tumors occur almost exclusively in the cortical hemispheres (Figure 1.1). G34R/V tumors also tend to occur in an older age range compared to H3K27M tumors (Mackay et al., 2018; Sturm et al., 2012).

1.4.2 H3K27M inhibits canonical PRC2 function

The polycomb repressive complex 2 (PRC2) includes the methyltransferase enhancer of zeste homolog 2 (EZH2) and is responsible for di- and tri-methylation of H3K27. The lysine-to-methionine substitution observed in pediatric gliomas inhibits PRC2 activity, lowering H3K27me2 and -me3 levels through a direct interaction with EZH2 (Lewis et al., 2013). Subsequent studies have proposed various mechanisms for the genome-wide patterns in H3K27me3 distribution observed in H3K27M gliomas (Bayliss et al., 2016; Bender et al., 2013; Harutyunyan et al., 2019; S U Jain et al., 2019; S C Mack et al., 2014). In addition to H3K27me3 depletion, H3K27M expression is linked to a rise in H3K27ac (Krug et al., 2019a; Nagaraja et al., 2017; Piunti et al., 2017).

1.4.3 Current H3K27M biomarkers and therapeutic approaches

Given the alterations in H3K27M DMGs' chromatin landscapes, a variety of epigenetic inhibitors have been employed to test for therapeutic efficacy. Efforts to reverse the depletion of H3K27me3 with H3K27 demethylase inhibitors has shown efficacy in cell line and mouse xenograft models (Hashizume et al., 2014), but clinical translation of this class of drugs has been difficult. A subsequent screen of epigenetic inhibitors in H3K27M DMGs identified histone deacetylase (HDAC) inhibitors as a potential option (Grasso et al., 2015). Additional approaches have shown that inhibition of transcriptional machinery via the compounds JQ1 and THZ1 also show efficacy in preclinical settings (Nagaraja et al., 2017; Piunti et al., 2017).

1.4.4 H3G34R/V mutations occur in distinct spatiotemporal profile

Unlike H3K27M, the H3G34 mutations sit at a residue without any known post-translational modifications. In addition to the arginine and valine substitutions, a tryptophan mutation at H3G34 is frequently observed in giant cell tumors of the bone. Work across the last decade, however, has shown that mutations in the residue affect the enzymatic activities of chromatin modifiers of the nearby lysine 36 (H3K36) residue. While it was initially observed that the common H3G34R mutants inhibit the histone methyltransferase of H3K36, SETD2 (Lewis et al., 2013), mutations also inhibit H3K36 demethylase activity and result in global changes in H3K36 methylation patterns as well as those of other marks including H3K27me3 (Siddhant U Jain, Khazaei, et al., 2020; Khazaei et al., 2020).

1.5 Biology of pediatric PFA ependymomas

1.5.1 Ependymomas arise throughout the CNS and comprise 9 molecular subgroups

Ependymomas are a subgroup of gliomas that exhibit histologic features similar to the nonmalignant ependymal cells that form the lining of the fluid-filled spaces of the CNS (Hübner et al., 2018; Louis et al., 2021). Ependymal tumors present as grade I-III neoplasms and may arise anywhere in the central nervous system, and anatomic site is highly correlated with age at presentation. Ependymomas are classified broadly as spinal or intracranial, and intracranial tumors further subdivided into supratentorial (ST) and posterior fossa (PF) groupings. Almost all pediatric ependymomas occur intracranially whereas the most frequent location in adults is in the spinal cord (Kilday et al., 2009; Kristian W Pajtler et al., 2015; Vera-Bolanos et al., 2015). DNA methylation and transcriptome profiling have further characterized three molecular subtypes for each of the three anatomic regions, resulting in nine total entities (Kristian W Pajtler et al., 2015).

Spinal ependymomas are associated with good prognoses and are rarely found in children. They are characterized histopathologically as sub-ependymomas, myxo-papillary ependymomas, and anaplastic ependymomas (Hübner et al., 2018; Kristian W Pajtler et al., 2015). Sub-ependymomas and myxo-papillary ependymomas are both low grade (WHO I), while myxo-papillary ependymomas tend to be grade III and harbor mutations in the tumor suppressor gene neurofibromatosis type 1 (*NF1*).

1.5.2 Overexpression of EZHIP characterizes an aggressive subset of PF ependymomas

DNA methylation and transcriptome- based classifications identified three classes of PF ependymomas: group A (PFA), which are found primarily in children and have 5-year OS rates of approximately 50-60%; group B (PFB), which occur in older individuals and have good

overall survival; and sub-ependymomas, low-grade neoplasms which are seen almost exclusively in adults and harbor good prognoses (Kristian W Pajtler et al., 2015). In addition to the segregation by DNA methylation landscapes, further epigenomic characterization revealed that PFA ependymomas exhibited global loss of H3K27me3 staining in contrast to PFB tumors in a strikingly similar manner to oncohistone-harboring H3K27M DMGs despite the lack of any histone mutation (Bayliss et al., 2016; Panwalkar et al., 2017). Data from large cohorts enabled identification of alterations in and PFA-specific upregulation of a previously uncharacterized gene, *CXorf67*, now termed enhancer of zeste homologs inhibitory protein (*EZHIP*) (K W Pajtler et al., 2018). Molecular studies have since demonstrated that EZHIP inhibits PRC2 H3K27 methylation activity in a similar fashion as the H3K27M-mutant histone tail (Hubner et al., 2019; S U Jain et al., 2019; Siddhant U Jain, Rashoff, et al., 2020; Piunti et al., 2019).

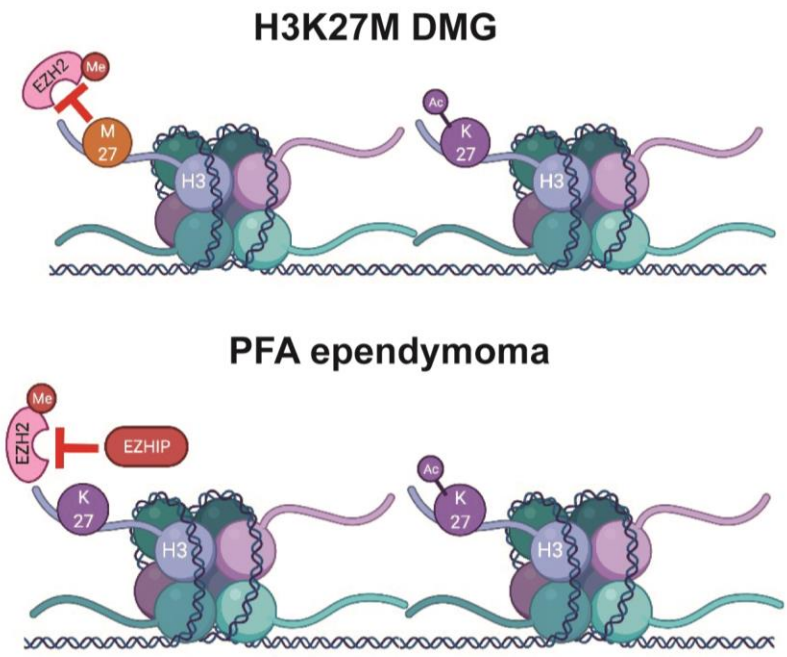

Figure 1.2: Modes of H3K27me3 inhibition in pediatric brain tumors.

H3K27M mutations in DMGs interfere with EZH2 catalytic activity and prevent trimethylation of unmutated residues (top), and PFAs overexpress EZHIP which blocks EZH2 in a similar manner.

1.5.3 ZFTA fusions in ST ependymomas are associated with aggressive tumors

Similarly to PF ependymomas, ST ependymomas are comprised of three groups, two of which are associated with good prognoses, and a third with 5-year overall survival rates around 50% (Kristian W Pajtler et al., 2015). As in the other anatomic compartments, subependymomas are low-grade neoplasms, and these primarily are seen in adults. The pediatric subsets of ST ependymomas are characterized by gene fusion events in one of two genes: Yes1 Associated Transcriptional Regulator (*YAP1*) and Zinc Finger Translocation Associated (*ZFTA*, previously referred to as *C11orf95*) (Horbinski et al., 2022). Whereas YAP1 fusions are associated with good prognosis and represent a small fraction of ST cases, ST ependymomas, ZFTA-positive (ST-ZFTA) are the most common ST ependymoma and are extremely aggressive with 5-year progression free survival rates (PFS) of less than 30% (Kristian W Pajtler et al., 2015).

1.6 Biology of chordoma

1.6.1 Chordomas are one of the most common primary tumors of the spine

Primary tumors of the spine present substantial treatment challenges due to their anatomic location and the limited effectiveness of non-surgical treatment modalities (Bilsky et al., 2008). While spine tumor datasets have been historically limited due to the low prevalence of these tumors and complicated by issues of initial misdiagnosis, chordomas are consistently reported as one of the most commonly found tumors along the spinal axis (Kerr et al., 2019; McMaster et al., 2001). Demographically, chordomas most frequently present in patients in their 50s-70s; however, a subtype of chordomas called dedifferentiated chordomas are predominantly pediatric. Additionally, current data suggest chordomas are most common in white individuals; though, researchers concede this may be confounded by factors such as access to care (Das et al., 2020).

Chordomas arise all along the spine with the majority of cases occurring at its extremes. Although estimates vary, 30-40% of chordomas are found at the base of the skull in the spheno-occipital region and clivus, and up to 45% are found in the sacrococcygeal region. The remainder occur along the mobile spine (Bakker et al., 2018; McMaster et al., 2001; Unni & Inwards, 2010; Whelan et al., 2012). Additionally, chordomas fall into three WHO-defined subtypes by histology: conventional and/or chondroid, poorly differentiated, and dedifferentiated (Wedekind et al., 2021). Conventional/chondroid chordomas account for greater than 90% of cases (I. J. Lee et al., 2017). Poorly differentiated chordomas show loss of the chromatin remodeling protein SMARCB1/INI1 and mostly are found in pediatric and young-adult cases (Yeter et al., 2019). Less is known about the epidemiology of dedifferentiated chordomas, but nearly 50% of cases are found in recurrences of patients with prior conventional chordoma (Hung et al., 2020).

1.6.2 Chordomas are hypothesized to derive from vestiges of the embryological notochord

Originally postulated by Rudolf Virchow to derive from cartilaginous lineages, observational and experimental lines of evidence have since converged on a model proposing that chordomas derive from remnants of the notochord (Sahyouni et al., 2018). The notochord is a mesoderm-derived structure and a conserved trait central to defining the chordata phylum (Cleaver & Krieg, 2001). In humans, it plays critical structural and signaling roles in embryologic development and is a key determinant of left-right asymmetry in complex vertebrates (Cleaver & Krieg, 2001). In humans, the definitive notochord initiates centrally and extends in both cranial and caudal directions (de Bree et al., 2018). After its critical role in patterning, human notochord proceeds to involute. After 9 weeks gestation, notochordal tissue is only present within developing

intervertebral disks (Pazzaglia et al., 1989). By a year of postnatal development, notochord tissue is generally absent (Pazzaglia et al., 1989); however, a number of studies have identified candidate remnant tissues of the notochord suggestive of potential origins for chordoma (Weiss et al, 1952; Amprino, 1934). Chordomas universally overexpress brachyury, a master transcription factor encoded by *TBXT/T* that is highly specific to notochordal tissue, and duplications of *TBXT* are found in a hereditary form of chordoma (Vujovic et al., 2006; X. R. Yang et al., 2009).

1.6.3 Limited treatment options are available for chordoma

Chordomas are slow growing tumors, but typically present at advanced stages due to largely nonspecific symptoms such as headache for skull base tumors and back pain for vertebral and sacral tumors. Surgery is the most effective form of treatment, but is associated with substantial morbidity, and local recurrence is the best predictor of long-term mortality.

Conventional/chondroid chordomas are largely resistant to conventional chemo- and radiotherapies (Azzarelli et al., 1988; Catton et al., 1996; Wedekind et al., 2021). While high-dose radiotherapy is advised on a case-by-case basis as an adjuvant to surgery, and limited studies involving chordoma and other bone tumors demonstrate promising local control rates (DeLaney et al., 2014), this approach has not been shown to provide a definitive survival benefit (Yolcu et al., 2019). There is also limited recent evidence for a benefit of control of recurrent disease in skull base chordomas with stereotactic radiosurgery compared to re-resection or chemotherapy (Evans et al., 2020).

Systemic medical therapies for chordoma have not had great success. There have been 11 completed Phase II clinical trials of systemic treatments in chordoma patient populations without any clearly efficacious results (Wedekind et al., 2021). Targeted therapies have focused on candidate pathways identified from the overexpression of epidermal growth factor receptor (EGFR) and platelet-derived growth factor receptor beta (PDGFRB) and alterations in the cell-cycle genes CDKN2A/B and homologous repair pathways. Other approaches have included generating a vaccine to target brachyury, as its expression is highly unique to chordoma tumor cells. Trials using the PDGFR inhibitor imatinib and several EGFR inhibitors have accrued the greatest number of patients and resulted in scattered cases of partial responses and many cases of stable disease but did not achieve their primary endpoints for efficacy (Wedekind et al., 2021).

1.6.4 Chromatin modifiers are among the most commonly mutated in chordoma

The mutational landscape of chordoma is largely quiescent relative to other malignancies (Tarpey et al., 2017). In the largest cohorts of chordomas that have undergone sequencing and copy number analysis, chromatin remodeling genes including *SETD2*, *PBRM1*, and the poorly differentiated subtype-associated *SMARCB1* are among the most frequently altered. Additional SWI/SNF complex members *ARID1A* and *ARID1B* were identified as recurrently altered in individual cohorts as well (Tarpey et al., 2017; L. Wang et al., 2016).

1.6.5 Preclinical data show brachyury is a critical vulnerability of chordomas

Loss of the notochordal transcription factor brachyury has the greatest deleterious effect in genome-wide screens of cell line models of chordoma (Sharifnia et al., 2019). It mediates a critical autoregulatory loop, in which it promotes its own super-enhancer supported transcription

(Sheppard et al., 2021), rendering chordoma cells sensitive to small molecule inhibitors of transcriptional machinery including THZ1 and NVP-2 (Sharifnia et al., 2019). These approaches have a variety of off-target effects compared to targeted *in vitro* approaches that reduce brachyury levels, and efforts to target brachyury directly with small-molecule inhibitors or targeted degradation approaches, while incredibly challenging, are underway (H. Robinson et al., 2020; Samarasinghe et al., 2021; Sheppard et al., 2021).

1.6.6 Maintenance of low H3K27me3 may be a prognostic marker and targetable vulnerability in chordoma

Recent work from a screen of epigenetic compounds in chordoma revealed that cell line models are highly sensitive to the H3K27 demethylase inhibitor KDOBA67 (Cottone et al., 2020). Cottone et al. found that the genome-wide increase in H3K27me3 resulted in downregulation of brachyury expression. Furthermore, brachyury re-expression partially rescued deficits in cell proliferation, highlighting the approach as a way to target brachyury. More recently, a single-institution study assessing H3K27me3 levels of 145 chordomas across tumor sites revealed that low H3K27me3 status was associated with worse overall and recurrence-free survival (OS and PFS) (Wei et al., 2022). These changes remained significant after adjusting for age, site, gender, and recurrence status, further supporting a role for H3K27me3 maintenance in chordomas.

1.6.7 Chordoma cells display unique structural features

While genomic, epigenomic, and transcriptomic studies have yielded promising preclinical targets, the translational impact has been limited. Chordomas have extremely distinct histology, and the metabolic states of these tumors have been largely unexplored. First described by

Virchow and then Muller, the heterogenous mix of cells embedded in dense extracellular matrix in chordomas include smaller spindle-shaped cells and large highly vacuolated cells. Virchow termed this highly vacuolated cytoplasm 'physaliferous' (blister bearing) (Sahyouni et al., 2018). The precise contents and function of these vacuoles remain unclear, but they mirror the vacuolated cells see in the notochord (Corallo et al., 2015).

1.6.8 Studies of chordoma metabolism have been limited

Initial characterizations of chordoma cell lines revealed that their growth improves with collagen and slightly alkaline conditions and that growth rates remain unchanged in either hypoxic or low-glucose (3-fold reduction) conditions (Ostroumov & Hunter, 2007; C. Yang et al., 2010). Despite their slow growth clinically, chordomas are still significantly metabolic active as they exhibit moderate uptake of the glucose analog and imaging tool fludeoxyglucose (FDG) (Olson et al., 2021).

Additional studies evaluating changes that occur in recurrence have also examined chordoma metabolism. A single-patient comparison of recurrent and primary tissue demonstrated carbohydrate metabolism as significantly increased in recurrence (S. Chen et al., 2015). A more expansive study profiling proteomics in rapid vs. slow recurrence in a cohort of skull base chordomas identified asparagine synthetase (ASNS) as a prognostic marker and validated its importance for growth *in vitro* (Bai et al., 2021). Altogether, despite the importance of metabolic reprogramming in cancer and the evidence of unique cellular structures and biosynthetic pathways in chordoma, little is known about the metabolic pathways chordoma cells rely on for growth.

1.7 Increasing understanding of the biology of rare bone and brain tumors lays the groundwork for needed therapeutic development

Discoveries across genomics, epigenomics, and metabolism in the past 25 years have provided detailed molecular portraits of the brain and bone tumor landscapes and provided critical information for understanding tumor biology, especially for rare tumors. Improvements in survival rates for these two classes of tumor have shown few improvements, and a better understanding of the heterogeneous drivers of these tumors is necessary to develop targeted therapies. The work presented in the following chapters leverages approaches across metabolism and multi-omics to further characterize the molecular alterations that drive brain and bone cancers and test novel treatment strategies.

Chapter 2
Common Molecular Features of H3K27M DMGs and PFA Ependymomas Map to Hindbrain Developmental Pathways

2.1 Introduction

Brain tumors account for the highest amount of mortality among all pediatric cancers (Curtin et al., 2016). Moreover, in contrast with other pediatric cancers, fatality rates in pediatric brain cancer have remained stable (D. A. Siegel et al., 2020). Unlike in adult populations, pediatric brain tumors frequently arise in infratentorial regions (I F Pollack, 1999), suggesting a spatiotemporal susceptibility to tumorigenesis. Indeed, transcriptional analysis of pediatric brain tumors including medulloblastoma, gliomas, and ependymomas suggest shared expression programs within certain developmental lineages (C. C. L. Chen et al., 2020; Filbin et al., 2018; Gillen et al., 2020; Gojo et al., 2019; Hendrikse et al., 2022; Jessa et al., 2019; K. S. Smith et al., 2022; Vladoiu et al., 2019).

2.1.1 Group A posterior fossa ependymomas (PFAs) and diffuse midline gliomas (DMGs), H3K27-altered exhibit similar epigenetic landscapes of depleted H3K27me3

Group A posterior fossa ependymomas (PFAs) and diffuse midline gliomas (DMGs), H3K27-altered, are characterized by global reduction of the histone modification histone 3 lysine 27 trimethylation (H3K27me3), a mark associated with gene repression (Bender et al., 2013; Lewis et al., 2013; Schwartzentruber et al., 2012; Sturm et al., 2012; G. Wu et al., 2012). Global H3K27me3 depletion is mediated by inhibition of the function of the polycomb repressive

complex-2 (PRC2), which contains the H3K27-specific methyltransferase enhancer of zeste homolog 2 (EZH2). The majority of DMGs harbor missense mutations in histone 3-encoding genes (primarily *H3-3A* and *H3C2*) (Schwartzentruber et al., 2012; Sturm et al., 2012; G. Wu et al., 2012) that result in a lysine-to-methionine substitution at position 27 (H3K27M). This histone tail mutation inhibits PRC2 activity (Bender et al., 2013; Chan et al., 2013; Lewis et al., 2013). Most PFAs, in contrast, exhibit overexpression of EZH inhibitory protein (EZHIP) (Antin et al., 2020; K W Pajtler et al., 2018) that similarly suppresses PRC2 activity. EZHIP contains a methionine residue at position 406 that mimics the H3K27M mutant histone (Hubner et al., 2019; S U Jain et al., 2019; Siddhant U Jain, Rashoff, et al., 2020; Piunti et al., 2019; Ragazzini et al., 2019). In addition to depleting H3K27me3, each of these tumors demonstrates increased global levels of the activation-associated mark H3K27 acetylation (H3K27ac) (S U Jain et al., 2019; Krug et al., 2019a; Nagaraja et al., 2017; K W Pajtler et al., 2018; Panwalkar et al., 2021; Piunti et al., 2017, 2019; Ragazzini et al., 2019).

2.1.2 PFAs and DMGs rely on residual H3K27me3 methyltransferase activity

With their epigenetic similarities, H3K27M DMGs and PFAs also share sensitivities to inhibitors targeting histone-modifying enzymes, including histone lysine demethylases, and histone deacetylases (Anastas et al., 2019; Grasso et al., 2015; Hashizume et al., 2014; Nagaraja et al., 2017; Panwalkar et al., 2021; Piunti et al., 2017). Although H3K27me3 levels are greatly reduced globally, specific regions of the genome retain H3K27me3, most of which are CpG islands commonly known to be canonical PRC2 binding sites (Bayliss et al., 2016; Bender et al., 2013; Harutyunyan et al., 2019; S U Jain et al., 2019; S C Mack et al., 2014). Moreover, both tumor types appear to rely on residual EZH2 activity. Both pharmacologic and genetic inhibition

of EZH2 reduce tumor viability in models of H3K27M DMGs and PFAs (S C Mack et al., 2014; Michealraj et al., 2020; Mohammad et al., 2017), suggesting that the tumors require residual PRC2 activity.

2.1.3 PFAs and DMGs likely arise in neighboring regions of the developing human hindbrain

In addition to their molecular similarities, PFAs and H3K27M DMGs arise in nearby structures associated with the hindbrain. The floor of the fourth ventricle is formed by the pons and the roof by the cerebellum. Whereas the majority of H3K27M DMGs arise from the pons, most PFAs are found in association with the fourth ventricle and cerebellum (Mackay et al., 2017; Kristian W Pajtler et al., 2015). Moreover, it is increasingly recognized that a rare population of H3-wildtype, low-H3K27me3 DMGs overexpress EZHIP, and that a similarly small percentage of PFAs harbor H3K27M mutations (Castel et al., 2020; Mariet et al., 2022; K W Pajtler et al., 2018; D Pratt et al., 2020). The extent to which these two tumor subtypes share biology, and how this relates to hindbrain development, remains an unanswered question. To address this gap in our knowledge, I hypothesized that shared molecular features of H3K27M DMGs and PFAs will reveal key programs within the developing human hindbrain that may drive susceptibility to PRC2-inhibiting alterations. I addressed this hypothesis by examining genomic, transcriptomic, and epigenomic characterizations of each tumor type to characterize shared biology to better understand the origins and potential vulnerabilities of these tumors.

2.2 Methods

2.2.1 Copy number alteration analyses

Arm-length copy number alterations for PFAs and DMGs were obtained from supplementary data of published datasets (Mackay et al., 2017; Kristian W Pajtler et al., 2015). For tumor samples from the NCI, tumors were classified with the Molecular Neuropathology classifier (v11b6) (Capper et al., 2018). Genomic Identification of Significant Targets in Cancer (GISTIC) version 2.0.23 was used to identify and score broad copy number events. Score cutoffs of +/-0.3 were used to call a gain or loss of a chromosome arm consistent with the methods employed by Mackay et al. (Mackay et al., 2017).

2.2.2 Gene expression analyses

PFA (GSE100240, GSE64415) microarray expression data and DMG (Mackay et al. 2017) meta-analysis expression data were obtained. A limited differential expression analysis was conducted by dividing the expression datasets by the variable of interest and applying a two-sided student's t test. Multiple testing correction was applied by the Benjamini-Hochberg method. For gene set enrichment analysis (GSEA), ranked gene lists were generated by taking the product of the negative log-10 transformation of the q-value and the difference in expression for each gene. GSEA 4.2.3 was used to run GSEA Preranked on the resulting gene lists with the following parameters: 15-500 as min-max gene set size; weighted scoring scheme; meandiv normalization; Abs_max_of_probes mode. For standard deviation analyses, the probe with the maximum average value across samples in PFAs was used. Any genes that did not appear in both gene sets were excluded from plotting.

2.2.3 Protein immunoblotting

Whole cell protein lysates were isolated by treating phosphate buffered saline (PBS)-washed cell pellets with Pierce™ Radioimmunoprecipitation assay (RIPA) buffer (Thermo Fisher Scientific #89900) with added protease inhibitor cocktail (Sigma #P8340) for 20 minutes and then pelleting to remove debris. Protein quantification was performed by using Pierce™ BCA Protein Assay Kit (Thermo Fisher Scientific #23225). Equal masses of each sample were then loaded into 4–15% Mini-PROTEAN® TGX™ Precast Protein Gels (BIO-RAD #4561084) for electrophoresis, and protein was transferred to a PVDF membrane using Trans-Blot Turbo RTA Mini 0.2 μm Transfer Kit (BIO-RAD #1704272) systems. Membranes were blocked with 5% blotting-grade milk blocker (BIO-RAD #1706404) in tris buffered saline (TBS) supplemented with 0.1% Tween-20 (Thermo Fisher Scientific #J20605.AP) (TBST) at room temperature for one hour with rocking agitation. Membranes were then incubated with specific primary antibodies at 4°C overnight on a rocker. After three 10-minute washes with TBST, membranes were incubated with either Goat Anti-Rabbit IgG (H + L)-HRP Conjugate (BIO-RAD #1706515) or Goat Anti-Mouse IgG (H + L)-HRP Conjugate (BIO-RAD #1706516) secondary antibodies according to the primary antibodies' specifications at room temperature for one hour. Then, membranes were washed for 10 minutes with TBST three times, rinsed with TBS, and incubated with either Pierce™ ECL Western Blotting Substrate (Thermo Fisher Scientific #32106) or reagents for signal detection on an autoradiography film (dotScientific #BDB57-Lite). The following primary antibodies were used: MDMX (MDM4), polyclonal (Proteintech 17914-1-AP) at 1:1000 primary dilution and 1:5000 secondary dilution, beta-Actin (Sigma) at 1:20,000 and 1:20,000, and EZH2 (Cell Signaling, D269) at 1:5,000 and 1:10,000.

2.2.4 Histone 3 lysine 27 trimethylation (H3K27me3) ChIP-seq analyses

For samples from Bender et al. (Bender et al., 2013), BED files with hg19 alignment were obtained from the authors. BED files aligned to hg19 from Harutyunyan et al. (Harutyunyan et al., 2019) were obtained from the Genetics and Genomics Analysis Platform (GenAP). Data aligned to hg19 from Bayliss et al. (Bayliss et al., 2016) (GSE89451) and Mack et al. (S C Mack et al., 2014) (GSE89451) were obtained from GEO. Bedtools 2.29.2 was used to intersect peaks from each dataset with a custom BED file containing genes and their promoters defined as 2 kb upstream from the transcription start site (TSS). Genes with peaks in greater than two-thirds of tumor samples for each class of tumor were defined as common H3K27me3-retaining genes and used for downstream analyses.

2.2.5 H3K27ac and enhancer analyses

I obtained published H3K27M DMG-specific enhancer-associated genes from Krug et al. (Krug et al., 2019a) and PFA-specific enhancer-associated genes from Mack et al. (Stephen C Mack et al., 2018). I computed the overlap in genes from these two gene sets. Each of these curated gene sets was in part derived from comparison against enhancer profiles of other brain tumors. Therefore, to identify enhancers that were unique to each tumor type independent of these comparisons with non-PFAs and non-H3K27M DMGs, I accessed the ChIP-seq files available from each study and reanalyzed them. I conducted Rank-ordering of Super Enhancer (ROSE) analysis to call super enhancers for each tumor. I examined if PFA-specific enhancers from the original analysis were called as super enhancers in any of the DMG ChIP-seq samples. If an enhancer appeared at least once in the DMG samples, I included it the shared enhancer list. I repeated the converse process for DMG-specific enhancers. This method allowed us to avoid biases generated by comparisons with non-PFAs and non-H3K27M DMGs. Pathway analyses of

shared or unique enhancers were completed using Enrichr (E. Y. Chen et al., 2013; Kuleshov et al., 2016; Xie et al., 2021). Volcano plots were generated using code generated by Appyter.

2.2.6 Single-cell RNA-seq analyses

Published RNA-Seq by Expectation-Maximization (RSEM) values were obtained for PFA and DMG datasets (Filbin et al., 2018; Gojo et al., 2019) and loaded as Seurat objects using Seurat (4.1.1) and SeuratObject (4.1.0). Each dataset was independently normalized, and then variable features were selected. Seurat's SelectIntegrationFeatures and FindIntegrationAnchors were sequentially applied to the datasets, and then IntegrateData was applied based on the anchors identified. The resulting integrated dataset underwent dimensional reduction and clustering. FindConservedMarkers was used to identify differentially expressed genes by cluster. Developing brain single-cell RNA-seq data from Aldinger et al. (Aldinger et al., 2021) were obtained from https://cbl-dev.cells.ucsc.edu and analyzed using Seurat. AddModuleScore was used to generate a score for the H3K27me3-retained gene signature. Single-cell RNA-seq data from Eze et al. [17] was obtained from https://cells-test.gi.ucsc.edu/?ds=early-brain and processed using Seurat as described in [17], and *CRABP1* feature plots were generated using the Seurat ViolinPlot function, ggplot2 (3.3.5), and ggprism (1.0.3). For area under the curve measurements from the Sepp et al. (Sepp et al., 2021) dataset, raw count measurements were processed with AUCell (from Bioconductor 3.16) using the H3K27me3-retained gene signature.

2.2.7 Allen Brain Atlas analyses

Human data were obtained from BrainSpan, and mouse data were obtained from the Allen Developing Mouse Brain map. All resulting analyses were completed with GraphPad Prism 9.1.1.

2.2.8 Statistical analyses

Graphs were plotted and statistical analyses were performed using Prism software (version 9.1.1, Graphpad, La Jolla, CA). Data are represented as the means ± standard deviation (S.D.) or as violin plots. The sample size (n) along with the statistical test performed and corresponding p-values are indicated in each figure or figure legend. Progression-free and overall survival metadata, when available, was analyzed comparing survival curves utilized the Log-Rank (Mantel-Cox) test for significance. Unpaired two-tailed, two-sided, Student's t test or one-way ANOVA followed by multiple comparisons analysis using either Ordinary one-way ANOVA or Kruskal-Wallis tests were used to analyze data. Data were considered significant if p values, adjusted where appropriate, were below 0.05 (95% confidence intervals).

2.3 Results

2.3.1 H3.1K27M and EZHIP-DMGs share key copy-number alterations with PFAs

To characterize the shared features of H3K27M DMG and PFAs, I began by comparing copy number changes in two published data sets and from Mackay et al. (2017, H3K27M DMG = 295) and Pajtler et al. (2015, PFA = 240) (Mackay et al., 2017; K W Pajtler et al., 2018). Overall, H3K27M DMGs demonstrated far greater genomic instability compared to PFAs. Nevertheless, comparison of copy number alterations demonstrated that PFAs harbor several recurrent chromosome arm alterations that are shared with H3K27M DMGs. These included gain of the

long arm of chromosome 1 (1q) and loss of 6q (Figure 2.1A). I validated these findings in two independent, non-overlapping tumor cohorts (PFA=573 and H3K27M=271) curated by the National Cancer Institute (NCI) (Fig. 2.1B).

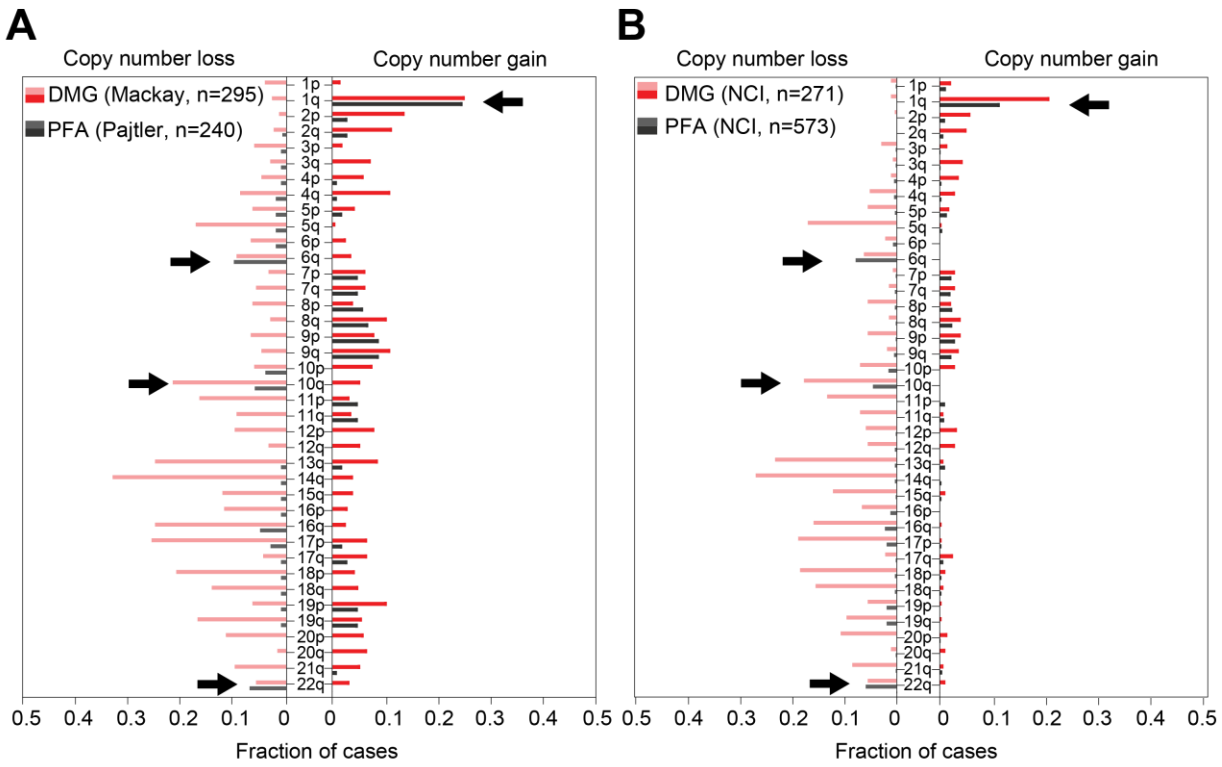

Figure 2.1 PFAs and DMGs share copy number alterations.

A. Copy number profiles (copy number loss left panel, copy number gain right panel) of H3K27M DMGs (Mackay et al., 2017, n=295) (Mackay et al., 2017) and PFAs (Pajtler et al., 2015, n=240) (Kristian W Pajtler et al., 2015) from published DNA methylation cohorts. Arrows indicate common shared recurrent alterations (more than 5% of tumors in all cohorts in **A** and **B** with known survival associations in PFAs.
B. Copy number profiles (copy number loss left panel, copy number gain right panel) of H3K27M DMGs (n=271) and PFAs (n=573) from the National Cancer Institute (NCI). Arm-level copy number gain/loss calls were made using GISTIC score cutoffs of +/-0.3. X-axis = chromosomes and Y-axis = fraction of cases.

2.3.2 The 1q gene MDM4 is commonly upregulated in 1q gain cohorts of PFAs and H3K27M DMGs and associated with PFA survival

I next asked whether 1q gain is associated with copy-number driven transcriptional changes that could point to potential therapeutic targets. Many, but not all genes along 1q showed increased expression in tumors with 1q gain compared to those without 1q gain (Figure 2.2A). Among these genes, MDM4 regulator of p53 (*MDM4)* was expressed more highly in 1q gain cohorts of both PFAs and DMGs (Figure 2.2A). Additionally, its expression was associated with worse survival in PFAs (Figure 2.2B).

While the majority of available H3K27M DMG and PFA cell lines have 1q gain, making 1q-gain-vs.-no-gain comparisons *in vitro* challenging, I next asked whether MDM4 overexpression might be specific to H3K27M DMGs and PFAs. Compared to other glioma and ependymoma models, as well as to an immortalized normal human astrocyte cell line, I found expression of MDM4 was elevated in H3K27M DMG and PFA models (Figure 2.2C).

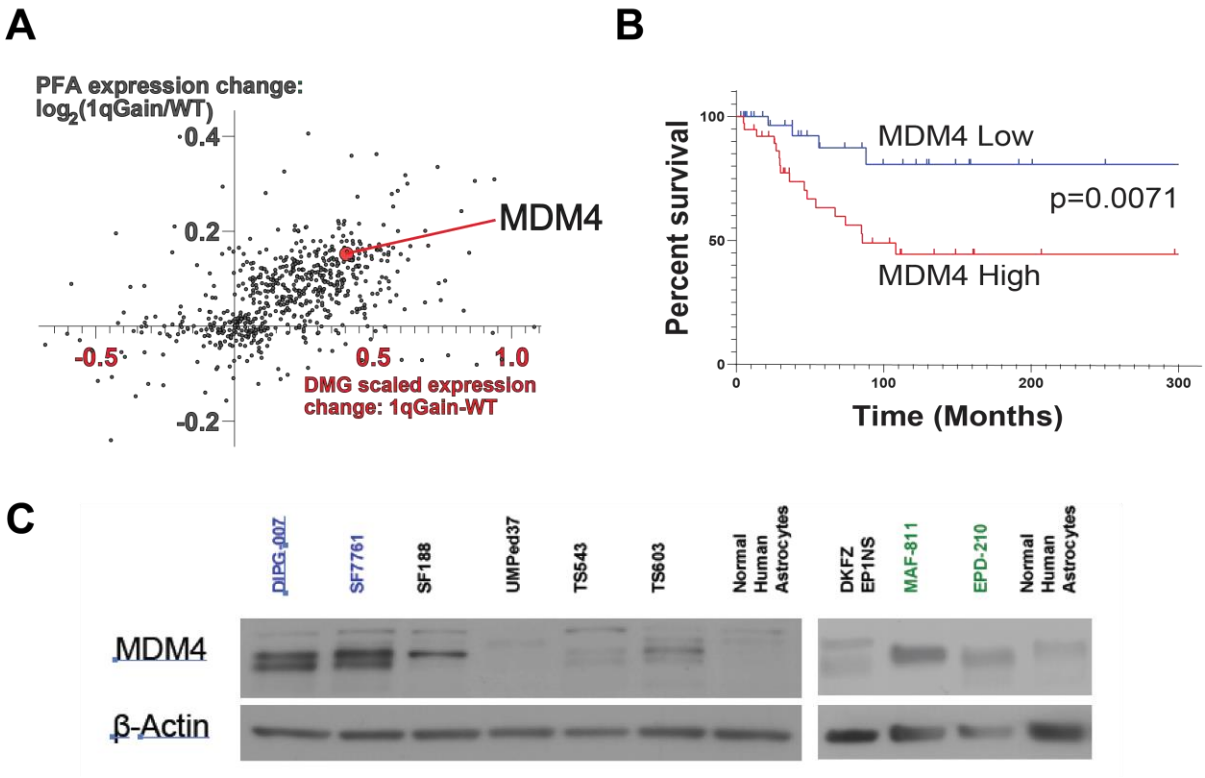

Figure 2.2 MDM4 is commonly upregulated in PFAs and DMGs.

A. Analysis of differential expression of genes on chromosome 1q comparing cohorts of DMGs (x-axis) or PFAs (y-axis) with 1q gain to those without 1q gain.
B. Survival curves comparing patients with PFAs exhibiting high *MDM4* expression compared to PFAs with low expression.
C. Immunoblots showing relative MDM4 expression in H3K27M DMG cell lines (DIPG-007 and SF7761) compared to non-histone-mutant gliomas and nonmalignant cell lines (SF188, UMPed37, TS543, TS603, and Normal Human Astrocytes) or in PFA cell lines (MAF-811, EPD-210) compared to non-PFA ependymoma (DKFZ EP1NS) or nonmalignant controls (Normal Human Astrocytes).

2.3.3 Patterns in 1q gain highlight differences between subtypes of H3K27-altered DMGs

Gain of 1q has previously been associated with worse overall survival outcome in PFAs in multiple studies (Godfraind et al., 2012; Mendrzyk et al., 2006; K W Pajtler et al., 2018; Rajeshwari et al., 2016; Varela et al., 2012), a finding reproduced in our investigation of the NCI PFA cohort (Figure 2.3A). I noted that 1q gain was also the most common recurrent arm-length gain in H3K27M DMGs; however, there was no significant difference in overall survival in H3K27M DMGs with or without 1q gain from the published cohorts (Figure 2.3B). Previous work had demonstrated differences in the copy-number landscapes based on the type of H3 mutation with H3.3- versus (vs.) H3.1- mutant tumors exhibiting increased genomic instability (Mackay et al., 2017). I examined copy number trends with respect to H3.3 vs. H3.1 status in the NCI cohort and evaluated how H3 wildtype (H3-WT) EZHIP-expressing DMGs compared to each histone subtype. I observed that H3.1-mutant and EZHIP-expressing DMGs had fewer arm-length copy-number events (Figure 2.3C) and focal amplifications and deletions (Figure 2.3D) compared to H3.3 mutant DMGs. Gain of 1q was observed at a higher frequency in H3.1 vs. H3.3K27M DMGs in both the Mackay et al. (H3.1=35.1% vs. H3.3= 10.5%; Figure 2.3E) and the NCI cohort (H3.1=41.7% vs. H3.3= 23.9%; Figure 2.3F). Notably, half of EZHIP expressing DMGs also exhibited 1q gain (Figure 2.3F).

Unexpectedly, 1q gain was associated with better overall survival in H3.1K27M tumors (Figure 2.3G), but not in H3.3K27M-mutant tumors (Figure 2.3H) or in other pediatric brain tumors—including other pediatric gliomas (Mackay et al., 2017, 2018), other posterior fossa ependymomas (Cavalli et al., 2018), and medulloblastomas (Cavalli et al., 2017)—with the

exception of a small sample-size cohort of group 4 medulloblastoma (Figure 2.4H) This intriguing finding of a 1q gain survival association in H3.1K27M tumors was unable to be assessed further in the NCI cohort as the majority of these tumors did not have sequencing information to distinguish H3.1 from H3.3 mutations.

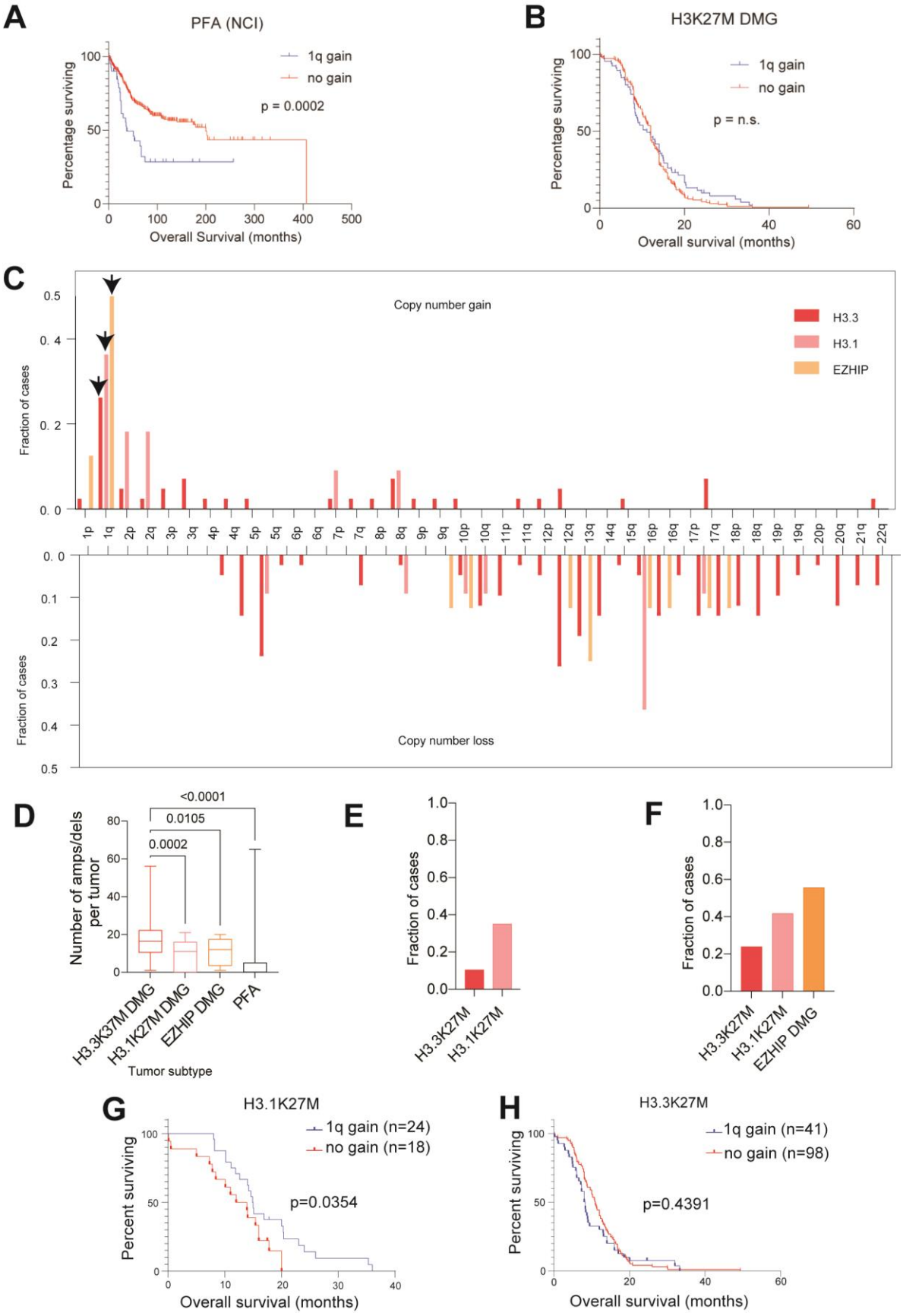
A
PFA (NCI)
1q gain
no gain
p = 0.0002
Percentage surviving
Overall Survival (months)
B
H3K27M DMG
1q gain
no gain
p = n.s.
Percentage surviving
Overall survival (months)
C
Copy number gain
H3.3
H3.1
EZHIP
Fraction of cases
Copy number loss
D
<0.0001
0.0105
0.0002
Number of amps/dels per tumor
H3.3K37M DMG
H3.1K27M DMG
EZHIP DMG
PFA
Tumor subtype
E
Fraction of cases
H3.3K27M
H3.1K27M
F
Fraction of cases
H3.3K27M
H3.1K27M
EZHIP DMG
G
H3.1K27M
1q gain (n=24)
no gain (n=18)
p=0.0354
Percent surviving
Overall survival (months)
H
H3.3K27M
1q gain (n=41)
no gain (n=98)
p=0.4391
Percent surviving
Overall survival (months)

Figure 2.3: H3.1K27M and EZHIP-DMGs share key copy-number alterations with PFAs.

A. Overall survival (months, X-axis) analysis of PFA ependymomas from the NCI cohort with (n=41) or without (n=365) 1q gain.
B. Overall survival (months, X-axis) analysis of H3K27M DMGs with (n=66) or without (n=178) 1q gain.
Data in **A**, **B** analyzed using Kaplan-Meier, Log-Rank test with 95% confidence intervals.
C. Frequency of chromosome arm-level copy number alterations (copy number gain top panel, copy number loss bottom panel) for H3K27-altered DMGs from b segregated by molecular alterations - H3.3 mutant (n=42), H3.1 mutant (n=11) and H3-wildtype (H3-WT), EZHIP-expressing (n=8). X-axis = fraction of cases and Y-axis = chromosomes.
D. Quantification of the frequency of amplifications (amps) and deletions (dels, Y-axis) in DMGs segregated by molecular alterations (X-axis) and in PFAs from the NCI cohort. Data analyzed by one-way ANOVA with 95% confidence intervals. H3.3 mutant (n=48), H3.1 mutant (n=12), and EZHIP (n=8).
E. Frequency of 1q gain (Y-axis) for subtypes of H3K27M DMG and PFAs from published datasets depicted in a. H3.3 mutant (n=245), H3.1 mutant (n=49), and PFA (n=240). DMG sample pHGG_META_0223 was excluded from as it is H3.2-mutant.
F. Frequency of 1q gain (Y-axis) for subtypes of H3K27-altered DMG and PFA ependymoma from the NCI cohort depicted in 1b. H3.3 mutant (n=42), H3.1 mutant (n=11), and EZHIP (n=8).
G. Overall survival (months) analysis of 1q gain in H3.1K27M DMGs with (n=24) or without (n=18) 1q gain.
H. Overall survival (months) analysis of 1q gain in H3.3K27M DMGs with (n=41) or without (n=98) 1q gain.
Data in **G**, **H** analyzed using Kaplan-Meier with Log-Rank test with 95% confidence intervals.

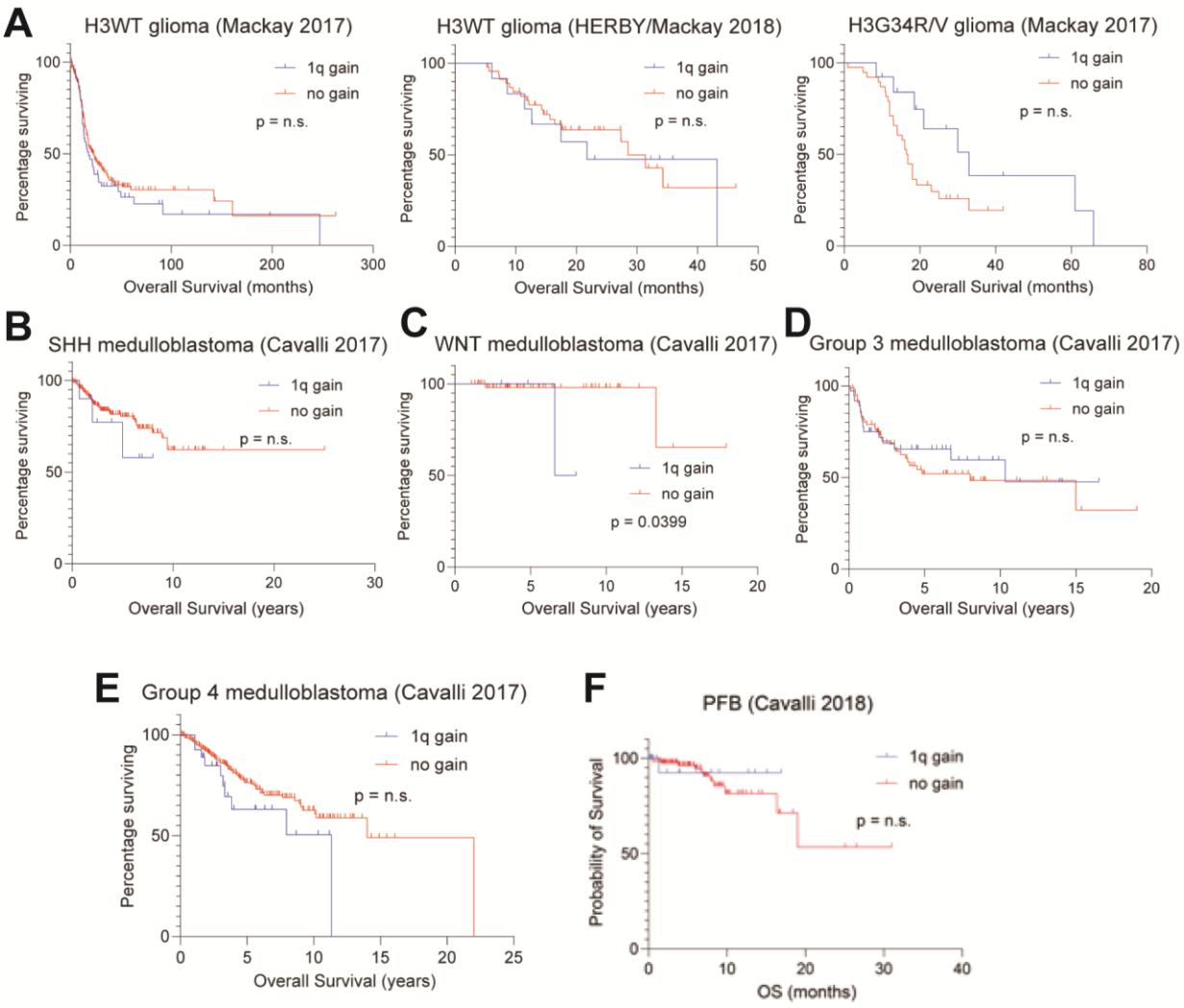

Figure 2.4: 1q gain is not prognostic in other pediatric brain tumors.

Overall survival analyses of 1q gain in other pediatric brain tumor cohorts from Mackay et al. (2017) and Mackay et al. (2018) pediatric gliomas in **A**, Cavalli et al. (2017) medulloblastomas in **D-E**, and Cavalli et al. (2018) PFB ependymomas in **F**. Sample sizes with or without 1q gain are as follows: H3WT, Mackay 2017- n=54, 179; H3WT, HERBY- n=12, 46; H3G34R/V- n=13, 38; SHH- n=10, 162; WNT- n=4, 59; Group 3- n= 36, 77; Group 4- n=28, 236; PFB- n=20, 117. Data analyzed using Kaplan-Meier, Log-Rank test with 95% confidence intervals.

2.3.4 The recently identified PFA prognostic marker 6q loss recurs in DMGs and trends toward worse survival in DMGs

In addition to recurrent 1q gain, the other alterations observed in at least 5% of each cohort were losses of 6q, 10q, and 22q (Figure 2.1A). Loss of 6q has recently been associated with a subset of PFAs with poor survival rates (Baroni et al., 2021). Assessment of the 6q loss in the DMG cohort demonstrated a trend toward worse survival in 6q loss tumors (Figure 2.5A). In H3K27M DMGs, there was no major difference in 6q status when comparing H3.1 and H3.3-mutant cohorts (Figure 2.5B). Given the genomic instability of DMGs in general, I asked if 6q alterations were associated with high arm-level alterations. In every cohort, tumors with 6q loss were associated with higher levels of arm-level losses across the genome. In contrast, the frequency of arm gains in these tumors was not significantly different from non-6q loss tumors in each cohort (Figure 2.5C). I hypothesized that despite the relatively quiescent genome PFAs exhibit compared to H3K27M DMGs, the two tumor types might share certain alterations that permit or enhance tumorigenicity in the context of H3K27me3 dysregulation. Our findings highlight a spectrum of genomic alteration patterns that varies by driving alteration with H3.3-mutant gliomas exhibiting the greatest alteration frequencies.

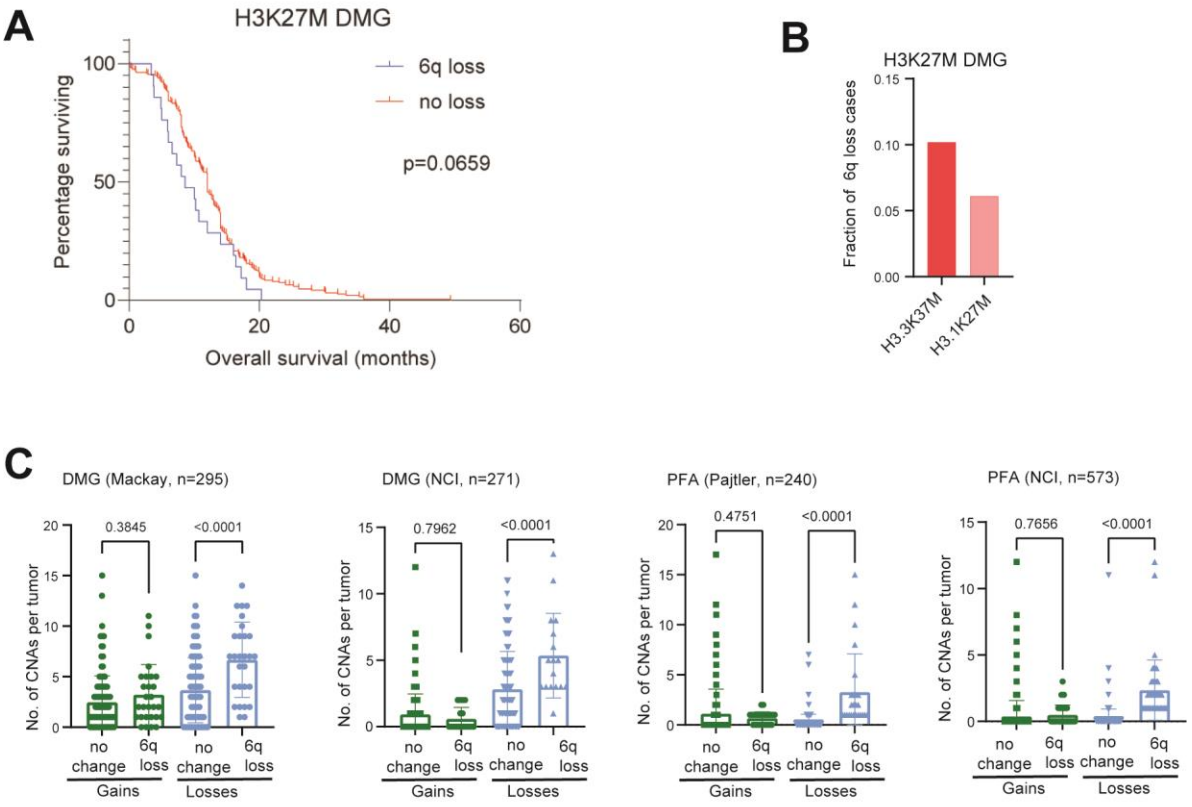

Figure 2.5: The recently identified prognostic marker of 6q loss for PFA ependymomas may play a role in H3K27M DMG biology.

A. Overall survival (months) analysis of H3K27M DMGs with (n=21) or without (n=216) 6q loss. Data analyzed using Kaplan-Meier, Log-Rank test with 95% confidence intervals.
B. Frequency of 6q loss (Y-axis) for subtypes of H3K27M DMG from published datasets depicted in 1a. H3.3 mutant (n=245) and H3.1 mutant (n=49).
C. Number of copy number alterations (CNAs, Y-axis) in DMGs and PFAs. All four cohorts were segregated by tumors overall chromosomal gains (green) with (n=28-Mackay, 17-NCI:DMG, 25-Pajtler, 45-NCI:PFA) or without 6q loss (n=267-Mackay, 254-NCI:DMG, 215-Pajtler, 528-NCI:PFA), or overall chromosomal losses (blue). Data analyzed by two-sided, unpaired, two-tailed t test.

2.3.5 **ACVR1** *expression is prognostic in PFAs and is associated with transcriptomic signatures observed in* **ACVR1**-*mutant DMGs.*

Due to the observed differences between H3.1 and H3.3 K27M DMGs and 1q status, I extended our comparative analysis to include other genomic alterations that segregate with mutant histone subtypes. Activating mutations in activin A receptor type 1 (*ACVR1*) occur more frequently in H3.1 vs. H3.3 DMGs (Buczkowicz et al., 2014; Castel et al., 2018; Fontebasso et al., 2014; Mackay et al., 2017). Initial characterizations of EZHIP-expressing DMGs also revealed a high frequency of *ACVR1* mutations (Castel et al., 2020). Concordant with our findings of 1q gain enrichment in H3.1 tumors, I observed increased frequency of *ACVR1* mutations in 1q gain tumors vs. non-1q gain tumors (Figure 2A).

Recent work has identified rare mutations of *ACVR1* in PFA tumors (Drew Pratt et al., 2022). These findings prompted us to investigate *ACVR1* in PF ependymomas. First, I observed increased expression of *ACVR1* in PFAs compared to group B posterior fossa ependymomas (PFBs), a subtype of PF ependymomas that lacks EZHIP expression (K W Pajtler et al., 2018) (Figure 2B). I found tumors with the highest levels of *ACVR1* expression in the Pajtler et al. cohort to be associated with worse progression-free and overall survival outcomes (Figure 2C-D). I next investigated whether *ACVR1*-mutant H3K27M DMGs and *ACVR1*-high PFAs shared transcriptomic signatures. I found that both tumors demonstrated enrichment of many *ACVR1*-mutant (Hoeman et al., 2019) and H3.1K27M-enriched (Castel et al., 2015) pathways including hypoxia/HIF1-α transcription factor network and epithelial-to-mesenchymal transition, as well as glycolysis, TNFα/NFkB signaling, and mTORC1 signaling (Figure 2E-G).

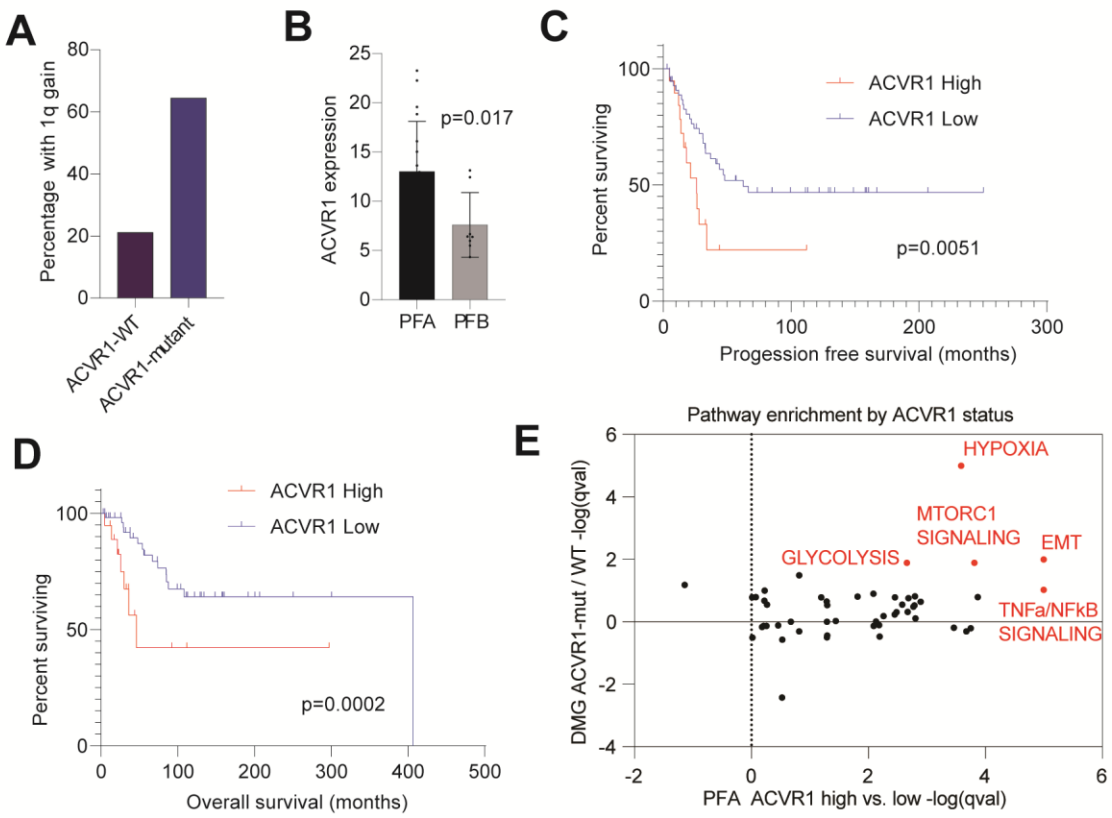
A
Percentage with 1q gain
ACVR1-WT
ACVR1-mutant
B
ACVR1 expression
p=0.017
PFA
PFB
C
ACVR1 High
ACVR1 Low
Percent surviving
p=0.0051
Progession free survival (months)
D
ACVR1 High
ACVR1 Low
Percent surviving
p=0.0002
Overall survival (months)
E
Pathway enrichment by ACVR1 status
HYPOXIA
MTORC1 SIGNALING
EMT
GLYCOLYSIS
TNFa/NFkB SIGNALING
DMG ACVR1-mut / WT -log(qval)
PFA ACVR1 high vs. low -log(qval)

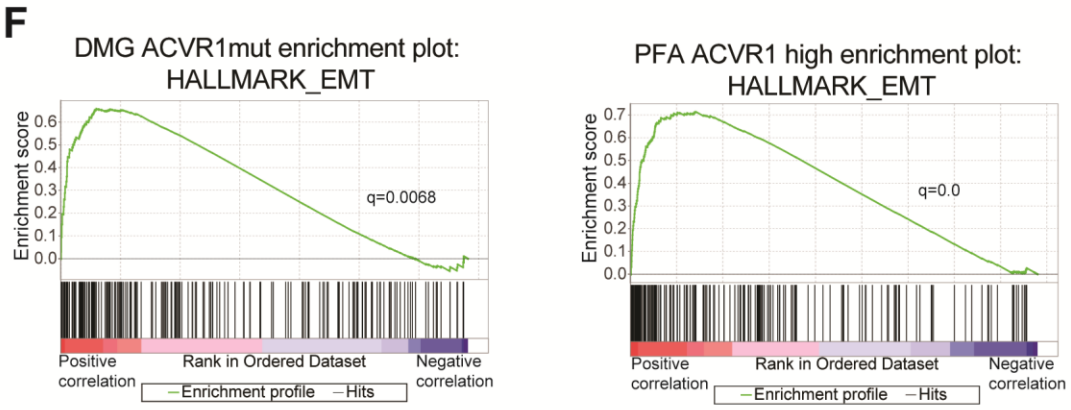
F
DMG ACVR1mut enrichment plot:
HALLMARK_EMT
q=0.0068
PFA ACVR1 high enrichment plot:
HALLMARK_EMT
q=0.0
Enrichment score
Positive correlation
Rank in Ordered Dataset
Negative correlation
Enrichment profile
Hits

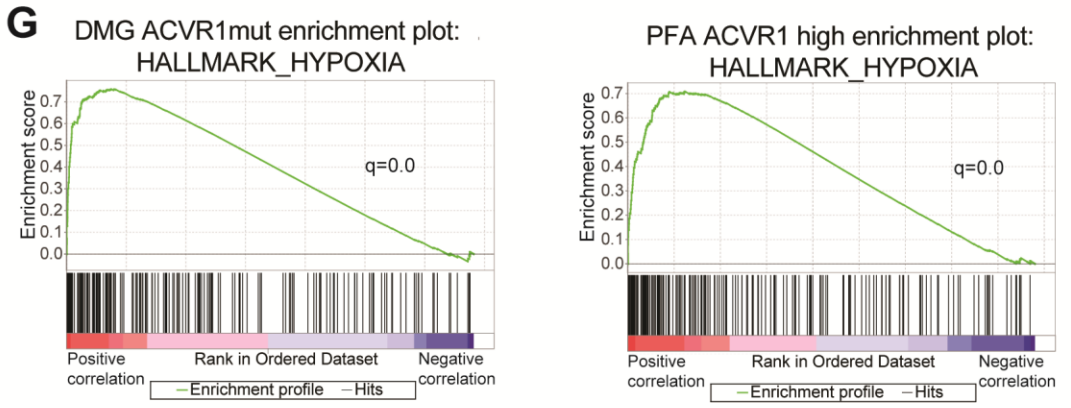
G
DMG ACVR1mut enrichment plot:
HALLMARK_HYPOXIA
q=0.0
PFA ACVR1 high enrichment plot:
HALLMARK_HYPOXIA
q=0.0
Enrichment score
Positive correlation
Rank in Ordered Dataset
Negative correlation
Enrichment profile
Hits

Figure 2.6: *ACVR1* expression is prognostic in PFAs and is associated with transcriptomic signatures observed in ACVR1-mutant DMGs.

A. Frequency of 1q gain (Y-axis) in ACVR1-mutant (n=31) vs. WT (n=137) H3K27M DMGs from Mackay et al.
B. *ACVR1* RNA expression levels (Y-axis) in PFAs (n=19) compared to PFBs (n=8) from Bayliss et al. 2016 61. Data analyzed by two-sided, unpaired, two-tailed t test.
C. Progression-free survival (months) analysis comparing PFAs with *ACVR1* high (the top quartile, n=19) vs. low (lower three quartiles, n=57) expression.
D. Overall survival (months) analysis comparing PFAs with *ACVR1* high (the top quartile, n=19) vs. low (lower three quartiles, n=57) expression.
Data in 2c-d analyzed using Kaplan-Meier, Log-Rank test with 95% confidence intervals.
E. Comparison of enriched pathways from differentially expressed genes in ACVR1 mutant vs. wildtype H3K27M DMGs (from 2a, Y-axis) and *ACVR1* high vs. low PFAs (from 2d, X-axis).
F. Gene set enrichment analyses of the Hallmark epithelial-to-mesenchymal transition (EMT) pathway for genes ranked by differential expression in ACVR1-mutant DMGs or in high *ACVR1* expressing PFAs.
G. Gene set enrichment analyses of the Hallmark hypoxia pathway for genes ranked by differential expression in ACVR1-mutant DMGs or in high *ACVR1* expressing PFAs.

2.3.6 DMGs and PFAs share many genes with retained H3K27me3, but degrees of silencing vary within tumor subtypes

I next focused my efforts on defining common epigenetic signatures in H3K27M DMGs and PFAs. Despite global reduction of H3K27me3, multiple studies have demonstrated that both tumors retain H3K27me3 at specific genomic sites (Bender et al., 2013; Chan et al., 2013; Harutyunyan et al., 2019; Siddhant U Jain, Rashoff, et al., 2020; S C Mack et al., 2014; Mohammad et al., 2017). Prior studies have established that the patterns of retained H3K27me3 are distinct from other pediatric brain tumors (Bender et al., 2013; S C Mack et al., 2014) and have pointed to several shared loci. While specific loci such as the *CDKN2A* locus have been pointed out as key sites of retained H3K27me3 in data from both tumor subtypes, more global analyses of the similarities and differences in H3K27me3 landscapes in these tumors are lacking. We performed a systematic comparison of the genes that retain H3K27me3 in H3K27M DMGs and PFAs to better understand this shared chromatin landscape.

H3K27me3 chromatin-immunoprecipitation with high throughput sequencing (ChIP-seq) profiles generated by our group (Bayliss et al., 2016) and others (Bender et al., 2013; Harutyunyan et al., 2019; S C Mack et al., 2014) were analyzed. We examined H3K27me3 enrichment in nine PFA ependymomas and six DMGs to define genes with commonly methylated promoters and gene bodies between the two tumors. We identified 551 genes with H3K27me3 retained in both tumor sets (Figure 2.7A). Because H3K27me3 is a repressive mark, the extent of repression was examined by analyzing standard deviation values of gene expression for each of these 551 genes within both H3K27M DMGs and PFAs. Analysis of bulk expression data from both tumor cohorts identified high variance in expression levels of several

H3K27me3-associated genes in both PFAs and H3K27M DMGs with greatest variability in homeobox genes including *HOXA2*, *HOXA4*, and *LHX2*. (Figure 2.7B). Examination of genomic H3K27me3 at *HOX* gene clusters in PFAs, H3K27M DMGs and patient-derived H3K27M-DMG cell lines demonstrated distinct variations in enrichment (Figure 2.7C-D). In both tumor sets, some samples showed H3K27me3 enrichment along the entire length of the *HOXA* and *HOXD* clusters, but others demonstrated variability in H3K27me3 at the *HOXA1* through *HOXA7* loci and the proximal HOXD locus (Figure 2.7C-D).

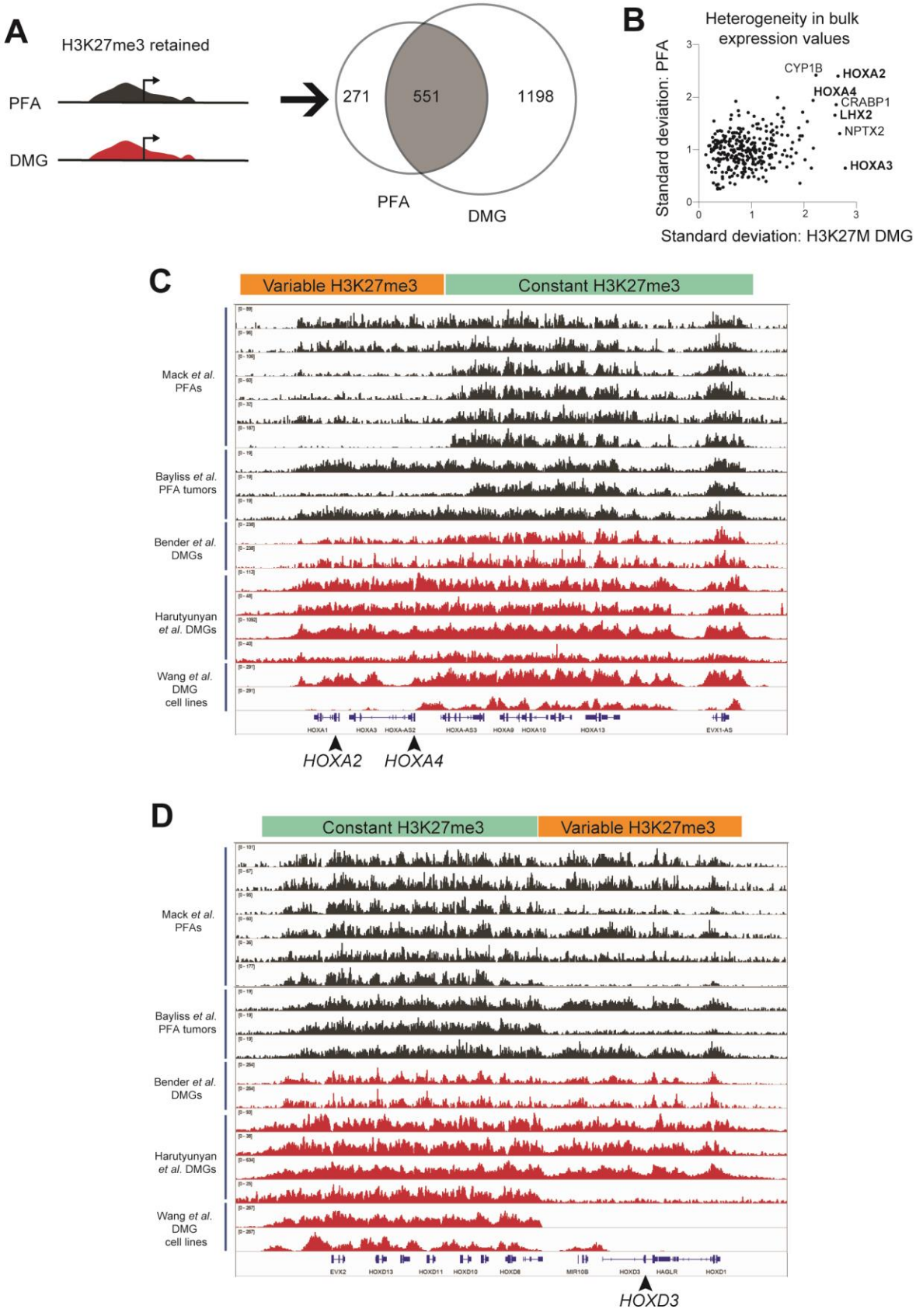
A
H3K27me3 retained
PFA
DMG
271
551
1198
PFA
DMG
B
Heterogeneity in bulk expression values
Standard deviation: PFA
Standard deviation: H3K27M DMG
CYP1β
HOXA2
HOXA4
CRABP1
LHX2
NPTX2
HOXA3
C
Variable H3K27me3
Constant H3K27me3
Mack et al. PFAs
Bayliss et al. PFA tumors
Bender et al. DMGs
Harutyunyan et al. DMGs
Wang et al. DMG cell lines
HOXA1
HOXA3
HOXA-AS2
HOXA-AS3
HOXA9
HOXA10
HOXA13
EVX1-AS
HOXA2
HOXA4
D
Constant H3K27me3
Variable H3K27me3
Mack et al. PFAs
Bayliss et al. PFA tumors
Bender et al. DMGs
Harutyunyan et al. DMGs
Wang et al. DMG cell lines
EVX2
HOXD13
HOXD11
HOXD10
HOXD8
MIR10B
HOXD3
HAGLR
HOXD1
HOXD3

Figure 2.7: Developmental patterning H3K27me3-enriched genes in PFAs and H3K27M DMGs display transcriptomic and epigenomic heterogeneity.

A. Workflow of H3K27me3 ChIP-seq analysis. Genes with promoter (2kb upstream) or gene-body H3K27me3 peaks in more than two-thirds of PFAs (≥7/9 samples) and H3K27M DMGs (≥5/6) were identified as H3K27me3-retaining genes in each tumor type. The resulting gene sets were then compared to identify shared and tumor-specific H3K27me3-retaining genes.
B. Heterogeneity in expression of H3K27me3-retaining genes was identified by plotting the standard deviation in expression of each gene identified from 3a in H3K27M DMGs (X-axis) and PFAs (Y-axis). Genes, including *HOXD3*, for which expression data were not available in both bulk expression data sets were excluded from plotting.
C. H3K27me3 ChIP-seq tracks for PFAs (black, n=9, from Mack et al., and Bayliss et al.) and H3K27M DMGs (red, middle, n=6, from Bender et al. 107 and Harutyunyan et al. 114) tumors and patient-derived H3K27M cell lines (red, bottom, n=2 from Wang et al.) at the *HOXA* cluster. Positions of proximal HOX genes associated with variation in expression (*HOXA2*, *HOXA4*, *HOXD3*) are indicated with arrowheads. Regions identified with differential patterns in H3K27me3 enrichment per tumor are labeled as variable (orange) and constant (green). Anatomic site for DMGs and PFA1/2 status were not available for tumor or cell-line samples.
D. H3K27me3 ChIP-seq tracks at the *HOXD* locus for the PFAs and DMGs depicted in **C**.

2.3.7 Differential expression patterns along H3K27me3-associated HOX loci correspond to anatomic origins

HOXA2, *HOXA3,* and *HOXA4* have been identified as transcriptional markers that differentiate PFA1 and PFA2 subgroups (K W Pajtler et al., 2018). Pajtler et al. proposed that the PFA1 tumors overexpress HOXA-family genes and hypothesized distinct anatomical origins for PFA1 vs. PFA2 ependymomas (K W Pajtler et al., 2018). Assessment of *HOXA2* bulk expression revealed a bimodal expression pattern in PFAs (Figure 2.8A). As expected, segregation of *HOXA2*-high vs. low PFAs occurred almost completely along PFA1 vs. PFA2 status with the majority of *HOXA2*-low tumors corresponding to the PFA2 subgroup (Figure 2.8B). H3K27M DMGs similarly exhibited a bimodal *HOXA2* expression distribution (Figure 2.8C). Moreover, *HOXA2* expression levels revealed similar anatomic segregation with majority of thalamic tumors demonstrating low *HOXA2* expression (Figure 2.8D). *HOXA4* expression demonstrated a similar, though less striking pattern (Figure 2.8E-H). *HOXD3,* for which expression data in PFAs were unavailable, also followed a similar bimodal distribution (Figure 2.8I) and pontine tumors tended to fall in the *HOXD3*-high category (Figure 2.8J). Evidence of *HOX* family expression in single-cell data from DMGs and PFAs (Filbin et al., 2018; Gojo et al., 2019) further supported this anatomic pattern in expression. Tumors derived from the pons and PFA1s showed higher *HOXA2* and *HOXA4* expression, while *HOXD3* expression was elevated in pontine vs. thalamic tumors but was not significantly different between PFA1 and PFA2 tumors (Figure 2.8K and L). This distinction in *HOX* gene expression patterns between DMGs and PFAs may reflect subtle regional differences in the cells of origin; however, *HOXD3* expression data from additional PFA tumors will be necessary to validate this hypothesis.

Differential H3K27me3 enrichment at these loci could be due to varying effects of PRC2 inhibition by the H3K27M mutation. To test this hypothesis, we examined published ChIP-seq tracks from DIPG-XIII and BT245 H3K27M patient-derived cell lines with or without H3K27M knockdown (Harutyunyan et al., 2019). In both cell lines, H3K27M knockdown did not alter H3K27me3 genomic distribution at these genomic loci (Figure 2.8M), suggesting that differential H3K27me3 at this site is not dependent on H3K27M. Overall, both H3K27M DMGs and PFA ependymomas showed differences in H3K27me3 genomic distribution at specific gene loci consistent with gene expression differences based on tumor anatomic location. These patterns are in contrast with the initial hypothesis that H3K27M and EZHIP might drive expression patterns through modulating the degree of retained H3K27me3 at PRC2-target sites and highlight the importance of the anatomic sites of origin on this epigenetic signature.

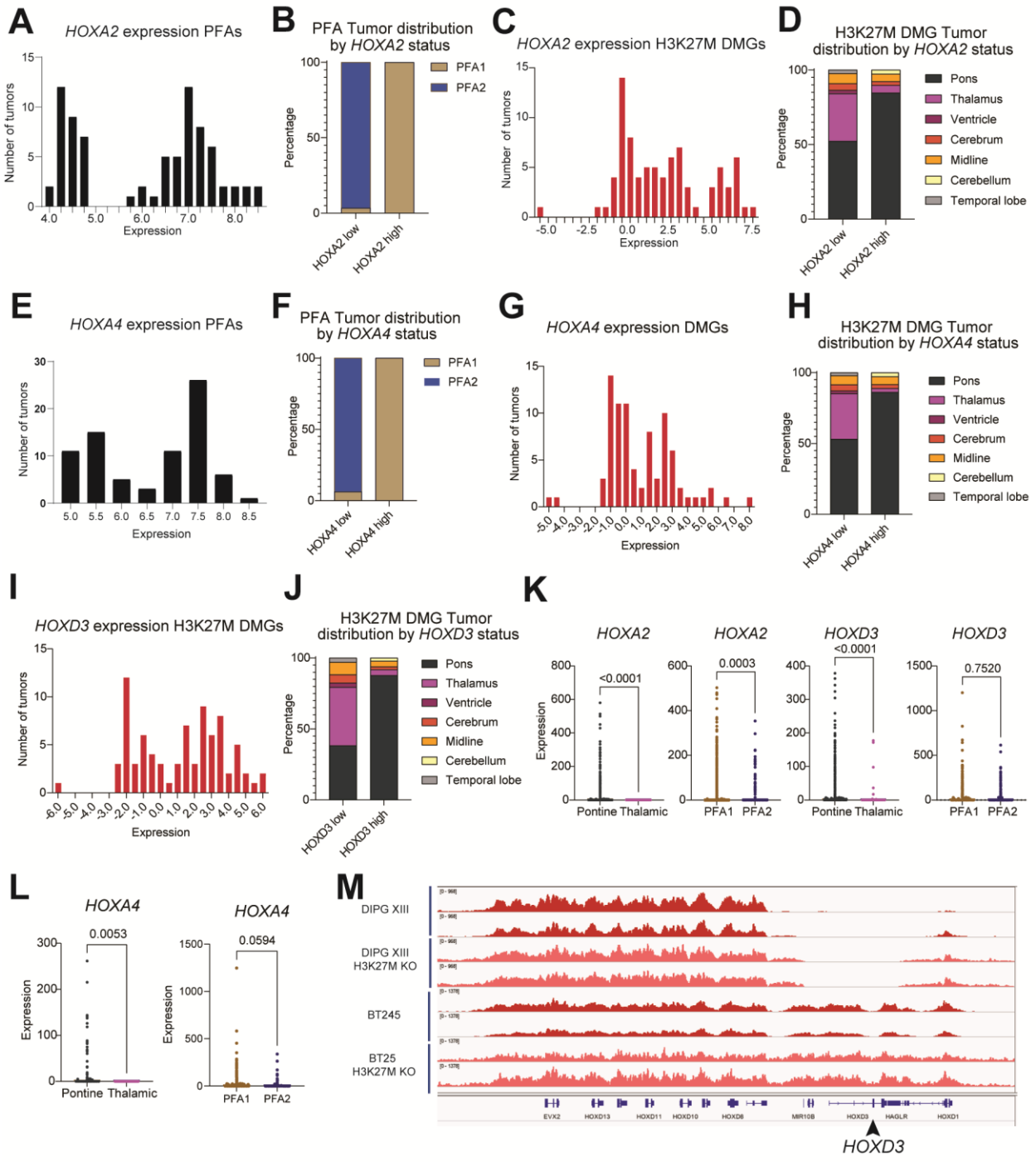

Figure 2.8: Heterogeneity in expression of commonly marked H3K27me3 genes is influenced by anatomic origin and not EZH2 inhibition.

A. Histogram of *HOXA2* expression values per tumor (X-axis = binned expression scores, Y-axis = number of tumors) in PFAs.

B. Comparison of *HOXA2*-high (expression < 5 units) vs. low (expression > 5.5 units) groups based on the local minimum between modes in DNA-methylation defined, anatomically distinct PFA1 (n=49) and PFA2 (n=29) subtypes of PFAs.
C. Histogram of *HOXA2* expression values per tumor (X-axis = binned expression scores, Y-axis = number of tumors) in H3K27M DMGs.
D. Comparison of *HOXA2*-high (expression < 4.5 units) vs. low (expression > 4.5 units) groups based on the local minimum between modes with anatomic location of H3K27M DMGs (pons=65; thalamus=26; midline not otherwise specified (NOS)=5; cerebellum=1, and other=2).
E. Histogram of *HOXA4* expression values per tumor (X-axis = binned expression scores, Y-axis = number of tumors) in PFAs.
F. Comparison of *HOXA4*-high (expression < 6 units) vs. low (expression > 6 units) groups based on the local minimum between modes in DNA-methylation defined, anatomically distinct PFA1 (n=49) and PFA2 (n=29) subtypes of PFAs.
G. Histogram of *HOXA4* expression values per tumor (X-axis = binned expression scores, Y-axis = number of tumors) in H3K27M DMGs.
H. Comparison of *HOXA4*-high (expression < 1 unit) vs. low (expression > 1 unit) groups based on the local minimum between modes with anatomic location of H3K27M DMGs (pons=65; thalamus=26; midline not otherwise specified (NOS)=5; cerebellum=1, and other =2).
I. Histogram of *HOXD3* expression values per tumor (X-axis = number of values, Y-axis = bin center) in H3K27M DMGs. Note that HOXD3 expression values were not available for PFAs.
J. Comparison of *HOXD3*-high (expression > 0.5 units) vs. low (expression < 0.5 units) groups based on the local minimum between modes with anatomic location of H3K27M DMGs (pons=65; thalamus=26; midline not otherwise specified (NOS)=5; cerebellum=1, and other=2). Note that HOXD3 expression values were not available for PFAs.
K. Expression patterns of *HOXA2* and *HOXD3* in single-cell RNA-sequencing (scRNA-seq) experiments (Filbin et al. and Gojo et al.). Tumors were grouped by anatomic site (pons vs. thalamus for H3K27M DMG) or methylation-based subtype (PFA1 vs PFA2 for PFAs).
L. Expression patterns of *HOXA4* in single-cell RNA-sequencing (scRNA-seq) experiments (Filbin et al. and Gojo et al.). Tumors were grouped by anatomic site (pons vs. thalamus for H3K27M DMG) or methylation-based subtype (PFA1 vs PFA2 for PFAs).
M. H3K27me3 ChIP-seq tracks at the *HOXD* locus from isogenic patient-derived H3K27M DIPG XIII and BT425 cell lines with or without H3K27M-knockdown.

2.3.8 Enhancer signatures in PFAs and H3K27M DMGs show high expression in astrocyte-like tumor cells

Both H3K27M mutations and EZHIP overexpression lead to a global increase in H3K27 acetylation (H3K27ac), a mark associated with active transcription (Krug et al., 2019a; Nagaraja et al., 2017; K W Pajtler et al., 2018; Panwalkar et al., 2021; Piunti et al., 2017, 2019). Moreover, H3K27M DMGs and PFAs exhibit unique H3K27ac-marked enhancer and super enhancer profiles (Krug et al., 2019b; Stephen C Mack et al., 2018; Nagaraja et al., 2019). We combined information from gene lists generated by Mack et al. and Krug et al. and reanalyzed publicly available H3K27ac ChIP-seq data from these studies to identify enhancers that are shared by, or unique to, each tumor. H3K27ac-marked gene enhancers shared by both H3K27M DMGs and PFAs (n=533) were mainly associated with axonogenesis, axon guidance, and cell motility pathways, as well as differentiation of glial and oligodendrocyte lineages (Figure 2.9A). DMG-specific enhancers mapped mainly to genes enriched for synaptic signaling (Figure 2.9B), whereas PFA-specific enhancers were associated with genes enriched for extracellular organization and angiogenesis (Figure 2.9C).

Due to the importance of enhancer activity in regulation of cell identity, we explored whether the enhancer signatures segregated with differentiation cell states within each tumor by assessing the single-cell RNA-seq datasets (Filbin et al., 2018; Gojo et al., 2019). Single-cell transcriptomics in H3K27M-DMGs and PFA ependymomas have demonstrated marked intratumoral heterogeneity (Filbin et al., 2018; Gojo et al., 2019). Both tumors contain malignant cells with varying expression of stem-cell-like, and more differentiated tumor cell signatures. H3K27M DMGs contain tumor cells bearing oligodendrocyte precursor (OPC)-like, oligodendrocyte (OC)-

like and astrocyte (AC)-like cells, (Filbin et al., 2018). Similarly, PFAs contain less differentiated neuronal stem cell (NSC)-like, glial progenitor (GP)-like, and neuronal precursor cell (NPC)-like, as well as more differentiated ependymal (Epd)-like and astroependymal (AE)-like tumor cells (Gojo et al., 2019). Mapping the expression signatures onto tumor cell-types showed highest average expression of shared enhancer signature within astrocyte-like cells in H3K27M DMGs and astroependymal-like and immune-reactive PFA tumor cells (Figure 2.9D). Evaluation of the tumor-specific enhancer signatures by single-cell type also showed increased expression in astrocytic-like lineages for both tumor types (Figure 2.9E-F). We initially hypothesized that because enhancers play critical roles in regulating cell identity, and super enhancers in particular have been associated with activation of tumor-specific transcriptional programs (Hnisz et al., 2013), the H3K27M DMG and PFA-specific enhancer signatures might associate closely with more potent progenitor-like cell types. However, our findings demonstrate that these previously identified enhancer signatures seem to more closely align with expression programs of cells within the tumor that demonstrate astrocytic lineage features.

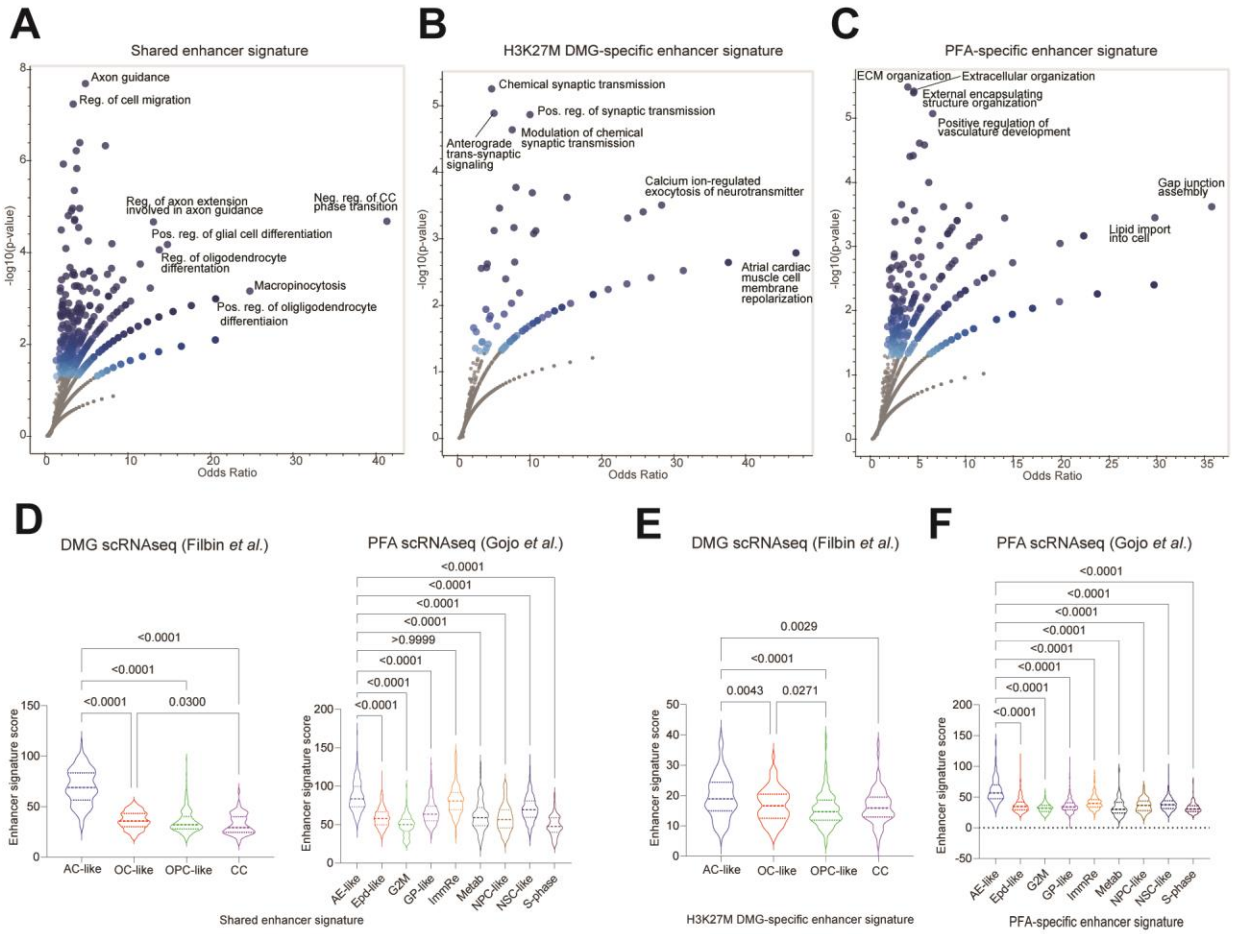

Figure 2.9: Astrocyte-like cell types show the highest expression of enhancer signatures in both PFAs and H3K27M DMGs.

A. Enriched gene ontology biological process (GO BP) gene sets (Y-axis Negative Log10 p value, X-axis Odds ratio) for genes associated with enhancers shared by PFAs and H3K27M DMGs. Shading of points is influenced by p-value (darker shade with lower p-values) and number of overlapping points.
B. Enriched gene ontology biological process (GO BP) gene sets (Y-axis Negative Log10 p value, X-axis Odds ratio) for genes associated with enhancers unique to H3K27M DMGs.
C. Enriched gene ontology biological process (GO BP) gene sets for genes (Y-axis Negative Log10 p value, X-axis Odds ratio) associated with enhancers unique to PFA ependymomas.
D. Comparison of expression of the shared enhancer signature by cell type in H3K27M DMGs and PFAs. Signature scores per cell were calculated by taking the mean of expression values for the genes in the signature.
E. Expression of the H3K27M DMG-specific enhancer signature by DMG cell type.
F. Expression of the PFA-specific enhancer signature by DMG cell type.
Data in 4d-f analyzed by non-parametric Kruskal-Wallis test and 95% confidence intervals. AC-like, Astrocyte-like; OC-like, Oligodendrocyte-like; OPC-like, Oligodendrocyte precursor-like; CC- cell cycle; AE-like, Astroependymal-like; Epd-like, Ependymal-like; G2M, G to M cell

cycle related; GP-like, Glialprecursor-like; ImmRe, Immune related; Metab, Metabolic; NPC-like, Neuronal precursor-like; NSC-like, Neuronal stem cell-like; S-phase, S-phase cell cycle.

2.3.9 H3K27me3-enriched CRABP1 is highly expressed in progenitor populations of both tumors

In further interrogation of the single-cell datasets, we asked whether genes with retained H3K27me3 exhibited preferential expression in single-cell defined tumor cell populations. In both tumors, cells with progenitor-like states including OPC-like tumor cells in H3K27M-DMGs, and NPC-like tumor cells in PFA ependymomas, tended to have higher expression of shared genes (between H3K27M DMGs and PFAs) retained H3K27me3 signature (Figure 2.10A and B).

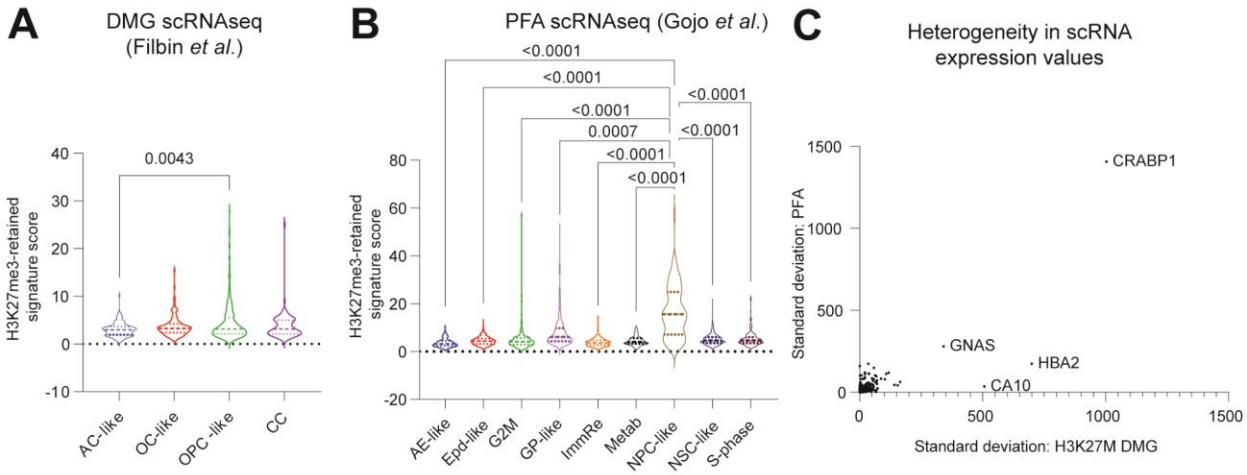
A
DMG scRNAseq
(Filbin et al.)
H3K27me3-retained signature score
0.0043
AC-like
OC-like
OPC-like
CC
B
PFA scRNAseq (Gojo et al.)
H3K27me3-retained signature score
<0.0001
<0.0001
<0.0001
0.0007
<0.0001
<0.0001
<0.0001
<0.0001
AE-like
Epd-like
G2M
GP-like
ImmRe
Metab
NPC-like
NSC-like
S-phase
C
Heterogeneity in scRNA expression values
Standard deviation: PFA
Standard deviation: H3K27M DMG
CRABP1
GNAS
HBA2
CA10

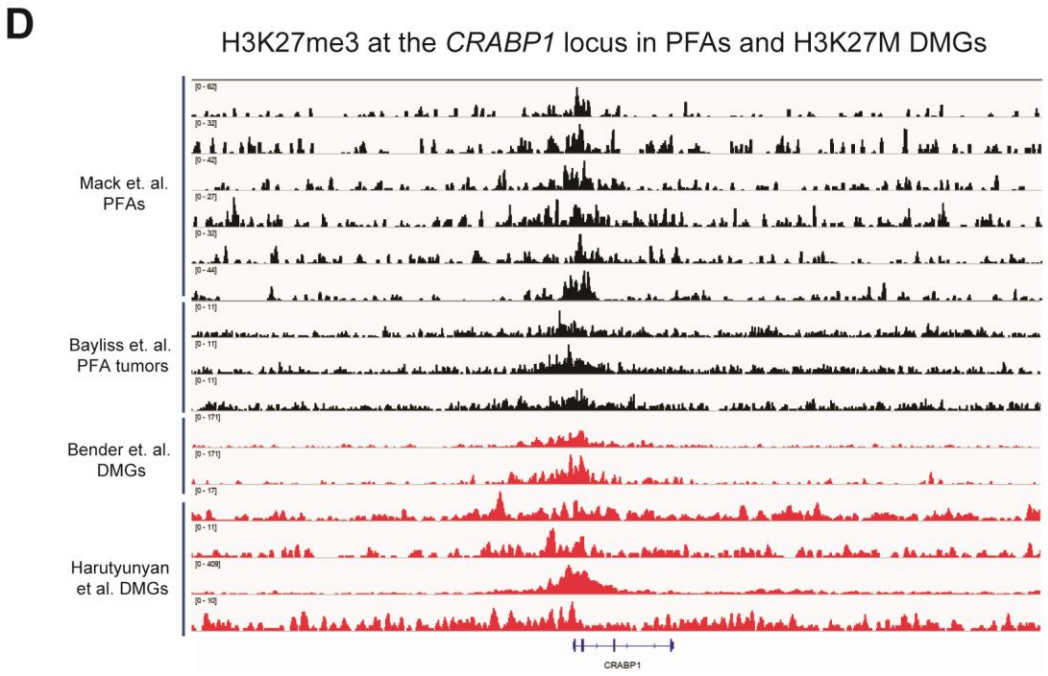
D
H3K27me3 at the CRABP1 locus in PFAs and H3K27M DMGs
Mack et. al. PFAs
Bayliss et. al. PFA tumors
Bender et. al. DMGs
Harutyunyan et al. DMGs
CRABP1

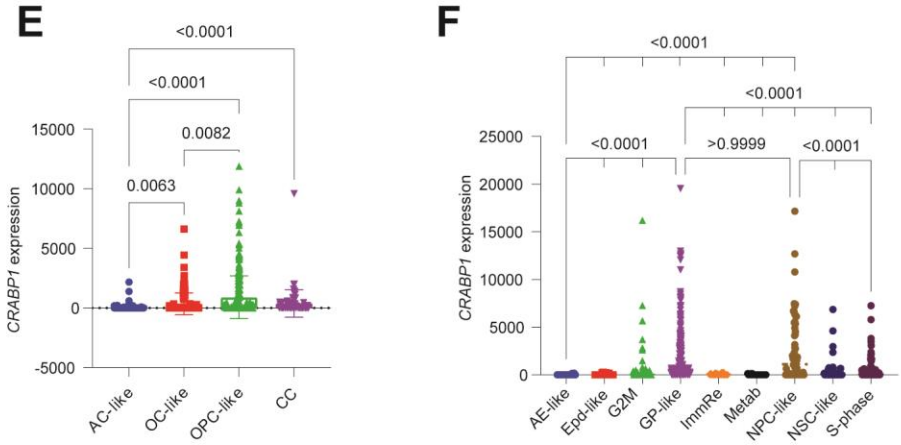
E
CRABP1 expression
<0.0001
<0.0001
0.0082
0.0063
AC-like
OC-like
OPC-like
CC
F
CRABP1 expression
<0.0001
<0.0001
<0.0001
>0.9999
<0.0001
AE-like
Epd-like
G2M
GP-like
ImmRe
Metab
NPC-like
NSC-like
S-phase

Figure 2.10: Heterogeneity in PFA and DMG H3K27me3-marked genes and *CRABP1*, in particular, is driven by expression in progenitor-like cells.

A. Expression of the shared H3K27me3-retaining gene signature across cell-types in scRNA-seq data from H3K27M DMGs (Filbin et al.). Expression scores per cell were determined as the average expression of all genes in each cell.
B. Expression of the shared H3K27me3-retaining gene signature across cell-types in scRNA-seq data from PFA ependymomas (Gojo et al.). Only p-values for comparisons involving NPC-like cells are shown.
C. Comparison of the heterogeneity in expression of H3K27me3-retaining genes as measured by the overall standard deviation in expression of each gene from the H3K27me3 shared signature in H3K27M DMGs (X-axis) and PFA ependymomas (Y-axis). Genes for which expression data were not available in both bulk expression data sets were excluded from plotting. A total of 397 genes were plotted.
H3K27me3 ChIP-seq tracks at the *CRABP1* locus for PFA (black, n=9, from Mack et al., and Bayliss et al.) and H3K27M DMG (red, n=6, from Bender et al. 107 and Harutyunyan et al. 114) tumors.
D. *CRABP1* expression values per cell from scRNA-seq data in H3K27M DMGs, grouped by cell type.
E. *CRABP1* expression values per cell from scRNA-seq data in PFAs, grouped by cell type. Only p-values for comparisons involving NPC-like and GP-like cells are shown.
Kruskal-Wallis test followed by multiple comparisons' correction were used to analyze data in Figs **A**, **B**, **E**, and **F**.

To further assess heterogeneity, we analyzed genes with the greatest variability in expression (by comparing standard deviation values for each gene) across all tumor cell types in both tumors. Expression of cellular retinoic acid binding protein 1 (*CRABP1*) was a clear outlier for both tumor subtypes (Figure 2.10C). Moreover, *CRABP1* was one of the H3K27me3-marked genes (Figure 2.10D) with the greatest variability in expression levels in the bulk datasets (Figure 2.7B). *CRABP1* is frequently dysregulated in cancer (Favorskaya et al., 2014; Lind et al., 2006; R.-Z. Liu et al., 2015; Tanaka et al., 2007; Q. Wu et al., 2007). *CRABP1* expression segregated strongly with OPC-like cells in DMGs (Figure 2.10E) and both glial progenitor-like (GP-like) and neuronal precursor-like (NPC-like) in PFAs (Figure 2.10F). We determined genes that correlate with *CRABP1* expression in bulk expression to find that the *HOX* genes were among the strongest correlates in both tumor datasets (Figure 2.11A). However, *HOXA2* and *HOXD3* did not demonstrate any distinct patterns of expression by cell-type in DMGs, and the significantly different changes observed in PFAs were far less drastic (Figure 2.11B-E).

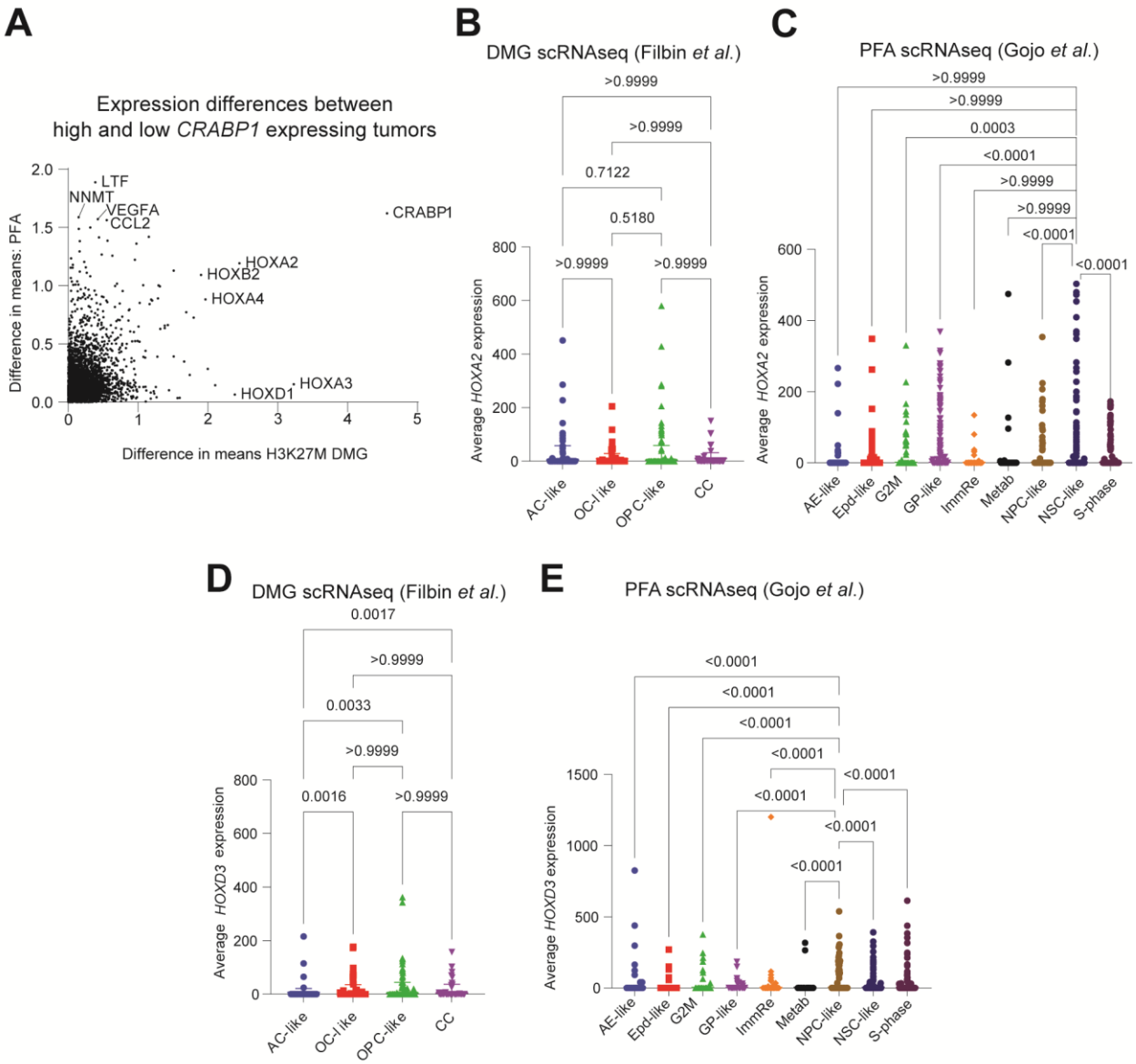

Figure 2.11: Differences in *CRABP1* expression are associated with differences in *HOX* gene expression but progenitor cell type enrichment is unique to *CRABP1*.

A. Analysis of genes co-expressed with CRABP1 in bulk RNA-seq datasets by comparison of difference in means for CRABP1-high and CRABP1-low tumors in H3K27M DMGs (X-axis) and PFA ependymomas (Y-axis). A split at the mean expression of CRABP1 from the Mack et al. dataset was used to delineate H3K27M DMG CRABP1-high (n=37) and CRABP1-low tumors (n=46). A split in the mean expression of the highest-level CRABP1 probe from the Pajtler et al. dataset was used to delineate PFA CRABP1-high (n=22) and -low tumors (n=56).
B and **C.** scRNA-seq expression of *HOXA2* grouped by cell-type in PFA (Gojo et al., 2019) and DMG (Filbin et al., 2018) datasets.
D and **E.** scRNA-seq expression of *HOXD3* grouped by cell-type in PFA (Gojo et al., 2019) and DMG (Filbin et al., 2018) datasets.

Kruskal-Wallis test followed by multiple comparisons' correction were used to analyze data in Figs **B**-**E**.

2.3.10 Integration of scRNA-seq datasets from PFAs and DMGs highlights potential role for CRABP1 in progenitor-type cells unique to PFA/DMGs

The scRNA-seq datasets from the two different tumor types were integrated to further explore similarities in expression patterns of H3K27M DMGs and PFAs. Integrated dimensional reduction analyses identified 20 clusters, four of which (clusters 0, 1, 4, and 13) included large populations of both PFA- and DMG-derived cells (arrows, Figure 2.12A and B). The top marker gene in the second-largest cluster (cluster 1) was *CRABP1* (Figure 2.12C and D). This cluster consisted primarily of progenitor and precursor cell states: OPC-like cells from the DMGs and GP-like cells from PFAs (Figure 2.12E). Moreover, assessment of single-cell populations from other pediatric brain tumors using a dataset with all four subgroups of medulloblastoma (Riemondy et al., 2022) failed to identify any populations with elevated *CRABP1* expression in those tumors (Figure 2.12F). Overall, these data support a role for *CRABP1* in specific tumor cell-states in both tumors, consistent with the hypothesis that PFA and DMG tumors may benefit from expression of similar genes to maintain progenitor states.

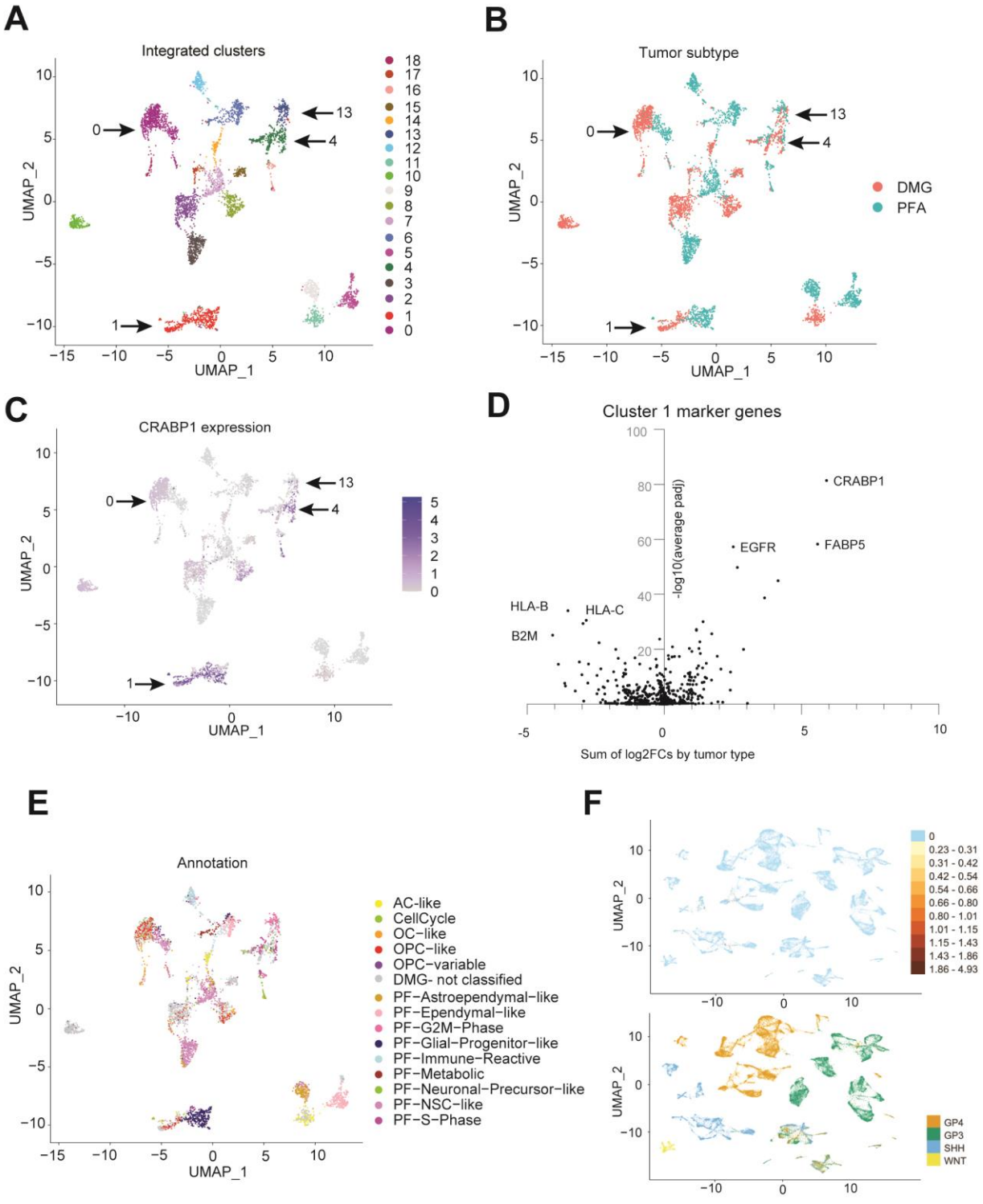

Figure 2.12: Integrated scRNA-seq from DMG and PFA cohorts reveals *CRABP1* is the top marker of a cluster of PFA and DMG cells with progenitor-like signatures.

A-C. (UMAP) embeddings of integrated scRNA-seq datasets of H3K27M DMG (Filbin) and PF ependymoma (Gojo). **A**: identification of 20 distinct clusters. **B**: labeling by tumor of origin. **C**: *CRABP1* expression across single cells with color scale minimum set to 0.
D. Volcano plot of Seurat conserved markers of Cluster 1 in the integrated H3K27M DMG/PFA scRNA-seq analysis from A-C (Y-axis = -log10-normalized average adjusted p-value across the two tumor sets, X-axis = sum of log2-transformed fold changes between Cluster 1 and all other clusters for the two tumor sets.
E. Uniform Manifold Approximation and Projection (UMAP) embeddings of integrated scRNA-seq datasets of H3K27M DMG (Filbin) and PF ependymoma (Gojo) with cells colored by cell-type (AC-like, Astrocyte-like; OC-like, Oligodendrocyte-like; OPC-like, Oligodendrocyte precursor-like; CC- cell cycle; AE-like, Astroependymal-like; Epd-like, Ependymal-like; G2M, G to M cell cycle related; GP-like, Glialprecursor-like; ImmRe, Immune related; Metab, Metabolic; NPC-like, Neuronal precursor-like; NSC-like, Neuronal stem cell-like; S-phase, S-phase cell cycle.)
F. Uniform Manifold Approximation and Projection (UMAP) embeddings of scRNA-seq data from all four subgroups of medulloblastoma (Riemondy et al.) with subgroup annotation (left) and CRABP1 expression (right).
Kruskal-Wallis test followed by multiple comparisons analysis were used to analyze data in Figs S4b-c.

2.3.11 Common H3K27me3 signatures mirror human hindbrain brain developmental patterns

H3K27M DMG and PFAs are proposed to arise from cells along developmental lineages in the hindbrain (Filbin et al., 2018; Gillen et al., 2020; Gojo et al., 2019; Jessa et al., 2019; Vladoiu et al., 2019). We first aimed to identify whether H3K27me3-associated genes exhibited specific patterns in normal human hindbrain development. We utilized published scRNA-seq dataset from fetal human cerebellum ranging from 9-21 weeks post-conception published by Aldinger et al. 2021 (Aldinger et al., 2021). Overall, average expression of H3K27me3-retained genes increased in more differentiated populations of cells associated with potential cells-of-origin for DMGs and PFAs. Committed OPCs demonstrated increased signature expression compared to OPCs, and brainstem-choroid/ependymal cells had higher levels of expression than early brainstem cells (Figure 2.13A). Cells of astrocytic lineage did not show a similar pattern (Figure 2.13A). Because OPCs are the leading cell of origin for H3K27M DMGs (Filbin et al., 2018; Nagaraja et al., 2019), we examined oligodendroglial lineages in more detail in a second single-cell dataset of human developing cerebellum (Sepp et al., unpublished) (Sepp et al., 2021). H3K27me3 signatures were low in progenitor cells but increased along stages of OPC differentiation with highest expression in late-OPCs and then decreased in more differentiated committed OPCs and oligodendrocytes (Figure 2.13B). Analysis of the astrocytic lineage cells did not yield a similar pattern (Figure 2.13C).

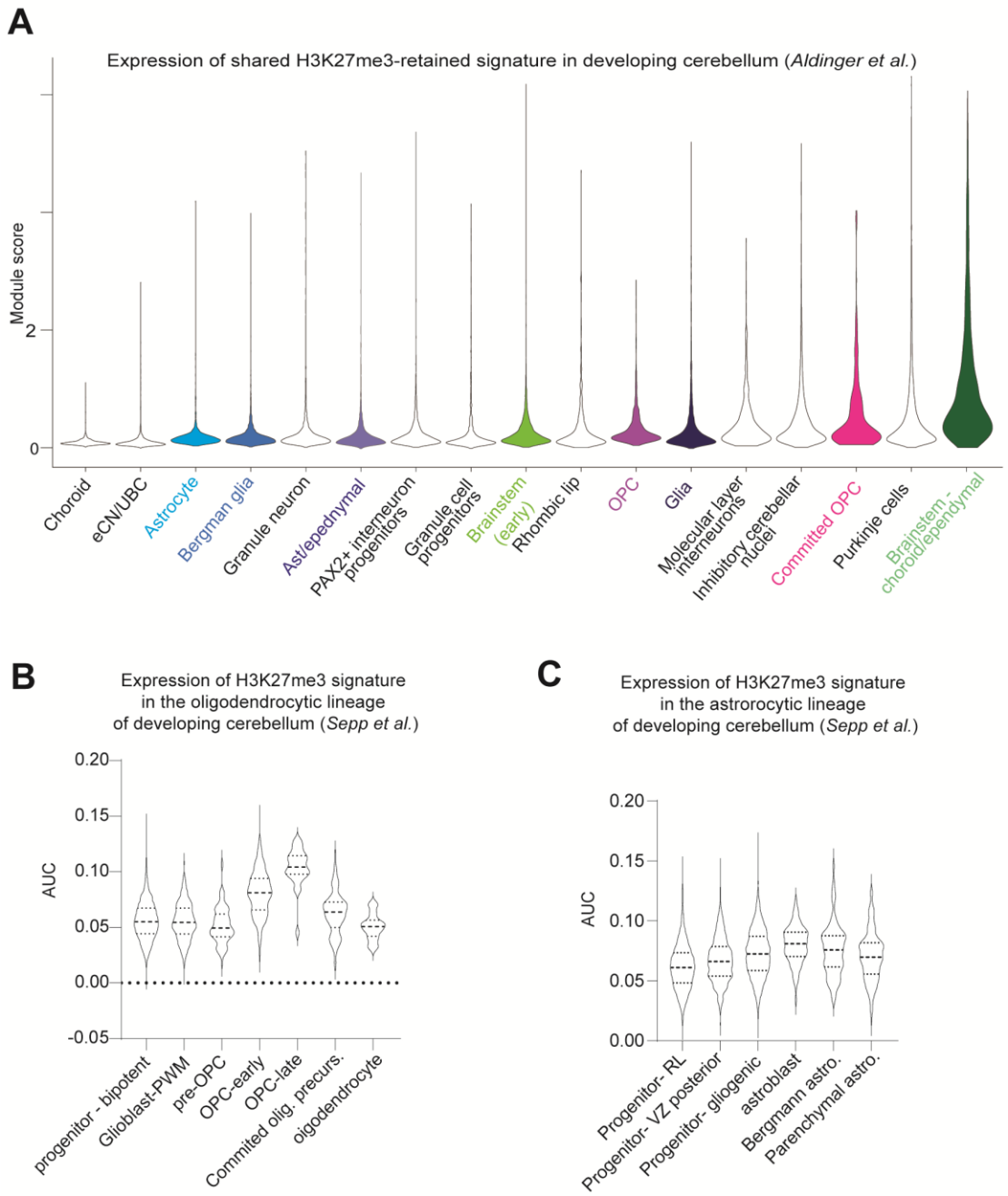

Figure 2.13: H3K27me3-associated genes from DMGs and PFAs are most highly expressed along oligodendrocyte and ependymal development.

A. Expression of the shared DMG/PFA-derived H3K27me3 gene signature in scRNA-seq data of the developing human posterior fossa (Aldinger et al.) grouped by cell-type. Highlighted groups indicate cell types pertinent to DMGs/PFAs.
B. H3K27me3 gene signature expression along the oligodendrocyte lineage in an independent scRNA-seq atlas of the developing posterior fossa (Sepp et al., unpublished).
C. H3K27me3 gene signature expression along the astrocytic lineage in the scRNA-seq atlas of the developing posterior fossa used in b.

2.3.12 CRABP1 *expression is seen in first trimester hindbrain and brainstem progenitor cells*

Given its notable expression pattern in the single-cell tumor datasets (Figure 2.12), we examined *CRABP1* expression in the developing hindbrain utilizing a scRNA-seq dataset generated from human brain samples from the first trimester (Eze et al., 2021). Carnegie stages are used to define period of human brain development (O'Rahilly & Müller, 2010). In the hindbrain, we noted a peak of *CRABP1* expression in stage 19, which corresponds to the peak in expression of *H3-3A*, the histone variant most commonly mutated in DMGs (Figure 2.14A). With respect to anatomic location, *CRABP1* expression was higher in the spinal cord and hindbrain vs. thalamus and cerebellum (Figure 2.14B). Known areas of high retinoic acid (RA)-signaling in development, including the olfactory placode and optic pathways demonstrated enrichment of *CRABP1* expression, whereas expression in forebrain/cortical-related structures was variable (Figure 2.14B). Similarly, *CRABP1* expression was restricted to a subset of brainstem cells in the Aldinger et al. developing cerebellum atlas (Figure 2.14C). At a cellular level, *CRABP1* expression was highest in the progenitor cell types compared to their more differentiated oligodendrocytic and astrocytic cells (Figure 2.14D).

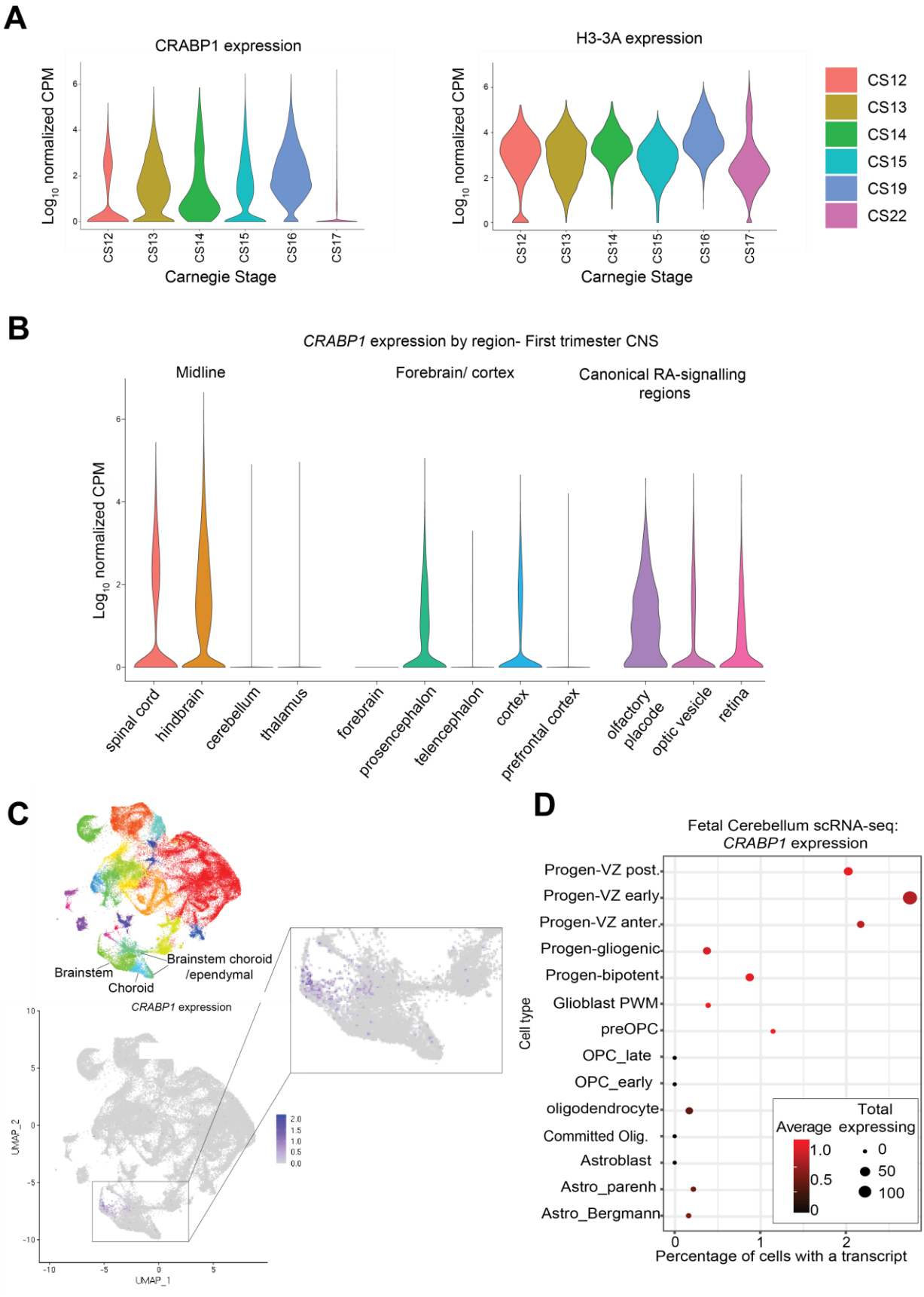
A
CRABP1 expression
H3-3A expression
Log10 normalized CPM
Carnegie Stage
CS12
CS13
CS14
CS15
CS16
CS17
CS19
CS22
B
CRABP1 expression by region- First trimester CNS
Midline
Forebrain/ cortex
Canonical RA-signalling regions
spinal cord
hindbrain
cerebellum
thalamus
forebrain
prosencephalon
telencephalon
cortex
prefrontal cortex
olfactory placode
optic vesicle
retina
C
Brainstem
Choroid
Brainstem choroid /ependymal
CRABP1 expression
UMAP_1
UMAP_2
D
Fetal Cerebellum scRNA-seq:
CRABP1 expression
Progen-VZ post.
Progen-VZ early
Progen-VZ anter.
Progen-gliogenic
Progen-bipotent
Glioblast PWM
preOPC
OPC_late
OPC_early
oligodendrocyte
Committed Olig.
Astroblast
Astro_parenh
Astro_Bergmann
Cell type
Average expressing
Total expressing
Percentage of cells with a transcript

Figure 2.14: *CRABP1* expression is associated with less differentiated cells of the hindbrain/brainstem.

A. First-trimester hindbrain *CRABP1* and *H3-3A* expression by Carnegie Stage (CS) of development (O'Rahilly & Müller, 2010).
B. First-trimester human brain scRNA-seq (Eze et al., 2021) expression patterns of *CRABP1* grouped by anatomic region. Left: midline structures, middle: forebrain and cortical structures, right: regions with canonical retinoic acid (RA) signaling.
C. *CRABP1* expression patterns in the developing cerebellum scRNA-seq atlas from **2.13A**. Top: UMAP embedding colored by cluster, bottom: *CRABP1* expression across all cells in UMAP embedding, right (inset): magnified depiction of *CRABP1* expression patterns in a subset of cells including brainstem and brainstem-derived choroidal/ependymal cells.
D. *CRABP1* expression patterns in astrocytic and oligodendrocyte lineages of the developing cerebellum scRNA-seq atlas from **2.13B** and **C**. Early progenitors are grouped along the top of the Y-axis, then the more differentiated oligodendrocyte and the astrocytic lineages are each grouped below along the Y-axis. The percentage of cells expressing at least one *CRABP1* transcript (X-axis), the total number of cells expressing at least one *CRABP1* transcript (point size) and the average expression value (color) are depicted.

2.3.13 **CRABP1** *demonstrates distinct positional expression patterns in human and mouse hindbrain consistent with prior studies in mice*

Data from mouse development have previously identified *CRABP1* expression as specific to rhombomeres 4-6 (r4-6) (Maden et al., 1992). The r4-6 segments give rise to the caudal portion of the basilar pons (r4) and retropontine structures (r5-6) (C Watson & Ullmann, 2015; Charles Watson et al., 2019). Given this spatial patterning, the Allen Brain Atlas' Developing Human Transcriptome was examined to determine patterns of *CRABP1* expression (Allen Institute for Brain Science, 2010; J. A. Miller et al., 2014). Within hindbrain structures CRABP1 expression strongly correlated with *HOX* genes including *HOXA2* and *HOXD3* (Figure 2.15A). Moreover, HOXD3, HOXA2 and CRABP1 expression in the developing human hindbrain at 15-weeks gestation was mainly restricted to developing human pontine and medullary structures (Figure 2.15B-E), a finding supported by developing mouse brain expression patterns (Figure 2.16). Altogether, these data support the positional expression patterns observed in both H3K27M DMGs and PFAs, consistent with these patterns reflecting epigenetic states from developmental lineages.

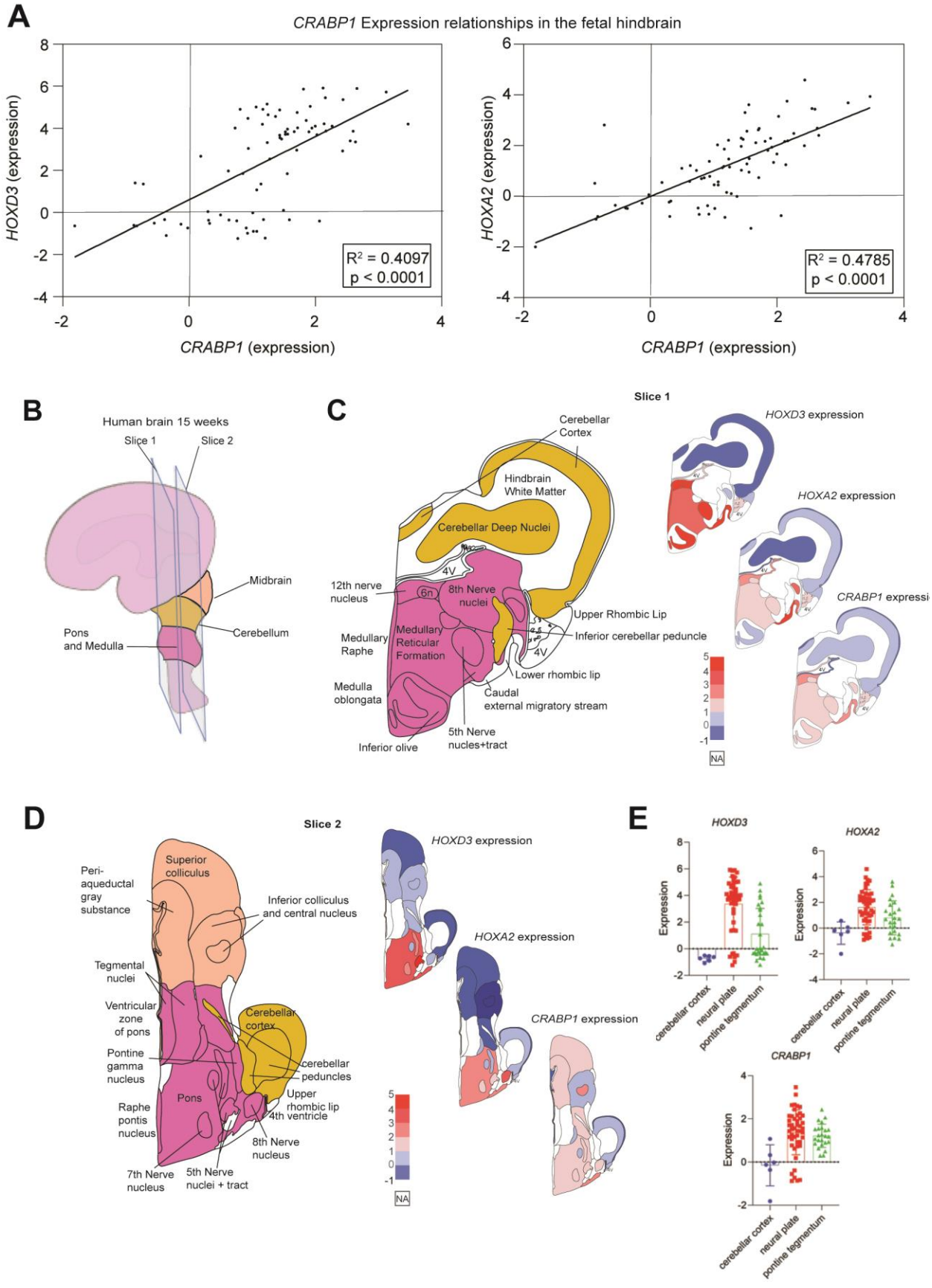
A
CRABP1 Expression relationships in the fetal hindbrain
HOXD3 (expression)
CRABP1 (expression)
R² = 0.4097
p < 0.0001
HOXA2 (expression)
CRABP1 (expression)
R² = 0.4785
p < 0.0001
B
Human brain 15 weeks
Slice 1
Slice 2
Midbrain
Cerebellum
Pons
and Medulla
C
Slice 1
Cerebellar
Cortex
Hindbrain
White Matter
Cerebellar Deep Nuclei
4V
12th nerve
nucleus
6n
8th Nerve
nuclei
Upper Rhombic Lip
Inferior cerebellar peduncle
Medullary
Raphe
Medullary
Reticular
Formation
4V
Lower rhombic lip
Medulla
oblongata
Caudal
external migratory stream
Inferior olive
5th Nerve
nucles+tract
HOXD3 expression
HOXA2 expression
CRABP1 expressi
NA
D
Slice 2
Peri-
aqueductal
gray
substance
Superior
colliculus
Inferior colliculus
and central nucleus
Tegmental
nuclei
Ventricular
zone
of pons
Cerebellar
cortex
Pontine
gamma
nucleus
cerebellar
peduncles
Pons
Upper
rhombic lip
4th ventricle
Raphe
pontis
nucleus
8th Nerve
nucleus
7th Nerve
nucleus
5th Nerve
nuclei + tract
HOXD3 expression
HOXA2 expression
CRABP1 expression
NA
E
HOXD3
HOXA2
CRABP1
Expression
cerebellar cortex
neural plate
pontine tegmentum

Figure 2.15: *CRABP1* maps to more caudal structures of developing human hindbrain in a similar manner as *HOXA2* and *HOXD3*.

A. Microarray-based log2 expression levels from micro-dissected fetal hindbrain tissue at 15- and 16-weeks post-conception from BrainSpan's Prenatal lateral microdissection (LMD) Microarray comparing *CRABP1* expression patterns to those of *HOXA2* and *HOXD3*. Data were analyzed with a simple linear regression and R-squared calculated with a goodness of fit test with 95% confidence intervals.
B. Schematic depicting sectioning of the 15-16 weeks post conception fetal brain utilized for depictions in **C** and **D**. Early anatomic structures of the infratentorial brain are colored in peach (midbrain), yellow (cerebellum), and deep pink (pons and medulla).
C and **D.** Expression of *HOXD3*, *HOXA2*, and *CRABP1* expression heatmaps at 15- and 16-weeks post conception infratentorial brain at slices 1 (**C**) and slices 2 (**D**) from **B**. Left: schematic of brain sub-structures colored by overarching structure corresponding to key in **B**. Right, from top to bottom heatmaps of *HOXD3*, *HOXA2*, and *CRABP1* expression in corresponding areas. Illustration adapted from reference figure from the Allen Brain Atlas.
E. Expression patterns of *CRABP1*, *HOXA2*, and *HOXD3* at 15 and 16 weeks post-conception in the BrainSpan prenatal LMD microarray dataset grouped by hindbrain substructures (Allen Institute for Brain Science, 2010; J. A. Miller et al., 2014).

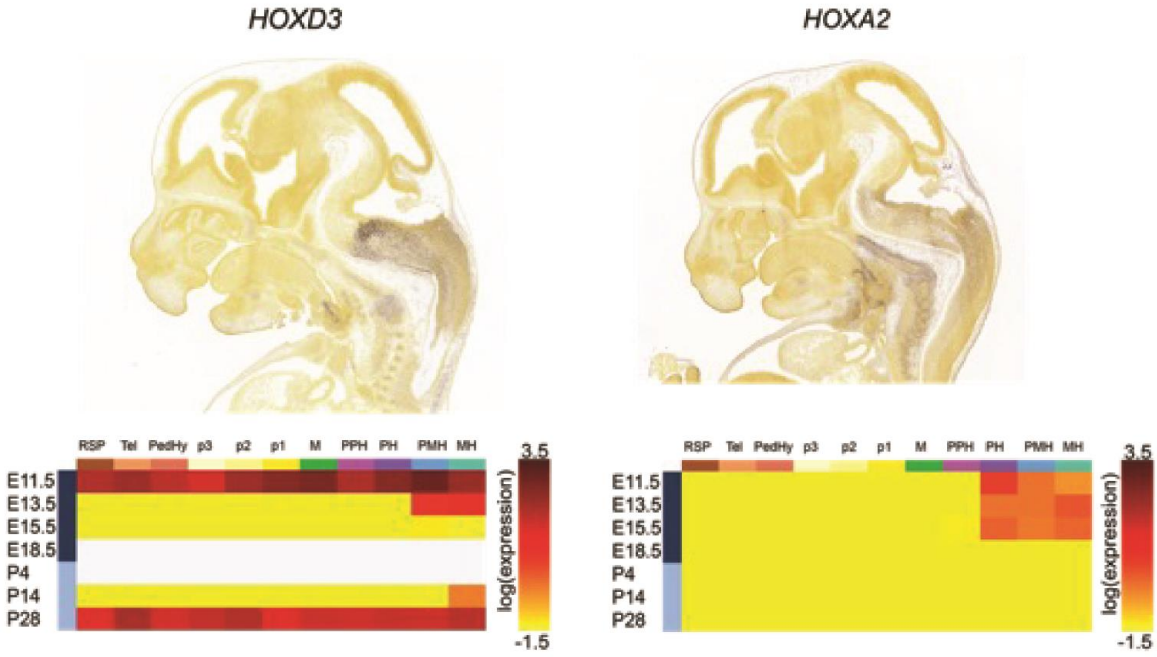

Figure 2.16: *HOXD3* and *HOXA2* are enriched in pontomedullary structures in mice.

HOXA2 and *HOXD3* expression patterns of the developing mouse from the Allen Brain Atlas. Top: *in situ* hybridization (ISH) staining for *HOXA2* and *HOXD3* in embryonic day 13.5 (E13.5). Bottom: Expression patterns of *HOXA2* and *HOXD3* across space and time in the developing mouse brain: RSP, rostral secondary prosencephalon; Tel, telencephalic vesicle; PedHy, peduncular hypothalamus; p3, prosomere 3; p2, prosomere 2; p1, prosomere 1; M, midbrain; PPH, prepontine hindbrain; PH, pontine hindbrain; PMH, pontomedullary hindbrain; MH, medullary hindbrain. Image credit: Allen Institute for Brain Science: https://developingmouse.brain-map.org/experiment/siv?id=100093342&imageId=101522680&initImage=ish (*HOXD3* ISH), https://developingmouse.brain-map.org/gene/show/15209 (*HOXD3* heatmap), https://developingmouse.brain-map.org/experiment/siv?id=100030618&imageId=100662735&initImage=ish (*HOXA2* ISH) https://developingmouse.brain-map.org/gene/show/15174 (*HOXA2* heatmap).

2.4 Discussion

While EZHIP-expressing PFAs and H3K27-altered DMGs (including H3.3 and H3.1K27M gliomas and EZHIP positive DMGs) have distinct natural histories and histologic features, evidence of their shared molecular features continues to mount as we profile broader samples of these tumor types. Furthermore, both tumors most commonly arise in neighboring hindbrain/posterior fossa-derived structures. This pattern suggests that developmental lineages in this region possess susceptibility to alterations that impede canonical PRC2 activity and therefore regulation of H3K27me3 state. Leveraging the existing molecular knowledge about each of these tumor types, we exploited genomic, bulk transcriptomic, scRNA-seq, and epigenomic profiles of both cancers to elucidate shared features that may improve our understanding of tumor biology.

Assessment of the genomic landscape of these tumors demonstrated that H3.1K27M DMGs showed greater copy number similarity with EZHIP-expressing DMGs than did H3.3K27M tumors. This similarity included more quiescent alteration landscapes and higher frequencies of 1q gain. These profiles of relatively lower genomic instability may point toward greater commonalities between PFAs and H3.1K27M vs. H3.3K27M DMGs. Consistent with this pattern, we identified high expression of *ACVR1*—a gene frequently altered in H3.1-mutant DMGs—to be associated with: (a) worse survival in PFAs, and (b) upregulation of pathways that were also enriched in *ACVR1*-mutated DMGs.

We additionally characterized common and unique features of H3K27M DMG and PFA chromatin landscapes based on patterns of H3K27me3/ac genomic deposition. The two tumors exhibited a considerable overlap in both H3K27me3-marked and H3K27ac-enhancer-associated

genes. Exploration of the transcriptional states associated with these gene sets demonstrated inter- and intra-tumoral heterogeneity of expression patterns. Common enhancer-associated genes enriched for cell motility, and oligodendrocyte and glial differentiation pathways. Moreover, scRNA-seq demonstrated the highest levels of expression of these genes in astrocytic lineage cell types, especially in comparison to progenitor cell types. These patterns highlight the unique insights single-cell resolution transcriptomics can provide and illustrate how tumor-specific enhancers generated from bulk-sequencing methods may not fully reflect the regulatory landscapes of the tumors.

Interrogation of genes associated with residual H3K27me3 also yielded important insights. The sensitivity of H3K27M DMGs and PFAs to EZH2 inhibition (S C Mack et al., 2014; Michealraj et al., 2020; Mohammad et al., 2017) points to a potential role for H3K27me3 in maintaining tumor cell proliferative capacity. Data from developing cerebellar atlases provide some support for this model in that upregulation of genes within these signatures is seen along oligodendrocyte lineages and in brainstem choroid/ependymal cells. Furthermore, we noted distinct expression profiles of proximal vs. distal *HOX* genes, which correlated with inferred anatomic origins of tumor, and these genes demonstrate distinct anterior-posterior boundaries of expression in the developing human hindbrain. These data suggest that developmental epigenetic profiles and origins of PFAs and H3K27M DMGs may influence the H3K27me3 landscape and gene expression profile in these tumors.

CRABP1, like the *HOX* genes, has been shown to have highly specific expression patterns in mouse nervous system development (Maden et al., 1992). In both PFAs and DMGs, its

expression correlated with specific tumor cell types, with an enrichment among progenitor-like cells. While its precise role remains unclear, *CRABP1* has been proposed to be a critical regulator of retinoic acid signaling, preventing canonical RA-induced transcriptional programs (Nhieu et al., 2022). This role is of particular interest due to retinoic acid's function in hindbrain patterning (Begemann & Meyer, 2001; Glover et al., 2006; Hernandez et al., 2007; Marshall et al., 1992; Niederreither et al., 2000) and the previous identification of the retinoic acid binding protein RXRA as the top ranked super-enhancer associated gene in H3K27M DMGs (Nagaraja et al., 2019). Together these data suggest that *CRABP1* may be associated with progenitor cells in early stages of the developing hindbrain that may be deregulated in both PFAs and H3K27M DMGs. Further investigation is needed to elucidate whether *CRABP1* contributes to maintenance of progenitor-type states in the presence of retinoids during development.

Overall, our studies further define molecular commonalities in the biology between DMGs and PFAs that express H3K27M and EZHIP and highlight similar patterns in the heterogeneity among tumors of each class. Moreover, some of these common epigenetic signatures showed specific patterns in human hindbrain development supporting the overall hypothesis that hindbrain developmentally and epigenetic deregulated molecular mechanisms may drive the biology of both tumors.

Note: A subset of this chapter has been adapted from work previously published in *Acta Neuropathologica Communications* (Pun et al., 2023). Per the journal's copyright policy, I retain the right to include the article in a dissertation.

Gene list 1 (551): Shared_me3				
MMEL1	FLT1	EN1	FERD3L	ISL2
TP73	OBI1-AS1	TBR1	ABCB5	CRABP1
HES2	FOXG1-AS1	SLC4A10	SP8	FOXL1
TNFRSF8	FOXG1	DLX1	SKAP2	MEIOC
LRRC38	LINC01551	DLX2	HOXA1	NPTX1
PAX7	SFTA3	DLX2-DT	HOTAIRM1	NXNL1
RUNX3	NKX2-1	SP9	HOXA2	GIPR
SLC30A2	NKX2-1-AS1	EVX2	HOXA3	NPAS1
LIN28A	NKX2-8	HOXD13	HOXA-AS2	SLC8A2
RSPO1	PAX9	HOXD12	HOXA4	LINC01869
EPHA10	FOXA1	HOXD11	HOXA-AS3	EPS8L1
RNF220	C14orf39	HOXD10	HOXA5	BCL11A
TAL1	SIX6	HOXD-AS2	HOXA6	PCGF1
FOXD2	SIX1	HOXD9	HOXA7	HOXD4
DMRTA2	VSX2	HOXD8	HOXA9	HOXD1
PCSK9	DIO3	HOXD3	HOXA10-AS	WNT6
DAB1	MIR203A	HAGLR	HOXA10	INSM1
FOXD3-AS1	GREM1-AS1	CERKL	HOXA11	CYP24A1
FOXD3	GREM1	NEUROD1	HOXA11-AS	GNAS-AS1
LHX8	DUOX2	ZDBF2	HOTTIP	MIR124-3
GFI1	DUOXA2	FEV	EVX1-AS	TBX1
SHE	ONECUT1	CRYBA2	EVX1	MPPED1
TDRD10	ALDH1A2	CFAP65	TBX20	PNPLA5
LMX1A	ALDH1A2-AS1	IHH	DLX6-AS1	ADM2
LHX4	CHRNA3	MIR3131	DLX6	DOCK3
C1orf53	BNC1	PTPRN	DLX5	HMX1
LHX9	SV2B	ALPP	CPED1	NWD2
NR5A2	HBM	ECEL1	WNT16	DCHS2
LGR6	HBAP1	TWIST2	FEZF1	MARCHF11
SYT2	HBA2	OVOL2	FEZF1-AS1	MARCHF11-DT
IRF6	HS3ST6	NKX2-4	KMT2C	RXFP3
ESRRG	MMP25	PAX1	EN2-DT	N4BP3
WNT3A	TRIM72	FOXA2	EN2	NRN1
RYR2	PYDC1	SLC32A1	SHH	POM121L2
GATA3-AS1	SLC6A2	MMP9	MNX1	GRM4
GATA3	ZFHX3	SLC12A5-AS1	MNX1-AS2	RUNX2
PTF1A	FENDRR	SLC12A5	MNX1-AS1	LIN28B-AS1
KIAA1217	FOXF1	TFAP2C	ERICH1	NEUROD6

GAD2	FOXC2-AS1	GNAS	SOX7	ABCB1
SYT15	ATP2A3	GATA5	PINX1	CFTR
NPY4R	ALOX15	NTSR1	XKR6	MIR124-1HG
DRGX	ASIC2	BHLHE23	GATA4	MIR124-1
CHAT	SLFN12L	SIM2	NKX2-6	FOXB2
SLC18A3	NEUROD2	TMPRSS2	EBF2	NTNG2
ANK3	IKZF3	TSPEAR	ADRB3	GRIN1
NEUROG3	KRT19	GSC2	SOX17	ARX
HHEX	SP6	EOMES	BHLHE22	TBX15
CYP26A1	SKAP1	CCK	PRDM14	NPHS2
FFAR4	HOXB2	PTPRG-AS1	MSC-AS1	RNU5F-2P
LINC01475	HOXB-AS1	FEZF2	MSC	FAM163A
NKX2-3	HOXB3	SYNPR	LINC02894	KCNK2
PAX2	HOXB-AS3	TAFA4	ESRP1	CNIH3
TLX1NB	HOXB4	GATA2	GDF6	ACTA1
TLX1	HOXB5	SOX14	STK3	FMN2
LBX1	HOXB6	LINC01391	OSR2	ADARB2
LBX1-AS1	HOXB7	FOXL2NB	MAFA	ENTPD1-AS1
VAX1	HOXB8	MME	DMRT1	HPSE2
MIR3663HG	HOXB9	SHOX2	DMRT3	SHTN1
MIR3663	HOXB-AS4	RSRC1	DMRT2	DHX32
EMX2OS	MIR196A1	NKX1-1	BNC2	TCERG1L
EMX2	HOXB13	OTOP1	CDKN2A-DT	NELL1
PRLHR	IGF2BP1	NKX3-2	CDKN2A	AVPR1A
HMX3	NGFR	LINC01096	CDKN2B-AS1	RPSAP52
HMX2	DLX4	PHOX2B	CDKN2B	HMGA2
FANK1	DLX3	PHOX2B-AS1	ARID3C	CUX2
FOXI2	TBX2-AS1	NKX6-1	PAX5	TBX5
VENTX	TBX2	ATOH1	ANKRD19P	NOS1
NLRP6	TBX4	PITX2	BARX1	GJB2
CALCB	ARHGAP27P2	NEUROG2	BARX1-DT	ESRRB
CALCA	USH1G	NEUROG2-AS1	FOXE1	ANKRD34C
DBX1	OTOP2	POU4F2	PAPPA	CDH8
SLC6A5	OTOP3	HAND2	LHX2	JPH3
SLC17A6	SRP68	HAND2-AS1	NR5A1	HAP1
BDNF	ZACN	SLC9A3	LMX1B-DT	CA10
WT1	GALR2	SLC6A3	LMX1B	ADCYAP1
WT1-AS	RBFOX3	IRX4	PRDM12	DCC
MIR129-2	GCGR	ISL1-DT	BARHL1	ST8SIA3

OVOL1	UTS2R	ISL1	LHX3	CYP1B1
FGF3	GATA6	CDC20B	CACNA1B	CYP1B1-AS1
MPZL3	SKOR2	MCIDAS	KANK4	KCNK12
MPZL2	ONECUT2	CCNO	ADGRL2	METAP1D
BSX	GRP	CCNO-DT	BARHL2	PCSK2
FLI1	RAX	OTP	BRINP3	VSX1
SENCR	CPLX4	PRDM6-AS1	C1QL3	CBLN4
PRMT8	CCBE1	PRDM6	GPRIN2	GHSR
COL2A1	KISS1R	PITX1	CTNNA3	GPAT3
HOXC13-AS	ARHGAP45	PITX1-AS1	GPR26	INTS12
HOXC13	ONECUT3	HAND1	EBF3	LEF1
HOXC12	ICAM5	TLX3	NKX6-2	LEF1-AS1
HOTAIR	SLC5A5	NKX2-5	ZNF511-PRAP1	MIR449C
HOXC11	COMP	MSX2	ASCL2	SLIT3
HOXC-AS3	NPHS1	FLT4	MYOD1	BTNL9
HOXC10	NCCRP1	FOXQ1	GAS2	PHACTR1
HOXC6	ARHGEF1	DSP	RAG1	RFX6
MIR196A2	KCNA7	TFAP2A	RAG2	PDE10A
HOXC9	PTH2	TFAP2A-AS1	FGF19	MEOX2
HOXC-AS1	GFY	SYCP2L	ROBO3	NPY
HOXC8	SLC17A7	TFAP2B	DBX2	CALCR
HOXC4	KLK10	PRDM13	DBX2-AS1	TAC1
HOXC5	TNNT1	SIM1	CYP27B1	NPTX2
MIR615	GDF7	LIN28B	ANKS1B	CNTNAP2
ALX1	SLC30A3	VGLL2	GJA3	ANK1
ASCL4	SIX3-AS1	TARID	ATP8A2	RALYL
LHX5	SIX3	TCF21	POU4F1	VPS13B
TBX3	EMX1	OLIG3	DIO3OS	ZFPM2
PIWIL1	NOTO	ULBP2	MIR1247	TSNARE1
P2RX2	EGR4	ULBP1	AMN	TRPM3
PLUT	LBX2	ESR1	EXOC3L4	
PDX1	TLX2	TBXT	GJD2-DT	
CDX2	FOXI3	FOXL3	FOXB1	
URAD	ACOXL	TWIST1	ISLR2	

Table 2.1: Genes with retained H3K27me3, shared by H3K27M DMGs and PFA ependymomas.

Gene list 2 (525) shared enhancers				
FAM171A2	NCALD	PPARD	ROBO4	DCHS1
FAM89A	NHLH1	TONSL	DSCAM	STH
GABRA5	PAH	S100A4	CAPN2	ME3
GRIP1	PGBD5	BRK1	MRVI1	BCR
MACROD2	PKNOX2	TRIB1	LRRN2	SBNO2
PLAG1	PLEKHG3	C6orf1	KIFC2	CSMD2
ZIC3	PLXNA2	CSMD3	BPIFB2	NNMT
C1QL4	PNMAL2	DISP1	ELFN1	CPEB4
PCDH7	POU3F1	C4A	PRKCH	PACSIN2
SGSM1	PREX1	VPS28	UST	GHRHR
ZFPM2	PRKCE	ASCC2	BEND6	PVRL1
ABTB2	PRKCZ	ATXN7L3	TNFRSF1B	NFKBIE
ADARB2	RAB11FIP4	INPPL1	LPP	MAPK8IP1
C11orf96	RORC	NFIL3	CISH	PRCP
CBX2	RTN4R	PPP1R37	DOCK3	ADCYAP1R1
CBX8	SASH1	KCNE3	ITGB4	KLF7
KSR1	SEMA4A	FBXW5	CD82	GPR153
MDFI	SLC45A1	SLC7A1	SDC3	AFAP1
PAX3	SMTNL2	SLC6A12	RAB6B	OLFML2B
PDE4DIP	SOX1	MYC	GEM	ELMO2
PDZD2	SSBP3	PPP1R18	ASAP1	PTPRE
PHACTR3	ST8SIA1	MIIP	PWP2	NFKBIA
PTP4A3	STOX2	FAM222A	PLIN4	ARHGEF3
RORA	TBC1D14	EPS15	PDGFRB	CREB3L2
SCUBE3	TEKT2	GSTM1	NTRK2	FILIP1L
BMP5	TEX40	TNR	MAD2L2	DIRAS1
GABRD	TPPP	NFYA	CHST11	KCNN3
SLC24A3	WNK2	SGTA	COL23A1	IGFBP2
TMEM132E	WWC1	SPRY2	MAD1L1	SEMA4C
TRIM71	ZBTB16	GEMIN7	NXPH4	DLK1
ADARB2-AS1	ZBTB18	NTNG2	LSAMP	MVP
C2orf40	ZNF521	ELL2	IFITM2	GSTM3
CD5	ADARB2-AS1	TNC	LRRTM4	ACO2
CD8A	C2orf40	EYA2	TIAM1	TMEM127
CNTNAP2	CD5	WNT3	P2RY6	VEGFA
CRABP1	CD8A	CACNA1C	CACNA1G	LHFPL3
CSRNP3	CNTNAP2	NRXN2	CASZ1	GSK3A
DAAM1	CRABP1	MGLL	BHLHE40	APOL1
DTNBP1	CSRNP3	AQP1	SPOCK2	MAPKAPK2
FAM110D	DAAM1	RNF144A	PFKL	TSHZ3
FAM163A	DTNBP1	NAV1	NAV2	SAPCD2
FBN3	FAM110D	SIRPA	OLFM2	PCDH12

GABRG3	FAM163A	SNPH	DPYSL4	RASD1
GRID2IP	FBN3	TSPAN18	SRL	WNT5A
IRX1	GABRG3	VIPR2	NPAS2	SLC35F6
IZUMO1	GRID2IP	ANGPTL2	PTN	GRID1
JPH4	IRX1	C2CD2	IFITM3	MAML2
KCNA6	IZUMO1	PSD4	ZNF385A	DGKI
KIAA1211	JPH4	MAPKAPK3	PIP4K2A	KIRREL
KY	KCNA6	PDE8A	PLEKHO1	MAPT
LY6H	KIAA1211	GRK5	PDZRN3	GALNT15
MASP1	KY	C1QL1	EFTUD2	CLN8
NCKAP5	LY6H	GRAMD1B	XXYLT1	PLIN3
NINL	MASP1	SNAI1	TTYH3	PIP5K1C
OCA2	NCKAP5	SLC29A1	SLC25A18	CHST1
PPP2R2C	NINL	TSPAN9	FRMD4A	SCARA3
SCARF2	OCA2	ZFP36L1	ITPK1	GPER1
SESN3	PPP2R2C	ENG	SEMA5B	ATP1A2
SH3GL3	SCARF2	LEMD1	HIF3A	SNX33
SKOR1	SESN3	MSRA	IGSF9B	PKDCC
SYN3	SH3GL3	PCBP3	RNF215	CDH22
TSPAN11	SKOR1	FIBCD1	DAAM2	MYO1D
TTC9B	SYN3	KCNK3	CD44	FGR
ABLIM2	TSPAN11	PDK2	CDH23	MOCS1
ACSS1	TTC9B	COL6A1	ACVRL1	RRP1
ALOX12B	NCK2	ROR2	SERPINH1	SUN2
ARVCF	DRAP1	PGAM2	PDIA5	CLU
ASGR1	RTL1	GRHL3	COMMD9	CD59
BCL11A	EVL	FAM198A	ZNF395	TENM4
C20orf203	DYNC1I1	LGALS3	PRKCA	ADAM17
CACNA2D2	SH3BP5	SLC22A23	SLC44A3	SUSD2
CAMK1D	KCND2	B3GNT7	SLC29A3	GALNT2
CCDC88C	PXDN	MECOM	RAB11FIP5	RBMS1
CDK5R1	LGI4	TMEM189	FTH1	FAM181B
CELF2	SLC6A13	RRBP1	SF3A2	CPAMD8
CSMD1	HSPB7	KRBOX1	COL1A1	SMOC1
CYP2A6	ST3GAL5	ZCCHC24	ZNF423	APOL2
DMTN	CD276	MFAP5	RHOU	PSRC1
DNAH2	GNAI3	PRIMA1	ID2	FAM168A
DNMT3A	IGF2BP3	PITPNM2	CBX4	CNTN2
DOC2B	PAG1	NTM	TMCC3	ZFPM1
DPF1	PBX3	LINGO1	SLC39A11	CHI3L1
EFNA2	RGS16	CSPG4	DOT1L	ACTG1
ENPP6	SCARF1	STEAP3	IFITM1	TMEM151B
FAM107B	GLRX	SCUBE2	TBC1D16	DST

FAM19A5	CD248	APLNR	WIPF1	STOML1
FLRT1	NDUFA4L2	AQP4	LDLRAD3	NOVA2
GHRH	OCIAD2	GREB1	MCF2L	TOB2
GLT1D1	TK1	ARL4C	HTRA3	CLIC4
GNG7	TUBB4A	ASS1	ATP1B1	PCGF3
GRASP	SLC25A23	ADCY5	ITGA5	COL27A1
IGDCC3	RGCC	DRAXIN	SOX13	PRR5L
IGSF9	GRIA4	GLUL	RELT	NAT8L
IRX2	HEYL	CSF1	PLCG2	KIF21B
ITM2C	TMUB2	COL4A2	APOL4	OSBPL11
KBTBD11-OT1	HMGA1	GFPT2	ABLIM3	FMNL2
KCNA3	IRAK2	EEPD1	SCD	DAPK1
KCNJ9	SEMA7A	SFN	RASSF5	KBTBD11
KCNK4	NAB1	NTRK3	HS6ST1	HYAL2
KIF1A	ZEB1	COL4A1	RLBP1	CAMK2G
LBR	SMARCB1	SERPINE2	RECQL4	MAPRE2
LDB2	GPC1	PPIF	OTOS	ZFP36L2
MEGF11	DOCK4	GAB2	DGKG	CYTH1
MIR4454	BTG1	RASGEF1A	SDC4	LMNB2
MN1	LAMA4	SLC35C2	LMOD1	EHD1

Table 2.2: Enhancer-associated genes, shared by H3K27M DMGs and PFA ependymomas.

Chapter 3
Characterizing the Epigenomic and Transcriptomic Impact of the Clinically Promising Compound ONC201 in H3K27M-mutant Diffuse Midline Gliomas

3.1 Introduction

3.1.1 Patients with H3K27M-mutant gliomas have limited treatment options

Diffuse midline gliomas harboring histone H3 residue 27 lysine-to-methionine mutations (H3K27M DMGs) are one of the most aggressive forms of brain cancer with median overall survival (OS) of 10-15 months (Hoffman et al., 2018; Mackay et al., 2017). H3K27M DMGs account for nearly half of pediatric high-grade gliomas and primarily arise in the pons and thalamus (Mackay et al., 2017). While a number of approaches have been identified as promising therapeutic avenues based on preclinical studies, none have yet to find success in clinical settings (Argersinger et al., 2021). To date, the only treatment with strong support for clinical benefit is radiation treatment, based on retrospective analysis (Langmoen et al., 1991), and it continues to be the standard of care.

Treatment strategies from adult glioblastomas have repeatedly failed to translate to these devastating pediatric tumors (Jones et al., 2017). The investigational dopamine receptor D2 (DRD2) antagonist ONC201 was originally proposed for adult tumors but has instead shown more promise for H3K27M DMGs. Phase II clinical trial studies in high grade gliomas/glioblastomas resulted in durable radiographic responses in two patients with histone H3K27M-mutant tumors in contrast to a lack of substantial responses for histone-wild type (WT) tumors (Arrillaga-Romany et al., 2020).

These promising cases prompted the initiation of two recently completed clinical studies (NCT03416530 and NCT03134131) for H3K27M DMGs. NCT03416530 (ONC201-014) included 30 post-radiation patients who met criteria for efficacy analysis and had a median age of 8.2 years (range 2-21) whereas the expanded access trial NCT03134131 (ONC201-018) included an additional 41 post-radiation patients 23.7 years (range 4-58).

3.1.2 Treatment with the investigative compound ONC201 is associated with unprecedented survival times in H3K27M DMG

While the primary outcome for ONC201-014 was dose-determination for a follow-up phase II study and is therefore limited by a lack of a randomized control group, the results of both trials demonstrate survival benefits in relation to historical comparison groups. Median OS in non-recurrent ONC201-treated tumors across the two studies was 26.3 months, whereas median OS for a historical cohort of non-recurrent H3K27M tumors was 12 months (Figure 3.1A), a difference which remained significant in multivariate regression, adjusting for age, sex, and tumor site. Analysis of recurrent H3K27M DMGs treated with ONC201 also revealed an increase in median OS compared to a historical cohort of patients with recurrent H3K27M DMGs (Figure 3.1B).

To further highlight the potential efficacy of ONC201 in H3K27M DMGs, median survival outcomes were compared against results from two recently completed clinical trials in H3K27M DMGs: HERBY Phase II (median OS 14.2 months) and PNOC003 (median OS 11.3 months).

Altogether, the data from ONC201-014 and ONC201-018, though limited by trial design, represented unprecedented responses for a disease with no effective medical therapies to date.

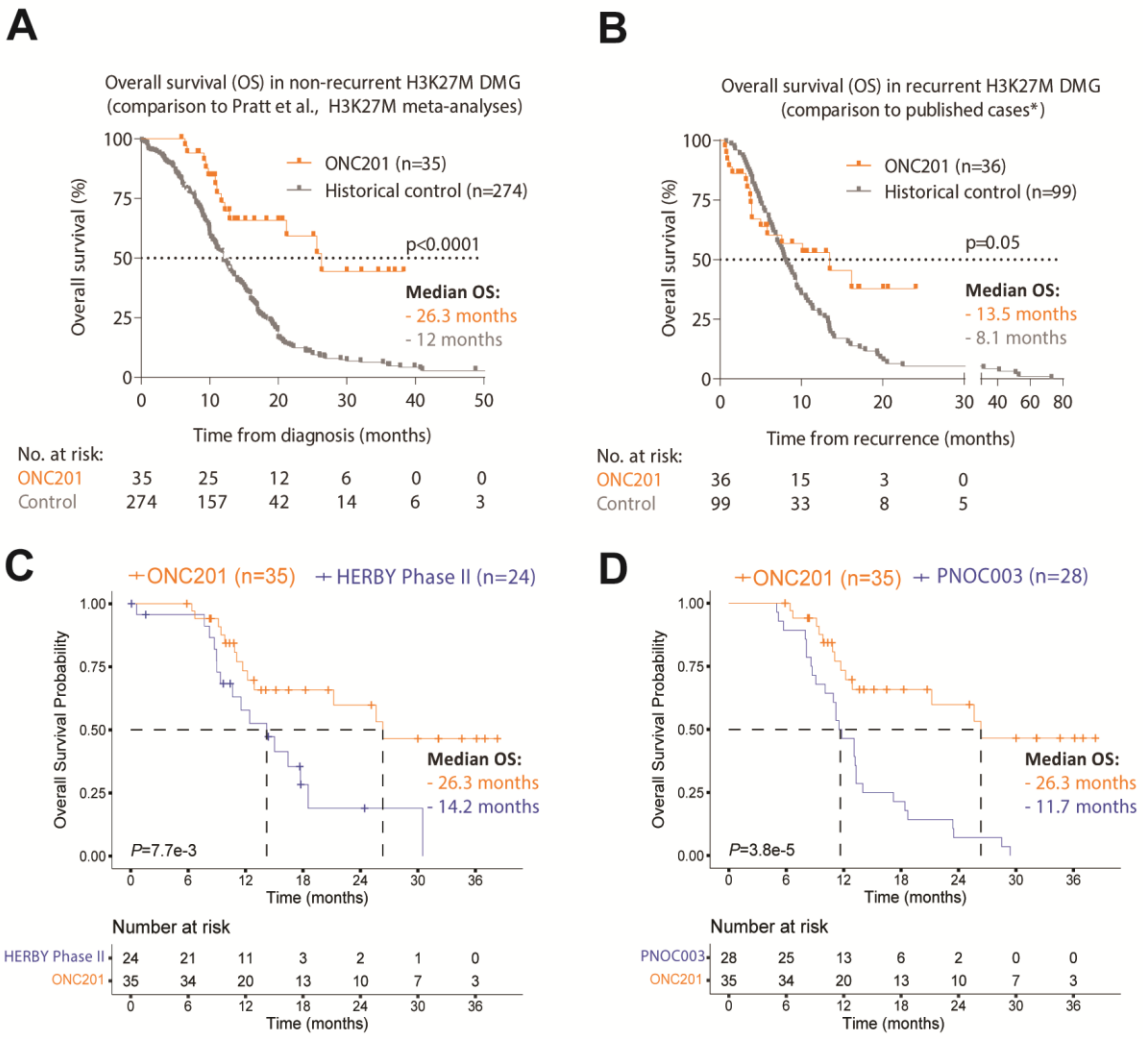

Figure 3.1: Patients treated with ONC201 demonstrate improved survival compared to available data from multiple historical cohorts

A. Kaplan-Meier curves (Y-axis: overall survival percentage, X-axis: time in months) comparing overall survival (OS) for patients with non-recurrent H3K27M DMGs undergoing ONC201 treatment with a cohort of historical controls compiled by Drew Pratt (Drew Pratt et al., 2018).
B. Kaplan-Meier curves comparing OS for patients with recurrent H3K27M DMGs undergoing ONC201 treatment to a compiled set of cases from Castel et al., Lobon-Iglesiaas et al., and an unpublished cohort from the Gustave Roussy Institute in France (Castel et al., 2018; Lobon-Iglesias et al., 2018).
C. Kaplan-Meier curves comparing OS for the non-recurrent H3K27M DMG patients treated with ONC201 from panel A compared to H3K27M DMG patients in the HERBY Phase II (Grill et al., 2018).
D. Kaplan-Meier curves comparing OS for the non-recurrent H3K27M DMG patients treated with ONC201 from panel A compared to H3K27M DMG patients in the PNOC003 trial (C. Kline et al., 2022).
All four curves are adapted from plots generated by Dr. Carl Koschmann and his collaborators.

3.1.3 The mechanism underlying efficacy in H3K27M DMGs remains unknown

In addition to its DRD2 antagonism, ONC201 has been found to modulate additional pathways involved in proteolysis and stress response (Endo Greer & Lipkowitz, 2016; J. O. Ishizawa et al., 2016; C. L. B. Kline et al., 2016), and its mechanism of toxicity in H3K27M DMG cells is not well understood. To develop a better understanding of the mechanisms contributing to these striking responses in patients treated with ONC201, we undertook an integrated approach, utilizing gene expression data from patient samples and a cell line model of H3K27M DMGs to investigate potential metabolic and epigenetic pathways indicative of tumor response. Complementing these transcriptional findings with data from metabolic and epigenetic assays, we identify dysregulation of the tricarboxylic acid (TCA) cycle and its epigenetic effects as a consequence of ONC201 treatment and a potential mechanism of toxicity in H3K27M DMGs.

3.2 Methods

3.2.1 In vitro modeling of H3K27M DMG ONC201 treatments

The H3.3K27M cell line HSJD-DIPG-007 (RRID: CVCL_VU70 ; DIPG-007) was donated by Rintaro Hashizume from the Northwestern University and cultured in a humidified 5% CO_2 incubator, 21% O_2 at 37°C. DIPG-007 cells were cultured in a 1:1 mixture of Neurobasal-A (Thermo Fisher Scientific #10888022, Grand Island, NY) and DMEM/F-12 (Thermo Fisher Scientific #11330032) media supplemented with HEPES (1 M) (Thermo Fisher Scientific #15630080), Sodium Pyruvate (100 mM) (Thermo Fisher Scientific #11360070), MEM Non-Essential Amino Acids Solution (Thermo Fisher Scientific #11140050), antibiotic-antimycotic (100X) (Thermo Fisher Scientific #15240096) and GlutaMAX™ Supplement (Thermo Fisher Scientific #35050061). Directly before use, B-27 Supplement, minus vitamin A (Thermo Fisher

Scientific #12587010), 20 ng/µl human EGF (Shenandoah #100-26, Warminster, PA), 20ng/µL human FGF- BASIC-154aa (Shenandoah #100-146), 10 ng/µl human PDGF-AA (Shenandoah #100-16), 10 ng/µL human PDGF-BB (Shenandoah #100-18), and 2 µg/ml Heparin Solution, 0.2% (StemCell Technologies, Inc. #07980, Cambridge, MA) were added.

ONC201 was purchased from Cayman Chemical, Ann Arbor, MI (catalog# 16109) and dissolved in dimethyl sulfoxide (DMSO) (Sigma #D2650, St. Louis, MO) and then diluted to its final concentrations in culture media. DMSO was used as a vehicle control for all experiments.

3.2.2 DIPG-007 (in vitro) RNA- and ChIP-seq sample preparation

RNA and chromatin immunoprecipitation samples were prepared from the same cultures. $2.5x10^6$ cells per replicate were seeded into T75 flasks and treated with either DMSO vehicle or 5 µM of ONC201. After 48 hours, one replicate was counted using trypan blue exclusion and Countess automated cell counters to assess viability. When samples passed an 80% viability threshold, cells from additional flasks were collected. 1×10^6 cells per flask were aliquoted for RNA extraction and the remainder were fixed for chromatin immunoprecipitation.

For RNA extraction, 750 µL of TRIzol™ was added to each sample and mixed by pipetting and then incubated for 5 minutes. Next, 200 µL of chloroform was added to each sample, mixed by shaking, incubated for 3 minutes, and then centrifuged to isolate the aqueous phase. RNA was precipitated on ice with isopropanol and washed with 75% ethanol prior to a final elution in water. With the support of the Advanced Genomics and Bioinformatics Cores of the University of Michigan Medical School's Biomedical Research Core Facilities, RNA samples were

evaluated for RNA integrity numbers, and polyA-enriched libraries were generated and sequenced single-end on the NovaSeq S4 300 in triplicate per condition.

For ChIP-seq, cells were fixed according to the Active Motif Epigenetics Services ChIP Cell Fixation Protocol. First cells were fixed with 1% formaldehyde (Sigma #F-8775) in media, rocking for 15 min and quenched with 0.125 M glycine. Cells were next washed with a PBS-Igepal solution and then finally washed with 1 mM phenylmethanesulfonyl fluoride (Sigma #P-7626) in PBS-Igepal before snap-freezing the pellets on dry ice.

In steps performed by Active Motif, chromatin was isolated by the addition of lysis buffer and disruption with a Dounce homogenizer. Lysates were sonicated and the DNA sheared to an average length of 300-500 bp. Chromatin aliquots were processed with RNase, proteinase K and heat for de-crosslinking. The resulting ethanol-treated precipitates were resuspended and quantified via NanoDrop spectrophotometer to determine chromatin yields. Subsequently, 30 µg of chromatin per replicate was precleared with protein A agarose beads (Invitrogen). Genomic DNA regions of interest were isolated using 4 ug of antibody against H3K27ac (Active Motif). Next immunoprecipitates were washed, eluted from the beads in an SDS buffer, and subjected to RNase and proteinase K treatment. Crosslinks were reversed by incubation overnight at 65°C, and ChIP DNA was purified by phenol-chloroform extraction and ethanol precipitation. Quantitative PCR (qPCR) reactions were carried out in triplicate on specific genomic regions using SYBR Green Supermix (Bio-Rad) for quality assessment. An automated system (Apollo 342, WaferGen Biosystems/Takara) was employed to generate Illumina sequencing libraries via

end-polishing, dA-addition, adaptor ligation, and PCR amplification. Resulting libraries were quantified and sequenced on an Illumina NextSeq 500 (75 nt reads, single-end).

3.2.3 RNA-seq processing

Raw sequencing reads underwent adapter trimming via Cutadapt (v2.3) (Martin, 2011) and screened for quality using FastQC (v0.11.8) and Fastq Screen (Andrews, 2010; Wingett & Andrews, 2018). Reference genome mapping was processed using STAR v2.7.8a (PMID: 23104886) and reference genome GRCh38/hg38 in accordance with ENCODE standards. Counts were quantified with RSEM (v1.3.3) (B. Li & Dewey, 2011). The above steps were performed by the Bioinformatics Core of the University of Michigan. Raw count data were then analyzed for differential expression with DEseq2 (v1.36.0) (Love et al., 2014).

3.2.4 ChIP-seq processing

Resulting raw reads were aligned to the human reference genome (hg38) using the BWA algorithm (default settings). Reads were deduplicated and screened for mapping quality greater than or equal to 25. H3K27ac peak locations were determined using the MACS algorithm (v2.1.0) with a cutoff of p-value = 1e-7. Peaks that were on the ENCODE blacklist (Amemiya et al., 2019) of known false ChIP-Seq peaks were removed. Spike-in of chromatin from another species, the fruit fly *Drosophila*, was performed and the number of test tags were normalized by the same number of spike-in Drosophila tags for each sample. Alignments were extended in silico at their 3'-ends to a length of 200 bp, which is the average genomic fragment length in the size- selected library and then assigned to 32-nt bins along the genome for visualization and

stored in bigWig files. ChIP-seq signal at promoter and enhancer sites was assessed using deepTools (v3.5.1) computeMatrix and plotHeatmap tools (Ramírez et al., 2016).

3.2.5 Super enhancers analysis

Previously identified H3K27M-specific super-enhancers from Krug *et al.* were mapped to hg38 reference genome coordinates using the UCSC genome browser's LiftOver tool (accessed September 2022). The resulting regions were evaluated for ChIP-seq signal in vehicle- or ONC201-treated DIPG007 cells using deepTools computeMatrix and plotProfile tools.

3.2.6 ATAC-seq analysis

Samples processed by Active Motif were sequenced with paired-end 42 base-pair sequencing on the NextSeq 500 sequencer (Illumina). Reads were aligned using the BWA algorithm (mem mode; default settings). Duplicate reads were removed, only reads mapping as matched pairs and only uniquely mapped reads (mapping quality >= 1) were used for further analysis. Alignments were extended in silico at their 3'-ends to a length of 200 bp and assigned to 32-nt bins along the genome. The resulting histograms (genomic "signal maps") were stored in bigWig files. Peaks were identified using the MACS 2.1.0 algorithm at a cutoff of p- value 1e-7, without control file, and with the –nomodel option. Peaks that were on the ENCODE blacklist of known false ChIP-Seq peaks were removed. Merged regions were composed from all peaks identified across conditions. ATAC-seq signal at promoter and enhancer sites was assessed using deepTools (v3.5.1) computeMatrix and plotHeatmap tools.

3.2.7 Mint ChIP analysis

MiNT-ChIP sample processing for 8 tumor samples at autopsy from 4 H3K27M-DMG patients (2 with previous ONC201 treatment and 2 without) was conducted by collaborators at the University Hospital in Bonn, Germany according to previously published protocol (van Galen et al., 2016). Briefly 50 mm^3 of snap frozen tumor tissue was digested with 2.5 mg/ml collagenase IV (Sigma-Aldrich, Germany) and dissociated via the gentleMACS Dissociator (Miltenyi, Germany). Subsequent immunoprecipitation for H3K27me3 was performed with 5 μg of ChIP-grade polyclonal rabbit anti-H3K27me3 (Merck Millipore, Germany). Over 50 million reads were sequenced in 50 bp paired-end sequencing runs on a NovaSeq 6000 system (NGS Core Facility, University Hospital, Bonn, Germany) and demultiplexed as described (Core Unit Bioinformatics Data Analysis, University Hospital Bonn, Germany). Reads were aligned against the human reference genome hg19 by Bowtie2 (v2.4.2). Tag directories of piled up reads were created using HOMER (v4.11) makeTagDirectory and visualized makeUCSCfile with the -fsize 5e8 option. Comparisons between conditions were made using the R package DiffBind (v3.8.4) (Ross-Innes et al., 2012), and visualizations were created in DeepTools as described in Section 3.2.3.

3.3 Results

3.3.1 ONC201 drives unfolded protein response in DIPG-007 cells

In addition to its initial characterization as a DRD2 antagonist, ONC201 has since been reported to cause cell death in multiple tumor models via cellular stress pathways mechanisms (Endo Greer & Lipkowitz, 2016; J. O. Ishizawa et al., 2016; C. L. B. Kline et al., 2016). Specifically, it has been shown that the mitochondrial protease caseinolytic peptidase P (ClpP) is necessary for ONC201 toxicity in H3K27M DMGs, and ONC201 activates ClpP proteolysis, triggering

mitochondrial damage (Greer et al., 2018; J. Ishizawa et al., 2019). Transcriptionally, ONC201-treated cells demonstrate activation of the integrated stress response, ER stress response, and unfolded protein response pathways (Przystal et al., 2022).

In our data examining the H3K27M DMG cell line DIPG-007's response to ONC201 treatment, we identified greater than 6000 genes significantly differentially regulated (padj<0.05, $\log_2$ fold change > 1 or < -1) (Figure 3.2A). Critically, integrated stress response pathway genes *ATF4*, TNF receptor superfamily member 10b (*TNFRSF10B*), and DNA damage inducible transcript 3 *(DDIT3I*) are all upregulated with ONC201 treatment, aligning with prior studies and known patterns of *ATF4* induction (Dey et al., 2010; C. L. B. Kline et al., 2016). To perform pathway enrichment, we examined genes at a more stringent cutoff of a $\log_2$ fold change > 2 for upregulated genes. Consistent with prior data, the top upregulated genes in ONC201-treated DIPG-007 are enriched for unfolded protein response, integrated stress response, and ER stress pathways (Figure 3.2C).

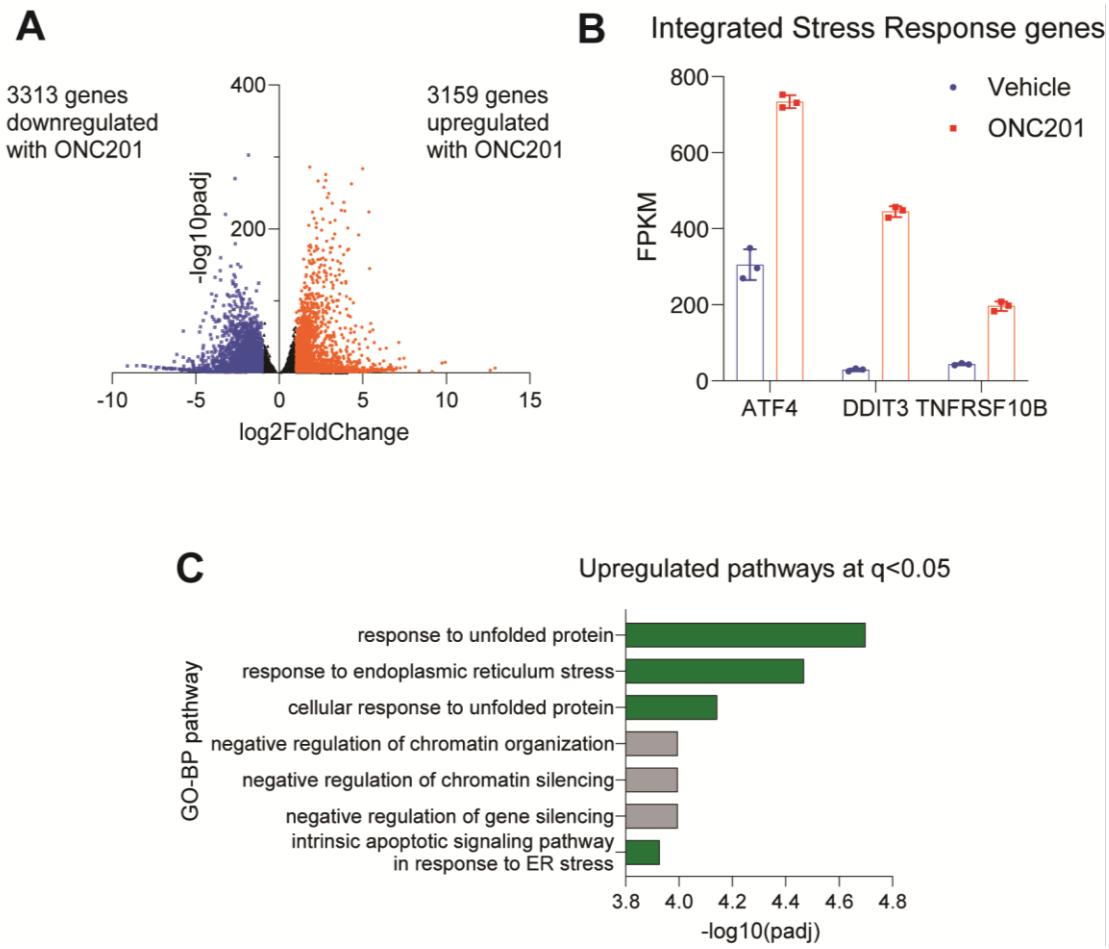

Figure 3.2: ONC201 treatment of DIPG-007 cells replicates observed upregulation of ER and metabolic stress response pathways.

A. Volcano plot showing expression changes with ONC201 treatment for DIPG-007 cells. Log_2fold change of expression in ONC201-treated cells over vehicle-treated cells (x-axis) is compared to log_{10}(adjusted p-value) (y-axis). Cutoffs for upregulated (orange) and downregulated (blue) genes shown here are log_{10}(adjusted p-value) < 0.05 and absolute value of Log_2fold change >1.
B. Expression levels in fragments per kilobase of exon per million mapped fragments (fpkm, y-axis) of integrated stress response genes (x-axis) for DIPG-007 cells treated with Vehicle or ONC201.
C. Upregulated pathways (y-axis) at a q-value < 0.05 significance level, ordered by -log_{10}(p-value). Previously observed stress response pathways shown in green.

3.3.2 Integration of tumor and cell line transcriptome data highlights the role of metabolic pathways in ONC201 response

In order to discover what transcriptional changes might have the greatest clinical relevance, we next examined our RNA-seq results in the context of RNA-seq from patient tumors treated with ONC201. Using RNA-seq samples from baseline tumors of patients enrolled in ONC201-014 and ONC201-018, correlations between gene expression and radiographic response were calculated. The top 500 genes that correlated with a positive radiographic response were enriched for genes in oxidative phosphorylation and the tricarboxylic acid (TCA) cycle (Figure 3.3B). Examination of gene expression changes in DIPG-007 ONC201-treated cells showed downregulation of multiple genes involved in glycolysis and the TCA cycle, including *OGDH*, *HK2*, and *ACLY* (Figure 3.3B). Experiments performed by Dr. Mateus Mota in the Venneti Lab confirmed decreases of these enzymes at the protein level with treatment, and metabolomic studies were performed to assess the impact of ONC201 on glycolysis and TCA cycle metabolism. These studies generated by Dr. Stefan Sweha in the Venneti Lab are shown in Figure 3.3C-E and summarized next.

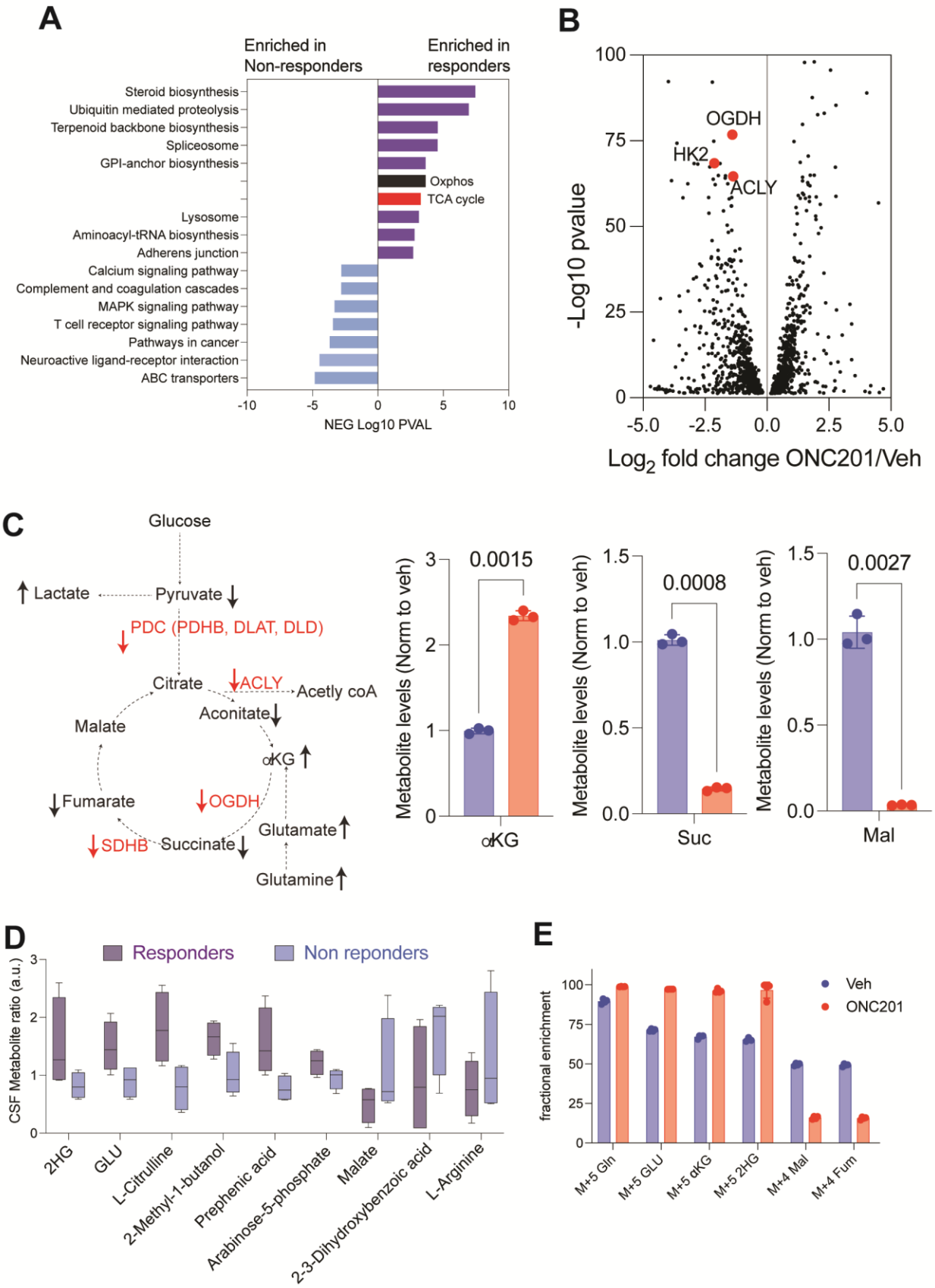
A
Enriched in Non-responders
Enriched in responders
Steroid biosynthesis
Ubiquitin mediated proteolysis
Terpenoid backbone biosynthesis
Spliceosome
GPI-anchor biosynthesis
Oxphos
TCA cycle
Lysosome
Aminoacyl-tRNA biosynthesis
Adherens junction
Calcium signaling pathway
Complement and coagulation cascades
MAPK signaling pathway
T cell receptor signaling pathway
Pathways in cancer
Neuroactive ligand-receptor interaction
ABC transporters
-10
-5
0
5
10
NEG Log10 PVAL
B
100
75
50
25
0
OGDH
HK2
ACLY
-Log10 pvalue
-5.0
-2.5
0.0
2.5
5.0
Log2 fold change ONC201/Veh
C
Glucose
Lactate
Pyruvate
PDC (PDHB, DLAT, DLD)
Citrate
ACLY
Acetly coA
Aconitate
Malate
αKG
Fumarate
OGDH
SDHB
Succinate
Glutamate
Glutamine
Metabolite levels (Norm to veh)
0.0015
αKG
0.0008
Suc
0.0027
Mal
D
Responders
Non reponders
CSF Metabolite ratio (a.u.)
2HG
GLU
L-Citrulline
2-Methyl-1-butanol
Prephenic acid
Arabinose-5-phosphate
Malate
2-3-Dihydroxybenzoic acid
L-Arginine
E
fractional enrichment
Veh
ONC201
M+5 Gln
M+5 GLU
M+5 αKG
M+5 2HG
M+4 Mal
M+4 Fum

Figure 3.3: Highly expressed TCA cycle genes in ONC201 responders are downregulated with treatment *in vitro* and reprogram metabolic pathways.

A. Pathway enrichment of top 500 genes associated with responders (y-axis, top, right) and top 500 genes associated with non-responders (bottom, left) as measured by correlation between RNA levels and radiographic response. Pathways are ordered by -log10(p-value) (x-axis).
B. Volcano plot of metabolic genes showing expression changes with ONC201 treatment for DIPG-007 cells. Log_2fold change of expression in ONC201-treated cells over vehicle-treated cells (x-axis) is compared to log_{10}(p-value) (y-axis).
C. TCA cycle pathway map with solid arrows indicating direction of change for metabolites (black) or genes (red) with ONC201 treatment in DIPG-007 cells (left) and metabolite levels (y-axis) for metabolites up- and downstream of OGDH in vehicle or ONC201-treated cells.
D. Metabolite measurements (y-axis) of patients treated with ONC201, comparing levels for responders (purple) to non-responders (blue) for various metabolites.
E. Fraction of isotope-labeled glutamine (y-axis) for glutamine (Gln), glucose (GLU) and TCA cycle metabolites.
The plots in A and D were generated by Dr. Carl Koschmann. The plots in C and E were generated by Dr. Sriram Venneti.

3.3.3 ONC201 restricts TCA cycle flux and drives production of 2-hydroxyglutarate (2HG)

Intracellular metabolomic profiling comparing DIPG-007 cells treated with ONC201 or vehicle resulted in striking alterations of TCA cycle metabolites. Consistent with the decrease in OGDH following treatment, downstream metabolites succinate, fumarate and malate all were lowered with treatment (Figure 3.3C). In contrast, the OGDH substrate oxoglutarate, also known as alpha-ketoglutarate (αKG), accumulated with treatment. To contextualize the potential clinical significance of these findings, collaborators from Dr. Carl Koschmann's lab collected cerebrospinal fluid (CSF) from patients on ONC201-014 and -018 and performed metabolomic profiling. These data demonstrate decreased levels of malate in responders compared to non-responders (Figure 3.3D).

Glucose and glutamine are the major carbon sources for TCA metabolites. To decipher how ONC201 rewired TCA cycle metabolism in H3K27M DMGs, Dr. Sweha next performed stable-isotope metabolic tracing studies with [13C5]-labeled glucose or glutamine in DIPG-007 cells. The tracing studies confirmed decreased flux of both glucose and glutamine to malate and fumarate. Additionally, glutamine-derived αKG increased with treatment (Figure 3.3E), while glucose-derived αKG in fact decreased.

Glutamine tracing revealed an additional surprising finding; levels of the oncometabolite 2-hydroxyglutarate (2HG) derived from labeled glutamine rose upon ONC201 treatment (Figure 3.3E). 2HG has been well-characterized in the studies of isocitrate dehydrogenase (IDH) 1-mutant gliomas and other tumors (L. Dang et al., 2009; Lu et al., 2012; Ward et al., 2010). In these tumors, it inhibits epigenetic modifiers responsible for demethylation of both DNA

methylation and histone methylation, including H3K27me3. In CSF metabolite profiles, responders demonstrated higher 2HG levels than non-responders (Figure 3.3D). Furthermore, metabolite profiling from serial CSF collections of a responder and non-responder demonstrated inverse trends in 2HG detection.

3.3.4 ONC201 treatment drives 2HG production, alters the chromatin landscape of H3K27M DMGs, and reverses pathognomonic H3K27me3 depletion

Given 2HG's known role in histone methylation states (Losman & Kaelin, 2013), we next asked how ONC201 influences the chromatin landscape. Due to the well-characterized hypo-methylated and hyper-acetylated H3K27 status of H3K27M gliomas, we assessed how our 5 μM, 24-hour treatment of DIPG-007 cells affected H3K27me3 levels. Drs. Stefan Sweha and Mateus Mota then conducted experiments in additional patient-derived cell line models (SF7761, DIPG-XIII-P*, DIPG-IV) and an isogenic mouse neural stem cell model expressing a human H3.3K27M construct. Gain in H3K27me3 and loss of H3K27ac were observed across multiple models through immunoblotting of histone lysates. In collaboration with the Koschmann lab, we stained tumors from ONC201-treated patients and identified a striking reversal of the pathognomonic low H3K27me3 state for H3K27M DMGs treated with ONC201 (Figure 3.4A).

In addition, the Koschmann lab had previously conducted multiplexed, indexed T7 ChIP-seq (Mint-ChIP) for a separate, ongoing project in the lab that included patients from the ONC201 clinical trials. This study included samples from two patients treated with ONC201 and two patients with H3K27M DMGs who were not exposed to ONC201. Two samples of tumor were taken from each patient as replicates. Because, the comparison was confounded by sex, we

excluded sex chromosomes from our analysis. We first assessed how H3K27me3 reads were distributed across the genomes of tumors based on H3K27me3 treatment status, showing that levels rose with treatment at peaks (Fig 3.4B). We next compared differential peaks, focusing on sites enriched in ONC201-treated tumors. Despite the limited sample size, we found 360 peaks that were gained in the ONC201-treated tumors compared to 85 lost (Figure 3.4C). We performed pathway analysis on the genes most closely associated with these ONC201 gained peaks, finding enrichment of neurogenesis and development pathways (Figure 3.4D). Intriguingly, comparison of the H3K27me3 read density at enriched sites in ONC201-treated tumors showed that gains at these sites corresponded with duration of ONC201 treatment and were highly consistent between samples obtained from the same tumor (Figure 3.4E).

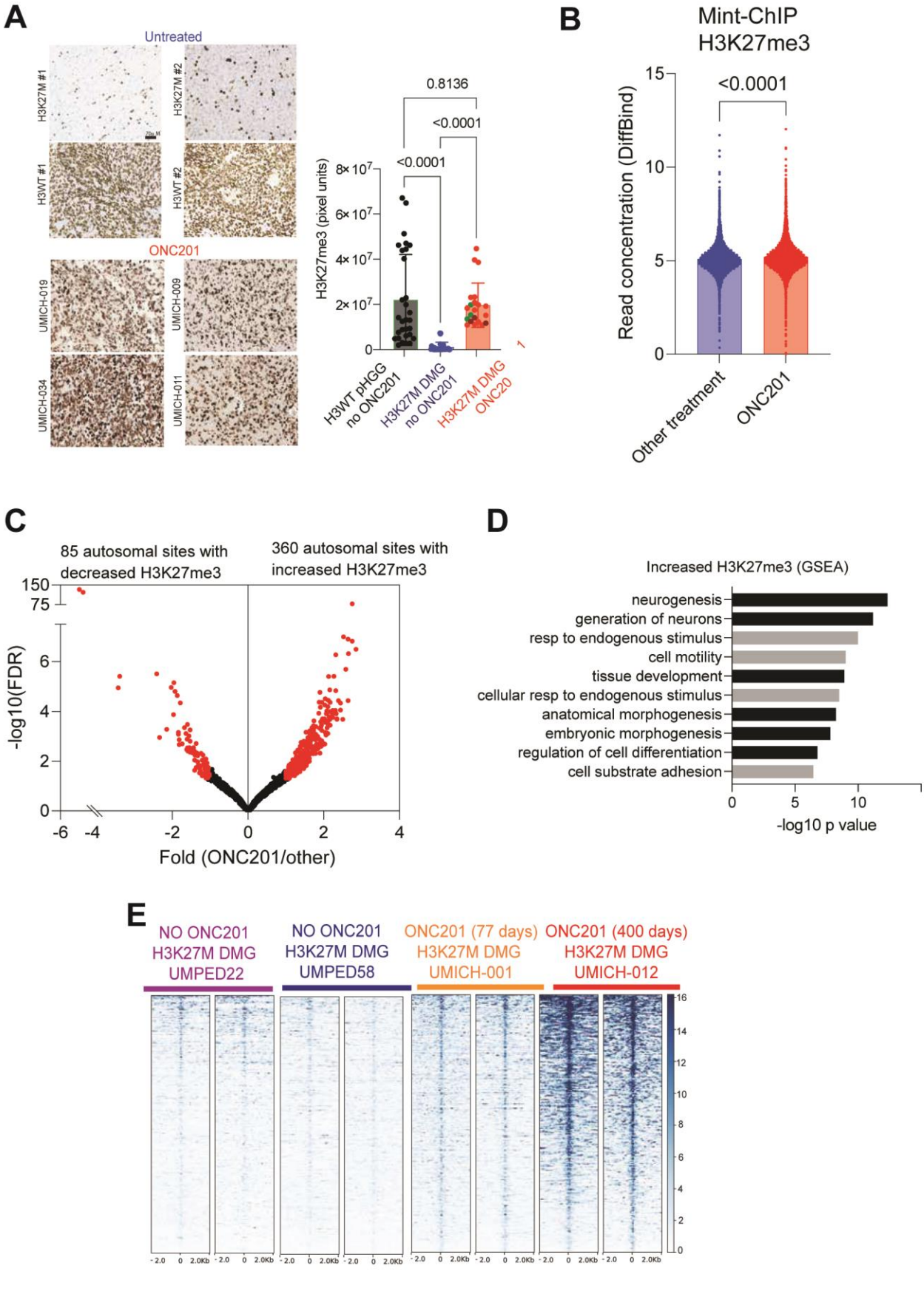
A
Untreated
H3K27M #1
H3K27M #2
H3WT #1
H3WT #2
ONC201
UMICH-019
UMICH-009
UMICH-034
UMICH-011
H3K27me3 (pixel units)
8×10^7
6×10^7
4×10^7
2×10^7
0
0.8136
<0.0001
<0.0001
H3WT pHGG no ONC201
H3K27M DMG no ONC201
H3K27M DMG ONC20
B
Mint-ChIP H3K27me3
Read concentration (DiffBind)
15
10
5
0
<0.0001
Other treatment
ONC201
C
85 autosomal sites with decreased H3K27me3
360 autosomal sites with increased H3K27me3
-log10(FDR)
150
75
6
4
2
0
-6
-4
-2
0
2
4
Fold (ONC201/other)
D
Increased H3K27me3 (GSEA)
neurogenesis
generation of neurons
resp to endogenous stimulus
cell motility
tissue development
cellular resp to endogenous stimulus
anatomical morphogenesis
embryonic morphogenesis
regulation of cell differentiation
cell substrate adhesion
0
5
10
-log10 p value
E
NO ONC201 H3K27M DMG UMPED22
NO ONC201 H3K27M DMG UMPED58
ONC201 (77 days) H3K27M DMG UMICH-001
ONC201 (400 days) H3K27M DMG UMICH-012
16
14
12
10
8
6
4
2
0
-2.0
0
2.0Kb

Figure 3.4: H3K27me3 levels are enriched in ONC201-treated tumors.

A. Immunohistochemical staining of untreated H3K27M (n=11, top left) and H3WT DMGs (n=10, middle left) and ONC201-treated H3K27M DMGs (n=6, bottom left) with quantification of staining across samples (right). This figure was generated by Dr. Sriram Venneti.
B. Comparison of Mint-ChIP H3K27me3 read concentration in ONC-201-treated tumors (n = 2 patients, 4 samples) compared to other H3K27M DMGs (n=2, 4).
C. Differential peak analysis comparing the samples from **B**. Significantly different peaks are shown in red.
D. Pathway analysis of genes linked to the 360 peaks with enriched H3K27me3 identified in **C**.
E. Heatmaps of H3K27me3 signal at the 360 peaks with enriched H3K27me3 in ONC201-treated tumors. Each tumor has data from two samples, and tumors are arranged in order of treatment duration and color-coded (No treatment: purple or blue; 77 days: orange; 400 days: red).

3.3.5 ONC201 drives loss of H3K27ac and a subset of ONC201-driven transcriptional changes are associated with loss of chromatin accessibility.

Due to the association of H3K27me3 with repressive areas of the genome, we revisited our RNA-seq and conducted assay for transposase accessible chromatin (ATAC)-seq and H3K27 acetylation (H3K27ac) ChIP-seq experiments in the DIPG-007 cell line to search for epigenetically driven silencing events in ONC201-treated DMG cells. ONC201 treatment resulted in a global decrease in both accessibility and H3K27ac levels, consistent with the rise in H3K27me3 observed. Changes in H3K27ac were particularly striking, with the majority of peaks across the genome showing decreased acetylation (Figure 3.5A). Chromatin accessibility trended toward a decrease, but there were a set of low accessibility peaks in vehicle-treated cells that greatly increased accessibility in ONC201 treatment as well (Figure 3.5 B). Super-enhancers are regulatory elements associated with H3K27ac deposition that are central to cell identity and transcriptional states, and prior work has characterized an essential role for these elements in H3K27M DMGs. Examining previously identified H3K27M DMG-specific super enhancers, we found a decrease in H3K27ac levels across replicates with ONC201 treatment (Figure 3.5C).

We next focused on how these changes in the chromatin landscape might influence the transcriptional state of H3K27M DMGs. First, we examined super enhancer-linked genes and observed that critical glial developmental genes such as *OLIG2* and *GFAP* were downregulated significantly (Figure 3.5D). Key epigenetic regulators such as *KDM2A*, *DAXX*, and *SMARCD2* also had significant downregulation in ONC201-treated cells.

Next, to take a more global view, sites with decreased accessibility and H3K27ac levels were linked to genes and compared to the set of downregulated genes from RNA-seq experiments. Pathway analysis of the resulting 348 downregulated genes revealed enrichment of cell-cycle regulation, as well as neurogenesis and CNS development, pathways (Figure 3.5E).

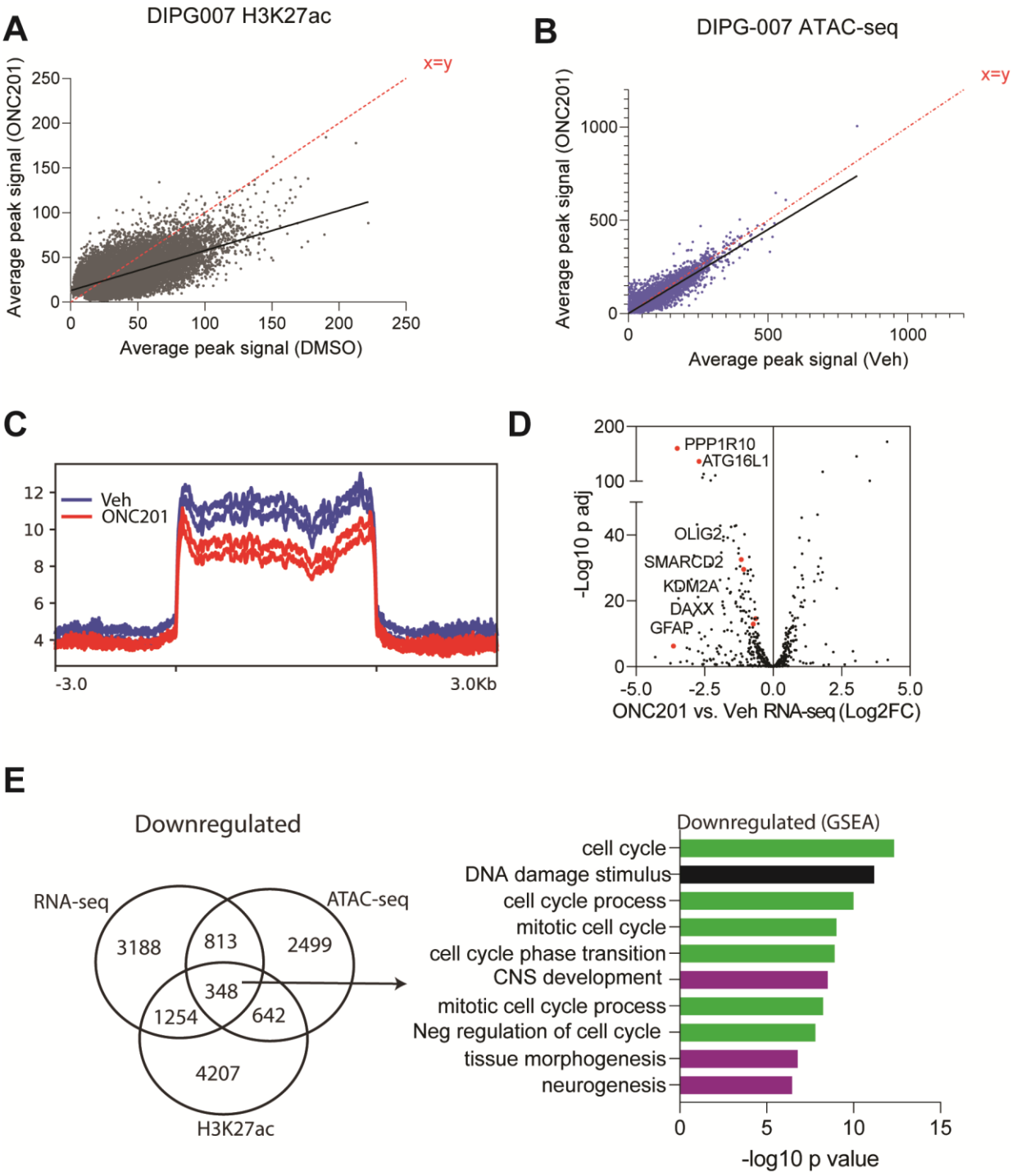

Figure 3.5: ONC201 treatment results in global loss of H3K27ac and downregulation of neural developmental pathways.

A. Scatter plot of average H3K27ac ChIP-seq signal averaged over replicates (n=2) for vehicle treated (x-axis) compared to ONC201-treated (y-axis) DIPG-007. A line of best fit (black) and, for comparison, an x=y line (red, dotted) are plotted.
B. Scatter plot of average ATAC-seq signal averaged over replicates (n=2) for vehicle treated (x-

axis) compared to ONC201-treated (y-axis) DIPG-007. A line of best fit (black) and, for comparison, an x=y line (red, dotted) are plotted.
C. Composite plot of H3K27ac distributed across super-enhancer sites, +/- 3 kilobases, previously identified by Krug et al. (Krug et al., 2019b).
D. Volcano plot of super-enhancer associated genes showing expression changes with ONC201 treatment for DIPG-007 cells. Log2fold change of expression in ONC201-treated cells over vehicle-treated cells (x-axis) is compared to log10(p-value) (y-axis).
E. Venn diagram demonstrating overlap of genes with transcriptional downregulation, lowered H3K27ac, and decreased ATAC-seq-based accessibility in ONC201-treated cells (left) and pathway analysis of the overlapping genes (right). Cell-cycle related pathways are shown in green, and neural developmental pathways are in purple.

3.4 Discussion

Clinical trial data demonstrate that treatment with the novel small-molecule ONC201 is associated with unprecedented survival rates in the nearly universally fatal tumor class of H3K27M DMGs. While first developed as a dopamine receptor antagonist, ONC201 has been demonstrated to target stress response and mitochondrial pathways in various tumor models (Endo Greer & Lipkowitz, 2016; Greer et al., 2018; J. Ishizawa et al., 2019; J. O. Ishizawa et al., 2016; Przystal et al., 2022), and its potential mechanism of toxicity in H3K27M DMGs is poorly understood.

In this project, we demonstrate that ONC201 treatment results in reduction of critical TCA cycle enzymes including OGDH and ACLY, and that patients with the greatest responses to ONC201 express these genes at higher levels at baseline. Integrating metabolomic profiles of a cell line model and of samples from responders' and non-responders' CSF, we found that ONC201 treatment is associated with decreased levels of TCA cycle metabolites downstream of OGDH such as malate. Surprisingly, we additionally discovered that ONC201 treatment induces production of 2HG in both cell models and in responder patients.

Lowered H3K27me3 levels are the histopathological hallmark of H3K27M DMGs. In contrast, 2HG is well-characterized to inhibit histone demethylases and associated with histone hypermethylation. In gliomas, IDH1 and H3K27M mutations are mutually exclusive (Schwartzentruber et al., 2012; Sturm et al., 2012). Furthermore, both 2HG supplementation and mIDH1 overexpression are toxic to H3K27M DMG models (Chung et al., 2020). Together, these prior data highlight the potential for ONC201-mediated 2HG production to cause toxicity in

H3K27M DMGs. We therefore examined the epigenomic impact of ONC201 treatment, finding globally increased H3K27me3 levels in cell models and remarkably in patient samples. Moreover, we identified decreased levels of the opposing H3K27ac mark across the genome and lower levels of chromatin accessibility. Finally, we identified downregulated genes associated with these chromatin states, which were enriched for cell-cycle and neural differentiation pathways.

Together these data demonstrate the transcriptomic, metabolic, and epigenomic consequences of ONC201 treatment with intriguing correlations to patient response. Moreover, these studies reveal a potential novel means of inducing 2HG-mediated toxicity in H3K27M DMGs. This unexpected finding opens several exciting windows of investigation. First, due to technical limitations of the original metabolite profiling approaches (LC-MS), the precise enantiomer of 2HG could not be determined in our initial studies. L-2HG can be produced by nonspecific activity of malate and lactate dehydrogenases (MDH and LDH) and is metabolized by L-2HG dehydrogenase (L2HGDH); D2HG, in contrast is the product of active-site mutant IDH1/2, but has been experimentally demonstrated to be produced by WT IDH1 as well (Fan et al., 2015; Intlekofer et al., 2017). While both isoforms can exert inhibitory effects on histone demethylases, identifying the isoform can help shed light on the potential route of generation.

Given the observed decrease in malate and increase in α-KG levels with ONC201 response, MDH may be more prone to acting on other substrates and generating 2HG. Measurement of 2HG levels in ONC201- vs. vehicle-treated cells following knockdown of MDH treatment could test this mechanism.

Additionally, while current data support a model where ONC201-generated 2HG production results in toxicity to H3K27M DMGs, further experimentation will be required to validate that mechanism. An initial approach would entail overexpressing D2HGDH or L2GHDH, the enzymes responsible for reverting 2HG to α-KG, and assessing if there is a protective effect under ONC201 treatment. In parallel, testing the ONC201 sensitivity and H3K27me3 levels of H3K27M DMG cell lines with transduced OGDH overexpression constructs could reveal if this ONC201-mediated deficits at this critical node of the TCA cycle are responsible for the observed changes in chromatin marks and cell viability.

Altogether, these initial findings integrating data from patients and from cell line models pose intriguing hypotheses about the potential role of the investigational compound ONC201 in the treatment of H3K27M DMGs. While promising, additional studies will be necessary to examine the influence of ONC201-driven epigenomic remodeling on H3K27M DMG biology and to further inform therapeutic approaches.

Chapter 4
Isocitrate Dehydrogenase 1 as a Therapeutic Vulnerability in Chordoma

4.1 Introduction

4.1.1 Chordomas are poorly understood, aggressive malignancies

Chordomas are aggressive malignancies with poor prognoses that develop along the spinal axis, most frequently in the sacrum and the base of the skull (clival) (Dahlin & Maccarty, 1952; McMaster et al., 2001). They have high morbidity and recurrence rates due to their anatomic location, relative radio-resistance, and poor response to systemic therapies (Walcott et al., 2012). Chordomas are hypothesized to derive from remnant cells of the notochord, a critical embryologic structure that degenerates during normal development. As early as 1858, Johannes Peter Müller postulated that chordoma tumors grew out of remnant notochord tissue, basing his hypothesis on his observations of remnant notochord cells observed in areas of cartilage along the spine, the midline pattern of chordoma incidence, and the distinct histological features that differentiated chordomas from benign and malignant cartilage (Müller, 1858).

4.1.2 Targeting chromatin modifiers in chordoma is a promising therapeutic avenue

Transcriptionally, chordomas are uniquely characterized by expression of the notochordal transcription factor brachyury (encoded by *TBXT* or *T*) (Vujovic et al., 2006), whose expression is essential for growth and regulated by a super-enhancer marked by histone 3 lysine 27 acetylation (H3K27ac) (Sharifnia et al., 2019; Sheppard et al., 2021). Furthermore, chordomas rely on the H3K27 demethylases KDM6A and KDM6B to maintain epigenetic activation of

TBXT (Cottone et al., 2020). Recent work has shown the utility of targeting the critical metabolite and KDM6A/B cofactor α-KG as a means of inhibiting H3K27me3 in pediatric gliomas (Chung et al., 2020) and offers a promising therapeutic angle for chordomas.

4.1.3 We hypothesized chordomas may alter metabolism to maintain their epigenomic regulation

Metabolism is commonly altered in cancer, but little is known about how chordoma's reprogram metabolic pathways to serve tumor growth. Given their reliance on low H3K27me3 states, we hypothesized chordomas may rely on upregulation of α-KG and explored the metabolic and epigenomic landscapes of chordoma.

4.2 Methods

4.2.1 Microarray-based transcriptional analysis

Affymetrix GeneChip® HG-U133 Plus 2.0 gene expression data generated by the Ramnik Xavier Lab were obtained from http://xavierlab2.mgh.harvard.edu/chordoma/Data.html. Expression values for notochord and chordoma samples were compared by a two-sided student's t test. Multiple testing correction was applied by the Benjamini-Hochberg method. For heatmap visualization, data were normalized across probes, and heatmaps were generated using Morpheus (https://software.broadinstitute.org/morpheus). Pathway analysis of differentially expressed genes was performed using Enrichr (E. Y. Chen et al., 2013; Kuleshov et al., 2016; Xie et al., 2021), and volcano plots were generated using code generated by Appyter. Gene set enrichment analysis (GSEA) was performed first by generating ranked gene lists using the product of the negative log-10 transformation of the q-value and the difference in expression for each gene. A

GSEA Preranked analysis (GSEA 4.2.3) was then performed on the resulting gene lists with the following parameters: 15-500 as min-max gene set size; weighted scoring scheme; meandiv normalization; Abs_max_of_probes mode.

4.2.2 Survival analysis

Matched gene expression and survival data for an unpublished cohort of chordomas curated by the Andrew Venteicher Lab were used to analyze associations between gene expression and progression-free survival. A log-rank test was utilized to test for significant differences between cohorts divided by expression values of the genes of interest.

4.2.3 Cell culture

CH22 cells were cultured in RPMI 1640 with 10% fetal bovine serum (FBS). UM-Chor1 and UM-Chor5 cells were cultured in a 4:1 preparation of IMDM:RPMI with 1% antibiotic-antimycotic, 0.2% prophylactic Plasmocin®, and 10% FBS. U-CH1 and U-CH2 were cultured in a 4:1 preparation of IMDM:RPMI with 10% FBS and an additional 1% of L-glutamine added. JHC7 was cultured in DMEM:F12 with 10% FBS for initial dose curves with IDH1 inhibitor treatment. For all other experiments, JHC7 was adapted to a 4:1 preparation of IMDM:RPMI with 10% FBS and an additional 1% of L-glutamine added. Cells were grown in humidified incubators at 37℃ in 21% O_2 and 5% CO_2.

4.2.4 Short-hairpin RNA (shRNA) mediated knockdown of IDH1

Bacterial stocks of five MISSION® shRNA constructs targeting the coding sequence of IDH1 were obtained from Sigma-Aldrich with the following identification numbers:

TRCN0000027249, TRCN0000027253, TRCN0000027284, TRCN0000027289, TRCN0000027298. Bacteria were streaked onto ampicillin-containing agar plates and grown overnight at 37℃. Single colonies were picked and cultured in Luria broth (LB) containing ampicillin with 250 rotations per minute (rpm) agitation at 37℃. After 18 hours, bacterial cultures were collected, and plasmid DNA was isolated using PureLink™ HiPure Plasmid Maxiprep Kit (Thermo Fisher Scientific, K210007). DNA was quantified and assessed for purity with a BioTek plate reader.

Plasmids passing quality standards were used for lentivirus production. First 293T cells were plated in DMEM media with 10% fetal bovine serum (FBS) but without antibiotics and grown 24 hours to 70% confluence. At that time, a preparation 0.26 mL of serum-free DMEM, 6.7 µL of pPackH1 packaging plasmid, 0.67 µg of the shRNA-containing plasmid were combined for each transduction. To each solution, 8 µL of PureFection transduction reagent was added, and the mixtures were vortexed for 10 seconds and then incubated for 30 minutes. After incubation, plasmid mixtures were added to 293T cells dropwise with frequent mixing of media. 293T cells were then incubated overnight at 37℃ and 5% CO_2. After 18-24 hours, transduction media was replaced with DMEM with 1% penicillin-streptomycin. Resulting viral supernatants were collected at 48 and 72 hours after transduction, pooled, filtered for cells and added to chordoma plated cell lines. Chordoma cells were incubated with virus-containing DMEM for 72 hours then returned to their respective media. Puromycin at 1 µg/mL was added to the chordoma cultures. This concentration was increased with subsequent passages if knockdown levels were not maintained, up to 4 µg/mL.

4.2.5 Cell proliferation assays

Unless otherwise specified, cells were trypsinized and counted in order to seed 25,000 cells/well in 24-well plates. Cells were counted four days later. Each well underwent trypsinization, cell collection and resuspension with trypan blue exclusion. Count estimates were made using Countess automated cell counters.

For nutrient withdrawal experiments, cells for seeding were resuspended in PBS following trypsinization and collection to wash out residual complete media. Cells were then centrifuged and resuspended in base media lacking glucose, sodium pyruvate, and glutamine. Dilutions for seeding were made into media with the final concentrations of glucose and/or glutamine. Cells were then seeded in 1 mL of media per well in 24-well plates.

For experiments in lentivirally transduced cell lines, cells were plated in 1 mL of media per well containing puromycin, the selection antibiotic. This step was necessary to maintain selection for the shRNA expressing cells as knockdown was observed to diminish with removal of the selective antibiotic. Initial passages were tested in 1 µg/mL puromycin. For experiments in CH22, this dose was increased step-wise to 3 µg/mL with increasing passages.

For pharmacologic treatment experiments, cells were plated at 25,000 cells/well in 500 µL of media per well. On the subsequent day, inhibitors were prepared in media at 2X concentrations and 500 µL of the resulting preparations were applied to each of the appropriate wells. Cells were counted 96 hours after treatment.

4.2.6 Transcriptomic profiling of chordoma cell lines with IDH1 inhibition

Cells were plated in 10-cm dishes at a concentration designed to reach 60-80% confluence in 96 hours. Initial seedings ranged between 500,000 and 1,000,0000 cells/plate. After adhering and within 24 hours, cells were treated with 3 μM IDH1 inhibitor or a 1:10,000 dilution of dimethyl sulfoxide (DMSO) in the corresponding media. At 72 hours post-treatment. Cells were trypsinized, counted, and placed on ice. At least 500,000 cells/replicate were then lysed with 750 μL of QIAzol (Qiagen 79306), vortexed for >1min, incubated at room temperature for 20 minutes and stored at -80°C. Upon thawing of samples, RNA was extracted with chloroform and purified using the RNeasy (Qiagen) kit. Samples were evaluated for RNA integrity index (RIN). Libraries were generated using KAPA RNA HyperPrep Kit with RiboErase (HMR).

4.2.7 Metabolite profiling of chordoma cell lines with IDH1 inhibition

For whole metabolite snapshot analysis, 1 million cells were plated in 10-cm dishes and cultured for 16 hours at 37°C in an incubator. Cells were then treated with DMSO or 3 μM of IDH1 inhibitor. Forty-six hours after treatment, a full media change was performed with either DMSO or IDH1 inhibitor. Metabolites were then collected two hours later by the following process. Methanol (80%) was made freshly using HPLC-grade methanol (Sigma 34860-1L-R) and water (Sigma 270733-4L) and chilled to -80°C. At room temperature, all media was carefully aspirated from each plate such that no media was remaining. To each plate. 4 ml of dry ice-cold 80% methanol was added, and plates were immediately transferred to rest on dry ice. Once all plates received methanol, they were incubated at -80°C. After 10 minutes, all cells were scraped off the dish and pipetted into 15-mL centrifuge conicals. Insoluble materials were pelleted at maximum speed (>3000 rpm) for 10 min at 4°C, and supernatants were transferred to fresh 15-mL conicals.

This step was repeated once, and samples were then stored at -80°C. A fifth replicate for each condition was collected after trypsinization, lysed in RIPA buffer, and quantified using BCA protein quantification.

Subsequent steps were performed by Anthony Andren of Dr. Costas Lyssiotis' lab. Methanol samples were thawed, and metabolites were pelleted by speedvac. Liquid chromatography coupled-tandem mass spectrometry (LC-MS/MS) metabolomics analysis was performed as described previously (H.-J. Lee et al., 2019). In brief, Agilent 1290 UHPLC and 6490 Triple Quadrupole (QqQ) Mass Spectrometer (LC-MS) were used for label-free targeted metabolomics analysis. Agilent MassHunter Optimizer and Workstation Software LC-MS Data Acquisition for 6400 Series Triple Quadrupole B.08.00 was used for standard optimization and data acquisition. Agilent MassHunter Workstation Software Quantitative Analysis Version B.0700 for QqQ was used for initial raw data extraction and analysis. For each MRM transition, its retention time of left delta and right delta of 1 min was used. Additional parameters include mass extraction window of 0.05 Da right and left from the extract m/z, Agile2 integrator algorithm, peak filter of 100 counts, noise algorithm RMS, noise SD multiplier of 5 min, S/N 3, Accuracy Max 20% max %Dev, and Quadratic/Cubic Savitzky-Golay smoothing algorithm with smoothing function width of 14 and Gaussian width of 5.

For reversed-phase liquid chromatography (RPLC), a Waters Acquity UPLC BEH TSS C18 column (2.1 x 100mm, 1.7µm) was used in the positive ionization mode with mobile phase (A) consisting of 0.5 mM NH4F and 0.1% formic acid in water; mobile phase (B) consisting of 0.1% formic acid in acetonitrile. Gradient program: mobile phase (B) was held at 1% for 1.5 min,

increased to 80% in 15 min, then to 99% in 17 min and held for 2 min before going to initial condition and held for 10 min. For hydrophilic interaction liquid chromatography (HILIC), a Waters Acquity UPLC BEH amide column (2.1 x 100mm, 1.7µm) was used in the negative ionization mode with mobile phase (A) consisting of 20 mM ammonium acetate (NH4OAc) in water at pH 9.6; mobile phase (B) consisting of acetonitrile (ACN). Gradient program: mobile phase (B) was held at 85% for 1 min, decreased to 65% in 12 min, then to 40% in 15 min and held for 5 min before going to the initial condition and held for 10 min.

Both columns were at 40℃ and 3 µl of each sample was injected into the LC-MS with a flow rate of 0.2 ml/min. Calibration was achieved through Agilent ESI-Low Concentration Tuning Mix. Optimization was performed on the 6490 QqQ in the RPLC-positive or HILIC-negative mode for each of 245 standard compounds (215 and 217 compounds for RPLC-positive and HILIC-negative, respectively) to obtain the best fragment ion and MS parameters such as fragmentation energy for each standard. Retention time (RT) for each standard was measured from a pure standard solution or a mix standard solution. The LC-MS/MS methods were created with dynamic MRM (dMRM) with RTs, RT windows, and transitions of all 245 standard compounds. Key parameters of electrospray ionization (ESI) in both the positive and the negative acquisition modes are: Gas temp 275℃, Gas Flow 14 l/min, Nebulizer at 20 psi, SheathGasHeater 250℃, SheathGasFlow 11 l/min, and Capillary 3000 V. For MS: Delta EMV 200V or 350V for the positive or negative acquisition mode respectively and Cycle Time 500ms and Cell Acc 4V for both modes.

Pre-processed data with Agilent MassHunter Workstation Software Quantitative Analysis were post-processed for further quality control in the programming language R. First, we examined the distribution of sums of all metabolite abundance peak areas across individual samples in a given experiment as a measure for equal sample loading into the instrument. Next, we calculated coefficients of variation (CVs) in all biological replicate groups for each metabolite given a cut-off value of peak areas in each of the RPLC and HILIC methods. We then compared distributions of CVs for the whole dataset for a set of peak area cut-off values of 0, 1000, 5000, 10000, 15000, 20000, 25000 and 30000 in each method. A noise cut-off value of peak areas in each method was chosen by manual inspection of the CV distributions. The noise-filtered data of individual samples were then normalized by the total intensity of all metabolites. We retained only those metabolites with at least 2 technical replicate measurements for a given experimental variable. Then, each metabolite abundance level in each sample was divided by the mean of all abundance levels across all samples in a given experiment for comparisons, statistical analyses, and visualizations among metabolites. This normalization and scaling method has been used in previous studies with biologically meaningful results (Halbrook et al., 2019). Pathway analysis was done using the webtool, MetaboAnalyst (https://www.metaboanalyst.ca/).

4.2.8 Chromatin-immunoprecipitation followed by high-throughput sequencing of chordoma cell lines with IDH1 inhibition

Chordoma cell lines treated with either DMSO vehicle or 3 μM IDH1 inhibitor were fixed as described in Chapter 3 of this dissertation and then processed by Active Motif with a drosophila spike-in for normalization of global changes in histone marks.

4.2.9 N-Acetyl-Cysteine proliferation rescue experiments

Chordoma cells were plated as described in section 4.2.5. In addition to the primary treatment of IDH1 inhibitor, either PBS or N-acetylcysteine at a final concentration of 5 mM was added to the media for treatment.

4.2.10 Reduced-to-oxidized glutathione quantification

Cells were plated at 2,500 (CH22) or 5,000 (JHC7 and UM-Chor1) cells/well into white-bottom 96-well plates and treated with IDH1 inhibitor at 3 μM for 24 or 48-hours. Subsequently, cells were processed with the GSH/GSSG-Glo Assay (Promega, V6611) which quantifies total and oxidize glutathione. Ratios were calculated from luminescent intensity and compared between IDH1 inhibitor-treated and vehicle-treated cells.

4.2.11 Summary of cell line models used

Table 4.1 details the chordoma cell lines utilized for the experiments of this dissertation. Cell lines were selected to represent the two most common sites, both sexes, and both the SMARCB1-null and SMARCB1 wildtype subsets of the disease.

Cell line	**JHC7**	**U-CH1**	**U-CH2**	**CH22**	**UM-Chor1**	**UM-Chor5**
Site	Sacral	Sacral	Sacral	Sacral	Clival	Clival
Age	61	56	72	56	66	<20
Sex	F	M	F	M	M	M
SMARCB1 status				Null		Null
Experiments						
• *shIDH1*				X	X	
• Post-*IDH1i* proliferation	X	X	X	X	X	X
• *Metabolomics*	X		X	X	X	
• *RNA-seq*	X		X	X	X	
• *ChIP-seq*	X		X	X		
• *Xenograft*				X		

Table 4.1: Demographic information and summary of experimental uses of chordoma cell lines.

4.3 Results

4.3.1 Chordomas exhibit elevated TCA cycle gene expression compared to notochordal tissue

In order to better understand the molecular factors supporting the malignant, invasive nature of chordomas, microarray expression data from notochord tissue and chordomas were compared. Gene set enrichment analysis of genes with increased expression in chordoma tumors and tumor-derived cell lines compared to notochordal tissue revealed upregulation of metabolic pathways, specifically the tricarboxylic acid (TCA) cycle and oxidative phosphorylation (Fig. 4.1A). To evaluate whether this TCA cycle upregulation might be an artifact of the inclusion of chordoma cell lines in the analysis, I reanalyzed the data using only chordoma tumors and notochord tissue. The top differentially expressed genes were still enriched for those encoding TCA cycle enzymes (Fig. 4.1B). A closer examination of the TCA cycle KEGG pathway demonstrated increases in expression for many of the genes, including malate dehydrogenase (*MDH*), succinate dehydrogenase (*SDH*) B and D, isocitrate dehydrogenase 3A (*IDH3A*). *IDH1* also showed increased expression in three of the four tumors and all of the cell lines compared to notochord samples.

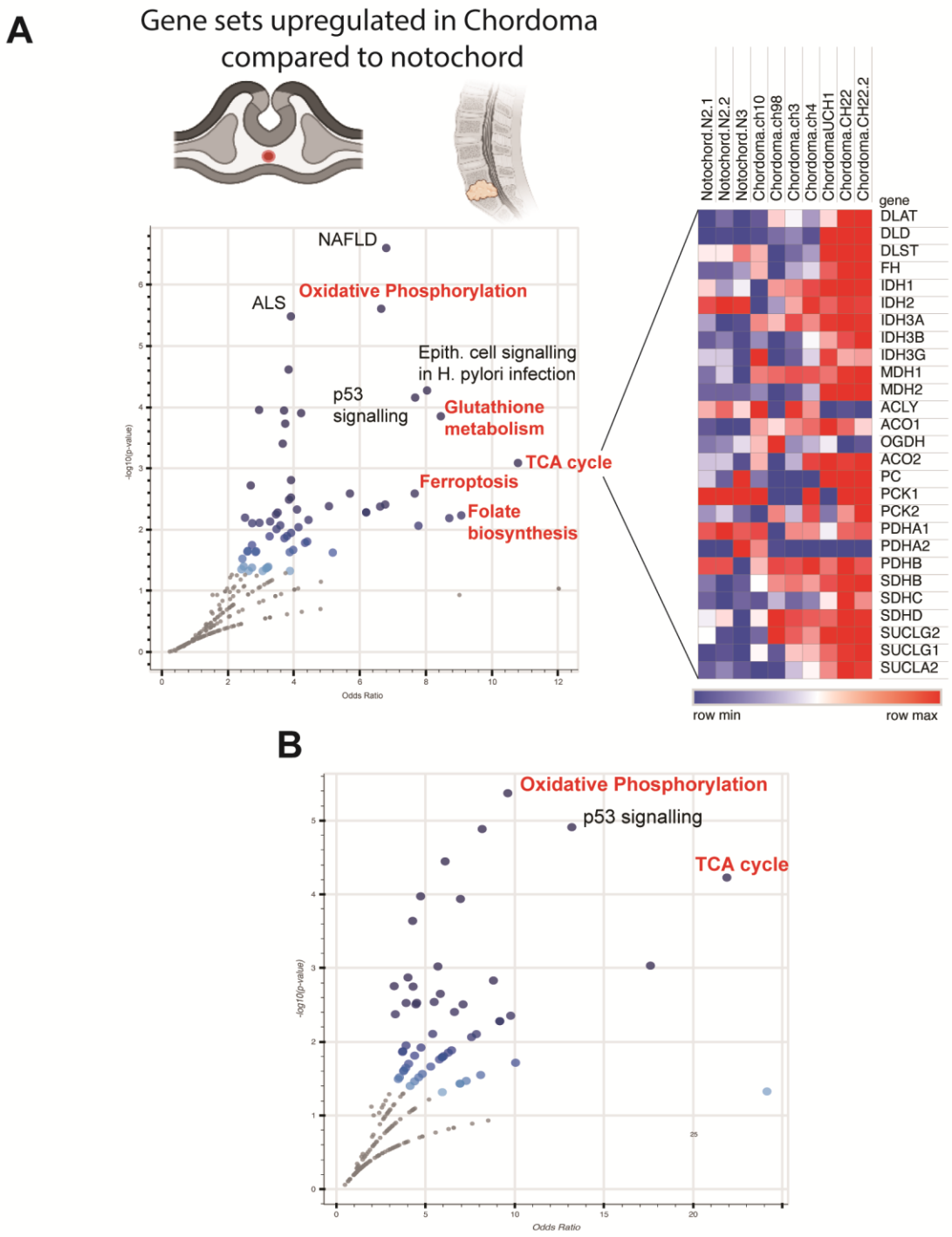

Figure 4.1: Pathway enrichment of tumor-upregulated centers on metabolism.

A. KEGG pathway enrichment of upregulated genes (p-adj. <0.05) plotted by -$\log_{10}$(p-value) (y-axis) and odds ratio (x-axis) with a schematic of the comparison between chordoma tumors and putative tissue of origin, the notochord. KEGG TCA cycle genes are shown on the heatmap (right).

B. Repeat of the pathway analysis performed in **A,** excluding the cell lines from the analysis to control for artifacts of tissue type, and using a less stringent cutoff (p-adj. <0.1). to account for the smaller sample sizes.

4.3.2 Elevated expression of the TCA cycle family enzyme IDH1 is associated with worse prognosis in chordomas

IDH1 is a cytosolic enzyme responsible for the conversion of isocitrate to alpha-ketoglutarate (α-KG), converting NADP+ to NADPH in the process. This reaction sits at a critical hub due to its potential influence on cellular energetics, chromatin modifying enzymes, and oxidative stress response pathways. Gain-of-function mutations in IDH1 have been well-characterized in gliomas, chondrosarcomas, and acute myelogenous leukemia. While IDH1 mutations are not observed in chordoma, recent studies have identified wildtype IDH1 as a potential therapeutic target in multiple tumors (Vaziri-Gohar et al., 2022; Zarei et al., 2021, 2022). Through a collaboration with the Venteicher Lab at the University of Minnesota, an unpublished cohort of skull base chordoma samples (n=152) with expression and clinical outcome data were interrogated to test if *IDH1* expression levels are associated with outcomes in chordoma. Cases were split by median *IDH1* expression level, and survival probabilities were compared between *IDH1*-high and -low groups. Survival analysis using expression of *IDH2*, which was not observed to be differentially expressed in chordomas compared to notochords, was used as a control. *IDH1* but not *IDH2* expression was significantly associated with survival, suggesting IDH1 levels may play a role in the progression of chordomas (Figure 4.2 A and B).

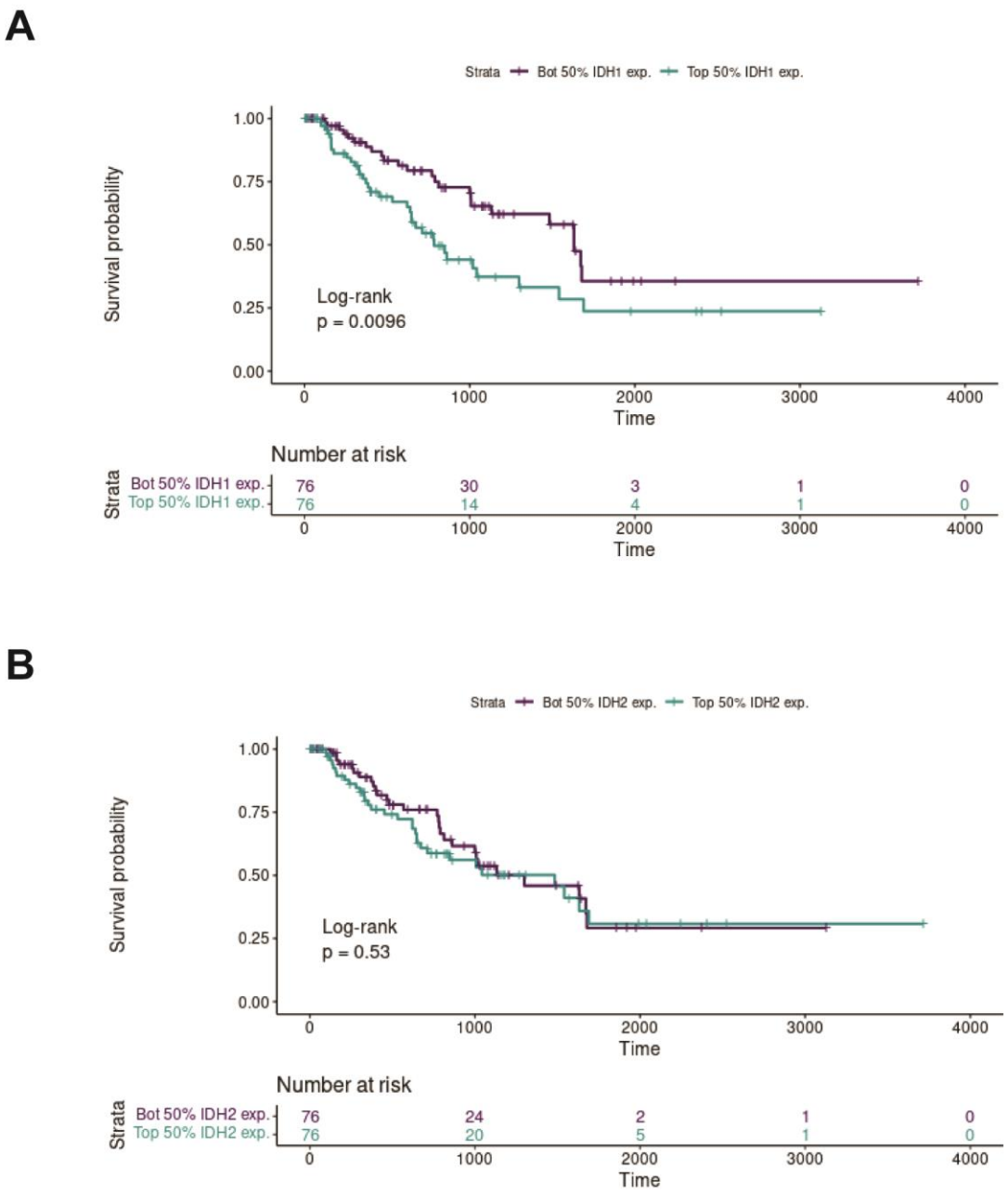

Figure 4.2: Elevated *IDH1* but not *IDH2* expression is associated with poor prognosis in chordoma.

A. Kaplan-Meier curves comparing progression free survival probability (y-axis) over time in months (x-axis) for patients with chordoma, stratified by median *IDH1* expression (n =76 per group).
B. Kaplan-Meier curves comparing progression free survival probability (y-axis) over time in months (x-axis) for patients with chordoma, stratified by median *IDH2* expression (n =76 per group).
p-values calculated by log-rank test.

4.3.3 Addition of the IDH1 product alpha-ketoglutarate provides partial rescue of TCA cycle carbon source depletion

The main carbon sources for TCA cycle intermediates are derived from either glucose or glutamine (Owen et al., 2002). To characterize the role these carbon sources play in chordoma growth, I evaluated proliferation under media conditions with full glucose (25mM) and glutamine (2-4 mM depending on cell line) compared to growth in media lacking glucose, glutamine, or both nutrients. Across four chordoma cell lines, either glucose or glutamine withdrawal reduced cell proliferation (Figure 4.3A). I next asked whether addition of a cell permeable form of α-KG, dimethyl-α-KG, could restore cell proliferation and observed partial growth rescue across multiple cell lines at concentrations of dimethyl-α-KG between 2-4 mM (Figure 4.3B).

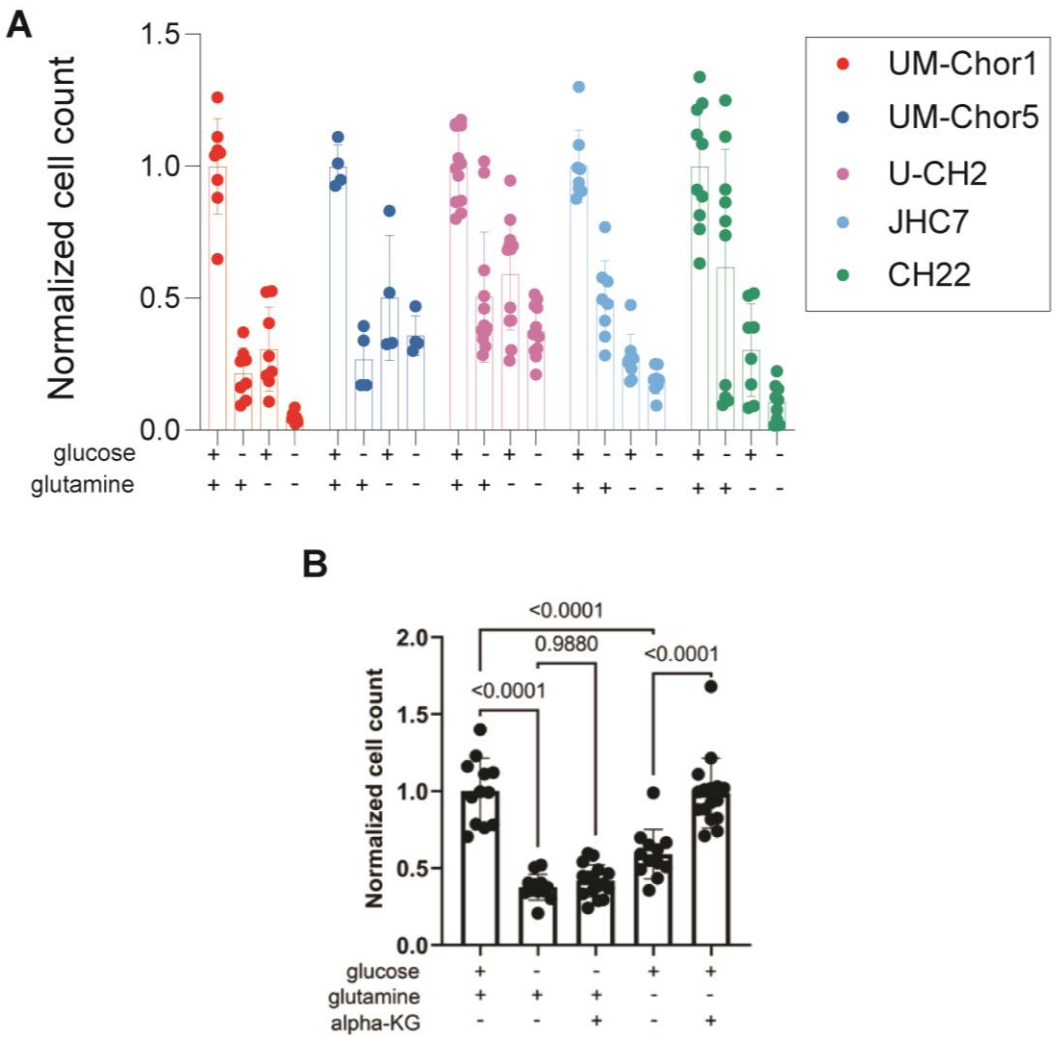

Figure 4.3: Chordoma cells rely on both glucose and glutamine for proliferation.

A Comparison of cell proliferation by normalized cell counts (y-axis) after 96 hours of metabolite withdrawal (x-axis) across five chordoma cell lines.
B Comparison of cell proliferation by normalized cell counts (y-axis) after 96 hours of metabolite withdrawal (x-axis) in the presence or absence of alpha-ketoglutarate supplementation for JHC7.

4.3.4 Cell culture models of chordoma rely on IDH1 for proliferation

Next, I asked whether IDH1 activity is necessary for chordoma cell growth using both genetic and pharmacologic approaches. Five short-hairpin RNA constructs targeting *IDH1* transcripts were transduced into UM-Chor1 cells, resulting in knockdown of IDH1 compared to an empty-vector-transduced control population (Figure 4.4A). Across all five knockdown constructs, cell proliferation was reduced (Figure 4.4A). Three of the shRNA constructs were then introduced into a second cell line, CH22. In this model, I observed greater variability in the extent of IDH1 knockdown, which diminished with passaging (Figure 4.4B). Subsequent analyses of proliferative capacity showed growth deficits that correlated with the extent of IDH1 knockdown (Figure 4.4B). Using a previously characterized wildtype IDH1 inhibitor that has been tested in other tumor models *in vivo*, proliferation studies demonstrated sensitivity in the low micromolar range across five chordoma models (Figure 4.4C).

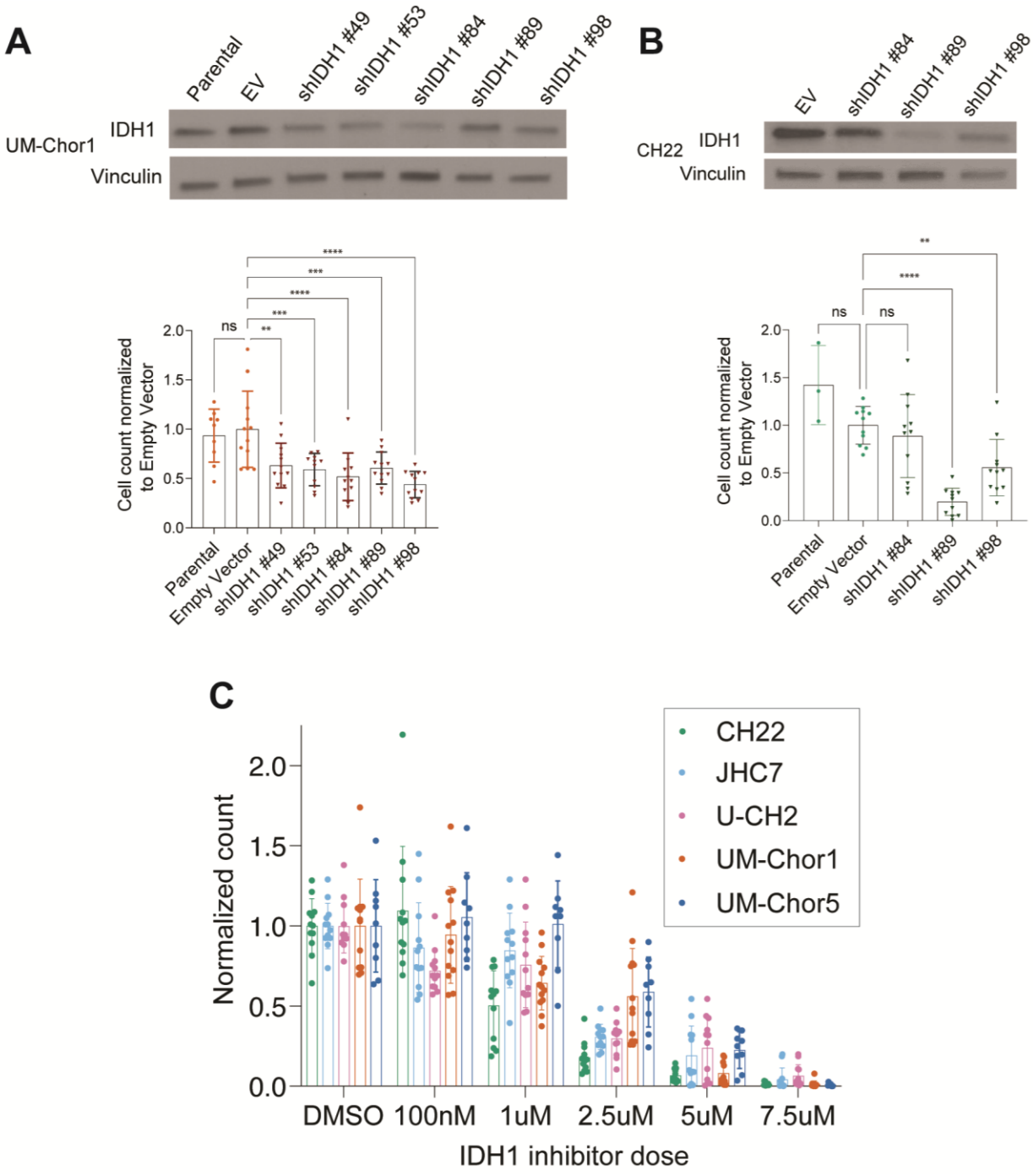

Figure 4.4: IDH1 inhibition through genetic and pharmacologic means reduces chordoma proliferation.

A. Immunoblotting (top) of IDH1 and vinculin (loading control) levels in UM-Chor1 cells with shRNAs targeting IDH1 or an empty vector control and normalized cell counts after 96 hours (bottom).
B. Immunoblotting (top) of IDH1 and vinculin levels in CH22 cells with shRNAs targeting IDH1 or an empty vector control and normalized cell counts after 96 hours (bottom).

C. Dose (x-axis) responses to a wildtype IDH1 inhibitor as measured by count normalized to DMSO vehicle control. Two or three separate experiments were conducted for each cell line.

4.3.5 Inhibition of a parallel α-KG-generating pathway has minimal effects in chordoma

Whereas IDH family enzymes metabolize isocitrate to α-KG, glutamate can also be used to generate α-KG using glutamate dehydrogenase (GDH) 1 or 2. Glutamate in turn is largely derived from glutamine. Given our findings that chordoma cell lines showed sensitivity to glutamine withdrawal that could be partially rescued with α-KG supplementation, I screened chordoma models for reliance on glutamine as a source of α-KG using a variety of small-molecule inhibitors. Overall, chordoma cell lines showed limited sensitivity to multiple glutamine metabolism inhibitors (Figure 4.5). While the cell count experiments were not repeated, subsequent viability experiments using CellTiter-Glo® also yielded evidence of limited chordoma sensitivity to these drugs, further supporting a resistance to glutamine-antagonizing approaches.

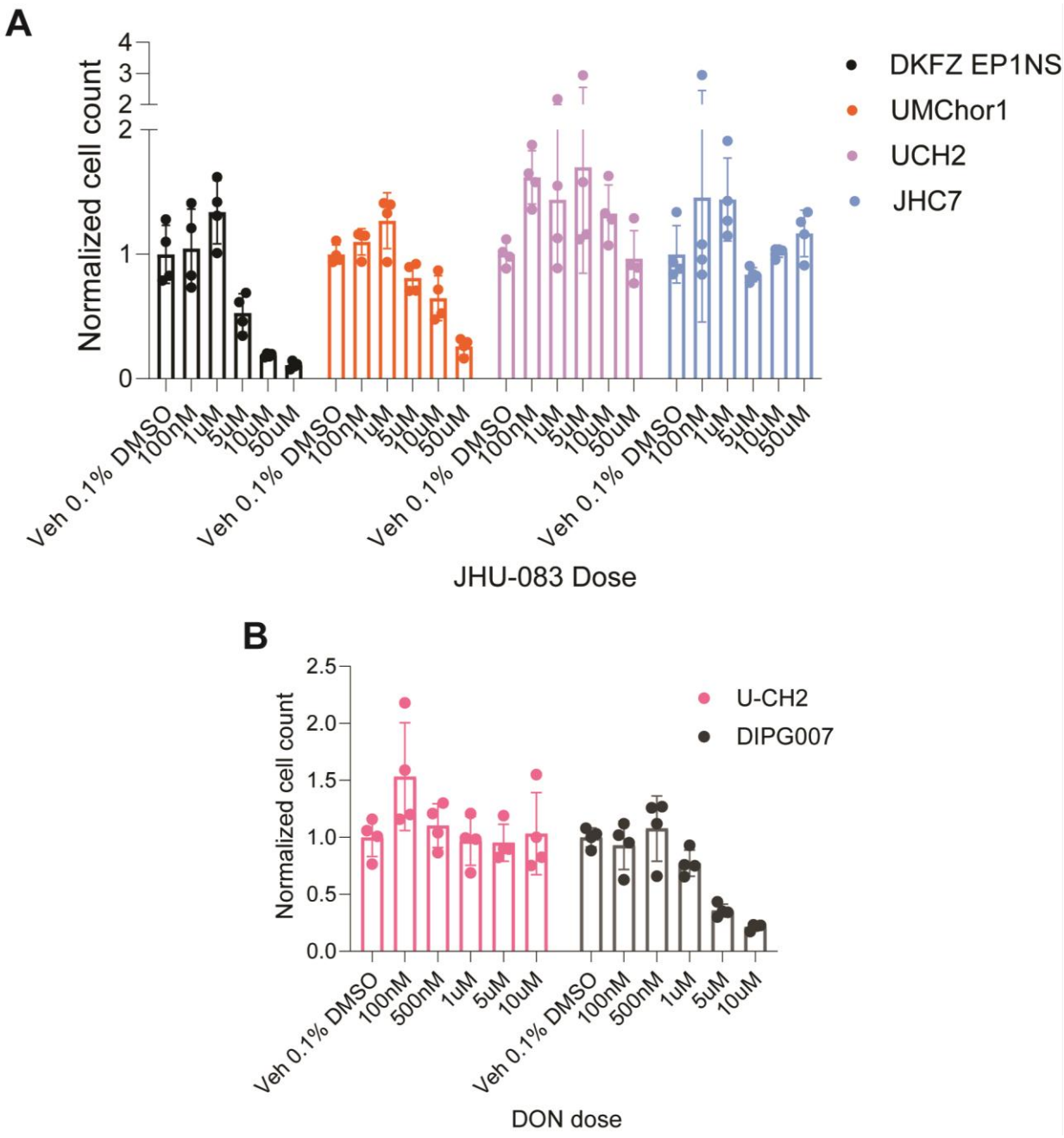

Figure 4.5: Chordoma cell lines do not display strong sensitivity to glutamine pathway antagonists.

A. Dose response plots measuring cell counts (y-axis) across different doses of glutamine antagonist JHU-083 in a glutamine-reliant ependymoma cell line and three chordoma cell lines. **B.** Dose response plots measuring cell counts (y-axis) across different doses of glutamine antagonist DON in a chordoma cell line (U-CH2) and a known sensitive glioma cell line (DIPG-007).

4.3.6 Alpha ketoglutarate-to-succinate ratios drop with IDH1 inhibition

Returning to the promising therapeutic response seen with inhibition of IDH1, I next moved to characterize the impact of IDH1 inhibition on the metabolome. Most importantly, I investigated how IDH1 inhibitor treatment influences the α-KG/succinate ratio in chordoma cells. Histone demethylases belong to the α-KG-dependent dioxygenase family, and the α-KG/succinate ratio has been shown to be a key determinant of histone demethylase activity, including for the H3K27me3 mark (Carey et al., 2015). Measurement of α-KG/succinate ratios across four cell lines after 48 hours of treatment demonstrated a reduction across all models, consistent with on-target activity of the compound (Figure 4.6A). This trend was observed despite significant decreases in succinate across the cell lines (Figure 4.6B), supporting a model where α-KG production is inhibited, and downstream TCA cycle products such as succinate and malate are also decreased (Figure 4.6C and D).

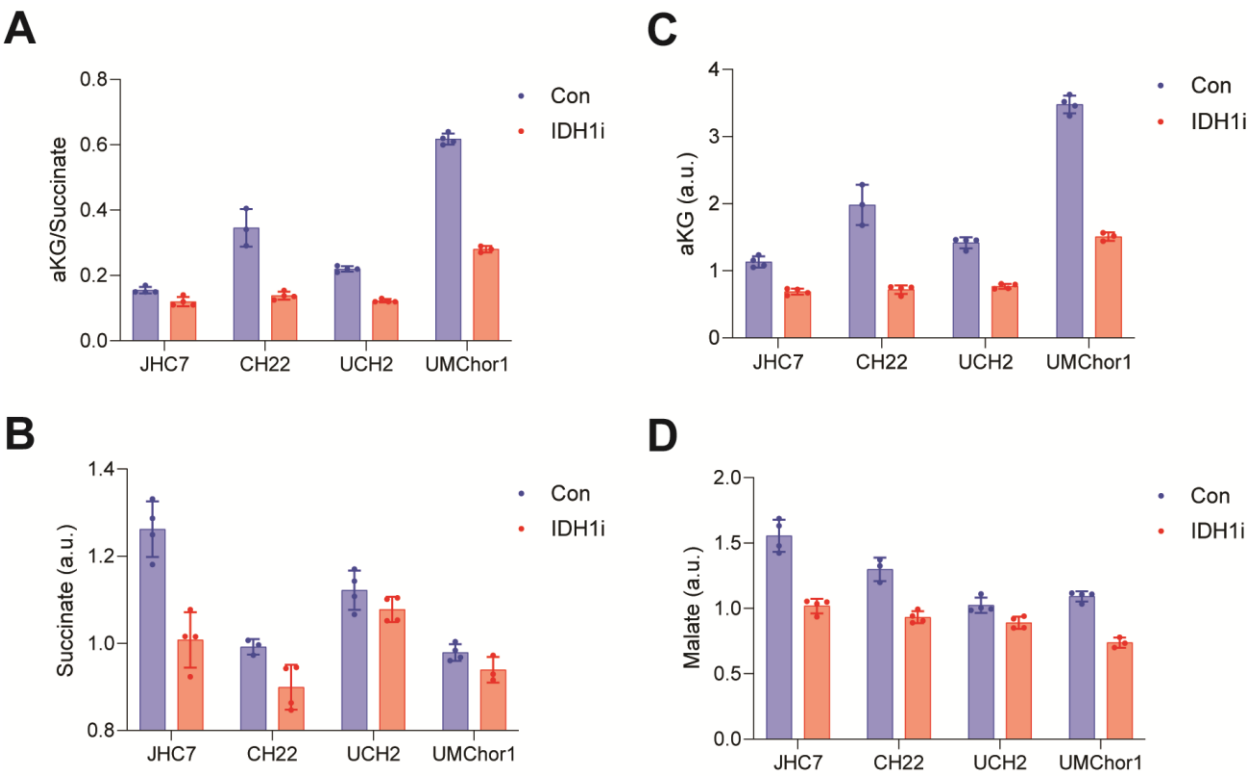

Figure 4.6: IDH1 inhibitor treatment reduces downstream TCA cycle metabolites and lowers the demethylase-driving α-KG/Succinate ratios.

A. Alpha-ketoglutarate/succinate ratios (y-axis) with Vehicle (blue) or with IDH1 inhibitor treatment (red) for four chordoma cell lines.
B. Alpha-ketoglutarate levels after median normalization (y-axis) with Vehicle (blue) or with IDH1 inhibitor treatment (red) for four chordoma cell lines.
C. Succinate levels after median normalization (y-axis) with Vehicle (blue) or with IDH1 inhibitor treatment (red) for four chordoma cell lines.
D. Malate levels after median normalization (y-axis) with Vehicle (blue) or with IDH1 inhibitor treatment (red) for four chordoma cell lines.

4.3.7 IDH1 inhibition increases H3K27me3 levels but has minimal effects at promoter regions

I next hypothesized that the observed fall in α-KG/succinate ratio would limit histone demethylase activity (Figure 4.7C). Given the prior work in chordomas demonstrating sensitivity to the H3K27me3-demethylase inhibitor KDOBA67, I first examined the influence of IDH1 inhibitor treatment on H3K27me3 in cell line models. Global levels as measured by protein immunoblotting revealed increased H3K27me3 at higher doses of inhibitor treatment, but heterogeneous effects at sub-IC50 doses (Fig 4.7D). I treated three cell lines at IC-50-level doses (3μM) of the IDH1 inhibitor or with vehicle and assessed genome-wide H3K27me3 landscapes using chromatin immunoprecipitation followed by high-throughput sequencing (ChIP-seq) with spike-in normalization. Assessment of vehicle-treated samples showed a high level of baseline heterogeneity with regard to H3K27me3 distribution (Fig 4.7A and B). Treatment with the IDH1 inhibitor led to an increase in the number of H3K27me3 peaks identified in each cell line (Figure 4.7E); however, total H3K27me3 signal at promoters increased for only two of the three cell lines with UM-Chor1 demonstrating lower levels of promoter-associated H3K27me3 (Figure 4.7F). Further characterization of how H3K27me3 distribution changes with IDH1 inhibition showed that sites in JHC7 and CH22 nearly uniformly increased in H3K27me3 levels, whereas UM-Chor1's landscape showed a more diverse response (Figure 4.7F). To assess the functional consequences of these changes, I performed RNA-sequencing (RNA-seq) on each of the ChIP-seq-profiled cell lines, as well as a fourth cell line, U-CH2. This integration demonstrated that sites gaining H3K27me3 were associated with minimal effects on transcription (Figure 4.7G).

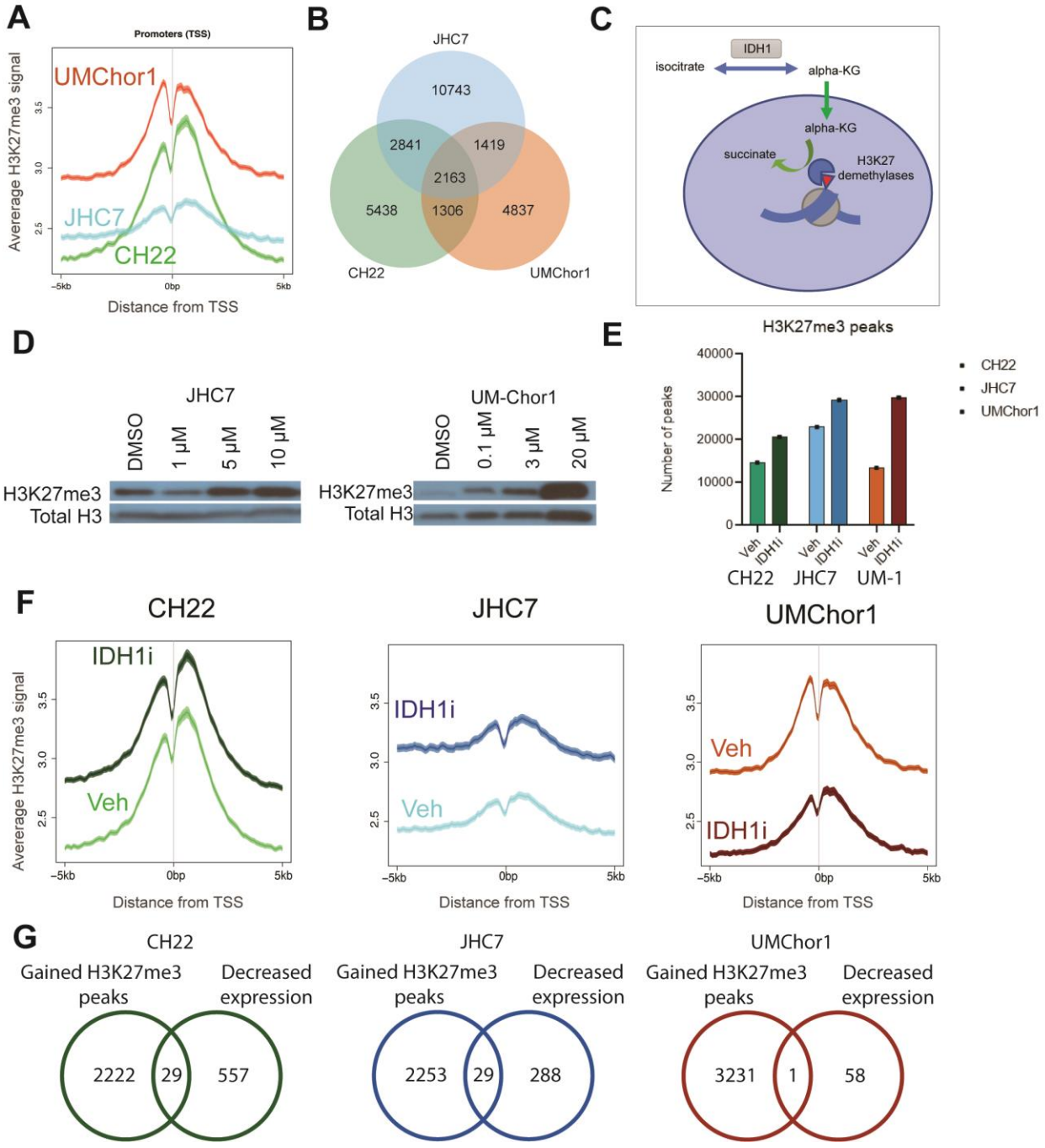

Figure 4.7: IDH1 inhibition raises H3K27me3 but drives minimal changes in transcription.

A. Baseline levels of H3K27me3 across promoters for 3 vehicle-treated chordoma cell lines (n =1 per sample).
B. Venn diagram comparing overlapping H3K27me3 peaks across the three chordoma cell lines.
C. Schematic of the pathway by which IDH1 links TCA cycle metabolites to chromatin modifications.

D. Immunoblotting of H3K27me3 (top) and total histone H3 in two chordoma cell lines, JHC7 (left) and UM-Chor1 (right) after treatment with DMSO vehicle or IDH1 inhibitor at increasing concentrations.
E. Total peak counts (y-axis) for vehicle and IDH1 inhibitor-treated chordoma cell lines CH22 (left), JHC7 (middle), and UMChor1 (right).
F. Composite H3K27me3 levels at promoters in CH22 (left), JHC7 (middle), and UMChor1 (right) with vehicle treatment (light) compared to IDH1 inhibitor treatment (dark).
G. Overlaps of genes with H3K27me3 gains and decreased expression upon IDH1 inhibitor treatment in CH22 (left), JHC7 (middle), and UMChor1 (right).

4.3.8 IDH1 inhibition significantly reduces brachyury expression in one model

In their work demonstrating the efficacy of H3K27me3 demethylase inhibition in chordoma, Cottone et al. showed that KDOBA67 treatment results in reduced expression of brachyury, the master transcription factor of notochord cells (Naiche et al., 2005). Brachyury is essential for chordoma cell growth (Sharifnia et al., 2019) and promotes escape from senescence (Sheppard 2021). We had hypothesized that IDH1 inhibition could induce a similar silencing effect on brachyury through its effect on demethylases. Transcriptomic data demonstrated that the U-CH2 cell line had substantial reduction of expression of *TBXT*, the gene encoding brachyury, but the other cell lines maintained similar levels despite treatment. Treatment at doses exceeding the IC50 demonstrate a reduction in brachyury expression at the protein level (Figure 4.8A and B). Notably, U-CH2 brachyury levels were rescued with α-KG supplementation (Figure 4.8C). Given the relative toxicity at lower doses despite maintenance of *TBXT* transcription, we pursued alternative explanations.

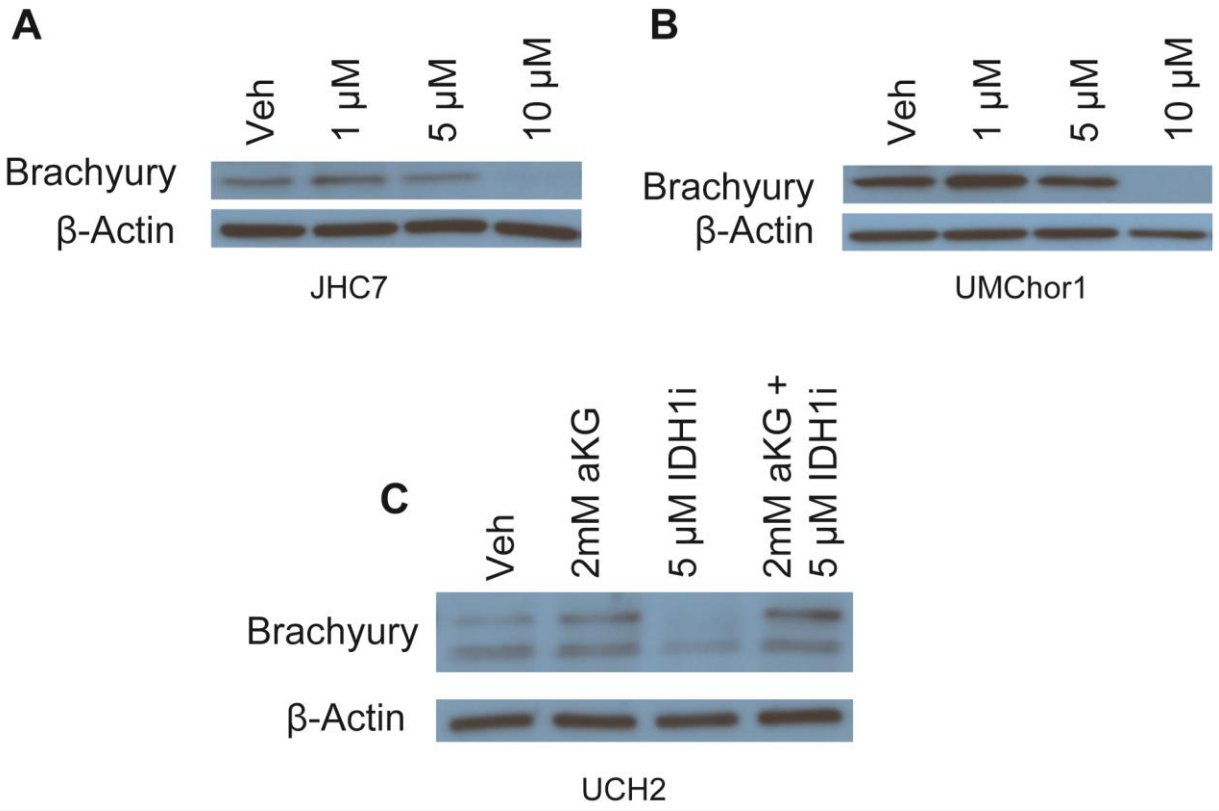

Figure 4.8: Preliminary studies suggested Brachyury may be regulated by IDH1 and alpha-ketoglutarate.

A. Immunoblots for brachyury and beta-Actin with increasing doses of IDH1 inhibitor in JHC7 chordoma cells.
B. Immunoblots for brachyury and beta-Actin with increasing doses of IDH1 inhibitor in UMChor1 chordoma cells.
C. Immunoblots for brachyury and beta-Actin with 2 mM of alpha-ketoglutarate (α-KG) and 5 μM of IDH1 inhibitor as single agents or in combination in U-CH2 chordoma cells.

4.3.9 Integrated analysis of changes in H3K27ac ChIP-seq and RNA-seq highlights stress response pathway activation

In parallel to profiling H3K27me3 ChIP-seq, we also conducted ChIP-seq for H3K27 acetylation (H3K27ac), a mark associated with actively transcribed regions of the genome (Allis & Jenuwein, 2016; Raisner et al., 2018). At promoters, we saw minimal changes in average H3K27ac signal with very small increases for JHC7 and CH22 and no change in UM-Chor1 (Figure 4.9A). Looking at average changes across the three cell lines, more regions experienced an increase in H3K27ac signal than a decrease (Figure 4.9A and B). Transcription factor motif analysis of the regions with increased H3K27ac revealed several candidate transcription factors (Figure 4.9 B and C), including the stress response transcription factor NRF2. Inspection of the top shared upregulated genes supported this model with enrichment for oxidative stress and NRF2-related pathways (Figure 4.9D and E).

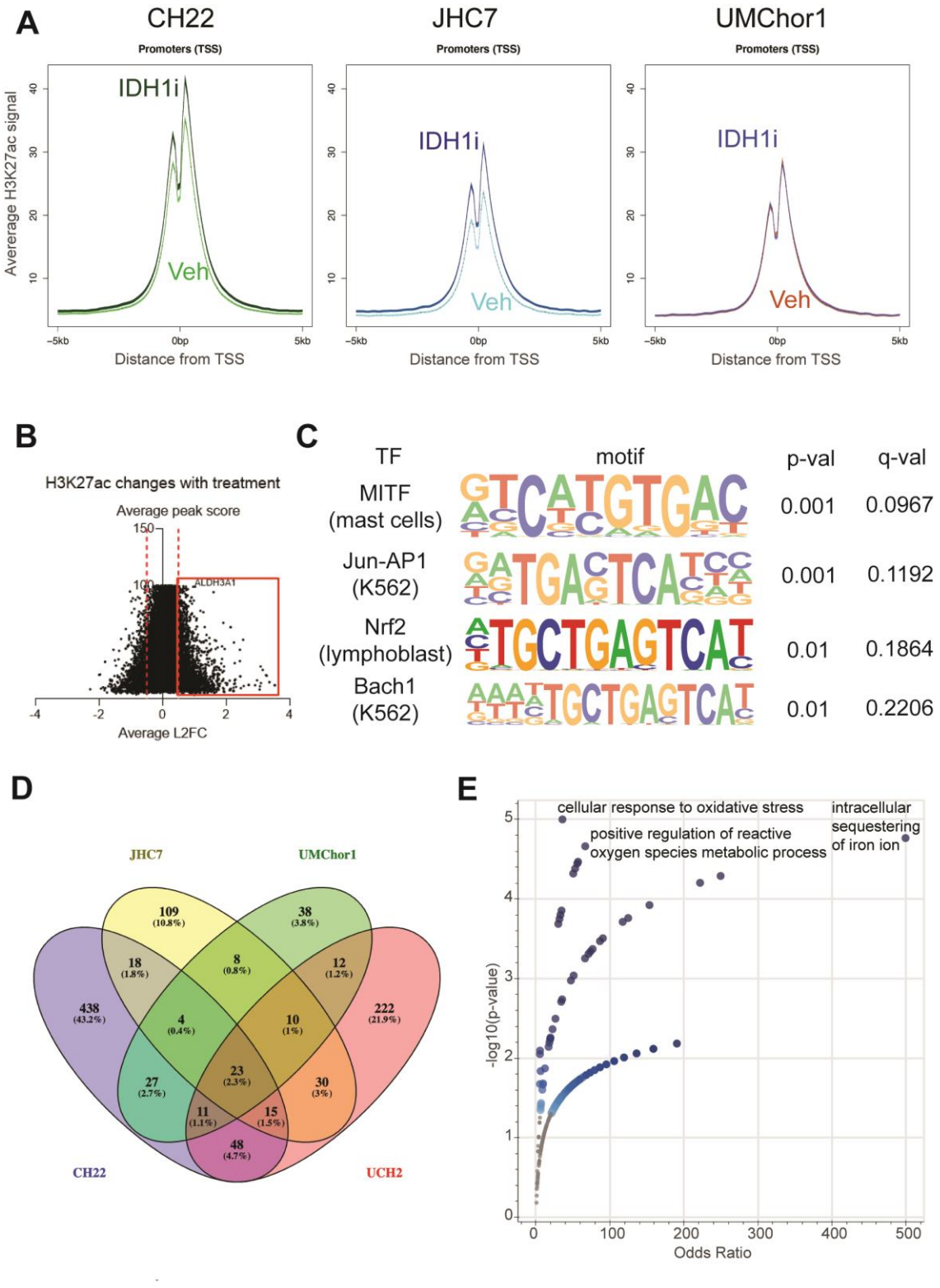

Figure 4.9: Integration of H3K27ac ChIP-seq and RNA-seq demonstrates IDH1 inhibitor induces stress response pathways.

A. Composite plots showing H3K27ac ChIP-seq average signal (y-axis) at promoters with or without IDH1 inhibition in three chordoma cell lines.
B. Scatter plot showing the average H3K27ac ChIP-seq peak score across the three cell lines with vehicle treatment (y-axis) compared to the fold change in acetylation with IDH1 inhibitor treatment (x-axis). The red box denotes peaks selected for motif analysis in **C**.
C. Motif enrichment of sites with an average $\log_2$ fold change of greater than 0.5 in H3K27ac signal with IDH1 inhibitor treatment compared to vehicle treatment across three cell lines, as depicted in **B**.
D. Venn diagram depicting overlap of upregulated genes from four chordoma cell lines.
E. Gene Ontology (GO) Biological process (BP) pathway enrichment analysis with the odds ratio of enrichment (x-axis) and a negative $\log_{10}$ transformation of the p-value (y-axis) depicted.

4.3.10 Glutathione synthesis pathway enzymes are among the highest overexpressed genes with IDH1 inhibitor treatment

Inspection of a number of NRF2 target genes demonstrated increased H3K27ac in the promoter and proximal gene body regions of *SLC7A11*, *GCLM*, and *GSR* (Figure 4.10A-C). SLC7A11 imports cystine which can be converted to cysteine, the rate-limiting substrate for glutathione synthesis. *GCLM* encodes Glutamate-Cysteine Ligase Modifier Subunit, a subunit of the rate-limiting enzyme in glutathione synthesis. *GSR* encodes glutathione reductase, the enzyme responsible for restoring glutathione to its reduced form (GSH) from its oxidized form (GSSG). Each is substantially overexpressed with IDH1 inhibition across all three cell lines profiled with both ChIP- and RNA-seq (Figure 4.10A-C).

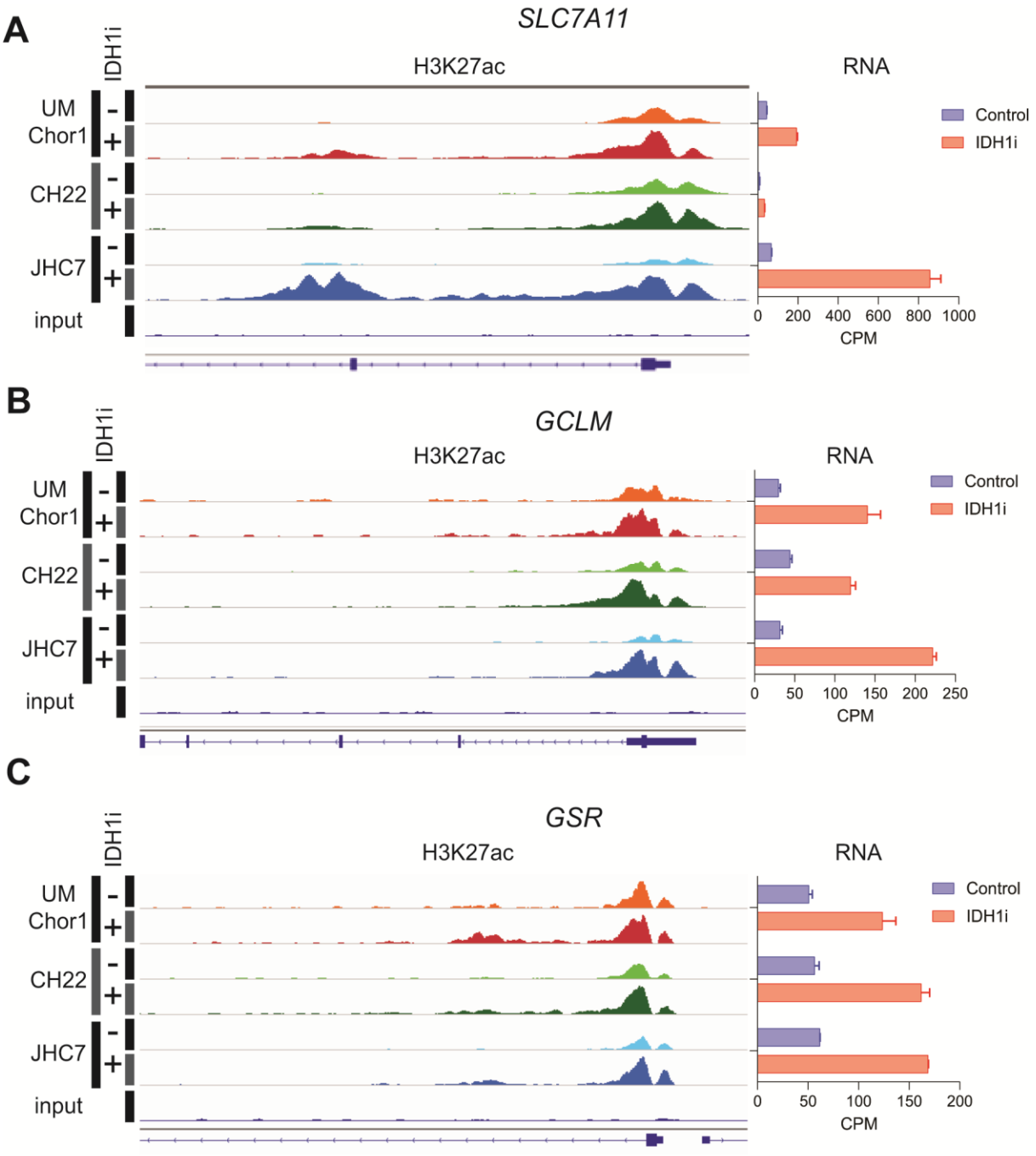

Figure 4.10: Glutathione metabolism genes show increased promoter acetylation and expression.

A. H3K27ac ChIP-seq tracks (left) at the *SLC7A11* promoter and proximal gene body for UM-Chor1 (reds), CH22 (greens), and JHC7 (blues) with or without IDH1 inhibitor treatment and corresponding RNA-seq changes for the same cell lines (right) measured by counts per million (CPM).
B. H3K27ac ChIP-seq tracks (left) at the *GCLM* promoter and proximal gene body for UM-Chor1 (reds), CH22 (greens), and JHC7 (blues) with or without IDH1 inhibitor treatment and corresponding RNA-seq changes for the same cell lines (right) measured by counts per million

(CPM).
C. H3K27ac ChIP-seq tracks (left) at the *GSR* promoter and proximal gene body for UM-Chor1 (reds), CH22 (greens), and JHC7 (blues) with or without IDH1 inhibitor treatment and corresponding RNA-seq changes for the same cell lines (right) measured by counts per million (CPM).

4.3.11 Chordoma cell lines increase glutathione production in response to IDH1 inhibition

Spurred the observations that critical proteins along the glutathione metabolic pathway were upregulated with IDH1 inhibitor treatment, we investigated our metabolomic profiles. Levels of oxidized glutathione increased in every cell line when treated with IDH1 inhibitor (Figure 4.11A). Furthermore, I utilized a luciferase-based assay to assess ratios of reduced-to-oxidized glutathione (GSH/GSSG) in response to blocking IDH1 activity. In the two cell lines examined, GSH/GSSG ratios dropped at multiple time points (Figure 4.11B).

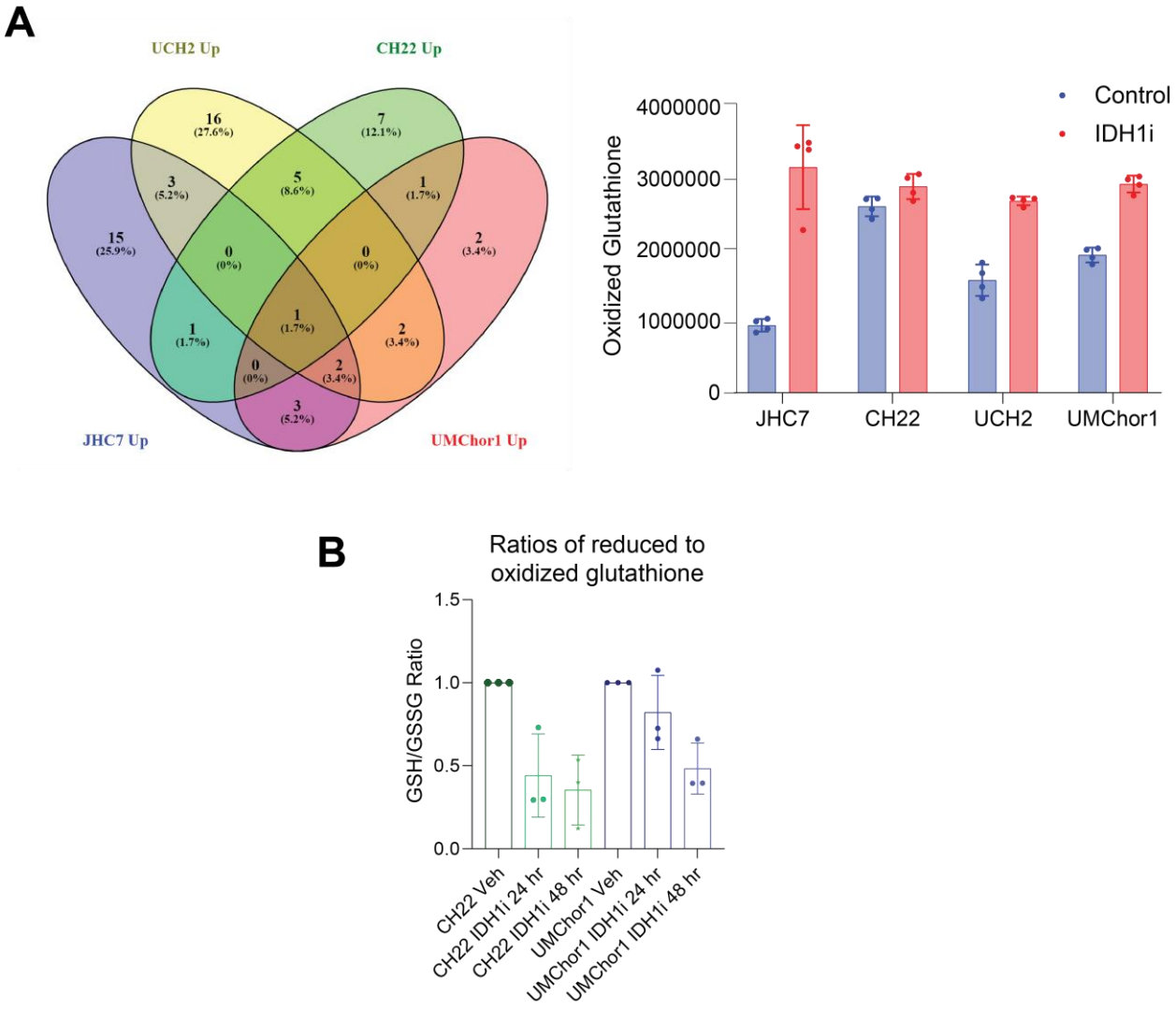

Figure 4.11: IDH1 inhibition drives increased levels of oxidized glutathione.

A. Venn diagram of metabolites upregulated with IDH1 inhibitor treatment (p-value < 0.05) across four chordoma cell lines (left) and levels of the one overlapping metabolite, oxidized glutathione (right), across all cell lines and conditions.
B. Ratios of reduced (GSH) to oxidized (GSSG) glutathione (y-axis) across two cell lines (CH22-greens, UMChor1-blues) at two timepoints (x-axis). Plotted points are derived from three experiments where ratios were GSH/GSSG calculated independently for each condition and then normalized to the vehicle condition. Vehicle treatments occurred over 48 hours.

4.3.12 N-acetylcysteine rescues proliferation with IDH1 inhibition

Since chordoma cell lines treated with IDH1 inhibition displayed oxidative stress pathway activation and increased levels of oxidized glutathione, we hypothesized that modulation of oxidative stress in the setting of IDH1 inhibition could reduce the toxic effects of the IDH1 inhibitor. To test this model, we supplemented chordoma cells with 5 mM of N-acetylcysteine or a matching volume of PBS and treated cells at a supra-IC50 dose of 5 μM IDH1 inhibitor and measured proliferation. Across two cell lines, N-acetylcysteine resulted in mildly decreased proliferation on its own but significantly rescued growth deficits mediated by the IDH1 inhibitor (Figure 4.12 A and B).

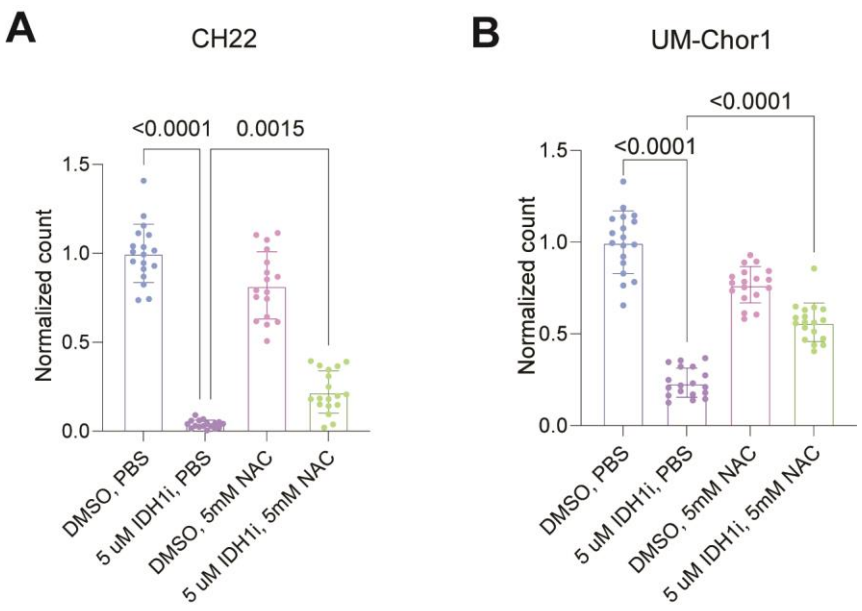

Figure 4.12: N-acetylcysteine supplementation reverses IDH1 inhibitor toxicity.

A. Cell counts of CH22 chordoma cells treated with DMSO/PBS vehicles (blue), 5 µM of IDH1 inhibitor (IDHi) and PBS vehicle (purple), DMSO and 5 mM N-acetylcysteine (NAC) (pink), or combined 5 µM IDHi and 5 mM NAC (green). Counts were made after 96 hours of treatment from three repeated experiments (n = 6 wells/experiment), and counts for each well were normalized to the average of the DMSO/PBS treated cell count for each experiment. P-values determined by one-way ANOVA, adjusted for multiple comparisons (all vs. all).
B. Cell counts of UM-Chor1 chordoma cells treated with DMSO/PBS vehicles (blue), 5 µM of IDH1 inhibitor (IDHi) and PBS vehicle (purple), DMSO and 5 mM N-acetylcysteine (NAC) (pink), or combined 5 µM IDHi and 5 mM NAC (green). Counts were made after 96 hours of treatment from three repeated experiments (n = 6 wells/experiment), and counts for each well were normalized to the average of the DMSO/PBS treated cell count for each experiment. P-values determined by one-way ANOVA, adjusted for multiple comparisons (all vs. all).

4.3.13 IDH1 inhibitor treatment reduces tumor proliferation in a mouse xenograft model

No medical therapies are approved for the treatment of chordoma in the U.S., highlighting the need for targeted approaches that can be used in conjunction with the standards of care of surgery and radiation. We generated flank tumors using the CH22 cell line in NOD scid gamma (NSG) immunodeficient mice and randomized animals to IDH1 inhibitor treatment or control. Treatment resulted in impaired growth of tumors as quantified by fold-change in volume (Figure 4.13B). Volume of tumors at multiple timepoints was significantly decreased with IDH1 inhibitor treatment, and tumor weights were also decreased (Figure 4.13C and D). Two IDH1 inhibitor-treated mice died during the course of this experiment, though it was not evident what the cause of death was. The dose (10 mg/kg) used in this study had previously been tolerated and is being further investigated in additional chordoma xenografts. A reduced dose is also being tested for efficacy.

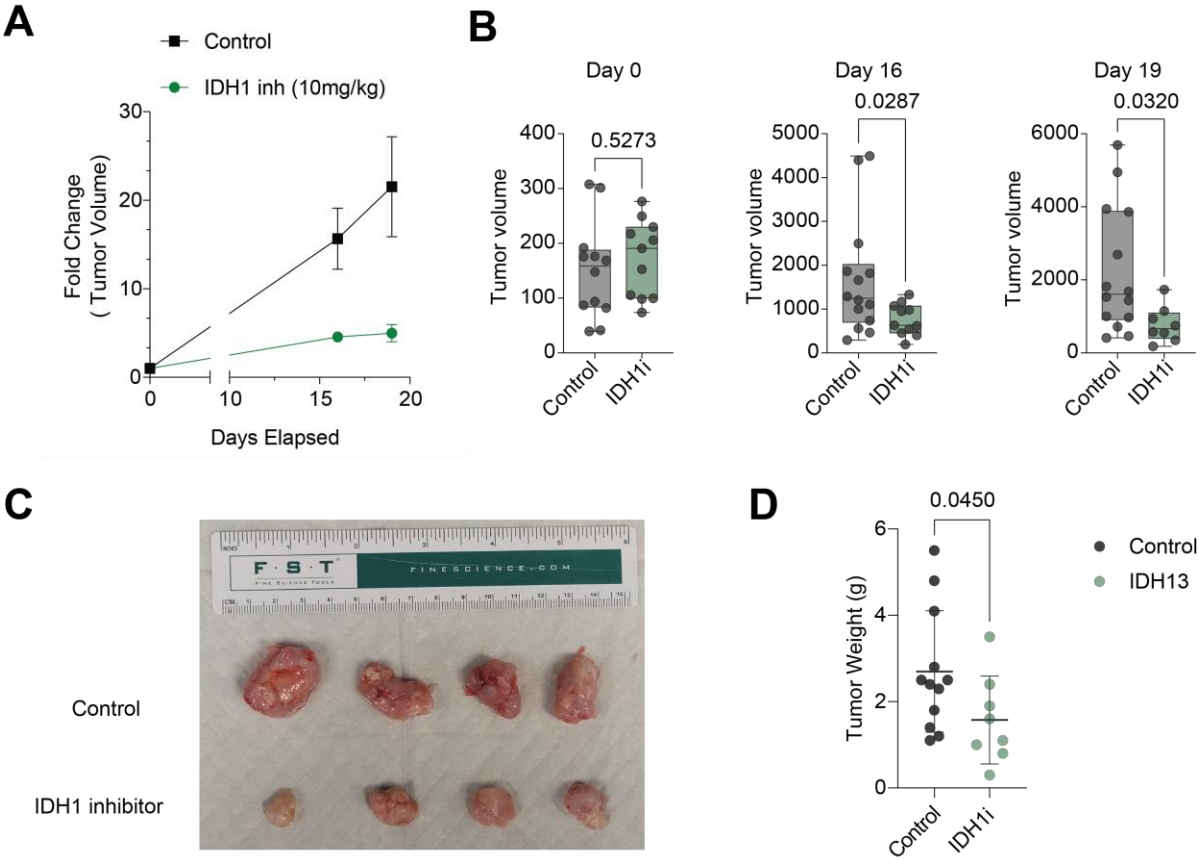

Figure 4.13: IDH1 inhibitor treatment limits tumor growth in chordoma xenografts in mice.

A. Tumor growth curves as measured by fold change from baseline measurements (y-axis) over time in days (x-axis) comparing control (black) and IDH1 inhibitor-treated (green) flank xenografts of the CH22 cell line.
B. Tumor volumes for control (black) and IDH1 inhibitor-treated (green) flank xenografts at the day prior to treatment initiation (Day 0, left, n = 12 control, 11 IDH1i) and two subsequent timepoints (Day 16, middle, n =14 control, 11 IDHi; and Day 19, right, n = 14 control, 8 IDHi). P-values calculated by two-sided student's t-test.
C. Dissected tumors from control (top) and IDH1 inhibitor-treated (bottom) mice.
D. Comparison of tumor weights from control (black, n = 12) and IDH1 inhibitor-treated (green, n = 8) flank xenografts.

4.4 Discussion

While metabolic reprogramming is a hallmark of cancer, its role in the aggressive, difficult-to-treat tumor chordoma is poorly understood. In addition to this knowledge gap, recent advances in our understanding of the links between metabolic and epigenetic pathways and our increasing understanding of the role H3K27me3 maintenance in chordomas (Cottone et al., 2020; Wei et al., 2022) provide strong rationale to probe for metabolic and epigenetic vulnerabilities in chordoma.

The studies presented here demonstrate upregulation of the TCA cycle genes in chordoma tumors compared to the putative developmental tissue of origin for chordoma and demonstrate that TCA cycle family gene *IDH1* is associated with unfavorable outcomes in patients. We characterized chordoma cells' reliance on both glucose and glutamine as carbon sources and showed that both modulation of *IDH1* transcription with shRNAs and its activity with an inhibitor leads to deficits in proliferative capacity of chordoma cells. Our initial hypothesis that targeting IDH1 could influence epigenomic state and regulation of brachyury was only partially supported. IDH1 inhibition lowered the α-KG/succinate ratio that drives demethylase activity, but at IC50 doses, only led to large changes in in brachyury transcription of one cell line, U-CH2. These results may represent cell line to cell line heterogeneity in sensitivity to α-KG depletion but do not appear to correlate with baseline α-KG/succinate ratios, as U-CH2—the cell line with the greatest changes in trimethylation and brachyury expression—had similar ratios to CH22.

Our data additionally suggest that IDH1 inhibition activates stress response pathways, and we show that addition of an antioxidant, NAC, rescues cell-proliferation deficits, suggesting cellular

stresses are involved in the growth inhibition. Ongoing work in the lab is aimed at identifying the precise mechanism of inhibited proliferation through measurements of redox stress, assessment of apoptosis and necrosis rates, and evaluation for activation the oxidative stress related controlled death pathway ferroptosis.

Together, these studies present novel observations about the metabolic state of chordomas, intriguing results regarding the interplay of histone methylation and TCA metabolites, and a promising therapeutic approach for a tumor lacking medical treatments.

Chapter 5
Probing Transcriptomic and Epigenomic Alterations Lays the Groundwork for Therapeutic Interventions across Multiple Brain Tumors

5.1 Introduction

Molecular subtyping of tumors has increasingly guided research strategies as discussed in Chapter 1. The identification of candidate driver events in particular has provided the basis both for the generation of novel tumor models and the probing of specific pathways for therapeutic vulnerabilities. The affordability of high-throughput DNA sequencing has greatly increased the power to explore consequences of a given alteration. In this chapter, we explore how transcriptome and epigenome profiling can characterize how tumor alterations drive global changes in the genome regulatory landscape and influence cell states. I apply these approaches to five brain tumors:

- Pediatric Histone H3 lysine-27-to-methionine-mutant diffuse midline glioma (H3K27M DMG)
- Pediatric H3 glycine-34-mutant H3G34R/V glioma
- Adult, isocitrate dehydrogenase 1 mutant (mIDH1) glioma
- Pediatric supratentorial Zinc-finger translocation associated (ZFTA)-fusion ependymoma
- Pediatric posterior fossa Group A ependymoma (PFA)

5.2 Methods

5.2.1 RNA sequencing analysis

For the H3K27M DMG project and H3G34R/V glioma projects, RNA sequencing (RNA-seq) data were generated and analyzed by the Michigan Center for Translational Pathology (MCTP), producing differentially expressed genes. Subsequent pathway analyses were conducted with Enrichr (E. Y. Chen et al., 2013; Kuleshov et al., 2016; Xie et al., 2021).

For the mIDH1 glioma data, RNA-seq data were generated by the University of Michigan Advanced Genomic core. Subsequent analyses of differential expression were conducted using DEseq2 as described in Chapters 3 and 4.

For the ZFTA-fusion ependymoma project, RNA-seq files were generated and pseudo-mapped to the mouse (mm10) transcriptome using Kallisto by the MCTP. Subsequent analyses of differential expression were conducted using DEseq2 as described in Chapters 3 and 4.

5.2.2 ATAC sequencing analysis

For the H3K27M DMG project, assay for transposase accessible chromatin with sequencing (ATAC-seq) data were generated by the company Active Motif.

For the ZFTA-RELA project, a protocol modified from Omni-ATAC (Corces et al., 2017) was performed in collaboration with the Michigan Center for Translational Pathology (MCTP). Cells were cultured with the specified treatments and then collected. A single cell suspension was made by adding Accutase (Innovative Cell Technologies, Inc. Cat# AT104), checked for viability > 85% with trypan blue exclusion, and counted. Aliquots of 500,000 cells were made for each sample and stored on ice.

Samples were centrifuged at 500 RCF at 4°C for 5 minutes, and supernatant was discarded. Cells were then resuspended in 500 µL of ATAC-Resuspension Buffer (10 mM Tris-HCl pH 7.4 Invitrogen 15567-027, 10 mM NaCl Sigma, and 3mM $MgCl_2$ Ambion AM9530G in sterile water) containing 0.1% NP40 (abcam ab142227), 0.1% Tween-20 (Sigma/Roche cat# 11332465001),

0.01% Digitonin (Promega cat# G9441), and protease/phosphatase inhibitor to lyse the cells on ice for 3 minutes. Per replicate, 50 nuclei at 500 RCF for 10 min at 4°C in of the now-isolated nuclei were added to a new tube with 100 µL of ATAC-Resuspension Buffer with 0.1% tween and protease/phosphatase inhibitor but NO NP40 or digitonin to quench the lysis.

Nuclei were then pelleted at 500 RCF for 10 min at 4°C, and supernatants were carefully removed. Cells were then resuspended in 50 µL of transposition mixture from Illumina DNA TDE1 Enzyme and Buffer kits (20034197/8), pipetting gently four times. Resuspended samples were then incubated at 37°C for 30 minutes.

Following this reaction, DNA was purified by the Qiagen minElute kit (Cat 28004). DNA was eluted into 24 µL of elution buffer and 20 µL was used for PCR amplification using the indices listed in Table 5.1 and NEBNext 2x MasterMix (Cat M0541S). Cycling conditions were: 72°C for 5 minutes, 98°C for 30 seconds and then 12 cycles of 98°C for 10 seconds, 63°C for 30 seconds, and 72°C for 1 minute.

ID	Sequence	Bp	Index No.
AP_ATAC-NoIndex	AATGATACGGCGACCACCGAGATCTACACTCGTCGGCAGCGTCAGATGTG	50	
AP_ATAC-6bp-index1	CAAGCAGAAGACGGCATACGAGATCGTGATGTCTCGTGGGCTCGGAGATGT	51	1
AP_ATAC-6bp-index2	CAAGCAGAAGACGGCATACGAGATACATCGGTCTCGTGGGCTCGGAGATGT	51	2
AP_ATAC-6bp-index3	CAAGCAGAAGACGGCATACGAGATGCCTAAGTCTCGTGGGCTCGGAGATGT	51	3
AP_ATAC-6bp-index4	CAAGCAGAAGACGGCATACGAGATTGGTCAGTCTCGTGGGCTCGGAGATGT	51	4
AP_ATAC-6bp-index5	CAAGCAGAAGACGGCATACGAGATCACTGTGTCTCGTGGGCTCGGAGATGT	51	5
AP_ATAC-6bp-index6	CAAGCAGAAGACGGCATACGAGATATTGGCGTCTCGTGGGCTCGGAGATGT	51	6
AP_ATAC-6bp-index7	CAAGCAGAAGACGGCATACGAGATGATCTGGTCTCGTGGGCTCGGAGATGT	51	7
AP_ATAC-6bp-index8	CAAGCAGAAGACGGCATACGAGATTCAAGTGTCTCGTGGGCTCGGAGATGT	51	8
AP_ATAC-6bp-index9	CAAGCAGAAGACGGCATACGAGATCTGATCGTCTCGTGGGCTCGGAGATGT	51	9

AP_ATAC-6bp-index10	CAAGCAGAAGACGGCATACGAGATAAGCTAGTCTCGTGGGCTCGGAGATGT	51	10
AP_ATAC-6bp-index11	CAAGCAGAAGACGGCATACGAGATGTAGCCGTCTCGTGGGCTCGGAGATGT	51	11
AP_ATAC-6bp-index12	CAAGCAGAAGACGGCATACGAGATTACAAGGTCTCGTGGGCTCGGAGATGT	51	12
AP_ATAC-6bp-index13	CAAGCAGAAGACGGCATACGAGATTTGACTGTCTCGTGGGCTCGGAGATGT	51	13
AP_ATAC-6bp-index14	CAAGCAGAAGACGGCATACGAGATGGAACTGTCTCGTGGGCTCGGAGATGT	51	14
AP_ATAC-6bp-index15	CAAGCAGAAGACGGCATACGAGATTGACATGTCTCGTGGGCTCGGAGATGT	51	15
AP_ATAC-6bp-index16	CAAGCAGAAGACGGCATACGAGATGGACGGGTCTCGTGGGCTCGGAGATGT	51	16
AP_ATAC-6bp-index17	CAAGCAGAAGACGGCATACGAGATGCGGACGTCTCGTGGGCTCGGAGATGT	51	18
AP_ATAC-6bp-index18	CAAGCAGAAGACGGCATACGAGATTTTCACGTCTCGTGGGCTCGGAGATGT	51	19
AP_ATAC-6bp-index19	CAAGCAGAAGACGGCATACGAGATGGCCACGTCTCGTGGGCTCGGAGATGT	51	20
AP_ATAC-6bp-index20	CAAGCAGAAGACGGCATACGAGATCGAAACGTCTCGTGGGCTCGGAGATGT	51	21

AP_ATAC-6bp-index21	CAAGCAGAAGACGGCATACGAGATCGTACGGTCTCGTGGGCTCGGAGATGT	51	22
AP_ATAC-6bp-index22	CAAGCAGAAGACGGCATACGAGATCCACTCGTCTCGTGGGCTCGGAGATGT	51	23
AP_ATAC-6bp-index23	CAAGCAGAAGACGGCATACGAGATATCAGTGTCTCGTGGGCTCGGAGATGT	51	25
AP_ATAC-6bp-index24	CAAGCAGAAGACGGCATACGAGATAGGAATGTCTCGTGGGCTCGGAGATGT	51	27

Table 5.1: Indices used for PCR amplification of ATAC-seq libraries.

Samples were then purified again with the Qiagen MinElute Kit and eluted in 66 µL of elution buffer. To 42 µl from the previous 60 µl purified PCR amplified DNA, add 21µl well-resuspended KAPA pure beads (KK8000) were added and mixed by pipetting 10 times. Samples were incubated at room temperature for 10 minutes then beads were extracted by magnet for 6 minutes, and 60 µl samples were collected. 72 µl of beads were added to each sample, mixed 30 times by pipetting and incubated for another 10 minutes at room temperature. After 6 minutes of magnet extraction of the beads, the supernatant was discarded and beads were washed twice with 80% ethanol, freshly made and chilled on ice.

Following ethanol washes, the beads were dried at room temperature for 6 minutes and then at 37°C for 1 minute to completely dry. Each sample was then eluted with 25µl 10mM Tris pH 8.0 and mixed 30 times by pipetting, followed by 10 minutes of room-temperature incubation and 6 minutes of bead extraction by magnet. Finally, the eluted samples are isolated and analyzed by Bioanalyzer High Sensitivity DNA chip for quality. Resulting samples were sequenced by the MCTP.

5.2.3 Hi-C data analysis

Hi-C chromatin conformation capture data generated by Wang et al. for the H3K27M DMG cell line DIPG-007 (J. Wang et al., 2021) were obtained from the 3D Genome Browser hosted by the Yue Lab at Northwestern University (Y. Wang et al., 2018). Genomic coordinates were obtained and used to generate aligned ATAC-seq tracks via the Integrative Genomics Viewer (IGV, v2.8.0) (J. T. Robinson et al., 2011).

5.2.4 DNA methylation

DNA methylation measurements by enhanced reduced representation bisulfite sequencing (ERRBS) and initial data processing were performed by the Epigenomics Core Facility at Weill Cornell Medicine. DNA was digested with the restriction enzyme MspI (R0106, New England Biolabs), phenol-extracted, ethanol-precipitated, end-repaired, A-tailed, and ligated to methylated TruSeq adapters (Illumina Inc). Fragment lengths of 150– 250 bp and 250–400 bp were then gel isolated and subjected to overnight bisulfite conversion with the EZ DNA methylation kit (D5030, Zymo Research), purified, and PCR-amplified with TruSeq primers (Illumina). Sequencing was performed on an Illumina HiSeq 2500. Resulting files were processed and analyzed as described previously (Garrett-Bakelman et al., 2015). methylKit and eDMR were used to evaluate CpG sites for differential methylation with the following criteria: q value< 0.01 and methylation percentage difference of at least 25% (Akalin et al., 2012; S. Li et al., 2013). Methylation ratios were displayed with the Integrative Genomics Viewer (IGV, v2.8.0) (J. T. Robinson et al., 2011).

5.3 Targeting BAF complex dependencies in H3K27M DMGs

5.3.1 H3K27M DMGs show susceptibility to multiple epigenetically focused inhibitors in preclinical models

H3K27M DMGs are universally fatal pediatric brain tumors with limited treatment options. As discussed in depth in Chapters 1-3, these tumors harbor gain-of-function mutations in histone H3.1 or H3.3 that inhibit spreading of the polycomb repressive complex 2 (PRC2) and the catalytic activity of the its methyltransferase subunit enhancer of zeste homolog 2 (EZH2) (Harutyunyan et al., 2019; Lewis et al., 2013; Stafford et al., 2018), resulting in striking

depletion of H3K27 di- and trimethylation (H3K27me2/3), as well as increased levels of opposing H3K27 acetylation (H3K27ac). H3K27me3 is retained at certain sites throughout the genome that tend to be strong Polycomb targets (Mohammad et al., 2017; Piunti et al., 2017). Single cell analyses further demonstrate that the H3K27M mutation is associated with changes in other histone modification including increased levels of the active enhancer and promoter marks H3K4me1 and H3K4me3 and decreased heterochromatin-associated H3K9 methylation (Harpaz et al., 2022).

The unique epigenomic landscape of these tumors poses a potential therapeutic window. Indeed, multiple epigenetic inhibitors have shown promise in preclinical models of H3K27M DMGs. Early work showed that these tumors are sensitive to inhibition of the H3K27me3 demethylases with the compound GSK-J4 (Hashizume et al., 2014). Screening of further compounds showed that while H3K27M DMGs were resistant to chemotherapeutic agents, they harbored sensitivity to histone deacetylase inhibitors (HDACi), and that combination of HDACi and GSK-J4 had synergistic effects (Grasso et al., 2015). Further profiling of epigenetic-focused inhibitors revealed that H3K27M DMGs were sensitive to H3K27 methyltransferase inhibitors, suggesting reliance on residual EZH2 activity (Mohammad et al., 2017; Piunti et al., 2017; Y. Zhang et al., 2017). These and subsequent studies have nominated a number of other epigenetic and transcriptional inhibitors as promising therapeutic approaches (Anastas et al., 2019; Nagaraja et al., 2017). These include lysine-specific histone demethylase 1A (LSD1/KDM1A), cyclin-dependent kinase 7 (CDK7), and Bromodomain and Extra-Terminal motif (BET) inhibitors.

5.3.2 Mammalian SWI/SNF (BAF) complexes are frequently altered in cancer and represent a potential therapeutic target

SWItch/Sucrose Non-Fermentable (SWI/SNF) complexes comprise one of the four major families of ATP-dependent chromatin remodelers. Mammalian SWI/SNF (mSWI/SNF) complexes fall into three classes: canonical BRG1/BRM-associated factor (cBAF or BAF), polybromo-associated BAF (PBAF), and more recently elucidated noncanonical BAF (ncBAF) complexes. Sequencing studies have shown that, more than 20% of human cancers profiled have mutations in mSWI/SNF subunits (Kadoch et al., 2013). While mSWI/SNF mutations are not observed commonly in H3K27M DMGs, SWI/SNF activity has substantial influence on the distribution of histone modifications. Loss of its activity permits increased Polycomb-group activity and H3K27me3-mediated repression (Wilson et al., 2010), and its activity at enhancers is required for recruitment of histone acetyltransferases to maintain an active state (Alver et al., 2017). PRC2 inhibition has been employed as a therapeutic strategy in tumors with SWI/SNF loss-of-function alterations due to their antagonistic relationship, highlighting the therapeutic vulnerabilities inherent to the interplay of Polycomb and SWI/SNF activity. Recently, novel chemical approaches have been developed to disrupt BAF complex activity by promoting its degradation (Farnaby et al., 2019; Remillard et al., 2017; Xiao et al., 2022; Zoppi et al., 2018). In particular a proteolysis-targeting chimera (PROTAC) degrader (AU-15330) of the SWI/SNF ATPase subunits, SMARCA2 (SWI/SNF related, matrix associated, actin dependent regulator of chromatin, subfamily a, member 2) and SMARCA4 and of the ATPase-dependent subunit PBRM1 was shown to be highly potent against androgen-receptor (AR)-positive prostate cancer by disrupting core enhancer circuits driven by AR and the pioneer transcription factor forkhead box A1 (FOXA1) (Xiao et al., 2022).

5.3.3 The H3K27M mutation promotes sensitivity to mSWI/SNF complex inhibition in DMGs

At the start of this project, the role of mSWI/SNF complexes in H3K27M DMGs had been largely unknown. Dr. Mateus Mota in the Venneti Lab set out to characterize the expression of SWI/SNF subunits in H3K27M DMGs and test the sensitivity of H3K27M DMGs to AU-15330. He generated several critical lines of evidence supporting the role of mSWI/SNF ATPase and AU-15330 target SMARCA4 in H3K27M DMG biology.

First, both patient-derived H3K27M DMG cell lines and tumor samples exhibit higher expression of SMARCA4 compared to other pediatric gliomas. Next, proteomic and immunoblotting-based analysis revealed that knockdown of histone H3-3A expression in the H3-3A lysine 27 mutant DIPG-007 cell line resulted in significantly decreased SMARCA4 levels. Lastly, Dr. Mota showed that H3K27M DMGs displayed highly specific response to the mSWI/SNF ATPase PROTAC AU-15330 compared to non-H3K27M pediatric glioma models. In fact, when compared to the panel of cell lines profiled by Xiao et al., H3K27M DMGs showed some of the strongest sensitivity profiles (Figure 5.1). Importantly, knockdown of H3-3A reversed this sensitivity, leading to some of the most resistant profiles. While these comparisons must be interpreted cautiously due to the fact that they were performed in different laboratories, two projects published during our ongoing work identified SMARCA4 as a critical essential gene for H3K27M DMGs through genome-wide mutational screens (Mo et al., 2022; Panditharatna et al., 2022). Moreover, these studies highlighted additional pharmacologic inhibitors of SWI/SNF activity as efficacious therapeutic agents in preclinical models.

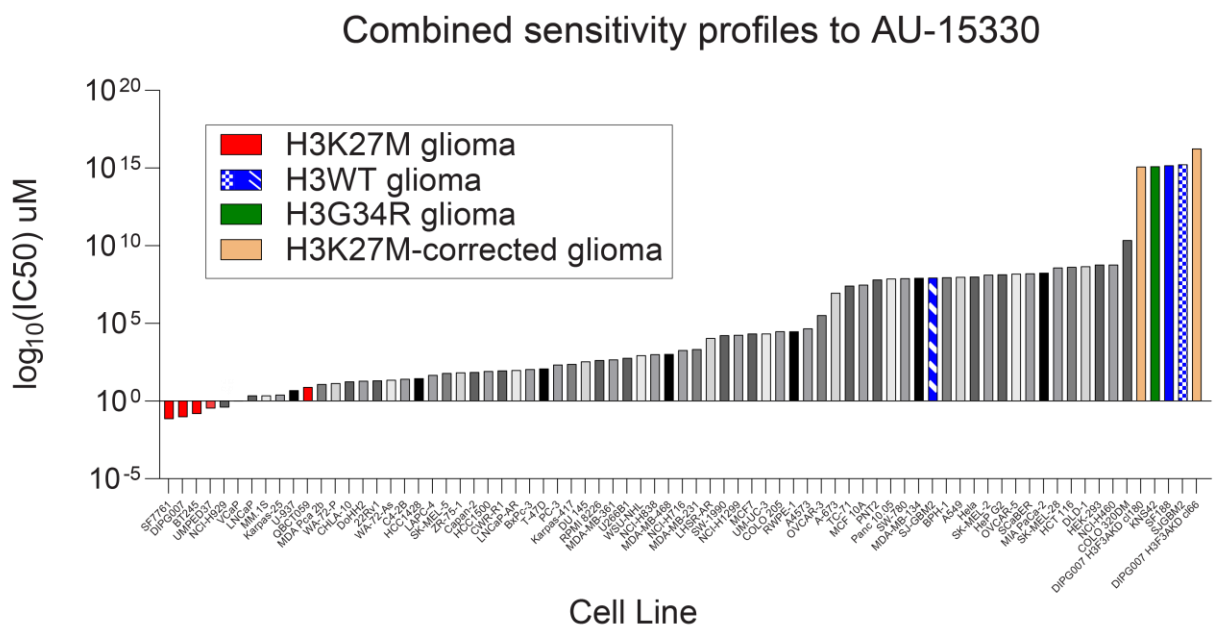

Figure 5.1: H3K27M DMGs are highly sensitive to treatment with the SWI/SNF ATPase PROTAC AU-15330.

Half-maximal inhibitory concentrations (IC50s, y-axis) of cell lines (x-axis) across a range of tumor types from Xiao et al. and from Dr. Mateus Mota in the Venneti Lab, ordered from low-to-high: H3K27M DMG cell lines are shown in red, H3K27M DMG cell lines with knockdown of the mutant-histone encoding H3-3A are shown in yellow. H3WT (blue) and G34R (green) cell lines are also highlighted for comparison. Within H3WT samples, pinstripes denote an H3WT glioma cell line as tested by the authors of the original and dots denote the same line as tested by Dr. Mota for comparison. Non-glioma cell lines profiled by Xiao et al. are depicted in shades of grey. All data were generated by Dr. Mota or Xiao et al.

5.3.4 SWI/SNF ATPase subunit and PBRM1 degradation targets enhancers, disrupting key developmental and structural pathways

To understand how SMARCA2/4 and PBRM1 degradation alters the chromatin landscape of H3K27M DMGs, we performed an assay for transposase accessible chromatin with sequencing (ATAC-seq) and an RNA sequencing (RNA-seq) experiment in vehicle- and AU-15330-treated DIPG-007 cells. Global assessment revealed decreased accessibility in a substantial subset of regions (Figure 5.2A). This change was supported with a decrease in global levels of H3K27ac, as observed by Dr. Mota through immunoblotting (Figure 5.2B). Parallel analysis of peaks associated with promoter regions and peaks found outside of promoters revealed that the majority of altered sites fell outside of promoters (Figure 5.2C and D), consistent with prior findings that the enhancer landscape is significantly changed with AU-15330 treatment (Xiao et al., 2022).

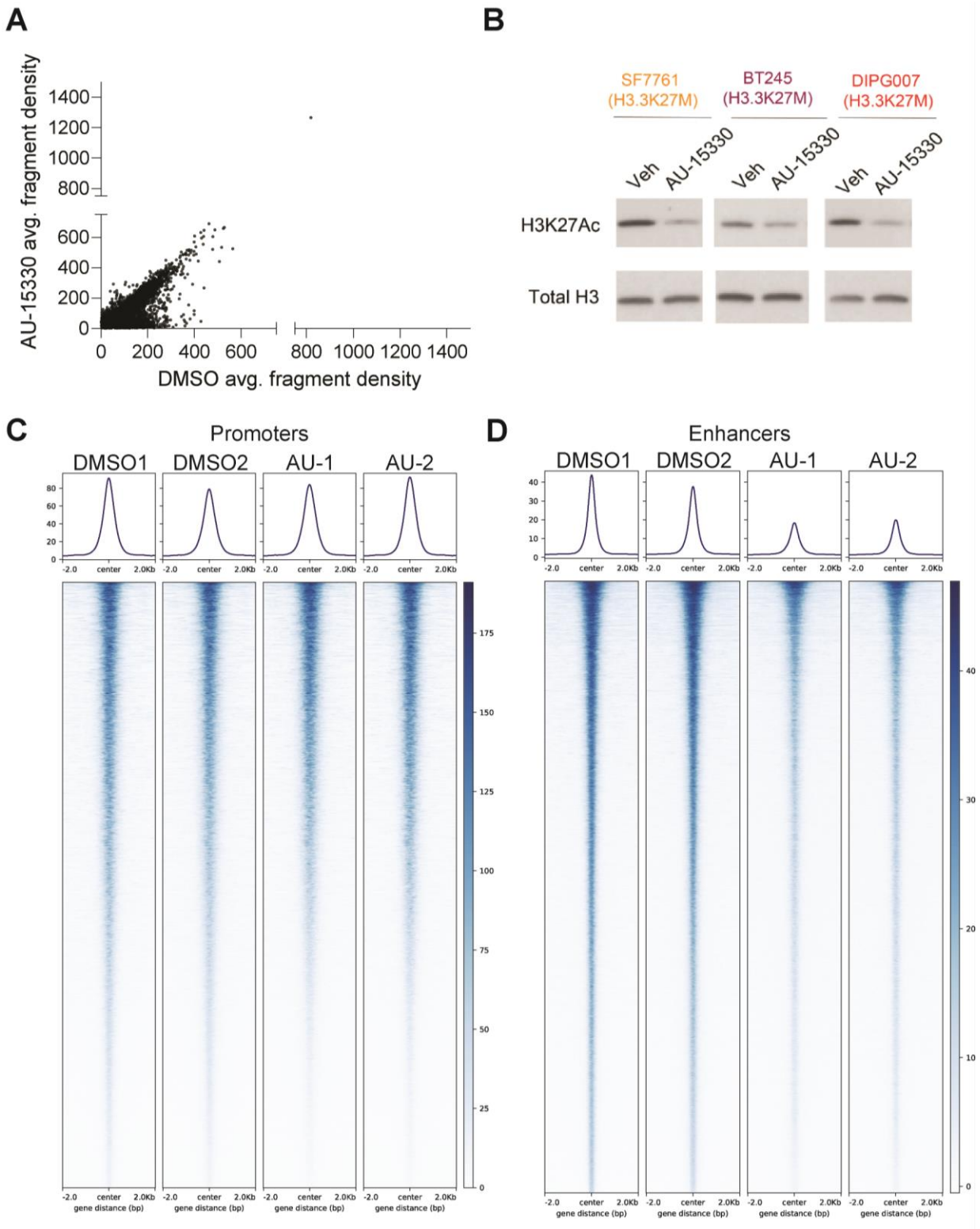

Figure 5.2: AU-15330 treatment decreased enhancer accessibility in DIPG-007.

A. Scatter plot displaying average fragment density of ATAC-seq sites across the genome, comparing density scores of DMSO vehicle-treated cells (x-axis) to AU-15330-treated cells (y-axis).
B. Immunoblots for H3K27ac and total histone H3 generated by Dr. Mateus Mota comparing levels of H3K27ac in AU-15330 vs. DMSO treated cells for three H3K27M DMGs.
C. ATAC-seq heatmap for all promoters with peaks identified in either DMSO (n = 2, left) or AU-15330 treated (n = 2, right) cells. Composite plots averaging signal at all sites are shown above and the peaks included are shown below for each sample, ordered from highest (top) to lowest (bottom) signal.
D. ATAC-seq heatmap for all enhancers with peaks identified in either DMSO (n = 2, left) or AU-15330 treated (n = 2, right) cells. Composite plots averaging signal at all sites are shown above and the peaks included are shown below for each sample, ordered from highest (top) to lowest (bottom) signal.

I examined the functional impact of these striking losses of accessibility by linking peaks with decreased ATAC-seq signal to genes within 10kb and overlapping the resulting gene list with downregulated genes from our proteomic and transcriptomic datasets, also generated from DIPG-007, identifying 161 genes (Figure 5.3). Pathway enrichment analysis centered on pathways involved in cell adhesion/motility consistent with the findings of Mo et al. and neurogenesis and development consistent with the top SMARCA4 peak sites identified by Panditharatna et al.

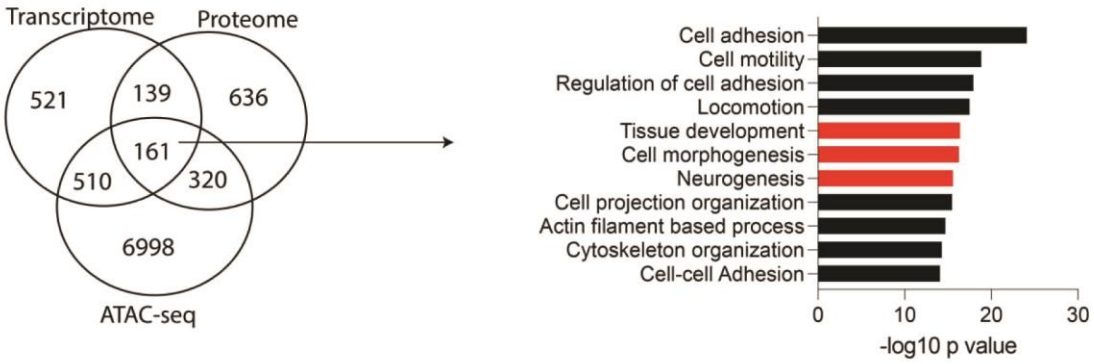

Figure 5.3: AU-15330 decreases expression of genes associated with cell motility and development.

Venn diagram (left) illustrating unique and shared genes with decreased RNA expression, lowered protein expression, or sites with reduced chromatin accessibility within 10kb and pathway analysis (right) of the 161 overlapping genes ordered by -$\log_{10}$ p-value.

5.3.5 *Motif enrichment analyses identifies FOXO1 as a critical SWI/SNF-regulated transcriptional factor for H3K27M DMGs*

To understand how the PROTAC AU-15330 alters H3K27M DMG expression patterns, I performed motif analysis on the ATAC-seq peaks with decreased signal in treated vs. control cells (Figure 5.4A) and found 162 motifs with a q-value of 0. These motifs included the top motifs identified as SMARCA4 targets in the recently published projects such as SOX10, BATF, TCF4, and ASCL1 (Mo et al., 2022; Panditharatna et al., 2022). I then looked to see if mSWI/SNF may directly regulate expression of transcription factors themselves by comparing the motifs enriched in lost ATAC-seq peaks with the genes we found to be downregulated. Forkhead family gene forkhead box protein O1 (*FOXO1*) was found to be the only gene satisfying both criteria (Figure 5.4A). Careful examination of ATAC-seq tracks in the regions surrounding the *FOXO1* locus revealed that while the *FOXO1* promoter showed similar signal levels with and without treatment, multiple sites upstream had evidence of reduced accessibility (Figure 5.4B). Mapping those sites to published Hi-C data on the chromatin conformation of the locus in DIPG-007 cells revealed strong evidence that these sites are likely in contact with the *FOXO1* promoter (Figure 5.4B).

Data generated by Dr. Mota and Dr. Stefan Sweha showed that FOXO1 was uniquely expressed in H3K27M and not H3WT or H3G34R gliomas when evaluated by protein immunoblotting. Next, they observed that AU-15330 treatment of multiple H3K27M models reduced FOXO1 expression. Moreover, short hairpin RNA (shRNA) knockdown and pharmacologic inhibition with AS-1842856 of FOXO1 in multiple H3K27M DMG models resulted in decreased proliferation, highlighting the importance of the transcription factor in H3K27M DMG biology.

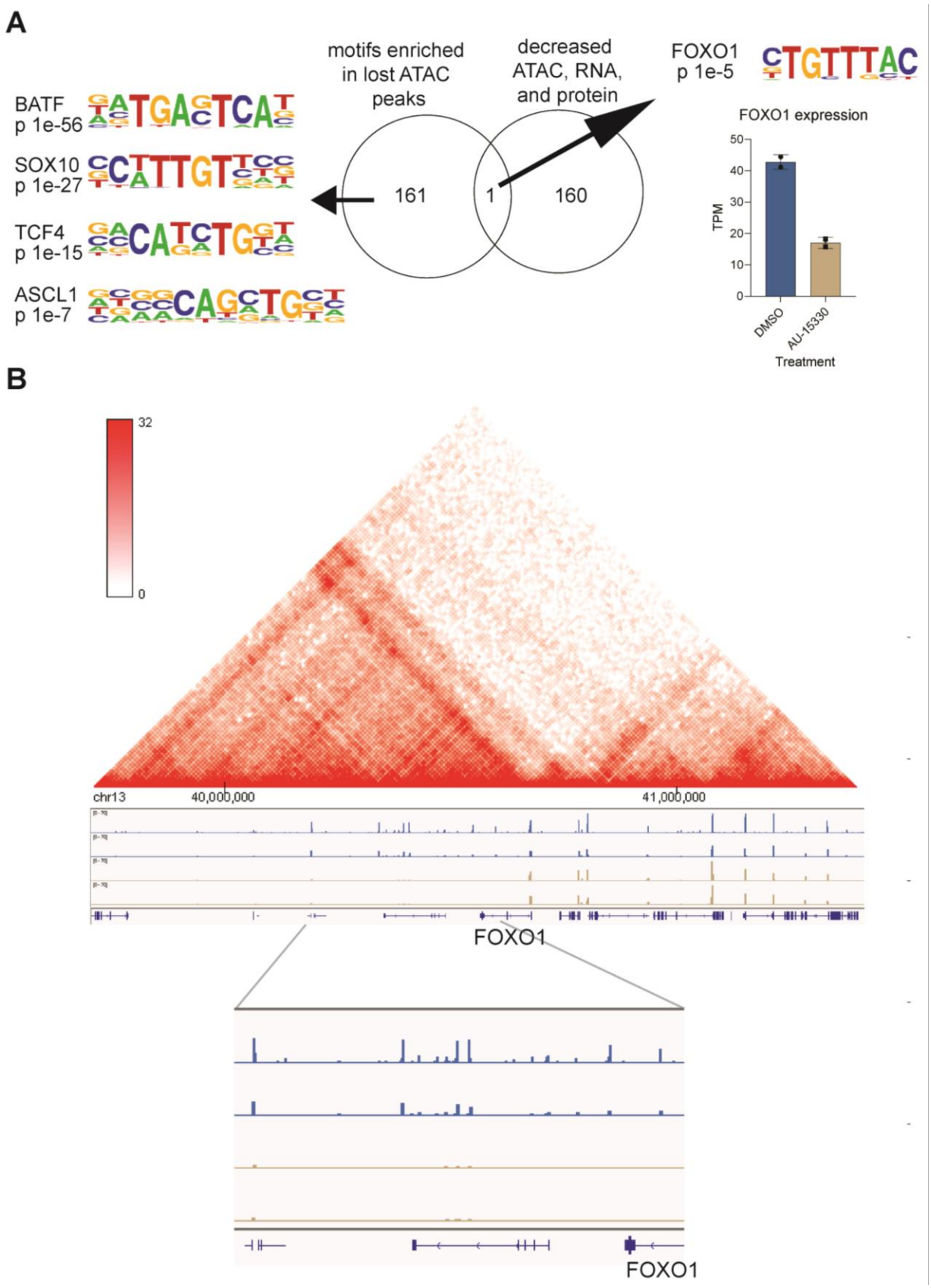
A
motifs enriched in lost ATAC peaks
decreased ATAC, RNA, and protein
BATF p 1e-56
SOX10 p 1e-27
TCF4 p 1e-15
ASCL1 p 1e-7
161
1
160
FOXO1 p 1e-5
FOXO1 expression
TPM
50
40
30
20
10
0
DMSO
AU-15330
Treatment
B
32
0
chr13
40,000,000
41,000,000
FOXO1
FOXO1

Figure 5.4: mSWI/SNF inhibition may disrupt *FOXO1* expression through enhancer modulation.

A. Venn diagram comparing motifs enriched in ATAC-seq sites with decreased signal in AU-15330 treated DIPG-007 cells and epigenetically downregulated genes identified in Figure 5.3. Motifs previously identified as SMARCA4-bound in H3K27M (Mo et al., 2022; Panditharatna et al., 2022) are highlighted on the left. The motif logo (top right) and expression score in transcripts per million mapped reads (TPM) for the single overlapping gene are displayed on the right.
B. From top to bottom: Published Hi-C chromatin conformation capture heatmap displaying frequency of association (red - high, white - low) along points connecting any two sites of the locus along the diagonals for DIPG-007 cells (J. Wang et al., 2021); ATAC-seq tracks for DMSO vehicle-treated (blue) or AU-15330-treated DIPG-007 cells near the *FOXO1* locus; and a magnified depiction of upstream sites with differential ATAC-seq signal. Hi-C data were accessed at http://3dgenome.fsm.northwestern.edu/.

5.3.6 Discussion

H3K27M DMGs are defined by a mutation in a critical chromatin factor and are sensitive to a variety of chromatin modifier inhibitors. The presented here work extends this spectrum of epigenetic approaches. Dr. Mota's experiments demonstrate that PROTAC-mediated degradation of the mSWI/SNF ATPases SMARCA2 and SMARCA4 and of the subunit PBRM1 results in substantial toxicity to H3K27M DMG models. This sensitivity is specific compared to H3WT and H3G34R glioma models and dependent on maintained expression of the H3K27M mutation.

Our integrated analyses of epigenomic, transcriptomic, and proteomic data further support the recent findings of Mo et al. and Panditharatna et al. that demonstrate disruption of the enhancer landscape and implicate the transcription factor SOX10 as an mSWI/SNF regulated gene. The work presented here extends the understanding of the mSWI/SNF-regulated transcriptional program and identifies FOXO1 as a critical downstream effector in H3K27M DMG biology. Its expression is dependent on mSWI/SNF function, essential for H3K27M DMG proliferation, and unique to H3K27M DMGs compared to other pediatric gliomas. Together these data illustrate one potential mechanism of H3K27M-specific toxicity of SWI/SNF ATPase inhibition.

While these data highlight an intriguing transcriptional dependency in H3K27M DMGs, additional studies may help elucidate the relative impact of FOXO1 in sensitivity to SWI/SNF targeting PROTAC therapies. Testing whether overexpression of FOXO1 in the presence of AU-15330 treatment rescues cell proliferation deficits will clarify if the toxicity we observe with AU-15330 treatment and with FOXO1 inhibition are along the same pathway.

Additionally, several other SWI/SNF targeting compounds including ATPase inhibitors and a degrader (JQ-dS-4) were shown to have similar epigenomic effects on H3K27M DMG cells (Panditharatna et al., 2022). Assessment of publicly available RNA-seq data (GSE212718) did not show a difference in FOXO1 expression after treatment with either of the two ATPase inhibitors. These findings may have several explanations. First, these data were generated from 24 hours of treatment as compared to the 48-hour timepoint employed across our studies. Next, a notable limitation of both our study and that of Panditharatna et al. is that the RNA-seq studies were each performed in a single cell line, and these cell lines differed between the two projects. Lastly, the work of Panditharatna et al. showed that H3K27M DMGs are more sensitive to AU-15330 compared to at least one of the two ATPase inhibitors when compared to the mean sensitivity across a panel of 880 cell lines. Therefore, it is possible that targeted degradation of mSWI/SNF ATPases may have distinct effects on downstream gene expression and phenotypic outcome compared to enzymatic inhibition.

Several future experiments may better dissect the mSWI/SNF-FOXO1 axis in H3K27M DMGs. First, assessment of FOXO1 expression levels at either the RNA or protein levels following treatment with the ATPase inhibitors and with the degrader JQ-dS-4 for a 48-hour timeframe will better clarify how targeting mSWI/SNF influences *FOXO1* expression. Next, because our findings suggest *FOXO1* is regulated at the transcriptional level at its endogenous locus by AU-15330 treatment, we can assess if transduction of H3K27M DMG cell lines with *FOXO1*-overexpression constructs can rescue or partially rescue proliferation deficits under AU-15330 treatment. Altogether these results nominate FOXO1 as a novel dependency in H3K27M DMGs that can be modulated through targeting of mSWI/SNF and support the findings of two recently

published projects highlighting mSWI/SNF as a promising therapeutic approach for a universally fatal pediatric cancer.

5.4 Redistribution of chromatin marks in H3G34-mutant pediatric gliomas reveals a therapeutic vulnerability to JAK/STAT pathway inhibition

5.4.1 Recurrent histone 3 glycine 34 mutations occur in cortical gliomas in adolescents and young adults

Histone mutations occur in approximately half of pediatric high-grade gliomas (HGGs) (Mackay et al., 2017). While the histone H3 lysine 27-to-methionine (H3K27M) mutations comprise the majority of histone mutations, arginine and valine substitutions in H3 glycine 34 (H3G34R/V) are present in greater than 5% of all pediatric HGGs (Mackay et al., 2017). In contrast to the midline distribution of H3K27M gliomas, H3G34R/V tumors are found almost exclusively in cortical hemispheres (Mackay et al., 2017; Sturm et al., 2012). Additionally, H3G34R/V tumors are associated with a later age at diagnosis (median age of 15 years) than H3K27M tumors (7.8 years), suggesting that each histone mutation requires a specific spatiotemporal window to promote oncogenicity. While H3G34R/V gliomas have a better prognosis that H3K27M tumors, the median survival time is only 18 months, underscoring the need for improved treatments in this class of disease.

In gliomas, mutations affecting H3G34 occur exclusively in the histone variant *H3-3A*, encoding H3.3, which can be incorporated into chromatin in a replication-independent manner (Ahmad & Henikoff, 2002). Additionally, unlike lysine 27, the mutated glycine residue is not a known site of post-translational modification. H3G34 nevertheless plays a critical, but still poorly

understood, role in post-translational modification of the nearby lysine 36 residue. Early studies demonstrated that H3G34R/V mutations decrease the activity of SETD2, a specific lysine 36 (H3K36) trimethyltransferase (Lewis et al., 2013), and subsequent work demonstrated that the histone mutations impair SETD2 catalytic activity (Fang et al., 2018). Intriguingly, loss-of-function of SETD2 itself is also implicated in hemispheric high-grade gliomas (Fontebasso et al., 2013), suggesting a susceptibility of cortical lineages to malignant transformation with H3K36me3 dysregulation.

Nevertheless, H3G34 mutations in gliomas do not result in depletion of global H3K36me3 as SETD2 loss-of-function does. Instead, follow up work has revealed that mutations result in a redistribution of the H3K36me3 landscape (Bjerke et al., 2013), with gains of H3K36me3 at sites enriched for H3.3 deposition due to mutant H3G34 inhibiting the H3K36me3 demethylase KDM4 (Voon et al., 2018). Studies of H3G34 tryptophan (H3G34W) mutations that are observed in bone tumors demonstrated similar dysregulation of H3K36me3 distribution (Siddhant U Jain, Khazaei, et al., 2020; Khazaei et al., 2020). In addition to their histone methylation patterns, H3G34R/V display distinct DNA methylation landscapes, demonstrating hypomethylation in comparison with histone wildtype (WT) and H3K27M pediatric gliomas (Sturm et al., 2012).

To investigate the impact of H3G34 high-grade glioma mutations on epigenetic and transcriptomic cell states and identify potential therapeutic vulnerabilities, Dr. Chan Chung, a postdoctoral fellow in the Venneti Lab at the time, generated isogenic models in mouse neural stem cells (mNSC) with a deletion of the tumor suppressor-encoding *Ink4a/Arf* locus. These cells

stably integrated expression vectors with human coding sequences for either wildtype H3.3 (H3.3WT) or for G34R mutant H3.3 (H3.3G34R). Dr. Chung and Dr. Stefan Sweha, a graduate student at the time, prepared samples of these isogenic models for RNA-sequencing (RNA-seq), DNA methylation profiling by enhanced reduced representation bisulfite sequencing (ERRBS), and chromatin immunoprecipitation with high-throughput sequencing (ChIP-seq) for several histone marks including H3K36me3. Together, we then integrated these transcriptomic and epigenomic datasets to identify crucial targets regulated by the H3.3G34R mutation.

5.4.2 Consistent with prior work, H3.3G34R alters H3K36me3 distribution, increasing deposition in gene bodies.

Spike-in normalized H3K36me3 ChIP-seq of the isogenic model demonstrated a slight decrease in average signal when assessed across the genome. Comparing signal between the isogenic pair of H3WT and H3G34R mNSCs, there was a linear trend in per-site methylation with a 95% slope confidence interval of 0.8456-0.8581 for H3G34R/H3WT signal (Figure 5.5A). Despite an overall trend of less H3K36me3, signal in H3G34R models was enriched at gene bodies, consistent with prior findings (Figure 5.5B).

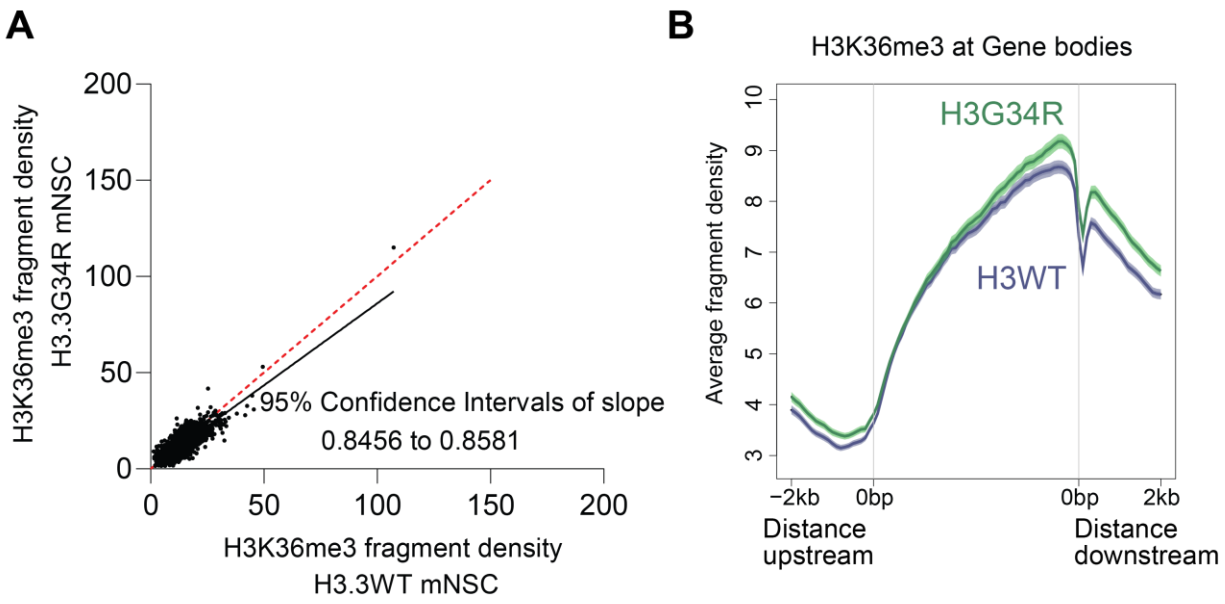

Figure 5.5: The H3G34R mutation redistributes H3K36me3 deposition in an isogenic model.

A. Scatter plot displaying H3K36me3 fragment density at peaks called across the genome for H3.3WT-overexpressing mNSCs (x-axis) and H3.3G34R-overexpressing mNSCs (y-axis).
B. Composite plot of H3K36me3 deposition at H3.3WT (purple) or H3.3G34R (green) mNSCs.

5.4.3 Integration of H3K36me3 ChIP-seq with RNA-seq highlights elevated Lif levels

As H3K36me3 is a mark of actively transcribed exons (Kolasinska-Zwierz et al., 2009), we conducted parallel RNA-seq experiments in the isogenic lines to identify relationships between epigenomic remodeling and gene expression. Hallmark pathway analysis of upregulated genes in H3G34R-mutant mNSCs highlighted several inflammatory pathways including the IL-6/JAK/STAT pathway (Figure 5.6A). Integration of H3K36me3 ChIP-seq and RNA-seq data revealed a subset of genes with striking increases in both H3K36me3 and expression, including the IL-6 class member leukemia inhibitory factor (*Lif*) (Figure 5.6B). Examination of the Lif locus demonstrated enrichment of H3K27ac, elevated levels of the active promoter mark H3K4me3, and DNA hypomethylation at the promoter in H3G34R mutants compared to H3WT mNSCs (Figure 5.6C).

Together these findings highlighted Lif-mediated JAK/STAT signaling as a potential consequence of the H3G34R epigenomic landscape. Dr. Sweha's analysis of published data (Khazaei et al., 2020) demonstrated that Lif expression depends on H3G34 mutant expression as knockdown of the H3G34W mutation in a bone tumor model or knock-in of the WT H3 allele both dramatically reduce LIF expression. Additionally, knockdown of H3-3A in the patient-derived G34V cell line KNS42 results in reduced LIF levels in supernatant, and immunostaining of tumor tissues highlighted elevated STAT activation in H3G34-mutant gliomas compared to H3WT. Lastly, Dr. Sweha showed the STAT3 inhibitors Stattic and WP1066 were specifically toxic to H3G34R/V cells compared to H3WT and H3K27M cells, and they improved survival in two separate tumor models in mice.

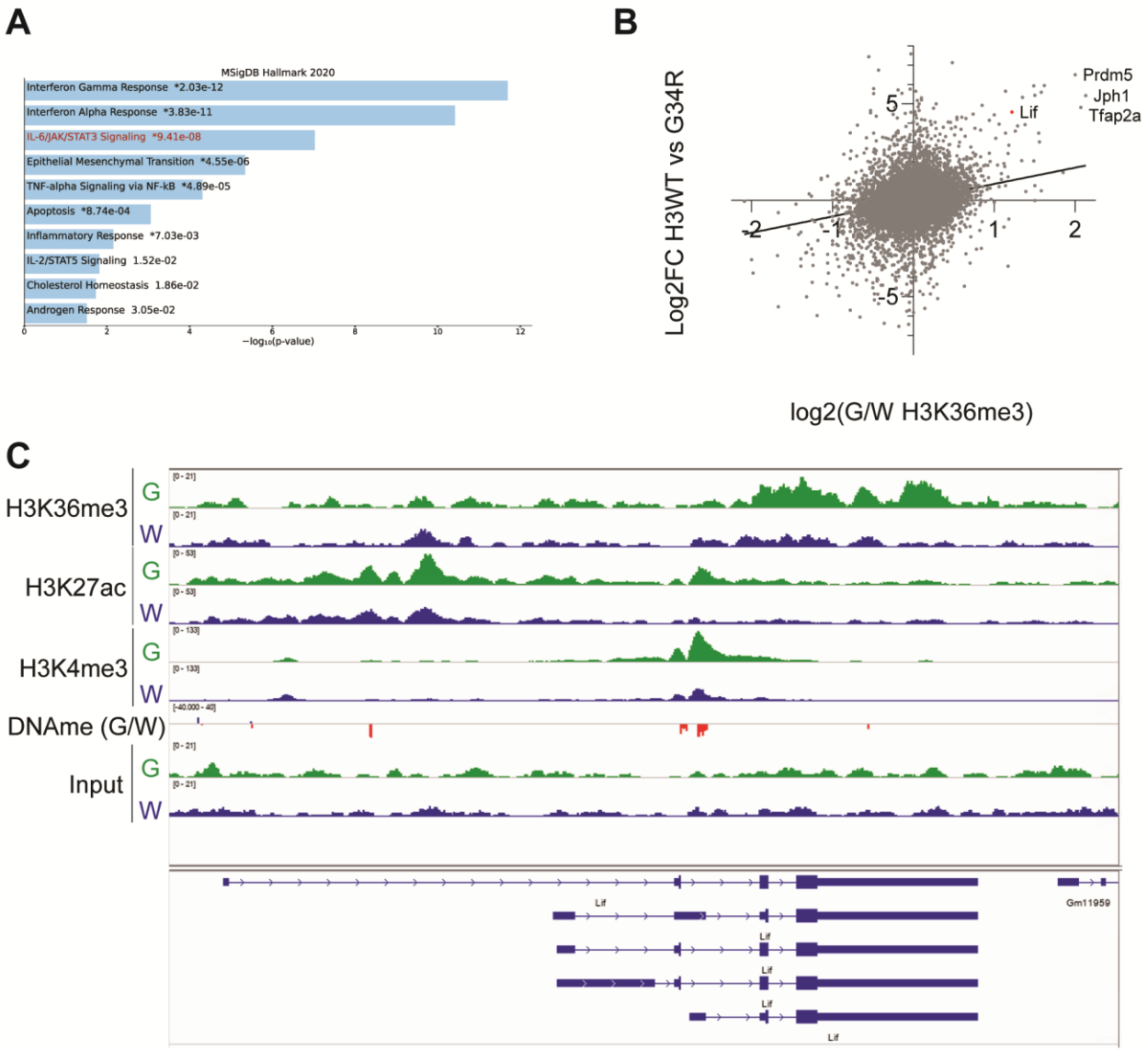

Figure 5.6: Integrated epigenomic and transcriptomic profiling of H3G34R-expressing mNSCs support Lif activation as a potential targetable alteration.

A. Pathway analysis of genes upregulated in H3G34R-expressing mNSCs vs. H3WT mNSCs.
B. Scatter plot comparing changes in H3K36me3 levels in H3G34R mNSCs vs. H3WT mNSCs (x-axis) and changes in expression (G34R/WT, y-axis) with a best-fit line.
C. Integrative genomics viewer tracks at the *Lif* locus of, from top-to bottom, H3K36me3, H3K27ac, H3K4me3, the ratio of DNA methylation (DNAme) in H3G34R to H3WT mNSCs, and inputs for H3G34R mNSCs (G, green) and H3WT mNSCs (W, blue).

5.4.4 Discussion

H3G34 mutations occur in greater than five percent of pediatric high-grade gliomas, and treatments are lacking for this class of tumor. Our epigenomic and transcriptomic profiling of this histone mutation enabled the discovery of a targetable pathway unique to H3G34-mutant tumors. H3G34R-expressing mNSCs demonstrate redistribution of H3K36me3. Among the H3K36me3-altered genes was the JAK/STAT pathway mediator Lif. Dr. Sweha's downstream experiments elegantly highlighted how JAK/STAT signaling is dependent on expression of the histone mutation and how the pathway's inhibition represents a unique vulnerability for these tumors.

These findings support a promising therapeutic strategy for a tumor with limited treatment options. They also suggest intriguing follow-up experiments to more clearly dissect how the H3G34 mutations influence Lif expression. First, repeating the transduction of H3G34R and H3WT overexpression vectors into mNSCs lacking the H3K36 methyltransferase SETD2 could test whether Lif activation is indeed dependent on H3K36me3 deposition. Additionally, SETD2 knockdown experiments in the already transduced mNSCs could allow for determination of whether continued H3K36 methylation is necessary for maintenance of Lif expression.

While H3K36me3 may be necessary maintenance of Lif expression, an alternative mechanism is that expression may require the DNA hypomethylation we observed. This hypomethylation phenotype mirrors what has been observed in other models (Sangatsuda et al., 2020). H3K36 methylation has been observed as necessary for the DNA methylation mediated by DNA methyltransferase 3 alpha (DNMT3A) (Yano et al., 2022). It is possible that H3G34-mutant

histones affect the interactions between H3K36-methylated histones and DNMT3A. Parallel ChIP-seq experiments probing the genome-wide occupancy of Dnmt3a and our HA-tagged H3.3G34R protein in mNSCs could further clarify whether their localizations are mutually exclusive or overlapping. Furthermore, targeting Dnmt3a activity to the *Lif* promoter using a catalytically inactive Cas9 (dCas9) could rescue DNA methylation levels to H3WT levels and enable observation of how DNA methylation contributes to Lif expression.

Overall, this epigenomic-transcriptomic approach to understanding the tumorigenic role of the H3G34 family of mutations has supported investigation of a novel therapeutic strategy and provides the framework for understanding how reshaping of the chromatin landscape alters transcriptional programs.

Note: A portion of this chapter section has been adapted from work previously published in *Science Translational Medicine* (Sweha et al., 2021). Per the journal's copyright policy, I retain the right to include the work in a dissertation.

5.5 *PTEN* haploinsufficiency may drive metabolic-epigenomic rewiring of mIDH1 astrocytomas to promote a more aggressive G-CIMP-low phenotype

5.5.1 Copy number loss of PTEN segregates with DNA methylation status in mIDH1 astrocytoma

Gain-of-function mutations in isocitrate dehydrogenase 1 (IDH1) are found in the majority of low-grade gliomas in adults (Brat et al., 2015). Whereas wildtype IDH1 (wtIDH1) is responsible for the catalyzing the oxidative decarboxylation of isocitrate to alpha-ketoglutarate (α-KG),

mutant IDH1 (mIDH1) has the capacity to further metabolize α-KG into D-2-hydroxyglutarate (D2HG) (L. Dang et al., 2009). D2HG, in turn, competitively inhibits critical α-KG-dependent epigenetic regulators, most importantly dioxygenases that are responsible for demethylation of histone and DNA residues. Due to inhibition of these demethylating pathways, tumors with high levels of D2HG subsequently exhibit hypermethylation patterns (Lu et al., 2012; Turcan et al., 2012). DNA methylation occurs throughout the genome at sites where cytosines are followed by guanines (CpGs) and the methylation status of a region has implications on trans-factor binding and transcriptional regulation (Newell-Price et al., 2000; J. Smith et al., 2020). In gliomas, mIDH1 is strongly associated with a hypermethylated DNA landscape, termed the glioma-CpG island methylation phenotype (G-CIMP) (Noushmehr et al., 2010). With larger cohorts of gliomas to sequence, it became evident that even within mIDH1 astrocytomas, there existed variability in DNA methylation status. When stratified based on high (G-CIMP-high) and low DNA methylation levels (G-CIMP-low), a striking decrease in survival could be seen for G-CIMP-low subtypes (Ceccarelli et al., 2016). Moreover, these analyses highlighted cases of G-CIMP-high progressing to G-CIMP-low status at time of recurrence. Dr. Drew Pratt, a pathologist and former research fellow in the Venneti Lab identified single allele deletion of the tumor suppressor phosphatase and tensin homolog (*PTEN*) as one of the most common alterations in G-CIMP-low compared to G-CIMP-high tumors using the cohort from Ceccarelli et al.

5.5.2 PTEN is a critical regulator of growth signaling and its loss can shunt carbon away from the TCA cycle

PTEN is a phosphatase that negatively regulates the phosphoinositide 3-kinase (PI3K)–AKT–mammalian target of rapamycin (mTOR) signaling pathway, and its mutation or deletion is observed across a wide range of tumors, including glioblastoma (Di Cristofano et al., 1998; Podsypanina et al., 1999; A. Suzuki et al., 1998). Moreover, whereas the classic tumor suppressor model involves bi-allelic loss of function to inactivate both copies of the gene, data across multiple models demonstrate that haploinsufficiency of *PTEN* has pro-tumorigenic consequences in certain contexts (Alimonti et al., 2010; Di Cristofano et al., 1999, 2001). Thus, there is convincing precedent that monoallelic PTEN loss can have substantial impact on tumorigenicity. Additionally, the PI3K-AKT-mTOR signaling pathway has substantial metabolic impacts, including enhancement of glycolysis with shunting of glucose away from mitochondrial metabolism (Lien et al., 2016). Therefore, dysregulation of the PI3K-AKT-mTOR signaling may reduce capacity to produce D2HG.

5.5.3 Orthologous approaches across species demonstrate PTEN reduction enhances tumor growth and reduces D2HG levels

James Haggerty-Skeans, a graduate student in the Venneti Lab, has taken two orthologous approaches to modeling partial loss of PTEN in order to understand its potential role in G-CIMP-low methylation status. First, he has knocked down PTEN levels in a mIDH1 cell line, TB-096, using short-hairpin RNAs (shRNAs) targeting *PTEN* to achieve partial reduction mimicking haploinsufficiency. These tumors exhibit enhanced proliferation, hyperactivation of the PI3K-AKT-mTOR signaling pathway, and reduced levels of D2HG, supporting the hypothesis that PTEN haploinsufficiency contributes to G-CIMP-low/high status.

Second, he has utilized a black 6 mouse model with heterozygous deleterious mutation of *PTEN* ($PTEN^{+/-}$) (A. Suzuki et al., 1998). In this mouse model, he has performed in-utero electroporation (IUE) to introduce multiple tumor-promoting vectors into the developing brains of fetal mice. Mice receive vectors expressing R132H *mIDH1*, the growth-factor-encoding *PDGFRA* with an activating mutation (PB-CAG-PdgfraD824V-Ires-EGFP), and a dominant negative version of the tumor suppressor *TP53* (PB-CAG-DNp53-Ires-luciferase) to promote tumor formation. Compared to tumors developed in a control mouse strain with WT PTEN, tumors from $PTEN^{+/-}$ mice display more aggressive tumors (median survival time of 32 vs. 92 days). James has additionally developed cell lines from tumors derived from both WT and $PTEN^{+/-}$ mice. In these models, he finds a similar reduction in D2HG as measured by mass spectroscopy, enhanced Akt pathway activation, and maintenance of the more aggressive phenotype when transplanted back into WT PTEN mouse brains compared to WT PTEN cell lines (mean survival 36 vs. 72 days). Additionally, *in vitro* experiments with these cell lines show enhanced proliferation responses of $PTEN^{+/-}$ cells to inhibition of the PI3K-AKT pathway via paxalisib.

Due to the observed phenotypes in growth and D2HG production, James prepared RNA-sequencing (RNA-seq) samples for both his human and mouse tumor-derived cell lines to dissect the transcriptional consequences of PTEN reduction in mIDH1 astrocytomas.

5.5.4 PTEN reduction results in durable transcriptional changes in both models

While mIDH1 expression results in prompt accumulation of D2HG, the subsequent effects on methylation are not immediate upon introduction (Turcan et al., 2012). We therefore investigated

transcriptional differences in the human mIDH1 cell line TB-096 +/- shPTEN or in the mouse-derived $PTEN^{WT}$ vs. $PTEN^{+/-}$ mIDH1 tumor cells across a wide range of passages. In both models, samples clustered primarily by PTEN status, and changes across passages were minimal (Figure 5.7).

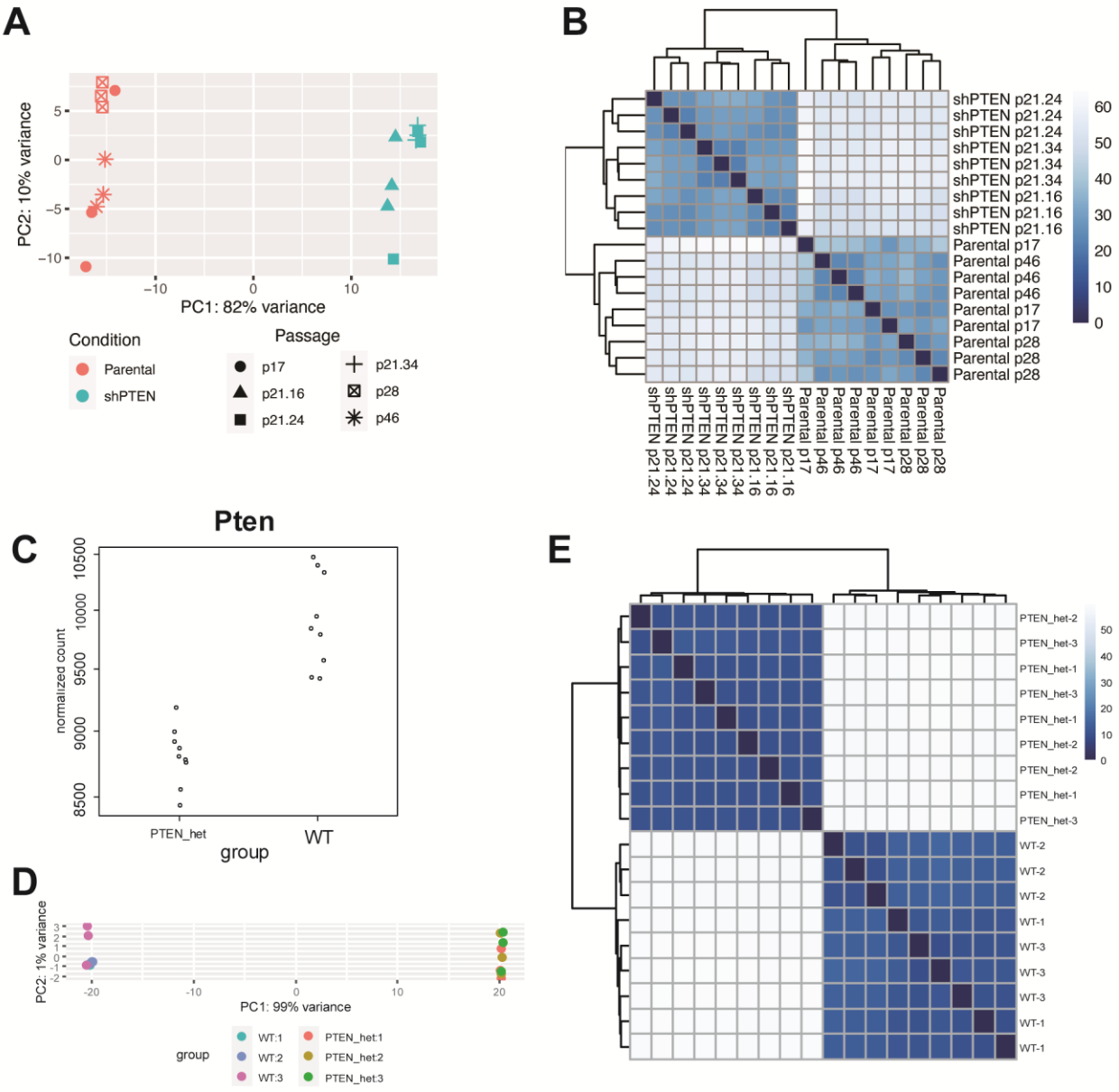

Figure 5.7: PTEN knockdown in mIDH1 cell lines or mIDH1 tumor development in a PTEN heterozygous background produce strong transcriptional changes.

A. Principal component analysis (PCA) of TB-096 cells with or without PTEN knockdown across 3 separate passages per condition.
B. Hierarchical clustering of TB-096 samples with or without PTEN knockdown from **A**.
C. *Pten* RNA levels (normalized counts, y-axis) in cell lines derived from mIDH1 tumors developed in mice with a heterozygous or WT *Pten* status
D. PCA of mIDH1 tumor-derived cells from WT or *Pten* heterozygous mice.
E. Hierarchical clustering of samples WT and *Pten* heterozygous mIDH1 samples from **D**.

5.5.5 Reduction in PTEN results in upregulation of genes with H3K27me3-marked high-CpG promoters in neural progenitor cells

Given the striking transcriptional changes induced by PTEN haploinsufficiency, we next employed gene set enrichment analysis (GSEA) to assess if any gene sets were significantly enriched in upregulated or downregulated genes. In both models, genes upregulated with PTEN loss were significantly enriched for a series of gene sets associated with high-CpG promoters (HCP) (Figure 5.8). More specifically, one of the top gene sets associated with both models was Mikkelsen et al.'s H3K27me3-marked HCP sites in neural progenitor cells (NPCs) (Mikkelsen et al., 2007).

CpG islands in promoters are critical regions of transcriptional regulation, and high levels of either DNA methylation and H3K27me3 are each often associated with transcriptional repression at HCP promoters (Deaton & Bird, 2011). While DNA methylation is associated with more stable patterns of silencing, H3K27me3 may be more easily reversible (Deaton & Bird, 2011). In contrast to low CpG promoter genes, genes with HCP include housekeeping genes and genes that are tightly regulated in embryonic development. On the other hand, H3K27me3 status often marks genes that are silenced in a lineage or are poised for potential upregulation in a "bivalent" state containing H3K4me3—a mark seen at actively transcribed promoters—as well. The convergence of PTEN loss upregulating HCP genes characterized in this NPC lineage suggests a fascinating potential reshaping of the epigenomic landscape mediated by PTEN and is being explored further with ongoing DNA methylation studies.

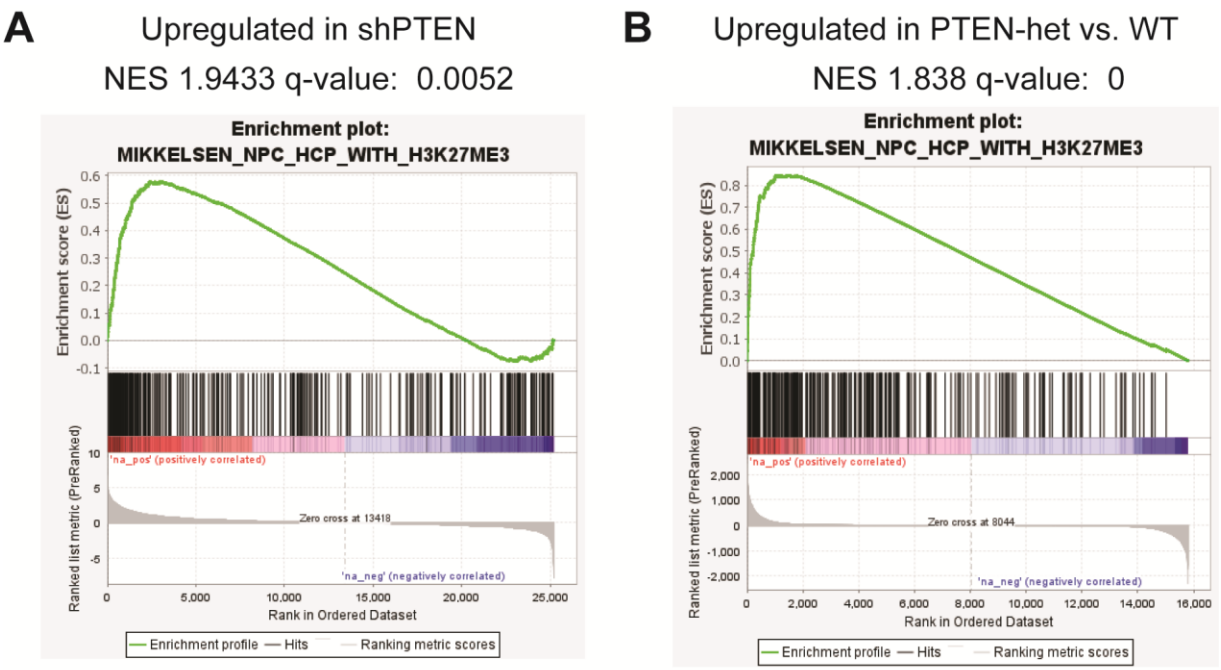

Figure 5.8: Upregulation of neural progenitor high-CpG island promoter gene sets with PTEN loss.

A Gene-set enrichment analysis (GSEA) of genes upregulated with shPTEN in TB-096 for the Mikkelsen curated neural progenitor cells (NPCs) with high-density CpG promoters and elevated H3K27me3.
B Gene-set enrichment analysis (GSEA) of genes upregulated with Pten-heterozygous mutation for the Mikkelsen curated neural progenitor cells (NPCs) with high-density CpG promoters and elevated H3K27me3.

5.5.6 Transcriptional analysis further identifies dampened immune signatures as a critical consequence of PTEN modulation

We next explored the genes that were significantly downregulated with either PTEN KD or heterozygous deletion in mIDH1 tumor models. In TB-096 cells with PTEN KD, immune gene sets including inflammatory response, IL-6/JAK/STAT3 signaling and interferon gamma response were all diminished (Figure 5.9A). Parallel analysis in the IUE generated $PTEN^{WT}$ vs. $PTEN^{+/-}$ mIDH1 cells showed similar but even stronger downregulation of immune pathways, again with enrichment for IL-6/JAK/STAT3 signaling and interferon gamma response (Figure 5.9B). James has followed up on these initial studies by profiling secreted cytokines in mIDH1 $PTEN^{+/-}$ cells and demonstrated decreased levels of several immune-related factors, including CCL2-5, CXCL1-2, and IL-6 in cells bearing hemizygous PTEN deletions. Interestingly, the only chemokine that was more abundant in $PTEN^{+/-}$ mIDH1 cells was CXCL12. James is currently working to replicate these findings in TB-096 cells +/- shPTEN.

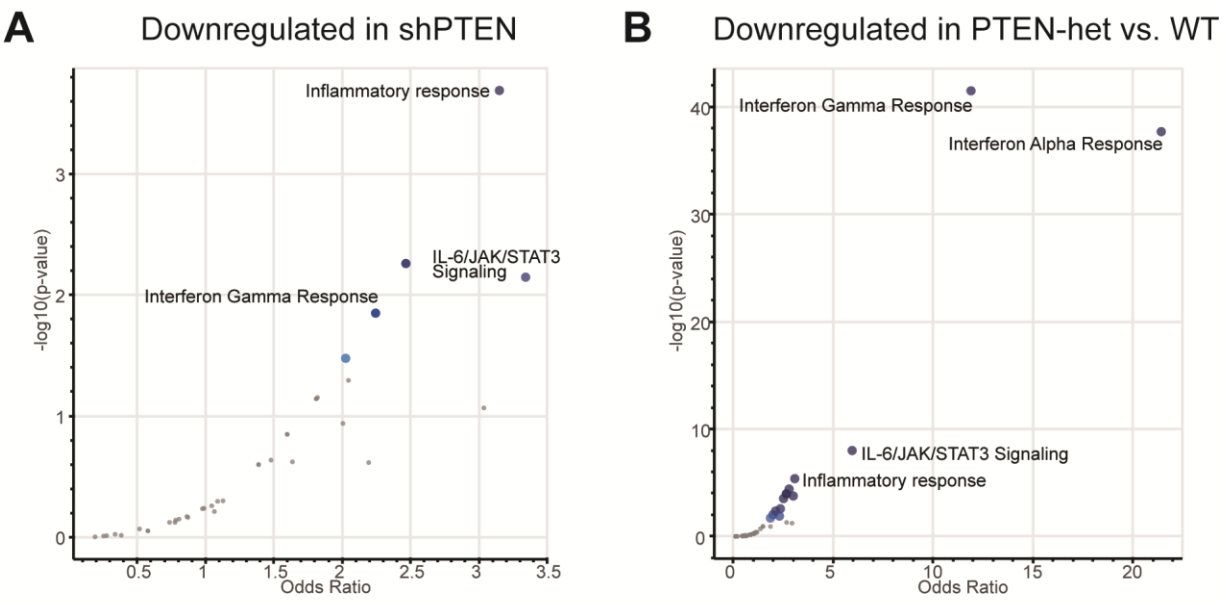

Figure 5.9: PTEN levels lead to dysregulation of immune response pathways.

A. Pathway analysis of genes downregulated in TB-096 cells with PTEN knockdown.
B. Pathway analysis of genes downregulated in mIDH1 mouse-derived tumor cells with WT or $PTEN^{+/-}$ backgrounds.

5.5.7 Discussion

G-CIMP-high vs. low status is a critical prognostic indicator for mIDH1 astrocytomas, but the underlying biology driving these changes remains unclear. Monoallelic *PTEN* loss can enhance tumorigenicity, and analysis of large mIDH1 cohorts demonstrate its strong association with G-CIMP-low tumors. Through its regulation of the PI3K-AKT-mTOR signaling pathway, dysregulation of PTEN can have substantial influences on tumor cell metabolism and signaling. Data from Venneti lab MD-PhD student James Haggerty-Skeans demonstrate that PTEN reduction enhances mIDH1 tumor cell growth *in vitro* and *in vivo* in multiple models. Moreover, metabolically, decreased PTEN levels result in diminished levels of the oncometabolite D2HG.

Assessment of the transcriptional consequences of reduced PTEN reveal fascinating changes that lay the groundwork for further discovery. First, PTEN reduction is associated with activation of high-CpG promoter genes that are likely under tight regulation in neural lineages. This finding supports a working model where PTEN enhances glycolysis, with its reduction diverting carbons away from the TCA cycle and therefore D2HG production. Reduced D2HG, in turn, limits the suppression of DNA demethylation via ten eleven translocation (TET) dioxygenases and of histone lysine demethylases. Finally, reduction of DNA hypermethylation by now-uninhibited TET enzymes may permit expression of potentially tumorigenic genes that had been silenced by G-CIMP-associated methylation. Ongoing work using bisulfite sequencing to assess DNA methylation status in James' models will elucidate whether the observed transcriptional changes are indeed associated with changes in DNA methylation. Additionally, isotope-labelled tracing of glucose carbons in $PTEN^{WT}$ vs. $PTEN^{+/-}$ mIDH1 cells will lend further support to the role PTEN plays in influencing D2HG production.

Second, both models of PTEN loss exhibited significant downregulation of immune gene sets with a particular focus on IL-6 and interferon pathways. These changes were validated by measurement of cytokine production in James' models and may inform therapeutic approaches targeting immune pathways in G-CIMP gliomas.

Ongoing studies profiling DNA methylation and histone methylation will provide a fuller picture of whether epigenomic remodeling is driving these transcriptional changes. Furthermore, comparison of the epigenomic signatures of reduced PTEN cell models can then be compared with the G-CIMP-low and -high signatures to validate whether the experimental models recapitulate the changes observed in patient cohorts.

5.6 Dissecting the metabolic and transcriptional nodes of ZFTA-fusion positive supratentorial ependymomas

5.6.1 ZFTA fusion ependymomas are the major form of supratentorial ependymomas and lack effective therapies

While two thirds of pediatric intracranial ependymomas develop in the posterior fossa, the remaining third are found in supratentorial (ST) regions (Kristian W Pajtler et al., 2015). The vast majority of ST ependymomas in term harbor fusion events between Zinc Finger Translocation Associated (*ZFTA*) and the proto-oncogene *RELA*, which is a transcriptional activator of the NF-kB signaling pathway and is classically associated with many tumor types. Additionally, molecular profiling of ST ependymomas has revealed tumors harboring *ZFTA*

fusions with other partners including *NOCA1/2, MAML,* and *MN1* that share molecular characteristics with ZFTA-RELA fusion tumors, suggesting a class of ZFTA-driven ependymomas with shared epigenetic features (Tamai et al., 2021; Tauziède-Espariat et al., 2021; Tomomasa et al., 2021; Zheng et al., 2021; Zschernack et al., 2021). Moreover, multiple groups have modeled ZFTA fusions and demonstrated that ZFTA fusions interact with a variety of chromatin modifiers and activate tumorigenic transcriptional proteins, independent of classic RELA transcriptional programs. Ependymomas are resistant to conventional therapeutic approaches, and to date, no targeted molecular therapies are approved for treatment (Zaytseva et al., 2021). Current efforts to target ZFTA-RELA fusion have had minimal success. In the clinical setting, an approach that was focused on the contribution of the RELA subunit by inhibiting the NFkB pathway using the proteosome inhibitor marizomib proceeded to clinical trial (NCT03727841) but was terminated early by the pharmaceutical company. Overall, targeted therapeutic approaches have been limited.

5.6.2 ZFTA-RELA fusion upregulates glutamine metabolism via the Akt pathway

Siva Kumar Natarajan, a graduate student in the Venneti lab, generated an isogenic system to interrogate the ways in which ZFTA-RELA fusion contributes to tumorigenicity, with an interest in identifying metabolic changes induced by the fusion. Using mouse neural stem cells (mNSCs) with a deletion of the tumor suppressor-encoding Ink4a/Arf locus, Siva lentivirally transduced expression vectors to create stable cell lines with expression of the human ZFTA-RELA fusion, ZFTA alone, RELA alone, or an empty vector control. While cells stably expressing the fusion form tumors when transplanted back into mice, the controls do not. He first conducted metabolomics comparing mNSCs with fusion expression to his three controls. In parallel, he

profiled metabolites in human tumor-derived ZFTA fusion cell lines compared to non-fusion ependymoma models. Pathway analysis of the two experiments converged on glutamine and glutathione metabolism, and both models demonstrated that the fusion was associated with higher levels of the glutamine importer SLC1A5 and glutaminase, the enzyme responsible for breaking glutamine down into glutamate for use by the cell. Siva's subsequent analyses demonstrated that the PI3K/Akt pathway, a previously identified regulator of glutaminase expression (Garcia-Cao et al., 2012), was hyperactive in fusion models compared to controls, and moreover, the Akt negative regulator Pten was significantly decreased in fusion models. He confirmed that this difference in PTEN expression translated back to clinical cases through immunohistochemical staining of ST ZFTA RELA fusion tumors compared to normal cortex and non-fusion ST ependymomas.

5.6.3 PTEN reduction in ZFTA-RELA fusion models occurs in part at the transcriptional level

To better elucidate the mechanism of PTEN regulation, we explored published RNA-sequencing (RNA-seq) data shared by the collaborating lab of Dr. Richard Gilbertson. In a similar isogenic model of ZFTA-RELA overexpression in mouse neural stem cells, we assessed *Pten* transcript levels in cells with the fusion compared to control cells and saw *Pten* levels are in fact significantly, though modestly, decreased at the RNA level (Figure 5.10A). Furthermore, we leveraged gene expression data from the Gilbertson group that included models with deletion mutant forms of the ZFTA-RELA fusion protein. Specifically, the Gilbertson lab had conducted RNA-seq on cells overexpressing a full-length ZFTA-RELA fusion, a fusion with the REL-homology domain (RHD) deleted, a fusion with the ZFTA-derived zinc-finger domains deleted (ZF), and a fusion with the ZFTA-derived trans-activating domain (TAD) deleted. While

expression remained low in the full-length fusion- and the ΔRHD-expressing cells, *PTEN* levels increased significantly in the ZF domain deletion line (Figure 5.10B). Siva has followed-up on these findings investigating the reliance of fusion expressing cells on glutamine metabolism and the PI3K-AKT pathway, and combinatorial therapy targeting both pathways results in striking increases in median survival by greater than 30% for both approaches.

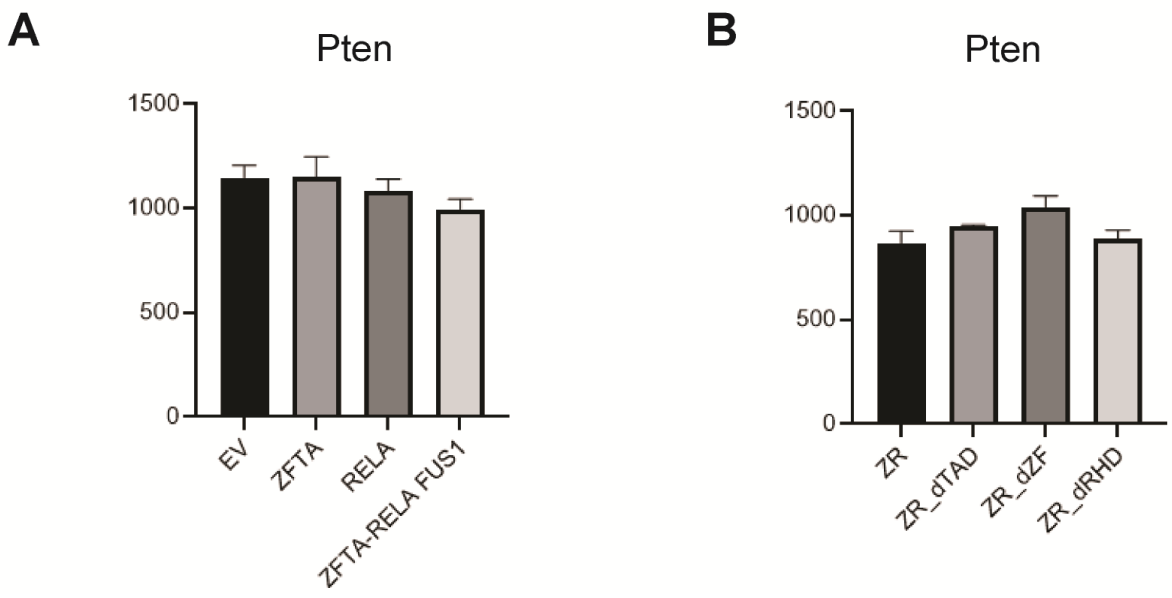

Figure 5.10: ZFTA-RELA fusion results in small but significant reduction of the tumor suppressor Pten.

A. Normalized expression levels (y-axis) of mouse neural stem cells (mNSCs) transduced with an empty vector (EV) or vectors expressing exogenous ZFTA, RELA, or the ZFTA-RELA fusion.
B. Normalized expression levels (y-axis) of human 293T cells transduced with a full length ZFTA-RELA (ZR) fusion expression vector, or vectors with deletion of critical domains: dTAD = Trans-activation domain deletion, dZF = Zinc-finger domain deletion, dRHD = Rel homology domain deletion.

5.6.4 The TCA cycle-derived metabolite itaconate is uniquely found in ZFTA fusion models

In addition to the upregulation of glutamine metabolism, Siva found that the greatest change in abundance for any metabolite was increased levels of itaconate in the ZFTA-RELA fusion overexpressing cell line. Itaconate is a metabolite largely restricted to immune cells such as macrophages (O'Neill & Artyomov, 2019) and has been characterized to exhibit an anti-inflammatory effect. Therefore, it may contribute to immune evasion in ZFTA-fusion ST ependymomas. To identify how itaconate was produced, Siva assessed his isogenic model and found that its best characterized source, the metabolic enzyme aconitate decarboxylase 1 (Acod1)/immunoresponsive gene 1 (Irg1) is expressed only in ZFTA-RELA fusion-expressing cells and not empty vector controls. Furthermore, ZFTA-RELA fusion expression is required for its expression as shRNAs targeting the fusion result in reduced Irg1 levels. Additionally, Irg1 is known to modulate cellular response to oxidative stress via alkylation of Keap1. Alkylation of Keap1 in turn results in release of Nrf2 and activation of an oxidative stress program. Siva found that shRNAs targeted to Irg1 can reverse this phenotype in ZFTA-RELA fusion cells, resulting in reduced levels of Nrf2 targets. Altogether Siva's findings uncover a metabolic pathway uniquely upregulated in ZFTA-RELA fusion cells with implications for immune modulation and oxidative stress resistance.

5.6.5 Multi-pronged approaches to dissect the impact of itaconate on ZFTA-RELA fusion driven biology in ST ependymomas

In collaboration with Dr. Abhjit Parolia and Dr. Eleanor Young at the Michigan Center for Translational Pathology (MCTP), directed by Dr. Arul Chinnaiyan, we conducted RNA-seq on our mNSC models of ZFTA-RELA fusion ependymoma in order to better understand the impact

of itaconate. We included in the experiment mNSCs with the empty vector as a control, mNSCs expressing the fusion (ZR mNSCs), ZR mNSCs with Irg1 KD (shIRG1 ZR mNSCs), and ZR mNSCs treated with the IRG1 inhibitor citraconate (ZR^{cit} mNSCs) (F. Chen et al., 2022) (Figure 5.11). We aimed to uncover what transcriptional changes induced by the ZFTA-RELA fusion vector are mediated by IRG1/itaconate.

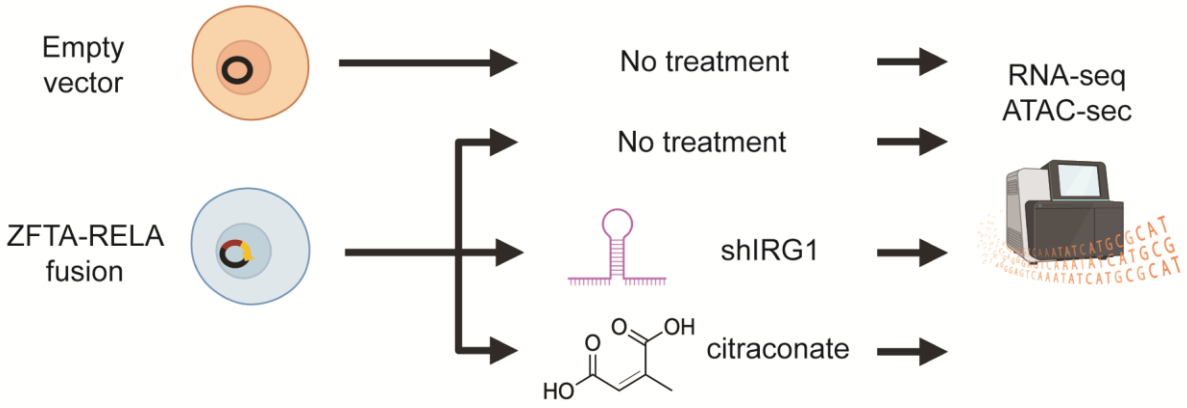

Figure 5.11: Experimental design investigating the transcriptional and epigenetic effects of the ZFTA-RELA fusion expression.

Mouse neural stem cells (mNSCs) harboring an empty vector or a ZFTA-RELA (ZR) fusion overexpression vector were profiled with RNA sequencing (RNA-seq) and assay for transposase accessible chromatin with sequencing (ATAC-seq). Additionally, the ZR target gene *Irg1* was knocked down by short-hairpin RNA in ZR fusion cells or the ZR fusion cells were treated with the Irg1 inhibitor citraconate. These cells were profiled in parallel.

5.6.6 ZFTA-RELA fusion cells upregulate immune response and PI3K/Akt pathways

First, we assessed the baseline changes associated with the ZFTA-RELA fusion. Consistent with prior studies (Arabzade et al., 2021; Kupp et al., 2021; Zheng et al., 2021), fusion expression resulted in a substantially altered transcriptome with approximately 2000 differentially regulated genes in each direction (Figure 5.12A). We conducted pathway analysis of up- and down-regulated genes using three sets of pathways in parallel: Hallmark, KEGG, and GO_BP. Compared to an empty vector control, ZFTA-RELA fusion mNSCs exhibited upregulation of NF-kB and TNF signaling consistent with prior studies (Figure 5.12C). In addition, these cells overexpressed genes involved in PI3K-Akt signaling, consistent with the upregulation observed in this study, and notably, upregulated genes were also enriched for interferon and cytokine signaling pathways (Figure 5.12E). In contrast, downregulated pathways included glycolysis—consistent with the cells' increased reliance on glutamine—and a number of pathways in neurogenesis and axon development (Figure 5.12B and D).

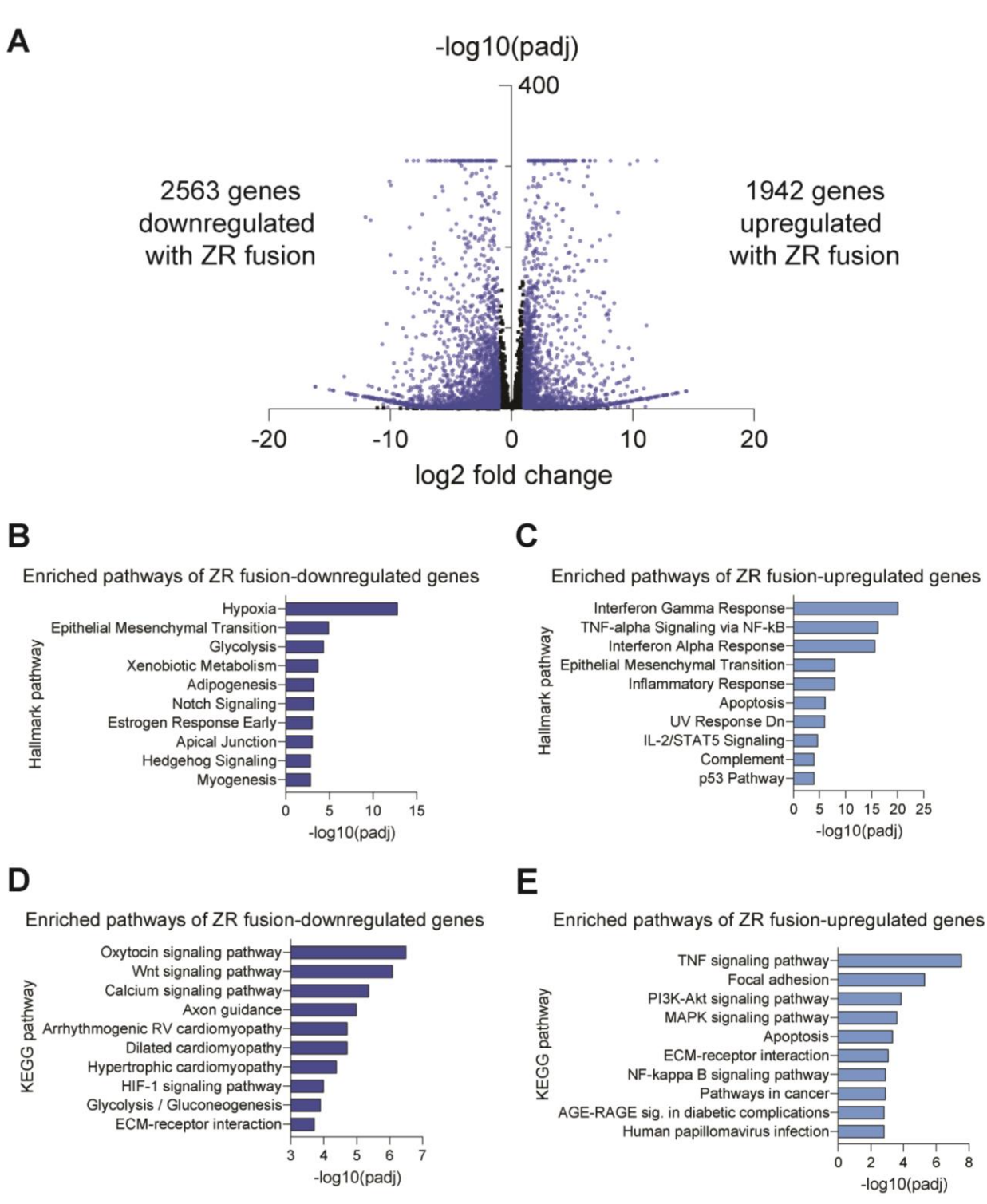

Figure 5.12: The ZFTA-RELA fusion isogenic model recapitulates known activation of NF-kB pathways and lends support for activation of PI3K-Akt pathway.

A. Volcano plot showing differentially expressed genes (blue) for empty vector mouse neural stem cells (mNSCs) compared to mNSCs with ZFTA-RELA (ZR) fusion overexpression. Log_2 fold changes (x-axis) and $-log_{10}$ transformations of the adjusted p-value (y-axis) for each gene are depicted.
B. Hallmark pathway analysis results for genes with significantly lower expression in ZR fusion mNSCs compared to EV mNSCs. Pathways (y-axis) are ordered by their $-log_{10}$(adjusted p-value) scores (x-axis).
C. Hallmark pathway analysis results for genes with significantly higher expression in ZR fusion mNSCs compared to EV mNSCs. Pathways (y-axis) are ordered by their $-log_{10}$(adjusted p-value) scores (x-axis).
D. Kyoto Encyclopedia of Genes and Genomes (KEGG) pathway analysis results for genes with significantly lower expression in ZR fusion mNSCs compared to EV mNSCs. Pathways (y-axis) are ordered by their $-log_{10}$(adjusted p-value) scores (x-axis).
E. KEGG pathway analysis results for genes with significantly higher expression in ZR fusion mNSCs compared to EV mNSCs. Pathways (y-axis) are ordered by their $-log_{10}$(adjusted p-value) scores (x-axis).

We next asked whether Irg1 KD reversed some of these observed transcriptional changes induced by the fusion. Strikingly, the top upregulated pathways in shIRG1 cells very closely mirrored the most heavily fusion-downregulated pathways relating to nervous system development. Moreover, while glycolysis did not meet significance thresholds for enrichment as a downregulated pathway, shIRG1 induced upregulation of a number of glycolytic enzymes in direct contrast to the fusion vs. EV comparison. On the other hand, Irg1 KD resulted in downregulation of many fusion-driven pathways including NF-kB and Pi3K signaling. Additionally, shIrg1 cells exhibited some downregulation of inflammatory response.

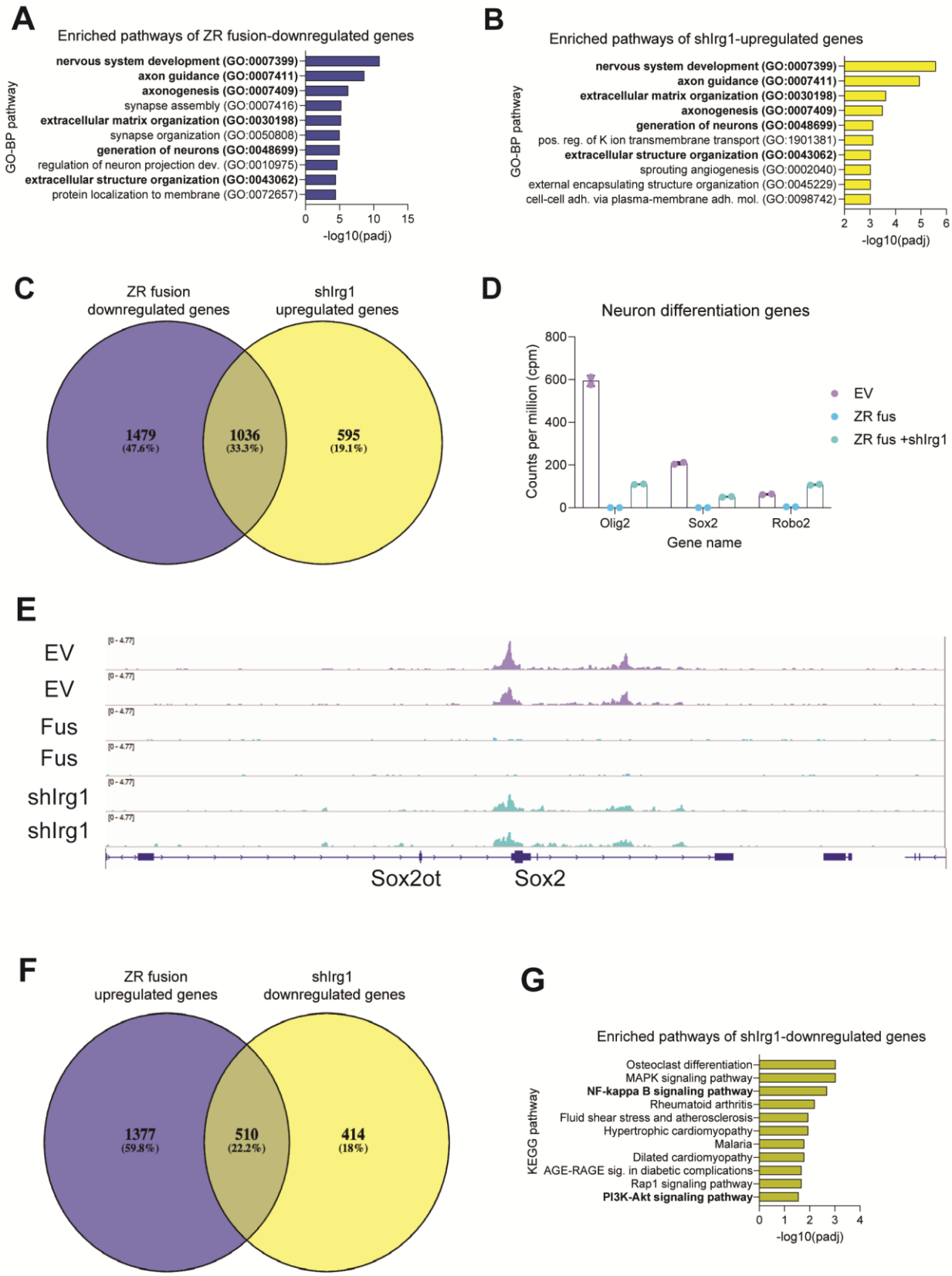
A
Enriched pathways of ZR fusion-downregulated genes
GO-BP pathway
nervous system development (GO:0007399)
axon guidance (GO:0007411)
axonogenesis (GO:0007409)
synapse assembly (GO:0007416)
extracellular matrix organization (GO:0030198)
synapse organization (GO:0050808)
generation of neurons (GO:0048699)
regulation of neuron projection dev. (GO:0010975)
extracellular structure organization (GO:0043062)
protein localization to membrane (GO:0072657)
0 5 10 15
-log10(padj)
B
Enriched pathways of shIrg1-upregulated genes
GO-BP pathway
nervous system development (GO:0007399)
axon guidance (GO:0007411)
extracellular matrix organization (GO:0030198)
axonogenesis (GO:0007409)
generation of neurons (GO:0048699)
pos. reg. of K ion transmembrane transport (GO:1901381)
extracellular structure organization (GO:0043062)
sprouting angiogenesis (GO:0002040)
external encapsulating structure organization (GO:0045229)
cell-cell adh. via plasma-membrane adh. mol. (GO:0098742)
2 3 4 5 6
-log10(padj)
C
ZR fusion downregulated genes
shIrg1 upregulated genes
1479 (47.6%)
1036 (33.3%)
595 (19.1%)
D
Neuron differentiation genes
Counts per million (cpm)
800
600
400
200
0
Olig2
Sox2
Robo2
Gene name
EV
ZR fus
ZR fus +shIrg1
E
EV
EV
Fus
Fus
shIrg1
shIrg1
[0 - 4.77]
Sox2ot
Sox2
F
ZR fusion upregulated genes
shIrg1 downregulated genes
1377 (59.8%)
510 (22.2%)
414 (18%)
G
Enriched pathways of shIrg1-downregulated genes
KEGG pathway
Osteoclast differentiation
MAPK signaling pathway
NF-kappa B signaling pathway
Rheumatoid arthritis
Fluid shear stress and atherosclerosis
Hypertrophic cardiomyopathy
Malaria
Dilated cardiomyopathy
AGE-RAGE sig. in diabetic complications
Rap1 signaling pathway
PI3K-Akt signaling pathway
0 1 2 3 4
-log10(padj)

Figure 5.13: Irg1 knockdown reverses fusion-mediated silencing of neuron differentiation program and upregulation of PI3K-Akt signaling.

A. Pathways (y-axis) enriched in genes downregulated in ZFTA-RELA (ZR) fusion expressing mouse neural stem cells (mNSCs) compared to mNSCs transduced with an empty vector (EV), ranked by a $-\log_{10}$ transformation of the adjusted p-value (x-axis).
B. Pathways (y-axis) enriched in genes upregulated in ZR fusion mNSCs with Irg1 knockdown by shRNA (shIrg1) compared to parental ZR fusion mNSCs, ranked by a $-\log_{10}$ transformation of the adjusted p-value (x-axis).
C. Venn diagram showing overlap of ZR fusion downregulated genes (blue) and shIRG1 upregulated genes (yellow).
D. Expression in counts per million mapped reads (CPM) of a subset of neuronal development genes in EV mNSCs, ZR fusion mNSCs, and ZR fusion shIrg1 mNSCs.
E. Chromatin accessibility as measured by assay for transposase accessible chromatin with sequencing (ATAC-seq) at the Sox2 locus in EV mNSCs, ZR fusion mNSCs, and ZR fusion shIrg1 mNSCs.
F. Venn diagram showing overlap of ZR fusion upregulated genes (blue) and shIRG1 downregulated genes (yellow).
G. Pathways (y-axis) enriched in genes downregulated in ZR fusion shIRG1 mNSCs compared to parental ZR fusion mNSCs, ranked by a $-\log_{10}$ transformation of the adjusted p-value (x-axis).

Lastly, we examined whether citraconate treatment resulted in reversal of fusion-associated transcriptional programs. In a more striking manner than the shIrg1 model, citraconate-treated fusion cells exhibited upregulation of glycolytic enzymes. In contrast to the shIrg1 model, however, citraconate treatment did not reverse the downregulation of neuronal development pathways. In fact, upregulation of PI3K signaling was enriched. The predominant signature, however, was glutathione synthesis, consistent with citraconate's known role as potent inducer of oxidative stress response activation. Downregulated pathways were most strongly enriched for cell cycle regulation but also exhibited evidence of downregulation of interferon pathways.

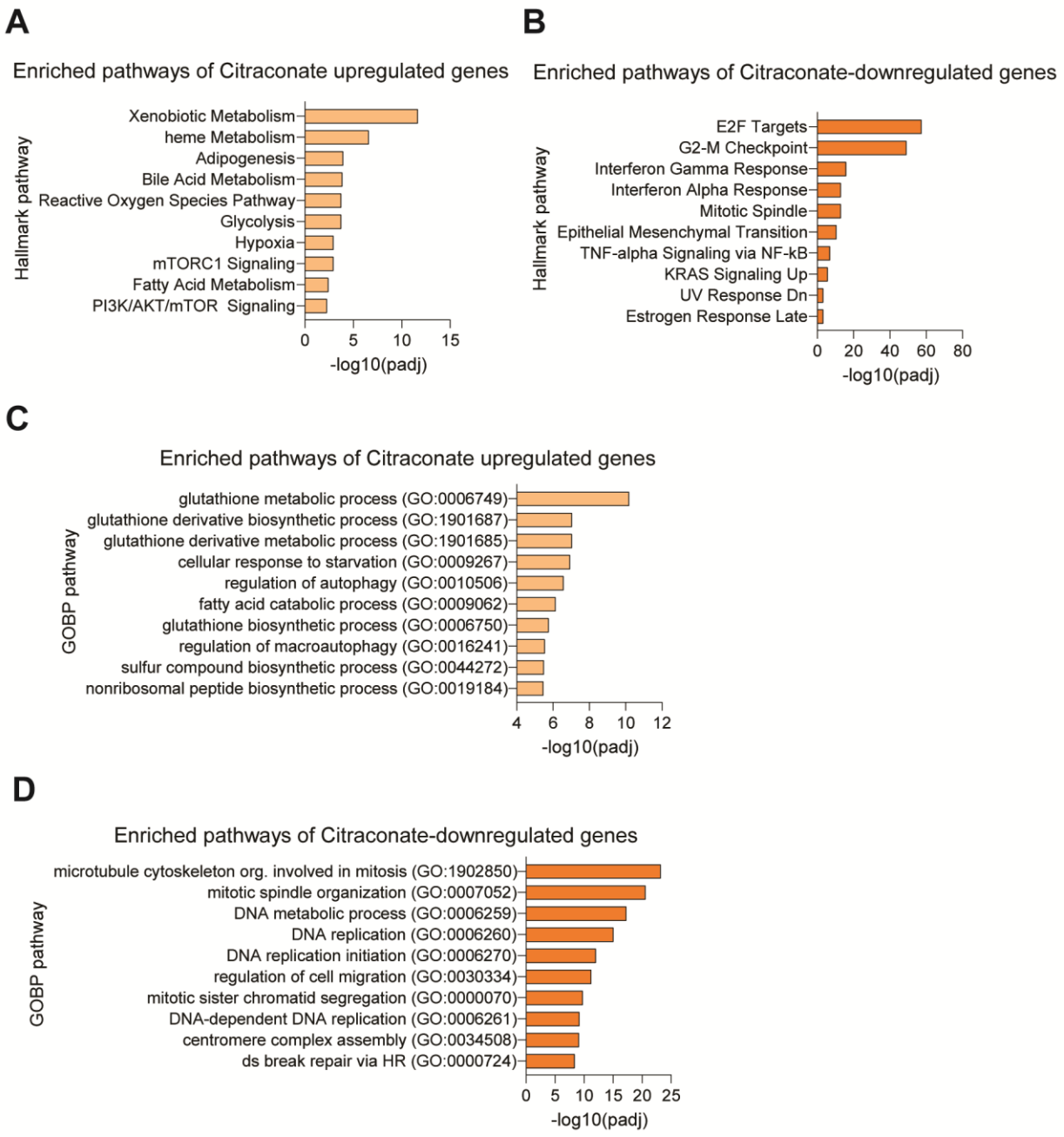

Figure 5.14: Citraconate treatment reverses downregulation of glycolysis and induces glutathione synthesis.

A. Hallmark pathways (y-axis) enriched in genes upregulated in citraconate-treated ZR fusion mNSCs compared to untreated ZR fusion mNSCs, ranked by a -$\log_{10}$ transformation of the adjusted p-value (x-axis).
B. Hallmark pathways (y-axis) enriched in genes downregulated in citraconate-treated ZR fusion mNSCs compared to untreated ZR fusion mNSCs, ranked by a -$\log_{10}$ transformation of the adjusted p-value (x-axis).

C. Gene ontology- biological process (GO-BP) pathways (y-axis) enriched in genes upregulated in citraconate-treated ZR fusion mNSCs compared to untreated ZR fusion mNSCs, ranked by a -$\log_{10}$ transformation of the adjusted p-value (x-axis).
D. GO-BP pathways (y-axis) enriched in genes downregulated in citraconate-treated ZR fusion mNSCs compared to untreated ZR fusion mNSCs, ranked by a -$\log_{10}$ transformation of the adjusted p-value (x-axis).

5.6.7 Discussion

Patients with ST ependymomas have limited therapeutic options. Fusions involving ZFTA occur in the majority of ST ependymomas and exhibit distinct transcriptional programs. Studies performed by Siva Kumar Natarajan have demonstrated that ZFTA-fusion tumors exhibit activation of PI3K-AKT signaling, heightened glutamine metabolism, and production of the macrophage-specific immunomodulatory and stress-response regulating metabolite itaconate.

We utilized published and new RNA-seq data to more deeply investigate the mechanism by which ZFTA fusions support oncogenesis. Our investigation of the transcriptomic consequences of ZFTA-RELA fusion expression showed some evidence for transcriptomic downregulation of *PTEN*, dependent on the zinc-finger domain of ZFTA. These reductions in *PTEN* may not fully account for the levels of protein reduction observed, and post-translational modifications must be considered.

Moreover, our data enabled closer dissection of the role of IRG1 and itaconate in ZFTA-RELA fusion-drive tumors. Knockdown of Irg1 in fusion expressing cells rescues expression of nervous system developmental genes that are downregulated with ZFTA-RELA fusion expression and reduces overexpression of NF-kB and PI3K pathway genes. Treatment with citraconate, an IRG1 inhibitor with additional impacts on the cell, paints a slightly less clear picture but resulted in extreme downregulation of cell cycle pathways and has since been shown by Siva to be effective *in vivo* for treatment of fusion-driven tumors. Citraconate may interact with other enzymes or proteins in the cell and therefore lead to a more nonspecific transcriptional response compared to

targeting Irg1 expression. Modulation of the dose to avoid hyperactivation of an oxidative stress response may allow for a clearer picture upon repeat transcriptome profiling.

5.7 Isogenic modeling of PFA ependymomas recapitulates tumor-informed super enhancer landscapes

5.7.1 Group A posterior fossa (PFA) ependymomas upregulate the TCA cycle

Group A posterior fossa (PFA) ependymomas are characterized by global H3K27 hypomethylation, driven by expression of enhancer of Zeste homologs inhibitory protein (EZHIP) and are associated with poor prognosis. As described in detail in Chapter 2, these tumors share several key characteristics with histone-mutant H3K27M diffuse midline gliomas (DMGs) with regard to chromatin landscapes and transcription. Recent work from the Venneti Lab had implicated DMG H3K27M mutations in metabolic reprogramming, demonstrating that the mutant histone upregulates glycolytic and tricarboxylic acid (TCA) cycle pathways (Chung et al., 2020). Furthermore, these metabolic alterations had downstream effects on chromatin regulators by modulating availability of the TCA cycle product alpha-ketoglutarate (α-KG) (Chung et al., 2020).

In a collaborative effort led by Dr. Pooja Panwalkar, a postdoctoral fellow in the lab, and Derek Dang, a graduate student in the lab, we set out to characterize whether EZHIP expression drove metabolic reprogramming similar to H3K27M mutations. Moreover, because PFAs have relatively quiescent genomes as discussed in Chapter 2, there are few genomic alterations to guide therapeutic strategies. Therefore, identification of potential metabolic and transcriptional-based vulnerabilities is an appealing approach.

Dr. Panwalkar began by exploring which metabolic genes showed increased expression in PFAs compared to group B posterior fossa ependymomas. Dr. Panwalkar explored a variety of transcriptomic and metabolic datasets and saw evidence of upregulation of glycolytic and TCA cycle enzymes and metabolites. In particular, she observed elevated expression of hexokinase 2, which mediates the critical regulatory step of glycolysis, and pyruvate dehydrogenase B, which commits glycolytic carbons to proceed to the TCA cycle. Moreover, noninvasive magnetic resonance spectroscopy (MRS), which enables quantification of a limited number of metabolites *in vivo*, revealed increased citrate levels in PFAs compared to PFBs, consistent with the elevated TCA cycle activity.

5.7.2 Generation of isogenic models to model PFA ependymoma metabolism

To model whether enhanced glycolysis and TCA cycle activity are direct effects of EZHIP expression, Dr. Panwalkar and Derek generated an isogenic model in mouse neural stem cells (mNSCs). mNSCs were stably transduced with expression vectors of either the wildtype coding sequence of the human *EZHIP* gene (WT-EZHIP) or of an *EZHIP* sequence edited to produce a methionine-to-lysine substitution at methionine 406 (M406K-EZHIP), the residue shown to interact with EZH2 in an inhibitory manner (Hubner et al., 2019). This M406K substitution was designed to mimic the endogenous lysine 27 of histone H3.

Comparing EZHIP overexpression to this control that mimics the wildtype histone H3 lysine 27 residue enabled assessment of the isolated effects of EZHIP. Subsequent immunoblots of extracted histone confirmed that H3K27me3 levels decreased in with WT-EZHIP but not

M406K-EZHIP expression. In order to understand how this EZHIP-expressing mNSC isogenic cell line models the PFA ependymoma H3K27ac landscape, we performed H3K27ac ChIP-seq and compared the H3K27ac landscape to data from PFA tumors.

5.7.3 EZHIP overexpression drives a super enhancer profile that overlaps with PFA tumors

To examine how well the H3K27ac landscape of the EZHIP-expressing mNSCs recapitulated that of PFA ependymomas, we assessed super enhancers identified in both datasets (Figure 5.15). Identification of EZHP mNSC super enhancers recapitulated many of the previously identified super enhancers that were identified as specific to PFA tumor samples compared to those found in other pediatric ependymomas.

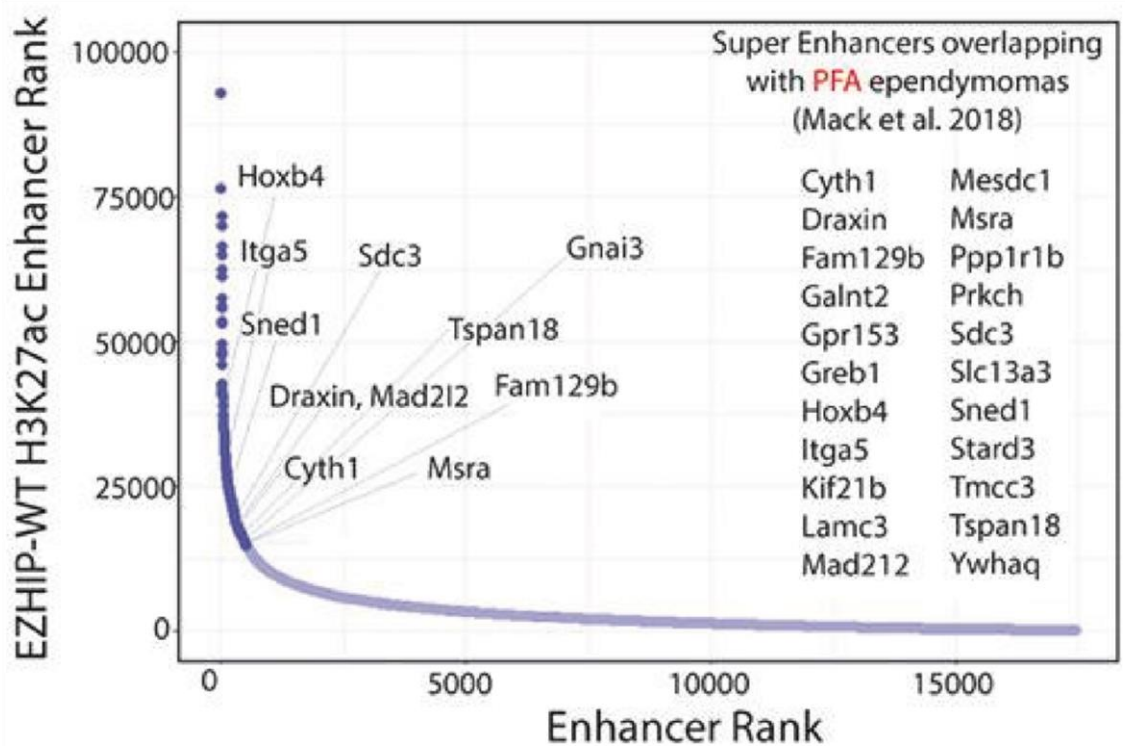

Figure 5.15: The super enhancer landscape of EZHIP-expressing mNSCs is similar to that of PFA tumors.

Stitched peaks of H3K27ac signal ordered (x-axis) by signal level (y-axis) from high to low with super enhancers denoted by dark blue vs. light blue and a list of associated genes that overlap the PFA-specific super enhancers previously identified (Stephen C Mack et al., 2018).

5.7.4 Discussion

Epigenetic profiling of an isogenic model of EZHIP expression allowed for investigation of how this model recapitulated in part the H3K27ac landscapes observed in tumors. Further work then highlighted how key glycolytic and TCA cycle genes exhibited enrichment of H3K27ac both in the isogenic model and in comparisons between PFAs and ST ependymomas. These data formed the foundation for pharmacologic approaches targeting TCA-cycle metabolism using the biguanide metformin, which can inhibit production of TCA cycle metabolites (Janzer et al., 2014). Ultimately, these findings offer a therapeutic strategy for a tumor with limited medical treatment options.

Note: A portion of this chapter has been adapted from work previously published in *Science Translational Medicine* (Panwalkar et al., 2021). Per the journal's copyright policy, I retain the right to include the work in a dissertation.

Chapter 6 Conclusions and Future Directions

6.1 Summary

Cancers of the central nervous system and spine present extraordinary clinical challenges. These tumors can invade anatomic structures responsible for critical neurological functions, limiting the efficacy of traditional solid-tumor treatment approaches such as surgery and radiation therapy. Moreover, despite an overall improvement in cancer mortality over the last three decades, survival rates for brain and bone tumors have remained relatively stagnant on the whole (Hu et al., 2021; D. A. Siegel et al., 2020). Technological advances have permitted reliable and affordable molecular profiling of large cohorts of tumors, and these approaches have increasingly been applied to cancer subtypes with relatively rare incidences. The research studies presented in this dissertation aimed to leverage molecular datasets spanning transcriptomics, genome-wide chromatin profiling, and metabolomics for improving our understanding of the biology of several deadly cancer subtypes and laying the groundwork for potential biomarkers and therapeutic approaches.

6.2 Summary of studies on diffuse midline gliomas and posterior fossa ependymomas

Molecular profiles of diffuse midline gliomas (DMG), histone 3 lysine 27 (H3K27)-altered, and group A posterior fossa (PFA) ependymomas have highlighted key similarities of these pediatric brain tumors that arise from developmental hindbrain locations. DMGs largely harbor H3K27 lysine-to-methionine (H3K27M) substitutions that result in altered activity of the H3K27

methyltransferase enhancer of zeste homolog 2 (EZH2). Patients with DMGs historically face a median overall survival of 10-15 months with limited treatment options beyond radiation therapy. PFAs, in contrast, are primarily characterized by overexpression of an endogenous protein called EZH inhibitory protein (EZHIP) that has a motif closely resembling the H3K27M histone tail. This molecular subgroup is the most aggressive of the ependymomas that arise in the posterior fossa and is associated with high rates of recurrence.

Prior work has characterized the striking similarities of EZH2 inhibition exhibited by these two tumors. Moreover, data from larger cohorts of tumors have shown that these putative molecular drivers can be found across these two tumor types. Occasionally, histologically classified DMGs are found to overexpress EZHIP in the absence of histone mutations, and histologic PFAs harbor H3K27M mutations, emphasizing the potential shared importance of EZH2 inhibition in the tumorigenesis of these two distinct cancer subtypes. In Chapter 2, I employ a systematic approach to evaluate genomic, transcriptomic, and epigenomic characterizations of each of these tumors and identify both common and divergent molecular traits of these two tumors.

Detailed evaluation of the copy number alteration profiles observed in PFAs and DMGs highlight that DMGs exhibit distinct genomic landscapes depending on the specific molecular alteration. Similar to PFAs, H3.1K27M-mutant and EZHIP-expressing DMGs harbor distinctly fewer alterations than their H3.3K27M-mutant counterparts yet higher levels of gain of the long arm of chromosome 1 (1q). This finding prompted a closer inspection of the similarities between H3.1-mutant DMGs and PFAs, and elevated expression of the H3.1K27M-associated gene

ACVR1 was found to be associated with worse survival outcomes among PFA tumors, nominating a potential prognostic marker for further investigation.

	DMG H3.3K27M	DMG H3.1K27M	DMG EZHIP	PFA
Median age (years)	~10	~7	~14 (Limited data)	~3
Anatomic site	Thalamus, Pons, Spinal Cord, other CNS	Pons	Brainstem	Fourth ventricle, cerebellum
Number of copy number alterations	High	Medium	Medium	Low
1Q gain	~10-15%	~35-40%	~50% (Limited data)	~15-25%
ACVR1 patterns	Infrequent activating mutations	Frequent activating mutations	Frequent activating mutations in (Castel et al. 2020)	Survival trends associated with expression; rare activating mutations

Table 6.1: Summary of clinical and genomic features of H3K27-altered DMG subtypes and PFA ependymoma

Data summarized from analyses of data from Mackay et al., 2017; Pajtler et al., 2015; and the National Cancer Institute cohort.

Next, an integrated transcriptomic-epigenomic analysis of the select regions that retain H3K27me3 in PFAs and DMGs yielded insights into how the anatomic origins of these tumors influence the chromatin landscape. *HOX* cluster genes in both tumor types exhibited distinct patterns of H3K27me3-associated silencing that corresponded to the anatomic sites of the tumors as well as known developmental expression patterns. During the preparation of the manuscript associated with Chapter 2, ChIP-seq and expression data from a larger cohort were published and shown to reproduce and extend the anatomic correlations proposed here (Jessa et al., 2022).

Analysis of patterns of the opposing chromatin mark, H3K27 acetylation (H3K27ac), highlighted similarities between the gene-enhancer landscape of the two tumors. Furthermore, investigation of these landscapes in available single-cell transcriptomic datasets underscored potential distinctions between the gene regulatory networks that can be inferred from bulk sequencing methods and those driving progenitor-like cell populations within the tumors.

Lastly, the results presented in Chapter 2 illustrate the potential benefits of integrating scarce single-cell datasets from the two tumors to identify shared transcriptional patterns of progenitor-like cell populations. This approach identifies the retinoic acid signaling regulator *CRABP1* as a potential critical transcriptional marker of progenitor-like cells for a subset of PFAs and DMGs

6.3 Outstanding questions for future research on DMGs and PFAs

The copy number patterns observed across two cohorts each of DMGs and PFAs suggest interesting distinctions between H3.3-mutant and H3.1-mutant/EZHIP-expressing DMGs. This initial observation of genomic similarities between H3.1-mutant and EZHIP-expressing DMGs

and PFAs may will need to be validated in additional cohorts. Moreover, profiles of EZHIP-expressing DMGs are extremely limited at this time. Further profiling of these tumors will identify their degree of genomic similarity to H3.1K27M DMGs.

The additional finding that expression levels of *ACVR1*, a gene prone to activating mutations in H3.1-mutant and EZHIP-expressing DMGs, are associated with a survival difference in PFAs highlights a potential benefit of further exploring the shared biology between PFAs and H3.1-mutant/EZHIP-expressing DMGs. Nevertheless, as additional cohorts of tumors are transcriptionally profiled, this finding must be validated. Furthermore, to pursue ACVR1 expression as a clinically useful biomarker, it will be necessary to evaluate it through immunohistochemical staining and subsequent quantification.

While data regarding *HOX* gene regulation in PFA and DMG tumors suggest that the patterns seen in cohorts are linked to anatomic origins, the role of *CRABP1* may be of great interest to future studies. In addition to being anatomically linked, its expression segregated with a more pluripotent cell type for both tumors and was among the highest genes expressed in scRNA-seq. Thus, while it may not play a role in all DMGs or PFAs, for a subset, it may play a critical role in the maintenance of progenitor populations, consistent with some of its previously seen roles in development. Since OPC-like DMG cells are the only subset of cells that can form tumors in mice, it will be important to assess whether *CRABP1* expression is associated with this phenotype. Additional single-cell RNA-seq datasets in PFAs and DMGs have been published since (Gillen et al., 2020; I. Liu et al., 2022), and integration of these datasets will help to further

assess the importance of *CRABP1* and identify further potential markers of shared and distinct PFA and DMG progenitor-like populations.

6.4 Summary of studies on ONC201 treatment for DMGs

Poor survival rates for H3K27-altered DMGs have not improved, and the critical anatomic location of these tumors limits treatment options. Recently, early data from clinical trials employing the compound ONC201 have demonstrated promising results with unprecedented responses in individual patients and improvements in survival outcomes compared to cohorts from other recent clinical trials and aggregated historical cases. In Chapter 3, through integration of multi-omic datasets both from patients treated in these trials and from cell line DMG models, we identified critical dysregulation of the tricarboxylic acid (TCA) cycle after ONC201 treatment with resulting alterations of the chromatin landscape.

First, by comparing transcriptomic profiles of responders and non-responders from the trial, we identified the TCA cycle and other metabolic pathways as enriched in responding patients at baseline. Because ONC201 is known to activate the mitochondrial protease ClpP, I utilized transcriptomic profiling of a cell line model to identify how DMG cells regulate TCA cycle genes' expression in response to treatment. Several key TCA cycle genes were downregulated transcriptionally, and some were among the most significantly altered, including oxoglutarate dehydrogenase (OGDH). Subsequent metabolic profiling demonstrated that TCA metabolites downstream of OGDH dropped with ONC201 treatment, while those upstream—such as alpha ketoglutarate (α-KG)—were in fact elevated. Unexpectedly, metabolite tracing studies revealed that ONC201-treated cells had elevated levels of 2-hydroxyglutarate (2HG), an oncometabolite

that can restrict DNA and histone methylation. Moreover, 2HG production was seen to be elevated in the cerebrospinal fluid of responders in comparison to non-responders.

Next, examination of the H3K27me3 status of tumors following ONC201 treatment highlighted striking increases in staining compared to before treatment and to other H3K27M tumors. Limited ChIP-seq data from ONC201-treated tumors showed increased H3K27me3 at sites associated with neurogenesis and development. Evaluation of the epigenetic landscape in our cell line model further suggested global decreases in active chromatin states as supported by a decrease in the opposing H3K27ac mark.

Altogether, the studies described in Chapter 3 illustrate the impact of the promising compound ONC201 on an integrated metabolic-epigenetic circuit and highlight the first treatment to reverse the pathognomonic loss of H3K27me3 in H3K27-altered DMGs.

6.5 Outstanding questions for future research on ONC201 treatment of PFAs

These initial studies investigating the impact of ONC201 treatment on DMGs demonstrate the drug's striking metabolic impact and highlight the downstream effects on the epigenetic landscape. They also raise fascinating questions about the degree to which these epigenetic changes contribute to the unprecedented responses observed in patients.

As discussed in Chapter 3, it will be critical to clarify which isomer of 2HG (D/L) is being produced through additional metabolomic profiling using different mass spectroscopy protocols. It will also be imperative to develop rescue models in DMG cell lines by knocking down or

knocking out potential enzymes that may generate 2HG and test whether these models exhibit resistance to ONC201 treatment.

It will also be important to acknowledge the potential limitations of cell line models to investigate these questions. ONC201 treatment has proved efficacious across a wide variety of glioma preclinical models; however, its clinical efficacy has been largely restricted to H3K27M DMGs—and within that tumor subgroup there have been a range of responses. Multiple targets have been identified for ONC201, and the acute effects on cell viability in culture systems may obscure modeling of longer-term epigenomic alterations that we have observed in the tumors. Modeling these tumors and potential rescue experiments that restrict 2HG production by employing mouse xenografts may be necessary to fully test the role of 2HG production in ONC201-mediated toxicity.

Lastly, should the role of 2HG production be more decisively implicated in the anti-tumor effects of ONC201, it will be interesting to see if H3K27 demethylase inhibitors might sensitize DMGs to ONC201 treatment by further inhibiting removal of H3K27me3 marks.

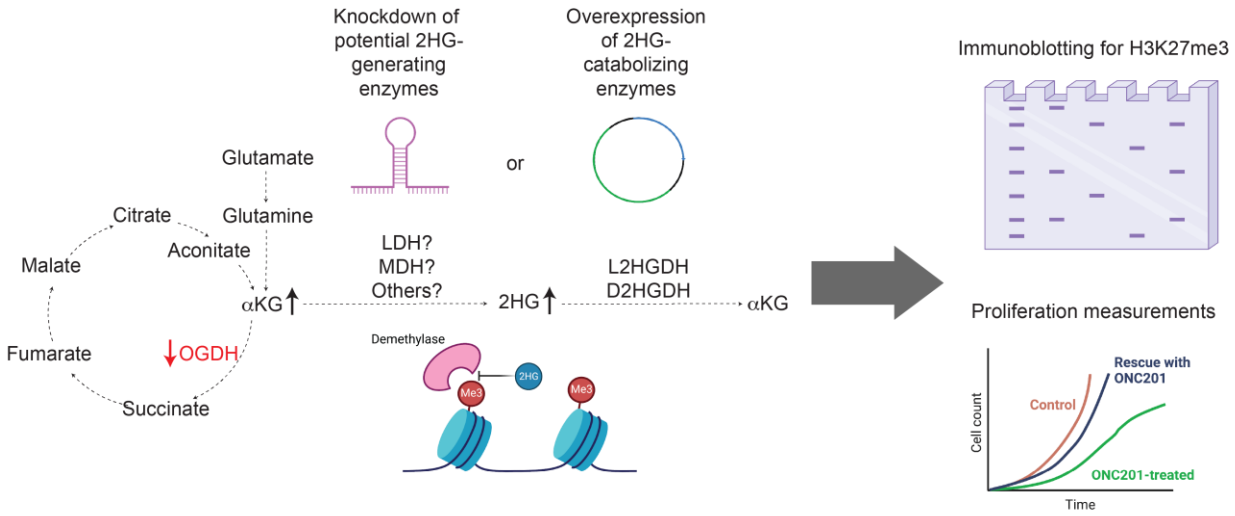

Figure 6.1: Proposed experiments to dissect the role of 2HG in DMG ONC201 response.

To test the impact of 2HG on ONC201-treated DMGs, we will plan to knockdown the most likely enzymatic sources of 2HG production or overexpress enzymes that catabolize either of the 2 isoforms of 2HG. We will then evaluate the impact on histone methylation by immunoblotting, in particular assessing for changes in H3K27me3. In parallel, we will evaluate whether reducing 2HG levels affects response to ONC201 treatment. These experiments will first be performed in DMG cell lines but can also be assessed in a xenograft approach to better model the long-term treatments seen in patients.

6.6 Summary of studies on chordoma

Chordomas are rare tumors associated with very high levels of morbidity and recurrence, and treatment options are limited to surgery and radiation. Investigation of the transcriptional changes between chordomas and their putative tissue of origin the notochord showed that the tumors exhibit enhanced transcription of metabolic pathway genes including those encoding several TCA cycle enzymes. Rewired metabolism is a hallmark of cancer and can serve many purposes including bioenergetic or biosynthetic needs, defense against tumor-associated stresses, and supply of co-factors for epigenetic pathways.

My studies demonstrated that isocitrate dehydrogenase 1 (IDH1) is an essential enzyme for chordoma models. Furthermore, elevated *IDH1* expression is associated with worse outcomes in the largest available cohort of chordomas with matched expression and survival outcomes data. IDH1 sits at a critical node of metabolism and epigenetics. Its role in converting isocitrate and NADP+ to αKG and NADPH drives availability of downstream TCA cycle metabolites and restores NADPH pools for redox metabolism. Through modulating αKG levels, it can also indirectly influence the activity levels of αKG-dependent histone lysine demethylases and DNA demethylating enzymes. In light of recently published data suggesting that chordomas rely on maintenance of a low H3K27me3 state, we tested whether IDH1 inhibition could inhibit chordoma tumor growth by modulating both metabolism and chromatin regulatory landscapes.

Integration of metabolic, epigenomic, and transcriptomic profiling revealed that inhibition of IDH1 resulted in variable effects on the H3K27me3, H3K27ac, and transcriptional landscapes. Additional analysis showed that IDH1 inhibitor treatment led to transcriptional evidence of

cellular stress response pathway activation. Importantly, supplementation of an antioxidant rescued proliferation deficits in chordoma, suggesting IDH1 modulation can result in a stress-driven therapeutic vulnerability in chordoma. Data from a xenograft model further supported the efficacy of the IDH1 inhibitor against chordoma.

6.7 Outstanding questions for future research on chordoma metabolism and IDH1 inhibition

While the IDH1 inhibitor utilized in this trial was effective in cell line and xenograft models, its safety profile in humans is unknown. Recent studies have demonstrated that inhibitors designed for mutant IDH1 are efficacious against wildtype IDH1 in low-nutrient conditions that resemble the tumor microenvironment, and these inhibitors have favorable safety profiles in trials. Testing of these inhibitors in chordoma models will be of great significance due to the rapid clinical translation potential of these drugs.

The results presented within this dissertation also lay the groundwork for a number of fascinating questions regarding chordoma metabolism. First, while glutamine withdrawal blocks proliferation similarly to glucose, employment of glutamine metabolism inhibitors has so far proven ineffective in chordoma models. Dissecting the flux of glutamine in chordoma using stable isotope tracing as employed in Chapter 3 may be of great value in chordomas as a means of identifying the critical metabolites glutamine feeds into.

One promising potential target is asparagine. Asparagine synthetase (ASNS) was recently identified as marker of rapid recurrence in a chordoma cohort. ASNS exchanges the nitrogen

group from glutamine to aspartate to generate asparagine. Degradation of asparagine is a key approach for childhood leukemia and asparagine may play a role in preventing apoptosis (Cui et al., 2007; J. Zhang et al., 2014). Two potential experiments to investigate this line of reasoning in addition to glutamine tracing studies are rescue of glutamine withdrawal via supplementation of asparagine and treating chordoma and other bone tumor cells with asparaginase to identify how gauge the sensitivity of chordomas.

We are additionally pursuing ongoing experiments to assess if there are synergistic effects of inhibiting IDH1 and either glutamine or glutathione pathways. While we do not know the source of carbon for αKG or glutathione in chordoma cells, glucose and glutamine are the most likely options. Thus, inhibition of glutamine metabolism in addition to blocking IDH1 may result in stronger epigenetic effects mediated by αKG depletion and oxidative stress effects due to loss of substrate to generate glutathione. Furthermore, targeting glutathione synthesis via compounds that inhibit import of cystine or the ligation of glutamate and cysteine could deplete glutathione synthesis and render chordoma more sensitive to IDH1 inhibition.

Lastly, the heterogeneity in the response of chordoma cell lines with respect to epigenomic changes poses fascinating questions about how epigenomic marks are regulated in cancer and specifically, whether classes of tumor that rely on maintenance of certain modifications, such as H3K27me3, can have varying levels of sensitivity to co-factor depletion.

6.8 Summary of studies on other brain tumors and outstanding questions

In Chapter 5, I utilized transcriptomic and epigenomic approaches to investigate the biology and potential therapeutic vulnerabilities of H3K27M DMGs, H3G34R/V gliomas, PTEN heterozygous IDH1-mutant (mIDH1) adult gliomas, supratentorial ZFTA-RELA fusion ependymomas, and PFAs.

Integration of transcriptomics, chromatin accessibility profiling, and chromatin conformation data in an H3K27M DMG cell line illuminated downstream effects of targeting components of the chromatin-modifying mammalian SWI/SNF complex. These results highlighted the transcription factor FOXO1 as a novel therapeutic vulnerability for DMGs. Future experiments should further examine whether FOXO1-inhibiting compounds may have a viable therapeutic window. The FOXO1 inhibitor AS1842856 has recently been tested in a large-animal model for improving diabetic wound healing with no reported adverse effects (Jeon et al., 2021). Testing the compound in DMG *in vivo* tumor models for efficacy and mouse safety profiles will be important for validating FOXO1 as a potential therapeutic target.

A multi-omic approach also laid the groundwork for understanding the transcriptional consequences of the H3G34R mutation in pediatric gliomas and provided the rationale for a novel therapeutic approach by targeting the upregulated JAK-STAT pathway. The data generated in these experiments also provide the basis for intriguing future experiments to dissect the roles of H3K36 methylation vs. DNA methylation in regulating expression of H3G34R-specific genes such as LIF. Utilization of clustered regularly interspaced short palindromic repeats (CRISPR) and catalytically inactive Cas9 (dCas9)-based technologies to target DNA methyltransferases to

the Lif locus in the isogenic models of H3WT and H3G34R could test if DNA methylation modulation can drive the changes seen in expression and histone marks.

Transcriptomic profiling of multiple models of mIDH1 gliomas with PTEN reduction has uncovered interesting patterns of expression in high-CpG promoter genes and in immune-related genes. These patterns may be directly related to PTEN-dependent modulation of levels of the oncometabolite D-2-hydroxyglutarate (D2HG), and ongoing DNA methylation profiling of the models will help investigate this hypothesis. This approach will allow for comparison of the DNA methylome with glioma-CpG island methylation phenotype (G-CIMP)-high and G-CIMP-low methylation landscapes. Additionally, these data will be integrated with the transcriptome profiles to assess for patterns of gene repression or activation. Lastly, chromatin profiling for marks of poised bivalent genes (H3K4me3 and H3K27me3) may shed additional light on the chromatin state changes that co-occur with reductions in PTEN levels.

Expression profiling of models of ZFTA-RELA fusion supratentorial ependymomas has permitted interrogation of how both the fusion and the downstream metabolite itaconate influence the cell state. Itaconate itself has been shown to modulate epigenetic modifiers such as TET family DNA dioxygenases that are responsible for DNA demethylation (L.-L. Chen et al., 2022), and Siva's preliminary data suggest that itaconate may influence levels of certain histone modifications. Future experiments will investigate chromatin and DNA modifications and integrate these analyses with the transcriptomic profiles generated so far to identify how itaconate shapes the epigenome of ZFTA-RELA fusion driven tumors.

Lastly, epigenomic profiling of an isogenic model of PFAs enabled direct comparisons to known chromatin landscapes from patient tumors, and future studies may benefit from the generation of this isogenic model. Nevertheless, unlike other isogenic mouse neural stem cell (mNSC) models expressing H3K27M or ZFTA-RELA fusion, the EZHIP-expressing mNSCs do not form tumors. As additional tumor samples become available with expression and H3K27ac profiling, a deeper investigation of the epigenomic and transcriptomic differences between the isogenic model and patient tumors may shed light on potential drivers of tumorigenesis for PFA ependymoma.

6.9 Concluding remarks

This dissertation nominates novel genes of interest for understanding the biology of pediatric brain tumors, describes epigenomic-metabolic rewiring as a therapeutic avenue for a pediatric brain tumor with devastating survival rates, and highlights the role of a metabolic pathway in a rare spine tumor. Additionally, it exploits both transcriptomic and epigenomic approaches to drive a deeper understanding of how putative molecular drivers of brain tumors alter cell states, leading to unique therapeutic vulnerabilities. In addition to highlighting insights about the biology of these tumors and elucidating novel treatment strategies, the work presented here lays the groundwork for many fascinating questions about the role of histones, chromatin-modifying enzymes, and their metabolic co-factors in the development and maintenance of a tumorigenic state.

Bibliography

Ahmad, K., & Henikoff, S. (2002). The histone variant H3. 3 marks active chromatin by replication-independent nucleosome assembly. *Molecular Cell*, *9*(6), 1191–1200.

Akalin, A., Kormaksson, M., Li, S., Garrett-Bakelman, F. E., Figueroa, M. E., Melnick, A., & Mason, C. E. (2012). methylKit: a comprehensive R package for the analysis of genome-wide DNA methylation profiles. *Genome Biology*, *13*(10), 1–9.

Aldinger, K. A., Thomson, Z., Phelps, I. G., Haldipur, P., Deng, M., Timms, A. E., Hirano, M., Santpere, G., Roco, C., Rosenberg, A. B., Lorente-Galdos, B., Gulden, F. O., O'Day, D., Overman, L. M., Lisgo, S. N., Alexandre, P., Sestan, N., Doherty, D., Dobyns, W. B., … Millen, K. J. (2021). Spatial and cell type transcriptional landscape of human cerebellar development. *Nature Neuroscience*, *24*(8), 1163–1175. https://doi.org/10.1038/s41593-021-00872-y

Alimonti, A., Carracedo, A., Clohessy, J. G., Trotman, L. C., Nardella, C., Egia, A., Salmena, L., Sampieri, K., Haveman, W. J., Brogi, E., Richardson, A. L., Zhang, J., & Pandolfi, P. P. (2010). Subtle variations in Pten dose determine cancer susceptibility. *Nature Genetics*, *42*(5), 454–458. https://doi.org/10.1038/ng.556

Allen Institute for Brain Science. (2010). *Allen Developing Human Brain Atlas: Microarray [dataset]*. Allen Institute for Brain Science. https://doi.org/RRID:SCR_008083

Allis, C. D., & Jenuwein, T. (2016). The molecular hallmarks of epigenetic control. *Nature Reviews Genetics*, *17*(8), 487–500. https://doi.org/10.1038/nrg.2016.59

Alver, B. H., Kim, K. H., Lu, P., Wang, X., Manchester, H. E., Wang, W., Haswell, J. R., Park, P. J., & Roberts, C. W. M. (2017). The SWI/SNF chromatin remodelling complex is required for maintenance of lineage specific enhancers. *Nature Communications*, *8*(1), 14648. https://doi.org/10.1038/ncomms14648

Amemiya, H. M., Kundaje, A., & Boyle, A. P. (2019). The ENCODE Blacklist: Identification of Problematic Regions of the Genome. *Scientific Reports*, *9*(1), 9354. https://doi.org/10.1038/s41598-019-45839-z

Anastas, J. N., Zee, B. M., Kalin, J. H., Kim, M., Guo, R., Alexandrescu, S., Blanco, M. A., Giera, S., Gillespie, S. M., Das, J., Wu, M., Nocco, S., Bonal, D. M., Nguyen, Q. D., Suva, M. L., Bernstein, B. E., Alani, R., Golub, T. R., Cole, P. A., … Shi, Y. (2019). Re-programing Chromatin with a Bifunctional LSD1/HDAC Inhibitor Induces Therapeutic Differentiation in DIPG. *Cancer Cell*, *36*(5), 528-544.e10. https://doi.org/10.1016/j.ccell.2019.09.005

Andrews, S. (2010). *FastQC: a quality control tool for high throughput sequence data*. Babraham Bioinformatics, Babraham Institute, Cambridge, United Kingdom.

Antin, C., Tauziède-Espariat, A., Debily, M.-A., Castel, D., Grill, J., Pagès, M., Ayrault, O., Chrétien, F., Gareton, A., Andreiuolo, F., Lechapt, E., & Varlet, P. (2020). EZHIP is a specific diagnostic biomarker for posterior fossa ependymomas, group PFA and diffuse midline gliomas H3-WT with EZHIP overexpression. *Acta Neuropathologica Communications*, *8*(1), 183. https://doi.org/10.1186/s40478-020-01056-8

Arabzade, A., Zhao, Y., Varadharajan, S., Chen, H.-C., Jessa, S., Rivas, B., Stuckert, A. J., Solis, M., Kardian, A., & Tlais, D. (2021). ZFTA–RELA Dictates Oncogenic Transcriptional Programs to Drive Aggressive Supratentorial EpendymomaZFTA-RELA Shapes Ependymoma Epigenomes. *Cancer Discovery*, *11*(9), 2200–2215.

Argersinger, D. P., Rivas, S. R., Shah, A. H., Jackson, S., & Heiss, J. D. (2021). New Developments in the Pathogenesis, Therapeutic Targeting, and Treatment of H3K27M-Mutant Diffuse Midline Glioma. In *Cancers* (Vol. 13, Issue 21). https://doi.org/10.3390/cancers13215280

Arrillaga-Romany, I., Odia, Y., Prabhu, V. V, Tarapore, R. S., Merdinger, K., Stogniew, M., Oster, W., Allen, J. E., Mehta, M., Batchelor, T. T., & Wen, P. Y. (2020). Biological activity of weekly ONC201 in adult recurrent glioblastoma patients. *Neuro-Oncology*, *22*(1), 94–102. https://doi.org/10.1093/neuonc/noz164

Azzarelli, A., Quagliuolo, V., Cerasoli, S., Zucali, R., Bignami, P., Mazzaferro, V., Dossena, G., & Gennari, L. (1988). Chordoma: natural history and treatment results in 33 cases. *Journal of Surgical Oncology*, *37*(3), 185–191. https://doi.org/10.1002/jso.2930370311

Bai, J., Shi, J., Li, C., Wang, S., Zhang, T., Hua, X., Zhu, B., Koka, H., Wu, H.-H., Song, L., Wang, D., Wang, M., Zhou, W., Ballew, B. J., Zhu, B., Hicks, B., Mirabello, L., Parry, D. M., Zhai, Y., … Yang, X. R. (2021). Whole genome sequencing of skull-base chordoma reveals genomic alterations associated with recurrence and chordoma-specific survival. *Nature Communications*, *12*(1), 757. https://doi.org/10.1038/s41467-021-21026-5

Bakker, S. H., Jacobs, W. C. H., Pondaag, W., Gelderblom, H., Nout, R. A., Dijkstra, P. D. S., Peul, W. C., & Vleggeert-Lankamp, C. L. A. (2018). Chordoma: a systematic review of the epidemiology and clinical prognostic factors predicting progression-free and overall survival. *European Spine Journal*, *27*, 3043–3058.

Barker II, F. G., Simmons, M. L., Chang, S. M., Prados, M. D., Larson, D. A., Sneed, P. K., Wara, W. M., Berger, M. S., Chen, P., & Israel, M. A. (2001). EGFR overexpression and radiation response in glioblastoma multiforme. *International Journal of Radiation Oncology* Biology* Physics*, *51*(2), 410–418.

Baroni, L. V, Sundaresan, L., Heled, A., Coltin, H., Pajtler, K. W., Lin, T., Merchant, T. E., McLendon, R., Faria, C., Buntine, M., White, C. L., Pfister, S. M., Gilbert, M. R., Armstrong, T. S., Bouffet, E., Kumar, S., Taylor, M. D., Aldape, K. D., Ellison, D. W., … Ramaswamy, V. (2021). Ultra high-risk PFA ependymoma is characterized by loss of

chromosome 6q. *Neuro-Oncology*, *23*(8), 1360–1370. https://doi.org/10.1093/neuonc/noab034

Bayliss, J., Mukherjee, P., Lu, C., Jain, S. U., Chung, C., Martinez, D., Sabari, B., Margol, A. S., Panwalkar, P., Parolia, A., Pekmezci, M., McEachin, R. C., Cieslik, M., Tamrazi, B., Garcia, B. A., La Rocca, G., Santi, M., Lewis, P. W., Hawkins, C., … Venneti, S. (2016). Lowered H3K27me3 and DNA hypomethylation define poorly prognostic pediatric posterior fossa ependymomas. *Sci Transl Med*, *8*(366), 366ra161. https://doi.org/10.1126/scitranslmed.aah6904

Baysal, B. E., Ferrell, R. E., Willett-Brozick, J. E., Lawrence, E. C., Myssiorek, D., Bosch, A., van der Mey, A., Taschner, P. E., Rubinstein, W. S., Myers, E. N., Richard, C. W. 3rd, Cornelisse, C. J., Devilee, P., & Devlin, B. (2000). Mutations in SDHD, a mitochondrial complex II gene, in hereditary paraganglioma. *Science (New York, N.Y.)*, *287*(5454), 848–851. https://doi.org/10.1126/science.287.5454.848

Begemann, G., & Meyer, A. (2001). Hindbrain patterning revisited: timing and effects of retinoic acid signalling. *Bioessays*, *23*(11), 981–986.

Bender, S., Tang, Y., Lindroth, A. M., Hovestadt, V., Jones, D. T. W., Kool, M., Zapatka, M., Northcott, P. A., Sturm, D., Wang, W., Radlwimmer, B., Højfeldt, J. W., Truffaux, N., Castel, D., Schubert, S., Ryzhova, M., Seker-Cin, H., Gronych, J., Johann, P. D., … Pfister, S. M. (2013). Reduced H3K27me3 and DNA hypomethylation are major drivers of gene expression in K27M mutant pediatric high-grade gliomas. *Cancer Cell*, *24*(5), 660–672. https://doi.org/10.1016/j.ccr.2013.10.006

Bernstein, B. E., Mikkelsen, T. S., Xie, X., Kamal, M., Huebert, D. J., Cuff, J., Fry, B., Meissner, A., Wernig, M., Plath, K., Jaenisch, R., Wagschal, A., Feil, R., Schreiber, S. L., & Lander, E. S. (2006). A bivalent chromatin structure marks key developmental genes in embryonic stem cells. *Cell*, *125*(2), 315–326. https://doi.org/10.1016/j.cell.2006.02.041

Bilsky, M. H., Gerszten, P., Laufer, I., & Yamada, Y. (2008). Radiation for Primary Spine Tumors. *Neurosurgery Clinics of North America*, *19*(1), 119–123. https://doi.org/https://doi.org/10.1016/j.nec.2007.09.002

Bjerke, L., Mackay, A., Nandhabalan, M., Burford, A., Jury, A., Popov, S., Bax, D. A., Carvalho, D., Taylor, K. R., & Vinci, M. (2013). Histone H3. 3 mutations drive pediatric glioblastoma through upregulation of MYCN. *Cancer Discovery*, *3*(5), 512–519.

Brat, D. J., Verhaak, R. G. W., Aldape, K. D., Yung, W. K. A., Salama, S. R., Cooper, L. A. D., Rheinbay, E., Miller, C. R., Vitucci, M., Morozova, O., Robertson, A. G., Noushmehr, H., Laird, P. W., Cherniack, A. D., Akbani, R., Huse, J. T., Ciriello, G., Poisson, L. M., Barnholtz-Sloan, J. S., … Zhang, J. (2015). Comprehensive, Integrative Genomic Analysis of Diffuse Lower-Grade Gliomas. *The New England Journal of Medicine*, *372*(26), 2481–2498. https://doi.org/10.1056/NEJMoa1402121

Brennan, C. W., Verhaak, R. G. W., McKenna, A., Campos, B., Noushmehr, H., Salama, S. R., Zheng, S., Chakravarty, D., Sanborn, J. Z., Berman, S. H., Beroukhim, R., Bernard, B., Wu,

C.-J., Genovese, G., Shmulevich, I., Barnholtz-Sloan, J., Zou, L., Vegesna, R., Shukla, S. A., … Chin, L. (2013). The somatic genomic landscape of glioblastoma. *Cell*, *155*(2), 462–477. https://doi.org/10.1016/j.cell.2013.09.034

Buczkowicz, P., Bartels, U., Bouffet, E., Becher, O., & Hawkins, C. (2014). Histopathological spectrum of paediatric diffuse intrinsic pontine glioma: diagnostic and therapeutic implications. *Acta Neuropathologica*, *128*(4), 573–581. https://doi.org/10.1007/s00401-014-1319-6

Buschbeck, M., & Hake, S. B. (2017). Variants of core histones and their roles in cell fate decisions, development and cancer. *Nature Reviews Molecular Cell Biology*, *18*(5), 299–314. https://doi.org/10.1038/nrm.2016.166

Cairncross, J. G., Ueki, K., Zlatescu, M. C., Lisle, D. K., Finkelstein, D. M., Hammond, R. R., Silver, J. S., Stark, P. C., Macdonald, D. R., & Ino, Y. (1998). Specific genetic predictors of chemotherapeutic response and survival in patients with anaplastic oligodendrogliomas. *JNCI: Journal of the National Cancer Institute*, *90*(19), 1473–1479.

Capper, D., Jones, D. T. W., Sill, M., Hovestadt, V., Schrimpf, D., Sturm, D., Koelsche, C., Sahm, F., Chavez, L., Reuss, D. E., Kratz, A., Wefers, A. K., Huang, K., Pajtler, K. W., Schweizer, L., Stichel, D., Olar, A., Engel, N. W., Lindenberg, K., … Pfister, S. M. (2018). DNA methylation-based classification of central nervous system tumours. *Nature*, *555*(7697), 469–474. https://doi.org/10.1038/nature26000

Carey, B. W., Finley, L. W. S., Cross, J. R., Allis, C. D., & Thompson, C. B. (2015). Intracellular α-ketoglutarate maintains the pluripotency of embryonic stem cells. *Nature*, *518*(7539), 413–416. https://doi.org/10.1038/nature13981

Castel, D., Kergrohen, T., Tauziede-Espariat, A., Mackay, A., Ghermaoui, S., Lechapt, E., Pfister, S. M., Kramm, C. M., Boddaert, N., Blauwblomme, T., Puget, S., Beccaria, K., Jones, C., Jones, D. T. W., Varlet, P., Grill, J., & Debily, M. A. (2020). Histone H3 wild-type DIPG/DMG overexpressing EZHIP extend the spectrum diffuse midline gliomas with PRC2 inhibition beyond H3-K27M mutation. *Acta Neuropathol*. https://doi.org/10.1007/s00401-020-02142-w

Castel, D., Philippe, C., Calmon, R., Le Dret, L., Truffaux, N., Boddaert, N., Pages, M., Taylor, K. R., Saulnier, P., Lacroix, L., Mackay, A., Jones, C., Sainte-Rose, C., Blauwblomme, T., Andreiuolo, F., Puget, S., Grill, J., Varlet, P., & Debily, M. A. (2015). Histone H3F3A and HIST1H3B K27M mutations define two subgroups of diffuse intrinsic pontine gliomas with different prognosis and phenotypes. *Acta Neuropathol*, *130*(6), 815–827. https://doi.org/10.1007/s00401-015-1478-0

Castel, D., Philippe, C., Kergrohen, T., Sill, M., Merlevede, J., Barret, E., Puget, S., Sainte-Rose, C., Kramm, C. M., Jones, C., Varlet, P., Pfister, S. M., Grill, J., Jones, D. T. W., & Debily, M. A. (2018). Transcriptomic and epigenetic profiling of "diffuse midline gliomas, H3 K27M-mutant" discriminate two subgroups based on the type of histone H3 mutated and not supratentorial or infratentorial location. *Acta Neuropathol Commun*, *6*(1), 117. https://doi.org/10.1186/s40478-018-0614-1

Catton, C., O'Sullivan, B., Bell, R., Laperriere, N., Cummings, B., Fornasier, V., & Wunder, J. (1996). Chordoma: long-term follow-up after radical photon irradiation. *Radiotherapy and Oncology : Journal of the European Society for Therapeutic Radiology and Oncology*, *41*(1), 67–72. https://doi.org/10.1016/s0167-8140(96)91805-8

Cavalli, F. M. G., Hübner, J.-M., Sharma, T., Luu, B., Sill, M., Zapotocky, M., Mack, S. C., Witt, H., Lin, T., Shih, D. J. H., Ho, B., Santi, M., Emery, L., Hukin, J., Dunham, C., McLendon, R. E., Lipp, E. S., Gururangan, S., Grossbach, A., … Ramaswamy, V. (2018). Heterogeneity within the PF-EPN-B ependymoma subgroup. *Acta Neuropathologica*, *136*(2), 227–237. https://doi.org/10.1007/s00401-018-1888-x

Cavalli, F. M. G., Remke, M., Rampasek, L., Peacock, J., Shih, D. J. H., Luu, B., Garzia, L., Torchia, J., Nor, C., Morrissy, A. S., Agnihotri, S., Thompson, Y. Y., Kuzan-Fischer, C. M., Farooq, H., Isaev, K., Daniels, C., Cho, B.-K., Kim, S.-K., Wang, K.-C., … Taylor, M. D. (2017). Intertumoral Heterogeneity within Medulloblastoma Subgroups. *Cancer Cell*, *31*(6), 737-754.e6. https://doi.org/10.1016/j.ccell.2017.05.005

Ceccarelli, M., Barthel, F. P., Malta, T. M., Sabedot, T. S., Salama, S. R., Murray, B. A., Morozova, O., Newton, Y., Radenbaugh, A., Pagnotta, S. M., Anjum, S., Wang, J., Manyam, G., Zoppoli, P., Ling, S., Rao, A. A., Grifford, M., Cherniack, A. D., Zhang, H., … Verhaak, R. G. W. (2016). Molecular Profiling Reveals Biologically Discrete Subsets and Pathways of Progression in Diffuse Glioma. *Cell*, *164*(3), 550–563. https://doi.org/10.1016/j.cell.2015.12.028

Chan, K.-M., Fang, D., Gan, H., Hashizume, R., Yu, C., Schroeder, M., Gupta, N., Mueller, S., James, C. D., Jenkins, R., Sarkaria, J., & Zhang, Z. (2013). The histone H3.3K27M mutation in pediatric glioma reprograms H3K27 methylation and gene expression. *Genes & Development*, *27*(9), 985–990. https://doi.org/10.1101/gad.217778.113

Chen, C. C. L., Deshmukh, S., Jessa, S., Hadjadj, D., Lisi, V., Andrade, A. F., Faury, D., Jawhar, W., Dali, R., Suzuki, H., Pathania, M., A, D., Dubois, F., Woodward, E., Hébert, S., Coutelier, M., Karamchandani, J., Albrecht, S., Brandner, S., … Jabado, N. (2020). Histone H3.3G34-Mutant Interneuron Progenitors Co-opt PDGFRA for Gliomagenesis. *Cell*, *183*(6), 1617-1633.e22. https://doi.org/10.1016/j.cell.2020.11.012

Chen, E. Y., Tan, C. M., Kou, Y., Duan, Q., Wang, Z., Meirelles, G. V., Clark, N. R., & Ma'ayan, A. (2013). Enrichr: interactive and collaborative HTML5 gene list enrichment analysis tool. *BMC Bioinformatics*, *14*, 128. https://doi.org/10.1186/1471-2105-14-128

Chen, F., Elgaher, W. A. M., Winterhoff, M., Büssow, K., Waqas, F. H., Graner, E., Pires-Afonso, Y., Casares Perez, L., de la Vega, L., Sahini, N., Czichon, L., Zobl, W., Zillinger, T., Shehata, M., Pleschka, S., Bähre, H., Falk, C., Michelucci, A., Schuchardt, S., … Pessler, F. (2022). Citraconate inhibits ACOD1 (IRG1) catalysis, reduces interferon responses and oxidative stress, and modulates inflammation and cell metabolism. *Nature Metabolism*, *4*(5), 534–546. https://doi.org/10.1038/s42255-022-00577-x

Chen, L.-L., Morcelle, C., Cheng, Z.-L., Chen, X., Xu, Y., Gao, Y., Song, J., Li, Z., Smith, M. D., Shi, M., Zhu, Y., Zhou, N., Cheng, M., He, C., Liu, K.-Y., Lu, G., Zhang, L., Zhang, C.,

Zhang, J., … Ye, D. (2022). Itaconate inhibits TET DNA dioxygenases to dampen inflammatory responses. *Nature Cell Biology*, *24*(3), 353–363. https://doi.org/10.1038/s41556-022-00853-8

Chen, S., Xu, W., Jiao, J., Jiang, D., Liu, J., Chen, T., Wan, Z., Xu, L., Zhou, Z., & Xiao, J. (2015). Differential proteomic profiling of primary and recurrent chordomas. *Oncology Reports*, *33*(5), 2207–2218.

Chung, C., Sweha, S. R., Pratt, D., Tamrazi, B., Panwalkar, P., Banda, A., Bayliss, J., Hawes, D., Yang, F., Lee, H.-J., Shan, M., Cieslik, M., Qin, T., Werner, C. K., Wahl, D. R., Lyssiotis, C. A., Bian, Z., Shotwell, J. B., Yadav, V. N., … Venneti, S. (2020). Integrated Metabolic and Epigenomic Reprograming by H3K27M Mutations in Diffuse Intrinsic Pontine Gliomas. *Cancer Cell*, *38*(3), 334-349.e9. https://doi.org/10.1016/j.ccell.2020.07.008

Cleaver, O., & Krieg, P. A. (2001). Notochord Patterning of the Endoderm. *Developmental Biology*, *234*(1), 1–12. https://doi.org/https://doi.org/10.1006/dbio.2001.0214

Corallo, D., Trapani, V., & Bonaldo, P. (2015). The notochord: structure and functions. *Cellular and Molecular Life Sciences*, *72*(16), 2989–3008. https://doi.org/10.1007/s00018-015-1897-z

Corces, M. R., Trevino, A. E., Hamilton, E. G., Greenside, P. G., Sinnott-Armstrong, N. A., Vesuna, S., Satpathy, A. T., Rubin, A. J., Montine, K. S., Wu, B., Kathiria, A., Cho, S. W., Mumbach, M. R., Carter, A. C., Kasowski, M., Orloff, L. A., Risca, V. I., Kundaje, A., Khavari, P. A., … Chang, H. Y. (2017). An improved ATAC-seq protocol reduces background and enables interrogation of frozen tissues. *Nature Methods*, *14*(10), 959–962. https://doi.org/10.1038/nmeth.4396

Cottone, L., Cribbs, A. P., Khandelwal, G., Wells, G., Ligammari, L., Philpott, M., Tumber, A., Lombard, P., Hookway, E. S., Szommer, T., Johansson, C., Brennan, P. E., Pillay, N., Jenner, R. G., Oppermann, U., & Flanagan, A. M. (2020). Inhibition of Histone H3K27 Demethylases Inactivates Brachyury (TBXT) and Promotes Chordoma Cell Death. *Cancer Research*, *80*(20), 4540–4551. https://doi.org/10.1158/0008-5472.CAN-20-1387

Cui, H., Darmanin, S., Natsuisaka, M., Kondo, T., Asaka, M., Shindoh, M., Higashino, F., Hamuro, J., Okada, F., Kobayashi, M., Nakagawa, K., Koide, H., & Kobayashi, M. (2007). Enhanced expression of asparagine synthetase under glucose-deprived conditions protects pancreatic cancer cells from apoptosis induced by glucose deprivation and cisplatin. *Cancer Research*, *67*(7), 3345–3355. https://doi.org/10.1158/0008-5472.CAN-06-2519

Curtin, S. C., Minino, A. M., & Anderson, R. N. (2016). Declines in Cancer Death Rates Among Children and Adolescents in the United States, 1999-2014. *NCHS Data Brief*, *257*, 1–8.

Dahlin, D. C., & Maccarty, C. S. (1952). Chordoma. A study of fifty-nine cases. *Cancer*, *5*(6), 1170–1178.

Dang, L., White, D. W., Gross, S., Bennett, B. D., Bittinger, M. A., Driggers, E. M., Fantin, V. R., Jang, H. G., Jin, S., Keenan, M. C., Marks, K. M., Prins, R. M., Ward, P. S., Yen, K. E.,

Liau, L. M., Rabinowitz, J. D., Cantley, L. C., Thompson, C. B., Vander Heiden, M. G., & Su, S. M. (2009). Cancer-associated IDH1 mutations produce 2-hydroxyglutarate. *Nature*, *462*(7274), 739–744. https://doi.org/10.1038/nature08617

Dang, C. V, & Semenza, G. L. (1999). Oncogenic alterations of metabolism. *Trends in Biochemical Sciences*, *24*(2), 68–72. https://doi.org/https://doi.org/10.1016/S0968-0004(98)01344-9

Das, P., Soni, P., Jones, J., Habboub, G., Barnholtz-Sloan, J. S., Recinos, P. F., & Kshettry, V. R. (2020). Descriptive epidemiology of chordomas in the United States. *Journal of Neuro-Oncology*, *148*(1), 173–178. https://doi.org/10.1007/s11060-020-03511-x

de Bree, K., de Bakker, B. S., & Oostra, R.-J. (2018). The development of the human notochord. *PLoS One*, *13*(10), e0205752.

Deaton, A. M., & Bird, A. (2011). CpG islands and the regulation of transcription. *Genes & Development*, *25*(10), 1010–1022.

DeBerardinis, R. J., & Chandel, N. S. (2016). Fundamentals of cancer metabolism. *Science Advances*, *2*(5), e1600200.

DeLaney, T. F., Liebsch, N. J., Pedlow, F. X., Adams, J., Weyman, E. A., Yeap, B. Y., Depauw, N., Nielsen, G. P., Harmon, D. C., Yoon, S. S., Chen, Y.-L., Schwab, J. H., & Hornicek, F. J. (2014). Long-term results of Phase II study of high dose photon/proton radiotherapy in the management of spine chordomas, chondrosarcomas, and other sarcomas. *Journal of Surgical Oncology*, *110*(2), 115–122. https://doi.org/10.1002/jso.23617

DeLange, R. J., Fambrough, D. M., Smith, E. L., & Bonner, J. (1969). Calf and Pea Histone IV: II. The complete amino acid sequence of calf thymus histone IV; presence of ε-N-acetyllysine. *Journal of Biological Chemistry*, *244*(2), 319–334.

Dey, S., Baird, T. D., Zhou, D., Palam, L. R., Spandau, D. F., & Wek, R. C. (2010). Both transcriptional regulation and translational control of ATF4 are central to the integrated stress response. *The Journal of Biological Chemistry*, *285*(43), 33165–33174. https://doi.org/10.1074/jbc.M110.167213

Di Cristofano, A., De Acetis, M., Koff, A., Cordon-Cardo, C., & Pandolfi, P. P. (2001). Pten and p27KIP1 cooperate in prostate cancer tumor suppression in the mouse. *Nature Genetics*, *27*(2), 222–224. https://doi.org/10.1038/84879

Di Cristofano, A., Kotsi, P., Peng, Y. F., Cordon-Cardo, C., Elkon, K. B., & Pandolfi, P. P. (1999). Impaired Fas response and autoimmunity in Pten+/- mice. *Science (New York, N.Y.)*, *285*(5436), 2122–2125. https://doi.org/10.1126/science.285.5436.2122

Di Cristofano, A., Pesce, B., Cordon-Cardo, C., & Pandolfi, P. P. (1998). Pten is essential for embryonic development and tumour suppression. *Nature Genetics*, *19*(4), 348–355. https://doi.org/10.1038/1235

Dorfman, H. D., & Czerniak, B. (1995). Bone cancers. *Cancer*, *75*(S1), 203–210. https://doi.org/https://doi.org/10.1002/1097-0142(19950101)75:1+<203::AID-CNCR2820751308>3.0.CO;2-V

Endo Greer, Y., & Lipkowitz, S. (2016). ONC201: Stressing tumors to death. *Science Signaling*, *9*(415), fs1–fs1. https://doi.org/10.1126/scisignal.aad7955

Evans, L. T., DeMonte, F., Grosshans, D. R., Ghia, A. J., Habib, A., & Raza, S. M. (2020). Salvage therapy for local progression following definitive therapy for skull base chordomas: is there a role of stereotactic radiosurgery? *Journal of Neurological Surgery Part B: Skull Base*, *81*(01), 97–106.

Eze, U. C., Bhaduri, A., Haeussler, M., Nowakowski, T. J., & Kriegstein, A. R. (2021). Single-cell atlas of early human brain development highlights heterogeneity of human neuroepithelial cells and early radial glia. *Nature Neuroscience*, *24*(4), 584–594.

Fan, J., Teng, X., Liu, L., Mattaini, K. R., Looper, R. E., Vander Heiden, M. G., & Rabinowitz, J. D. (2015). Human phosphoglycerate dehydrogenase produces the oncometabolite D-2-hydroxyglutarate. *ACS Chemical Biology*, *10*(2), 510–516. https://doi.org/10.1021/cb500683c

Fang, J., Huang, Y., Mao, G., Yang, S., Rennert, G., Gu, L., Li, H., & Li, G.-M. (2018). Cancer-driving H3G34V/R/D mutations block H3K36 methylation and H3K36me3–MutSα interaction. *Proceedings of the National Academy of Sciences*, *115*(38), 9598–9603.

Farnaby, W., Koegl, M., Roy, M. J., Whitworth, C., Diers, E., Trainor, N., Zollman, D., Steurer, S., Karolyi-Oezguer, J., & Riedmueller, C. (2019). BAF complex vulnerabilities in cancer demonstrated via structure-based PROTAC design. *Nature Chemical Biology*, *15*(7), 672–680.

Favorskaya, I., Kainov, Y., Chemeris, G., Komelkov, A., Zborovskaya, I., & Tchevkina, E. (2014). Expression and clinical significance of CRABP1 and CRABP2 in non-small cell lung cancer. *Tumor Biology*, *35*(10), 10295–10300.

Filbin, M. G., Tirosh, I., Hovestadt, V., Shaw, M. L., Escalante, L. E., Mathewson, N. D., Neftel, C., Frank, N., Pelton, K., Hebert, C. M., Haberler, C., Yizhak, K., Gojo, J., Egervari, K., Mount, C., van Galen, P., Bonal, D. M., Nguyen, Q. D., Beck, A., … Suva, M. L. (2018). Developmental and oncogenic programs in H3K27M gliomas dissected by single-cell RNA-seq. *Science*, *360*(6386), 331–335. https://doi.org/10.1126/science.aao4750

Fontebasso, A. M., Papillon-Cavanagh, S., Schwartzentruber, J., Nikbakht, H., Gerges, N., Fiset, P.-O., Bechet, D., Faury, D., De Jay, N., Ramkissoon, L. A., Corcoran, A., Jones, D. T. W., Sturm, D., Johann, P., Tomita, T., Goldman, S., Nagib, M., Bendel, A., Goumnerova, L., … Kieran, M. W. (2014). Recurrent somatic mutations in ACVR1 in pediatric midline high-grade astrocytoma. *Nature Genetics*, *46*(5), 462–466. https://doi.org/10.1038/ng.2950

Fontebasso, A. M., Schwartzentruber, J., Khuong-Quang, D.-A., Liu, X.-Y., Sturm, D., Korshunov, A., Jones, D. T. W., Witt, H., Kool, M., & Albrecht, S. (2013). Mutations in

SETD2 and genes affecting histone H3K36 methylation target hemispheric high-grade gliomas. *Acta Neuropathologica*, *125*, 659–669.

Fouad, Y. A., & Aanei, C. (2017). Revisiting the hallmarks of cancer. *American Journal of Cancer Research*, *7*(5), 1016–1036.

Frattini, V., Trifonov, V., Chan, J. M., Castano, A., Lia, M., Abate, F., Keir, S. T., Ji, A. X., Zoppoli, P., Niola, F., Danussi, C., Dolgalev, I., Porrati, P., Pellegatta, S., Heguy, A., Gupta, G., Pisapia, D. J., Canoll, P., Bruce, J. N., … Iavarone, A. (2013). The integrated landscape of driver genomic alterations in glioblastoma. *Nature Genetics*, *45*(10), 1141–1149. https://doi.org/10.1038/ng.2734

Gallia, G. L., Rand, V., Siu, I.-M., Eberhart, C. G., James, C. D., Marie, S. K. N., Oba-Shinjo, S. M., Carlotti, C. G., Caballero, O. L., Simpson, A. J. G., Brock, M. V, Massion, P. P., Carson Sr., B. S., & Riggins, G. J. (2006). PIK3CA Gene Mutations in Pediatric and Adult Glioblastoma Multiforme. *Molecular Cancer Research*, *4*(10), 709–714. https://doi.org/10.1158/1541-7786.MCR-06-0172

Garcia-Cao, I., Song, M. S., Hobbs, R. M., Laurent, G., Giorgi, C., de Boer, V. C. J., Anastasiou, D., Ito, K., Sasaki, A. T., Rameh, L., Carracedo, A., Vander Heiden, M. G., Cantley, L. C., Pinton, P., Haigis, M. C., & Pandolfi, P. P. (2012). Systemic Elevation of PTEN Induces a Tumor-Suppressive Metabolic State. *Cell*, *149*(1), 49–62. https://doi.org/https://doi.org/10.1016/j.cell.2012.02.030

Garrett-Bakelman, F. E., Sheridan, C. K., Kacmarczyk, T. J., Ishii, J., Betel, D., Alonso, A., Mason, C. E., Figueroa, M. E., & Melnick, A. M. (2015). Enhanced reduced representation bisulfite sequencing for assessment of DNA methylation at base pair resolution. *Journal of Visualized Experiments : JoVE*, *96*, e52246. https://doi.org/10.3791/52246

Gillen, A. E., Riemondy, K. A., Amani, V., Griesinger, A. M., Gilani, A., Venkataraman, S., Madhavan, K., Prince, E., Sanford, B., Hankinson, T. C., Handler, M. H., Vibhakar, R., Jones, K. L., Mitra, S., Hesselberth, J. R., Foreman, N. K., & Donson, A. M. (2020). Single-Cell RNA Sequencing of Childhood Ependymoma Reveals Neoplastic Cell Subpopulations That Impact Molecular Classification and Etiology. *Cell Reports*, *32*(6), 108023. https://doi.org/10.1016/j.celrep.2020.108023

Glover, J. C., Renaud, J., & Rijli, F. M. (2006). Retinoic acid and hindbrain patterning. *Journal of Neurobiology*, *66*(7), 705–725.

Godfraind, C., Kaczmarska, J. M., Kocak, M., Dalton, J., Wright, K. D., Sanford, R. A., Boop, F. A., Gajjar, A., Merchant, T. E., & Ellison, D. W. (2012). Distinct disease-risk groups in pediatric supratentorial and posterior fossa ependymomas. *Acta Neuropathologica*, *124*(2), 247–257. https://doi.org/10.1007/s00401-012-0981-9

Gojo, J., Pavelka, Z., Zapletalova, D., Schmook, M. T., Mayr, L., Madlener, S., Kyr, M., Vejmelkova, K., Smrcka, M., Czech, T., Dorfer, C., Skotakova, J., Azizi, A. A., Chocholous, M., Reisinger, D., Lastovicka, D., Valik, D., Haberler, C., Peyrl, A., … Sterba, J. (2019). Personalized Treatment of H3K27M-Mutant Pediatric Diffuse Gliomas Provides

Improved Therapeutic Opportunities. *Front Oncol*, *9*, 1436. https://doi.org/10.3389/fonc.2019.01436

Grasso, C. S., Tang, Y., Truffaux, N., Berlow, N. E., Liu, L., Debily, M.-A., Quist, M. J., Davis, L. E., Huang, E. C., & Woo, P. J. (2015). Functionally defined therapeutic targets in diffuse intrinsic pontine glioma. *Nature Medicine*, *21*(6), 555–559.

Greer, Y. E., Porat-Shliom, N., Nagashima, K., Stuelten, C., Crooks, D., Koparde, V. N., Gilbert, S. F., Islam, C., Ubaldini, A., & Ji, Y. (2018). ONC201 kills breast cancer cells in vitro by targeting mitochondria. *Oncotarget*, *9*(26), 18454.

Grill, J., Massimino, M., Bouffet, E., Azizi, A. A., McCowage, G., Cañete, A., Saran, F., Le Deley, M.-C., Varlet, P., Morgan, P. S., Jaspan, T., Jones, C., Giangaspero, F., Smith, H., Garcia, J., Elze, M. C., Rousseau, R. F., Abrey, L., Hargrave, D., & Vassal, G. (2018). Phase II, Open-Label, Randomized, Multicenter Trial (HERBY) of Bevacizumab in Pediatric Patients With Newly Diagnosed High-Grade Glioma. *Journal of Clinical Oncology : Official Journal of the American Society of Clinical Oncology*, *36*(10), 951–958. https://doi.org/10.1200/JCO.2017.76.0611

Halbrook, C. J., Pontious, C., Kovalenko, I., Lapienyte, L., Dreyer, S., Lee, H.-J., Thurston, G., Zhang, Y., Lazarus, J., Sajjakulnukit, P., Hong, H. S., Kremer, D. M., Nelson, B. S., Kemp, S., Zhang, L., Chang, D., Biankin, A., Shi, J., Frankel, T. L., … Lyssiotis, C. A. (2019). Macrophage-Released Pyrimidines Inhibit Gemcitabine Therapy in Pancreatic Cancer. *Cell Metabolism*, *29*(6), 1390-1399.e6. https://doi.org/https://doi.org/10.1016/j.cmet.2019.02.001

Hanahan, D, & Weinberg, R. A. (2000). The hallmarks of cancer. *Cell*, *100*(1), 57–70. https://doi.org/10.1016/s0092-8674(00)81683-9

Hanahan, Douglas, & Weinberg, R. A. (2011). Hallmarks of cancer: the next generation. *Cell*, *144*(5), 646–674. https://doi.org/10.1016/j.cell.2011.02.013

Harpaz, N., Mittelman, T., Beresh, O., Griess, O., Furth, N., Salame, T.-M., Oren, R., Fellus-Alyagor, L., Harmelin, A., & Alexandrescu, S. (2022). Single-cell epigenetic analysis reveals principles of chromatin states in H3. 3-K27M gliomas. *Molecular Cell*, *82*(14), 2696–2713.

Harutyunyan, A. S., Krug, B., Chen, H., Papillon-Cavanagh, S., Zeinieh, M., De Jay, N., Deshmukh, S., Chen, C. C. L., Belle, J., Mikael, L. G., Marchione, D. M., Li, R., Nikbakht, H., Hu, B., Cagnone, G., Cheung, W. A., Mohammadnia, A., Bechet, D., Faury, D., … Majewski, J. (2019). H3K27M induces defective chromatin spread of PRC2-mediated repressive H3K27me2/me3 and is essential for glioma tumorigenesis. *Nat Commun*, *10*(1), 1262. https://doi.org/10.1038/s41467-019-09140-x

Hashizume, R., Andor, N., Ihara, Y., Lerner, R., Gan, H., Chen, X., Fang, D., Huang, X., Tom, M. W., & Ngo, V. (2014). Pharmacologic inhibition of histone demethylation as a therapy for pediatric brainstem glioma. *Nature Medicine*, *20*(12), 1394–1396.

Heitz, E. (1928). Der bilaterale Bau der Geschlechtschromosomen und Autosomen bei Pellia

fabbroniana, P. epiphylla und einigen anderen Jungermanniaceen. *Zeitschrift Fur Wissenschaftliche Biologie. Abteilung E: Planta*, 725–768.

Hendrikse, L. D., Haldipur, P., Saulnier, O., Millman, J., Sjoboen, A. H., Erickson, A. W., Ong, W., Gordon, V., Coudière-Morrison, L., & Mercier, A. L. (2022). Failure of human rhombic lip differentiation underlies medulloblastoma formation. *Nature*, *609*(7929), 1021–1028.

Hernandez, R. E., Putzke, A. P., Myers, J. P., Margaretha, L., & Moens, C. B. (2007). *Cyp26 enzymes generate the retinoic acid response pattern necessary for hindbrain development*.

Hnisz, D., Abraham, B. J., Lee, T. I., Lau, A., Saint-André, V., Sigova, A. A., Hoke, H. A., & Young, R. A. (2013). Super-Enhancers in the Control of Cell Identity and Disease. *Cell*, *155*(4), 934–947. https://doi.org/https://doi.org/10.1016/j.cell.2013.09.053

Hoeman, C. M., Cordero, F. J., Hu, G., Misuraca, K., Romero, M. M., Cardona, H. J., Nazarian, J., Hashizume, R., McLendon, R., Yu, P., Procissi, D., Gadd, S., & Becher, O. J. (2019). ACVR1 R206H cooperates with H3.1K27M in promoting diffuse intrinsic pontine glioma pathogenesis. *Nature Communications*, *10*(1), 1023. https://doi.org/10.1038/s41467-019-08823-9

Hoffman, L. M., Veldhuijzen van Zanten, S. E. M., Colditz, N., Baugh, J., Chaney, B., Hoffmann, M., Lane, A., Fuller, C., Miles, L., Hawkins, C., Bartels, U., Bouffet, E., Goldman, S., Leary, S., Foreman, N. K., Packer, R., Warren, K. E., Broniscer, A., Kieran, M. W., … Fouladi, M. (2018). Clinical, Radiologic, Pathologic, and Molecular Characteristics of Long-Term Survivors of Diffuse Intrinsic Pontine Glioma (DIPG): A Collaborative Report From the International and European Society for Pediatric Oncology DIPG Registries. *Journal of Clinical Oncology*, *36*(19), 1963–1972. https://doi.org/10.1200/JCO.2017.75.9308

Horbinski, C., Berger, T., Packer, R. J., & Wen, P. Y. (2022). Clinical implications of the 2021 edition of the WHO classification of central nervous system tumours. *Nature Reviews Neurology*, *18*(9), 515–529. https://doi.org/10.1038/s41582-022-00679-w

Hu, X., Deng, K., Ye, H., Sun, Z., Huang, W., Sun, Y., & Yan, W. (2021). Trends in Tumor Site-Specific Survival of Bone Sarcomas from 1980 to 2018: A Surveillance, Epidemiology and End Results-Based Study. *Cancers*, *13*(21). https://doi.org/10.3390/cancers13215381

Hübner, J.-M., Kool, M., Pfister, S. M., & Pajtler, K. W. (2018). Epidemiology, molecular classification and WHO grading of ependymoma. *Journal of Neurosurgical Sciences*, *62*(1), 46–50. https://doi.org/10.23736/s0390-5616.17.04152-2

Hubner, J. M., Muller, T., Papageorgiou, D. N., Mauermann, M., Krijgsveld, J., Russell, R. B., Ellison, D. W., Pfister, S. M., Pajtler, K. W., & Kool, M. (2019). EZHIP/CXorf67 mimics K27M mutated oncohistones and functions as an intrinsic inhibitor of PRC2 function in aggressive posterior fossa ependymoma. *Neuro Oncol*, *21*(7), 878–889. https://doi.org/10.1093/neuonc/noz058

Hung, Y. P., Diaz-Perez, J. A., Cote, G. M., Wejde, J., Schwab, J. H., Nardi, V., Chebib, I. A.,

Deshpande, V., Selig, M. K., Bredella, M. A., Rosenberg, A. E., & Nielsen, G. P. (2020). Dedifferentiated Chordoma: Clinicopathologic and Molecular Characteristics With Integrative Analysis. *The American Journal of Surgical Pathology*, *44*(9), 1213–1223. https://doi.org/10.1097/PAS.0000000000001501

Intlekofer, A. M., Wang, B., Liu, H., Shah, H., Carmona-Fontaine, C., Rustenburg, A. S., Salah, S., Gunner, M. R., Chodera, J. D., Cross, J. R., & Thompson, C. B. (2017). L-2-Hydroxyglutarate production arises from noncanonical enzyme function at acidic pH. *Nature Chemical Biology*, *13*(5), 494–500. https://doi.org/10.1038/nchembio.2307

Ishizawa, J. O., Kojima, K., Chachad, D., Ruvolo, P., Ruvolo, V., Jacamo, R. O., Borthakur, G., Mu, H., Zeng, Z., & Tabe, Y. (2016). ATF4 induction through an atypical integrated stress response to ONC201 triggers p53-independent apoptosis in hematological malignancies. *Science Signaling*, *9*(415), ra17–ra17.

Ishizawa, J., Zarabi, S. F., Davis, R. E., Halgas, O., Nii, T., Jitkova, Y., Zhao, R., St-Germain, J., Heese, L. E., Egan, G., Ruvolo, V. R., Barghout, S. H., Nishida, Y., Hurren, R., Ma, W., Gronda, M., Link, T., Wong, K., Mabanglo, M., … Andreeff, M. (2019). Mitochondrial ClpP-Mediated Proteolysis Induces Selective Cancer Cell Lethality. *Cancer Cell*, *35*(5), 721-737.e9. https://doi.org/https://doi.org/10.1016/j.ccell.2019.03.014

Jain, S U, Do, T. J., Lund, P. J., Rashoff, A. Q., Diehl, K. L., Cieslik, M., Bajic, A., Juretic, N., Deshmukh, S., Venneti, S., Muir, T. W., Garcia, B. A., Jabado, N., & Lewis, P. W. (2019). PFA ependymoma-associated protein EZHIP inhibits PRC2 activity through a H3 K27M-like mechanism. *Nat Commun*, *10*(1), 2146. https://doi.org/10.1038/s41467-019-09981-6

Jain, Siddhant U, Khazaei, S., Marchione, D. M., Lundgren, S. M., Wang, X., Weinberg, D. N., Deshmukh, S., Juretic, N., Lu, C., & Allis, C. D. (2020). Histone H3. 3 G34 mutations promote aberrant PRC2 activity and drive tumor progression. *Proceedings of the National Academy of Sciences*, *117*(44), 27354–27364.

Jain, Siddhant U, Rashoff, A. Q., Krabbenhoft, S. D., Hoelper, D., Do, T. J., Gibson, T. J., Lundgren, S. M., Bondra, E. R., Deshmukh, S., Harutyunyan, A. S., Juretic, N., Jabado, N., Harrison, M. M., & Lewis, P. W. (2020). H3 K27M and EZHIP Impede H3K27-Methylation Spreading by Inhibiting Allosterically Stimulated PRC2. *Molecular Cell*, *80*(4), 726-735.e7. https://doi.org/https://doi.org/10.1016/j.molcel.2020.09.028

Janzer, A., German, N. J., Gonzalez-Herrera, K. N., Asara, J. M., Haigis, M. C., & Struhl, K. (2014). Metformin and phenformin deplete tricarboxylic acid cycle and glycolytic intermediates during cell transformation and NTPs in cancer stem cells. *Proceedings of the National Academy of Sciences*, *111*(29), 10574–10579.

Jeon, H. H., Yu, Q., Witek, L., Lu, Y., Zhang, T., Stepanchenko, O., Son, V. J., Spencer, E., Oshilaja, T., Shin, M. K., Alawi, F., Coelho, P. G., & Graves, D. T. (2021). Clinical application of a FOXO1 inhibitor improves connective tissue healing in a diabetic minipig model. *American Journal of Translational Research*, *13*(2), 781–791.

Jessa, S., Blanchet-Cohen, A., Krug, B., Vladoiu, M., Coutelier, M., Faury, D., Poreau, B., De

Jay, N., Hébert, S., & Monlong, J. (2019). Stalled developmental programs at the root of pediatric brain tumors. *Nature Genetics*, *51*(12), 1702–1713.

Jessa, S., Mohammadnia, A., Harutyunyan, A. S., Hulswit, M., Varadharajan, S., Lakkis, H., Kabir, N., Bashardanesh, Z., Hébert, S., & Faury, D. (2022). K27M in canonical and noncanonical H3 variants occurs in distinct oligodendroglial cell lineages in brain midline gliomas. *Nature Genetics*, 1–16.

Jones, C., & Baker, S. J. (2014). Unique genetic and epigenetic mechanisms driving paediatric diffuse high-grade glioma. *Nature Reviews Cancer*, *14*(10), 651–661. https://doi.org/10.1038/nrc3811

Jones, C., Karajannis, M. A., Jones, D. T. W., Kieran, M. W., Monje, M., Baker, S. J., Becher, O. J., Cho, Y.-J., Gupta, N., Hawkins, C., Hargrave, D., Haas-Kogan, D. A., Jabado, N., Li, X.-N., Mueller, S., Nicolaides, T., Packer, R. J., Persson, A. I., Phillips, J. J., … Weiss, W. A. (2017). Pediatric high-grade glioma: biologically and clinically in need of new thinking. *Neuro-Oncology*, *19*(2), 153–161. https://doi.org/10.1093/neuonc/now101

Kadoch, C., Hargreaves, D. C., Hodges, C., Elias, L., Ho, L., Ranish, J., & Crabtree, G. R. (2013). Proteomic and bioinformatic analysis of mammalian SWI/SNF complexes identifies extensive roles in human malignancy. *Nature Genetics*, *45*(6), 592–601.

Kerr, D. L., Dial, B. L., Lazarides, A. L., Catanzano, A. A., Lane, W. O., Blazer, D. G., Brigman, B. E., Mendoza-Lattes, S., Eward, W. C., & Erickson, M. E. (2019). Epidemiologic and survival trends in adult primary bone tumors of the spine. *The Spine Journal*, *19*(12), 1941–1949. https://doi.org/https://doi.org/10.1016/j.spinee.2019.07.003

Khazaei, S., De Jay, N., Deshmukh, S., Hendrikse, L. D., Jawhar, W., Chen, C. C. L., Mikael, L. G., Faury, D., Marchione, D. M., & Lanoix, J. (2020). H3. 3 G34W Promotes Growth and Impedes Differentiation of Osteoblast-Like Mesenchymal Progenitors in Giant Cell Tumor of BoneH3. 3 G34W Impedes Differentiation of Osteoprogenitors in GCT. *Cancer Discovery*, *10*(12), 1968–1987.

Kilday, J.-P., Rahman, R., Dyer, S., Ridley, L., Lowe, J., Coyle, B., & Grundy, R. (2009). Pediatric ependymoma: biological perspectives. *Molecular Cancer Research : MCR*, *7*(6), 765–786. https://doi.org/10.1158/1541-7786.MCR-08-0584

Kim, J., Lee, I.-H., Cho, H. J., Park, C.-K., Jung, Y.-S., Kim, Y., Nam, S. H., Kim, B. S., Johnson, M. D., Kong, D.-S., Seol, H. J., Lee, J.-I., Joo, K. M., Yoon, Y., Park, W.-Y., Lee, J., Park, P. J., & Nam, D.-H. (2015). Spatiotemporal Evolution of the Primary Glioblastoma Genome. *Cancer Cell*, *28*(3), 318–328. https://doi.org/10.1016/j.ccell.2015.07.013

Kline, C., Jain, P., Kilburn, L., Bonner, E. R., Gupta, N., Crawford, J. R., Banerjee, A., Packer, R. J., Villanueva-Meyer, J., Luks, T., Zhang, Y., Kambhampati, M., Zhang, J., Yadavilli, S., Zhang, B., Gaonkar, K. S., Rokita, J. L., Kraya, A., Kuhn, J., … Mueller, S. (2022). Upfront Biology-Guided Therapy in Diffuse Intrinsic Pontine Glioma: Therapeutic, Molecular, and Biomarker Outcomes from PNOC003. *Clinical Cancer Research : An Official Journal of the American Association for Cancer Research*, *28*(18), 3965–3978.

https://doi.org/10.1158/1078-0432.CCR-22-0803

Kline, C. L. B., Van den Heuvel, A. P. J., Allen, J. E., Prabhu, V. V, Dicker, D. T., & El-Deiry, W. S. (2016). ONC201 kills solid tumor cells by triggering an integrated stress response dependent on ATF4 activation by specific eIF2α kinases. *Science Signaling*, *9*(415), ra18–ra18.

Kolasinska-Zwierz, P., Down, T., Latorre, I., Liu, T., Liu, X. S., & Ahringer, J. (2009). Differential chromatin marking of introns and expressed exons by H3K36me3. *Nature Genetics*, *41*(3), 376–381. https://doi.org/10.1038/ng.322

Kornberg, R. D., & Thomas, J. O. (1974). Chromatin Structure: Oligomers of the Histones. *Science*, *184*(4139), 865–868. https://doi.org/10.1126/science.184.4139.865

Kranendijk, M., Struys, E. A., Salomons, G. S., Van der Knaap, M. S., & Jakobs, C. (2012). Progress in understanding 2-hydroxyglutaric acidurias. *Journal of Inherited Metabolic Disease*, *35*(4), 571–587. https://doi.org/10.1007/s10545-012-9462-5

Krug, B., De Jay, N., Harutyunyan, A. S., Deshmukh, S., Marchione, D. M., Guilhamon, P., Bertrand, K. C., Mikael, L. G., McConechy, M. K., Chen, C. C. L., Khazaei, S., Koncar, R. F., Agnihotri, S., Faury, D., Ellezam, B., Weil, A. G., Ursini-Siegel, J., De Carvalho, D. D., Dirks, P. B., … Mack, S. C. (2019a). Pervasive H3K27 Acetylation Leads to ERV Expression and a Therapeutic Vulnerability in H3K27M Gliomas. *Cancer Cell*, *35*(5), 782-797.e8. https://doi.org/10.1016/j.ccell.2019.04.004

Krug, B., De Jay, N., Harutyunyan, A. S., Deshmukh, S., Marchione, D. M., Guilhamon, P., Bertrand, K. C., Mikael, L. G., McConechy, M. K., Chen, C. C. L., Khazaei, S., Koncar, R. F., Agnihotri, S., Faury, D., Ellezam, B., Weil, A. G., Ursini-Siegel, J., De Carvalho, D. D., Dirks, P. B., … Mack, S. C. (2019b). Pervasive H3K27 Acetylation Leads to ERV Expression and a Therapeutic Vulnerability in H3K27M Gliomas. *Cancer Cell*, *36*(3), 338–339. https://doi.org/10.1016/j.ccell.2019.08.012

Kuleshov, M. V, Jones, M. R., Rouillard, A. D., Fernandez, N. F., Duan, Q., Wang, Z., Koplev, S., Jenkins, S. L., Jagodnik, K. M., Lachmann, A., McDermott, M. G., Monteiro, C. D., Gundersen, G. W., & Ma'ayan, A. (2016). Enrichr: a comprehensive gene set enrichment analysis web server 2016 update. *Nucleic Acids Research*, *44*(W1), W90-7. https://doi.org/10.1093/nar/gkw377

Kupp, R., Ruff, L., Terranova, S., Nathan, E., Ballereau, S., Stark, R., Sekhar Reddy Chilamakuri, C., Hoffmann, N., Wickham-Rahrmann, K., & Widdess, M. (2021). ZFTA Translocations Constitute Ependymoma Chromatin Remodeling and Transcription FactorsOncogenic Mechanism of Ependymoma ZFTA-Fusion Proteins. *Cancer Discovery*, *11*(9), 2216–2229.

Langmoen, I. A., Lundar, T., Storm-Mathisen, I., Lie, S. O., & Hovind, K. H. (1991). Management of pediatric pontine gliomas. *Child's Nervous System*, *7*(1), 13–15. https://doi.org/10.1007/BF00263825

Lee, H.-J., Kremer, D. M., Sajjakulnukit, P., Zhang, L., & Lyssiotis, C. A. (2019). A large-scale analysis of targeted metabolomics data from heterogeneous biological samples provides insights into metabolite dynamics. *Metabolomics*, *15*, 1–13.

Lee, I. J., Lee, R. J., & Fahim, D. K. (2017). Prognostic factors and survival outcome in patients with chordoma in the United States: a population-based analysis. *World Neurosurgery*, *104*, 346–355.

Leffak, I. M., Grainger, R., & Weintraub, H. (1977). Conservative assembly and segregation of nucleosomal histones. *Cell*, *12*(3), 837–845. https://doi.org/10.1016/0092-8674(77)90282-3

Lewis, P. W., Muller, M. M., Koletsky, M. S., Cordero, F., Lin, S., Banaszynski, L. A., Garcia, B. A., Muir, T. W., Becher, O. J., & Allis, C. D. (2013). Inhibition of PRC2 activity by a gain-of-function H3 mutation found in pediatric glioblastoma. *Science*, *340*(6134), 857–861. https://doi.org/10.1126/science.1232245

Li, B., & Dewey, C. N. (2011). RSEM: accurate transcript quantification from RNA-Seq data with or without a reference genome. *BMC Bioinformatics*, *12*, 323. https://doi.org/10.1186/1471-2105-12-323

Li, S., Garrett-Bakelman, F. E., Akalin, A., Zumbo, P., Levine, R., To, B. L., Lewis, I. D., Brown, A. L., D'Andrea, R. J., Melnick, A., & Mason, C. E. (2013). An optimized algorithm for detecting and annotating regional differential methylation. *BMC Bioinformatics*, *14*(5), S10. https://doi.org/10.1186/1471-2105-14-S5-S10

Lien, E. C., Lyssiotis, C. A., & Cantley, L. C. (2016). Metabolic Reprogramming by the PI3K-Akt-mTOR Pathway in Cancer. *Recent Results in Cancer Research. Fortschritte Der Krebsforschung. Progres Dans Les Recherches Sur Le Cancer*, *207*, 39–72. https://doi.org/10.1007/978-3-319-42118-6_3

Lind, G. E., Kleivi, K., Meling, G. I., Teixeira, M. R., Thiis-Evensen, E., Rognum, T. O., & Lothe, R. A. (2006). ADAMTS1, CRABP1, and NR3C1 identified as epigenetically deregulated genes in colorectal tumorigenesis. *Analytical Cellular Pathology*, *28*(5–6), 259–272.

Liu, I., Jiang, L., Samuelsson, E. R., Marco Salas, S., Beck, A., Hack, O. A., Jeong, D., Shaw, M. L., Englinger, B., LaBelle, J., Mire, H. M., Madlener, S., Mayr, L., Quezada, M. A., Trissal, M., Panditharatna, E., Ernst, K. J., Vogelzang, J., Gatesman, T. A., … Filbin, M. G. (2022). The landscape of tumor cell states and spatial organization in H3-K27M mutant diffuse midline glioma across age and location. *Nature Genetics*, *54*(12), 1881–1894. https://doi.org/10.1038/s41588-022-01236-3

Liu, R.-Z., Garcia, E., Glubrecht, D. D., Poon, H. Y., Mackey, J. R., & Godbout, R. (2015). CRABP1 is associated with a poor prognosis in breast cancer: adding to the complexity of breast cancer cell response to retinoic acid. *Molecular Cancer*, *14*(1), 1–16.

Lobon-Iglesias, M. J., Giraud, G., Castel, D., Philippe, C., Debily, M. A., Briandet, C., Fouyssac, F., de Carli, E., Dufour, C., Valteau-Couanet, D., Sainte-Rose, C., Blauwblomme, T.,

Beccaria, K., Zerah, M., Puget, S., Calmon, R., Boddaert, N., Bolle, S., Varlet, P., & Grill, J. (2018). Diffuse intrinsic pontine gliomas (DIPG) at recurrence: is there a window to test new therapies in some patients? *Journal of Neuro-Oncology*, *137*(1), 111–118. https://doi.org/10.1007/s11060-017-2702-7

Losman, J.-A., & Kaelin, W. G. (2013). What a difference a hydroxyl makes: mutant IDH,(R)-2-hydroxyglutarate, and cancer. *Genes & Development*, *27*(8), 836–852.

Louis, D. N., Holland, E. C., & Cairncross, J. G. (2001). Glioma classification: a molecular reappraisal. *The American Journal of Pathology*, *159*(3), 779–786.

Louis, D. N., Perry, A., Wesseling, P., Brat, D. J., Cree, I. A., Figarella-Branger, D., Hawkins, C., Ng, H. K., Pfister, S. M., Reifenberger, G., Soffietti, R., von Deimling, A., & Ellison, D. W. (2021). The 2021 WHO Classification of Tumors of the Central Nervous System: a summary. *Neuro-Oncology*, *23*(8), 1231–1251. https://doi.org/10.1093/neuonc/noab106

Love, M. I., Huber, W., & Anders, S. (2014). Moderated estimation of fold change and dispersion for RNA-seq data with DESeq2. *Genome Biology*, *15*(12), 550. https://doi.org/10.1186/s13059-014-0550-8

Lu, C., Ward, P. S., Kapoor, G. S., Rohle, D., Turcan, S., Abdel-Wahab, O., Edwards, C. R., Khanin, R., Figueroa, M. E., Melnick, A., Wellen, K. E., O'Rourke, D. M., Berger, S. L., Chan, T. A., Levine, R. L., Mellinghoff, I. K., & Thompson, C. B. (2012). IDH mutation impairs histone demethylation and results in a block to cell differentiation. *Nature*, *483*(7390), 474–478. https://doi.org/10.1038/nature10860

Mack, S C, Witt, H., Piro, R. M., Gu, L., Zuyderduyn, S., Stütz, A. M., Wang, X., Gallo, M., Garzia, L., Zayne, K., Zhang, X., Ramaswamy, V., Jäger, N., Jones, D. T. W., Sill, M., Pugh, T. J., Ryzhova, M., Wani, K. M., Shih, D. J. H., … Taylor, M. D. (2014). Epigenomic alterations define lethal CIMP-positive ependymomas of infancy. *Nature*, *506*(7489), 445–450. https://doi.org/10.1038/nature13108

Mack, Stephen C, Pajtler, K. W., Chavez, L., Okonechnikov, K., Bertrand, K. C., Wang, X., Erkek, S., Federation, A., Song, A., Lee, C., Wang, X., McDonald, L., Morrow, J. J., Saiakhova, A., Sin-Chan, P., Wu, Q., Michaelraj, K. A., Miller, T. E., Hubert, C. G., … Rich, J. N. (2018). Therapeutic targeting of ependymoma as informed by oncogenic enhancer profiling. *Nature*, *553*(7686), 101–105. https://doi.org/10.1038/nature25169

Mackay, A., Burford, A., Carvalho, D., Izquierdo, E., Fazal-Salom, J., Taylor, K. R., Bjerke, L., Clarke, M., Vinci, M., Nandhabalan, M., Temelso, S., Popov, S., Molinari, V., Raman, P., Waanders, A. J., Han, H. J., Gupta, S., Marshall, L., Zacharoulis, S., … Jones, C. (2017). Integrated Molecular Meta-Analysis of 1,000 Pediatric High-Grade and Diffuse Intrinsic Pontine Glioma. *Cancer Cell*, *32*(4), 520-537.e5. https://doi.org/10.1016/j.ccell.2017.08.017

Mackay, A., Burford, A., Molinari, V., Jones, D. T. W., Izquierdo, E., Brouwer-Visser, J., Giangaspero, F., Haberler, C., Pietsch, T., Jacques, T. S., Figarella-Branger, D., Rodriguez, D., Morgan, P. S., Raman, P., Waanders, A. J., Resnick, A. C., Massimino, M., Garrè, M. L., Smith, H., … Jones, C. (2018). Molecular, Pathological, Radiological, and Immune

Profiling of Non-brainstem Pediatric High-Grade Glioma from the HERBY Phase II Randomized Trial. *Cancer Cell*, *33*(5), 829-842.e5. https://doi.org/10.1016/j.ccell.2018.04.004

Maden, M., Horton, C., Graham, A., Leonard, L., Pizzey, J., Siegenthaler, G., Lumsden, A., & Eriksson, U. (1992). Domains of cellular retinoic acid-binding protein I (CRABP I) expression in the hindbrain and neural crest of the mouse embryo. *Mechanisms of Development*, *37*(1–2), 13–23.

Maintz, D., Fiedler, K., Koopmann, J., Rollbrocker, B., Nechev, S., Lenartz, D., Stangl, A. P., Louis, D. N., Schramm, J., Wiestler, O. D., & von Deimling, A. (1997). Molecular Genetic Evidence for Subtypes of Oligoastrocytomas. *Journal of Neuropathology & Experimental Neurology*, *56*(10), 1098–1104. https://doi.org/10.1097/00005072-199710000-00003

Mariet, C., Castel, D., Grill, J., Saffroy, R., Dangouloff-Ros, V., Boddaert, N., Llamas-Guttierrez, F., Chappé, C., Puget, S., & Hasty, L. (2022). Posterior fossa ependymoma H3 K27-mutant: an integrated radiological and histomolecular tumor analysis. *Acta Neuropathologica Communications*, *10*(1), 1–13.

Marshall, H., Nonchev, S., Sham, M. H., Muchamore, I., Lumsden, A., & Krumlauf, R. (1992). Retinoic acid alters hindbrain Hox code and induces transformation of rhombomeres 2/3 into a 4/5 identity. *Nature*, *360*(6406), 737–741.

Martin, M. (2011). Cutadapt removes adapter sequences from high-throughput sequencing reads. *EMBnet. Journal*, *17*(1), 10–12.

McMaster, M. L., Goldstein, A. M., Bromley, C. M., Ishibe, N., & Parry, D. M. (2001). Chordoma: incidence and survival patterns in the United States, 1973–1995. *Cancer Causes & Control*, *12*(1), 1–11.

McNamara, C., Mankad, K., Thust, S., Dixon, L., Limback-Stanic, C., D'Arco, F., Jacques, T. S., & Löbel, U. (2022). 2021 WHO classification of tumours of the central nervous system: a review for the neuroradiologist. *Neuroradiology*, *64*(10), 1919–1950. https://doi.org/10.1007/s00234-022-03008-6

Mendrzyk, F., Korshunov, A., Benner, A., Toedt, G., Pfister, S., Radlwimmer, B., & Lichter, P. (2006). Identification of gains on 1q and epidermal growth factor receptor overexpression as independent prognostic markers in intracranial ependymoma. *Clinical Cancer Research : An Official Journal of the American Association for Cancer Research*, *12*(7 Pt 1), 2070–2079. https://doi.org/10.1158/1078-0432.CCR-05-2363

Michealraj, K. A., Kumar, S. A., Kim, L. J. Y., Cavalli, F. M. G., Przelicki, D., Wojcik, J. B., Delaidelli, A., Bajic, A., Saulnier, O., MacLeod, G., Vellanki, R. N., Vladoiu, M. C., Guilhamon, P., Ong, W., Lee, J. J. Y., Jiang, Y., Holgado, B. L., Rasnitsyn, A., Malik, A. A., … Taylor, M. D. (2020). Metabolic Regulation of the Epigenome Drives Lethal Infantile Ependymoma. *Cell*. https://doi.org/10.1016/j.cell.2020.04.047

Mikkelsen, T. S., Ku, M., Jaffe, D. B., Issac, B., Lieberman, E., Giannoukos, G., Alvarez, P.,

Brockman, W., Kim, T.-K., Koche, R. P., Lee, W., Mendenhall, E., O'Donovan, A., Presser, A., Russ, C., Xie, X., Meissner, A., Wernig, M., Jaenisch, R., … Bernstein, B. E. (2007). Genome-wide maps of chromatin state in pluripotent and lineage-committed cells. *Nature*, *448*(7153), 553–560. https://doi.org/10.1038/nature06008

Miller, J. A., Ding, S.-L., Sunkin, S. M., Smith, K. A., Ng, L., Szafer, A., Ebbert, A., Riley, Z. L., Royall, J. J., & Aiona, K. (2014). Transcriptional landscape of the prenatal human brain. *Nature*, *508*(7495), 199–206.

Miller, K. D., Ostrom, Q. T., Kruchko, C., Patil, N., Tihan, T., Cioffi, G., Fuchs, H. E., Waite, K. A., Jemal, A., Siegel, R. L., & Barnholtz-Sloan, J. S. (2021). Brain and other central nervous system tumor statistics, 2021. *CA: A Cancer Journal for Clinicians*, *71*(5), 381–406. https://doi.org/10.3322/caac.21693

Mito, Y., Henikoff, J. G., & Henikoff, S. (2005). Genome-scale profiling of histone H3. 3 replacement patterns. *Nature Genetics*, *37*(10), 1090–1097.

Mo, Y., Duan, S., Zhang, X., Hua, X., Zhou, H., Wei, H.-J., Watanabe, J., McQuillan, N., Su, Z., & Gu, W. (2022). Epigenome programming by H3. 3K27M mutation creates a dependence of pediatric glioma on SMARCA4. *Cancer Discovery*, *12*(12), 2906–2929.

Mohammad, F., Weissmann, S., Leblanc, B., Pandey, D. P., Hojfeldt, J. W., Comet, I., Zheng, C., Johansen, J. V, Rapin, N., Porse, B. T., Tvardovskiy, A., Jensen, O. N., Olaciregui, N. G., Lavarino, C., Sunol, M., de Torres, C., Mora, J., Carcaboso, A. M., & Helin, K. (2017). EZH2 is a potential therapeutic target for H3K27M-mutant pediatric gliomas. *Nat Med*, *23*(4), 483–492. https://doi.org/10.1038/nm.4293

Müller, H. (1858). Über das Vorkommen von Resten des Chorda dorsalis bei Menschen nach der Geburt und über ihr Verhältniss zu den Gallertgeschwülesten am Clivus. *Z Ration Med*, *2*, 202–229.

Nagaraja, S., Quezada, M. A., Gillespie, S. M., Arzt, M., Lennon, J. J., Woo, P. J., Hovestadt, V., Kambhampati, M., Filbin, M. G., Suva, M. L., Nazarian, J., & Monje, M. (2019). Histone Variant and Cell Context Determine H3K27M Reprogramming of the Enhancer Landscape and Oncogenic State. *Mol Cell*, *76*(6), 965-980.e12. https://doi.org/10.1016/j.molcel.2019.08.030

Nagaraja, S., Vitanza, N. A., Woo, P. J., Taylor, K. R., Liu, F., Zhang, L., Li, M., Meng, W., Ponnuswami, A., Sun, W., Ma, J., Hulleman, E., Swigut, T., Wysocka, J., Tang, Y., & Monje, M. (2017). Transcriptional Dependencies in Diffuse Intrinsic Pontine Glioma. *Cancer Cell*, *31*(5), 635-652.e6. https://doi.org/10.1016/j.ccell.2017.03.011

Naiche, L. A., Harrelson, Z., Kelly, R. G., & Papaioannou, V. E. (2005). T-Box Genes in Vertebrate Development. *Annual Review of Genetics*, *39*(1), 219–239. https://doi.org/10.1146/annurev.genet.39.073003.105925

Newell-Price, J., Clark, A. J. L., & King, P. (2000). DNA methylation and silencing of gene expression. *Trends in Endocrinology & Metabolism*, *11*(4), 142–148.

Nhieu, J., Lin, Y.-L., & Wei, L.-N. (2022). CRABP1 in Non-Canonical Activities of Retinoic Acid in Health and Diseases. *Nutrients*, *14*(7), 1528.

Niederreither, K., Vermot, J., Schuhbaur, B., Chambon, P., & Dollé, P. (2000). Retinoic acid synthesis and hindbrain patterning in the mouse embryo. *Development*, *127*(1), 75–85.

Noushmehr, H., Weisenberger, D. J., Diefes, K., Phillips, H. S., Pujara, K., Berman, B. P., Pan, F., Pelloski, C. E., Sulman, E. P., Bhat, K. P., Verhaak, R. G. W., Hoadley, K. A., Hayes, D. N., Perou, C. M., Schmidt, H. K., Ding, L., Wilson, R. K., Van Den Berg, D., Shen, H., … Aldape, K. (2010). Identification of a CpG island methylator phenotype that defines a distinct subgroup of glioma. *Cancer Cell*, *17*(5), 510–522. https://doi.org/10.1016/j.ccr.2010.03.017

O'Neill, L. A. J., & Artyomov, M. N. (2019). Itaconate: the poster child of metabolic reprogramming in macrophage function. *Nature Reviews Immunology*, *19*(5), 273–281.

O'Rahilly, R., & Müller, F. (2010). Developmental stages in human embryos: revised and new measurements. *Cells Tissues Organs*, *192*(2), 73–84.

Olson, J. T., Wenger, D. E., Rose, P. S., Petersen, I. A., & Broski, S. M. (2021). Chordoma: 18F-FDG PET/CT and MRI imaging features. *Skeletal Radiology*, *50*(8), 1657–1666. https://doi.org/10.1007/s00256-021-03723-w

Ostroumov, E., & Hunter, C. J. (2007). The role of extracellular factors in human metastatic chordoma cell growth in vitro. *Spine*, *32*(26), 2957–2964. https://doi.org/10.1097/BRS.0b013e31815cde91

Owen, O. E., Kalhan, S. C., & Hanson, R. W. (2002). The Key Role of Anaplerosis and Cataplerosis for Citric Acid Cycle Function*. *Journal of Biological Chemistry*, *277*(34), 30409–30412. https://doi.org/https://doi.org/10.1074/jbc.R200006200

Pajtler, K W, Wen, J., Sill, M., Lin, T., Orisme, W., Tang, B., Hubner, J. M., Ramaswamy, V., Jia, S., Dalton, J. D., Haupfear, K., Rogers, H. A., Punchihewa, C., Lee, R., Easton, J., Wu, G., Ritzmann, T. A., Chapman, R., Chavez, L., … Ellison, D. W. (2018). Molecular heterogeneity and CXorf67 alterations in posterior fossa group A (PFA) ependymomas. *Acta Neuropathol*, *136*(2), 211–226. https://doi.org/10.1007/s00401-018-1877-0

Pajtler, Kristian W, Witt, H., Sill, M., Jones, D. T. W., Hovestadt, V., Kratochwil, F., Wani, K., Tatevossian, R., Punchihewa, C., Johann, P., Reimand, J., Warnatz, H.-J., Ryzhova, M., Mack, S., Ramaswamy, V., Capper, D., Schweizer, L., Sieber, L., Wittmann, A., … Pfister, S. M. (2015). Molecular Classification of Ependymal Tumors across All CNS Compartments, Histopathological Grades, and Age Groups. *Cancer Cell*, *27*(5), 728–743. https://doi.org/10.1016/j.ccell.2015.04.002

Panditharatna, E., Marques, J. G., Wang, T., Trissal, M. C., Liu, I., Jiang, L., Beck, A., Groves, A., Dharia, N. V, & Li, D. (2022). BAF complex maintains glioma stem cells in pediatric H3K27M glioma. *Cancer Discovery*, *12*(12), 2880–2905.

Panwalkar, P., Clark, J., Ramaswamy, V., Hawes, D., Yang, F., Dunham, C., Yip, S., Hukin, J., Sun, Y., Schipper, M. J., Chavez, L., Margol, A., Pekmezci, M., Chung, C., Banda, A., Bayliss, J. M., Curry, S. J., Santi, M., Rodriguez, F. J., … Venneti, S. (2017). Immunohistochemical analysis of H3K27me3 demonstrates global reduction in group-A childhood posterior fossa ependymoma and is a powerful predictor of outcome. *Acta Neuropathologica*, *134*(5), 705–714. https://doi.org/10.1007/s00401-017-1752-4

Panwalkar, P., Tamrazi, B., Dang, D., Chung, C., Sweha, S., Natarajan, S. K., Pun, M., Bayliss, J., Ogrodzinski, M. P., Pratt, D., Mullan, B., Hawes, D., Yang, F., Lu, C., Sabari, B. R., Achreja, A., Heon, J., Animasahun, O., Cieslik, M., … Venneti, S. (2021). Targeting integrated epigenetic and metabolic pathways in lethal childhood PFA ependymomas. *Science Translational Medicine*, *13*(614), eabc0497. https://doi.org/10.1126/scitranslmed.abc0497

Parsons, D. W., Jones, S., Zhang, X., Lin, J. C.-H., Leary, R. J., Angenendt, P., Mankoo, P., Carter, H., Siu, I.-M., & Gallia, G. L. (2008). An integrated genomic analysis of human glioblastoma multiforme. *Science*, *321*(5897), 1807–1812.

Paugh, B. S., Qu, C., Jones, C., Liu, Z., Adamowicz-Brice, M., Zhang, J., Bax, D. A., Coyle, B., Barrow, J., Hargrave, D., Lowe, J., Gajjar, A., Zhao, W., Broniscer, A., Ellison, D. W., Grundy, R. G., & Baker, S. J. (2010). Integrated Molecular Genetic Profiling of Pediatric High-Grade Gliomas Reveals Key Differences With the Adult Disease. *Journal of Clinical Oncology*, *28*(18), 3061–3068. https://doi.org/10.1200/JCO.2009.26.7252

Pazzaglia, U. E., Salisbury, J. R., & Byers, P. D. (1989). Development and involution of the notochord in the human spine. *Journal of the Royal Society of Medicine*, *82*(7), 413–415.

Piunti, A., Hashizume, R., Morgan, M. A., Bartom, E. T., Horbinski, C. M., Marshall, S. A., Rendleman, E. J., Ma, Q., Takahashi, Y. H., Woodfin, A. R., Misharin, A. V, Abshiru, N. A., Lulla, R. R., Saratsis, A. M., Kelleher, N. L., James, C. D., & Shilatifard, A. (2017). Therapeutic targeting of polycomb and BET bromodomain proteins in diffuse intrinsic pontine gliomas. *Nat Med*, *23*(4), 493–500. https://doi.org/10.1038/nm.4296

Piunti, A., Smith, E. R., Morgan, M. A. J., Ugarenko, M., Khaltyan, N., Helmin, K. A., Ryan, C. A., Murray, D. C., Rickels, R. A., Yilmaz, B. D., Rendleman, E. J., Savas, J. N., Singer, B. D., Bulun, S. E., & Shilatifard, A. (2019). CATACOMB: An endogenous inducible gene that antagonizes H3K27 methylation activity of Polycomb repressive complex 2 via an H3K27M-like mechanism. *Sci Adv*, *5*(7), eaax2887. https://doi.org/10.1126/sciadv.aax2887

Podsypanina, K., Ellenson, L. H., Nemes, A., Gu, J., Tamura, M., Yamada, K. M., Cordon-Cardo, C., Catoretti, G., Fisher, P. E., & Parsons, R. (1999). Mutation of Pten/Mmac1 in mice causes neoplasia in multiple organ systems. *Proceedings of the National Academy of Sciences of the United States of America*, *96*(4), 1563–1568. https://doi.org/10.1073/pnas.96.4.1563

Pollack, I F. (1999). Pediatric brain tumors. *Seminars in Surgical Oncology*, *16*(2), 73–90. https://doi.org/10.1002/(sici)1098-2388(199903)16:2<73::aid-ssu2>3.0.co;2-0

Pollack, Ian F, Finkelstein, S. D., Burnham, J., Holmes, E. J., Hamilton, R. L., Yates, A. J., Finlay, J. L., Sposto, R., & Group, C. C. (2001). Age and TP53 mutation frequency in childhood malignant gliomas: results in a multi-institutional cohort. *Cancer Research*, *61*(20), 7404–7407.

Pollack, Ian F, Hamilton, R. L., James, C. D., Finkelstein, S. D., Burnham, J., Yates, A. J., Holmes, E. J., Zhou, T., & Finlay, J. L. (2006). Rarity of PTEN deletions and EGFR amplification in malignant gliomas of childhood: results from the Children's Cancer Group 945 cohort. *Journal of Neurosurgery: Pediatrics*, *105*(5), 418–424.

Pott, S., & Lieb, J. D. (2015). What are super-enhancers? *Nature Genetics*, *47*(1), 8–12. https://doi.org/10.1038/ng.3167

Pratt, D, Quezado, M., Abdullaev, Z., Hawes, D., Yang, F., Garton, H. J. L., Judkins, A. R., Mody, R., Chinnaiyan, A., Aldape, K., Koschmann, C., & Venneti, S. (2020). Diffuse intrinsic pontine glioma-like tumor with EZHIP expression and molecular features of PFA ependymoma. In *Acta Neuropathol Commun* (Vol. 8, p. 37). https://doi.org/10.1186/s40478-020-00905-w

Pratt, Drew, Lucas, C.-H. G., Selvam, P. P., Abdullaev, Z., Ketchum, C., Quezado, M., Armstrong, T. S., Gilbert, M. R., Papanicolau-Sengos, A., Raffeld, M., Choo-Wosoba, H., Chan, P., Whipple, N., Nasrallah, M., Santi, M., Ramaswamy, V., Giannini, C., Ritzmann, T. A., Grundy, R. G., … Aldape, K. (2022). Recurrent ACVR1 mutations in posterior fossa ependymoma. *Acta Neuropathologica*, *144*(2), 373–376. https://doi.org/10.1007/s00401-022-02435-2

Pratt, Drew, Natarajan, S. K., Banda, A., Giannini, C., Vats, P., Koschmann, C., Mody, R., Chinnaiyan, A., & Venneti, S. (2018). Circumscribed/non-diffuse histology confers a better prognosis in H3K27M-mutant gliomas. In *Acta neuropathologica* (Vol. 135, Issue 2, pp. 299–301). https://doi.org/10.1007/s00401-018-1805-3

Przystal, J. M., Cianciolo Cosentino, C., Yadavilli, S., Zhang, J., Laternser, S., Bonner, E. R., Prasad, R., Dawood, A. A., Lobeto, N., & Chin Chong, W. (2022). Imipridones affect tumor bioenergetics and promote cell lineage differentiation in diffuse midline gliomas. *Neuro-Oncology*, *24*(9), 1438–1451.

Pun, M., Pratt, D., Nano, P. R., Joshi, P. K., Jiang, L., Englinger, B., Rao, A., Cieslik, M., Chinnaiyan, A. M., Aldape, K., Pfister, S., Filbin, M. G., Bhaduri, A., & Venneti, S. (2023). Common molecular features of H3K27M DMGs and PFA ependymomas map to hindbrain developmental pathways. *Acta Neuropathologica Communications*, *11*(1), 25. https://doi.org/10.1186/s40478-023-01514-z

Ragazzini, R., Perez-Palacios, R., Baymaz, I. H., Diop, S., Ancelin, K., Zielinski, D., Michaud, A., Givelet, M., Borsos, M., Aflaki, S., Legoix, P., Jansen, P., Servant, N., Torres-Padilla, M. E., Bourc'his, D., Fouchet, P., Vermeulen, M., & Margueron, R. (2019). EZHIP constrains Polycomb Repressive Complex 2 activity in germ cells. *Nat Commun*, *10*(1), 3858. https://doi.org/10.1038/s41467-019-11800-x

Raisner, R., Kharbanda, S., Jin, L., Jeng, E., Chan, E., Merchant, M., Haverty, P. M., Bainer, R., Cheung, T., Arnott, D., Flynn, E. M., Romero, F. A., Magnuson, S., & Gascoigne, K. E. (2018). Enhancer Activity Requires CBP/P300 Bromodomain-Dependent Histone H3K27 Acetylation. *Cell Reports*, *24*(7), 1722–1729. https://doi.org/https://doi.org/10.1016/j.celrep.2018.07.041

Rajeshwari, M., Sharma, M. C., Kakkar, A., Nambirajan, A., Suri, V., Sarkar, C., Singh, M., Saran, R. K., & Gupta, R. K. (2016). Evaluation of chromosome 1q gain in intracranial ependymomas. *Journal of Neuro-Oncology*, *127*(2), 271–278. https://doi.org/10.1007/s11060-015-2047-z

Ramírez, F., Ryan, D. P., Grüning, B., Bhardwaj, V., Kilpert, F., Richter, A. S., Heyne, S., Dündar, F., & Manke, T. (2016). deepTools2: a next generation web server for deep-sequencing data analysis. *Nucleic Acids Research*, *44*(W1), W160-5. https://doi.org/10.1093/nar/gkw257

Remillard, D., Buckley, D. L., Paulk, J., Brien, G. L., Sonnett, M., Seo, H., Dastjerdi, S., Wühr, M., Dhe-Paganon, S., & Armstrong, S. A. (2017). Degradation of the BAF complex factor BRD9 by heterobifunctional ligands. *Angewandte Chemie International Edition*, *56*(21), 5738–5743.

Rickert, C. H., Sträter, R., Kaatsch, P., Wassmann, H., Jürgens, H., Dockhorn-Dworniczak, B., & Paulus, W. (2001). Pediatric high-grade astrocytomas show chromosomal imbalances distinct from adult cases. *The American Journal of Pathology*, *158*(4), 1525–1532.

Riemondy, K. A., Venkataraman, S., Willard, N., Nellan, A., Sanford, B., Griesinger, A. M., Amani, V., Mitra, S., Hankinson, T. C., Handler, M. H., Sill, M., Ocasio, J., Weir, S. J., Malawsky, D. S., Gershon, T. R., Garancher, A., Wechsler-Reya, R. J., Hesselberth, J. R., Foreman, N. K., … Vibhakar, R. (2022). Neoplastic and immune single-cell transcriptomics define subgroup-specific intra-tumoral heterogeneity of childhood medulloblastoma. *Neuro-Oncology*, *24*(2), 273–286. https://doi.org/10.1093/neuonc/noab135

Robinson, H., McFarlane, R. J., & Wakeman, J. A. (2020). Brachyury: strategies for drugging an intractable cancer therapeutic target. *Trends in Cancer*, *6*(4), 271–273.

Robinson, J. T., Thorvaldsdóttir, H., Winckler, W., Guttman, M., Lander, E. S., Getz, G., & Mesirov, J. P. (2011). Integrative genomics viewer. *Nature Biotechnology*, *29*(1), 24–26. https://doi.org/10.1038/nbt.1754

Ross-Innes, C. S., Stark, R., Teschendorff, A. E., Holmes, K. A., Ali, H. R., Dunning, M. J., Brown, G. D., Gojis, O., Ellis, I. O., Green, A. R., Ali, S., Chin, S.-F., Palmieri, C., Caldas, C., & Carroll, J. S. (2012). Differential oestrogen receptor binding is associated with clinical outcome in breast cancer. *Nature*, *481*(7381), 389–393. https://doi.org/10.1038/nature10730

Sahyouni, R., Goshtasbi, K., Mahmoodi, A., & Chen, J. W. (2018). A historical recount of chordoma. *Journal of Neurosurgery: Spine*, *28*(4), 422–428.

Saksouk, N., Simboeck, E., & Déjardin, J. (2015). Constitutive heterochromatin formation and transcription in mammals. *Epigenetics & Chromatin*, *8*(1), 3. https://doi.org/10.1186/1756-8935-8-3

Samarasinghe, K. T. G., Jaime-Figueroa, S., Burgess, M., Nalawansha, D. A., Dai, K., Hu, Z., Bebenek, A., Holley, S. A., & Crews, C. M. (2021). Targeted degradation of transcription factors by TRAFTACs: TRAnscription Factor TArgeting Chimeras. *Cell Chemical Biology*, *28*(5), 648-661.e5. https://doi.org/https://doi.org/10.1016/j.chembiol.2021.03.011

Sangatsuda, Y., Miura, F., Araki, H., Mizoguchi, M., Hata, N., Kuga, D., Hatae, R., Akagi, Y., Amemiya, T., Fujioka, Y., Arai, Y., Yoshida, A., Shibata, T., Yoshimoto, K., Iihara, K., & Ito, T. (2020). Base-resolution methylomes of gliomas bearing histone H3.3 mutations reveal a G34 mutant-specific signature shared with bone tumors. *Scientific Reports*, *10*(1), 16162. https://doi.org/10.1038/s41598-020-73116-x

Schwartzentruber, J., Korshunov, A., Liu, X.-Y., Jones, D. T. W., Pfaff, E., Jacob, K., Sturm, D., Fontebasso, A. M., Quang, D.-A. K., Tönjes, M., Hovestadt, V., Albrecht, S., Kool, M., Nantel, A., Konermann, C., Lindroth, A., Jäger, N., Rausch, T., Ryzhova, M., … Jabado, N. (2012). Driver mutations in histone H3.3 and chromatin remodelling genes in paediatric glioblastoma. *Nature*, *482*(7384), 226–231. https://doi.org/10.1038/nature10833

Sepp, M., Leiss, K., Sarropoulos, I., Murat, F., Okonechnikov, K., Joshi, P., Leushkin, E., Mbengue, N., Schneider, C., & Schmidt, J. (2021). Cellular development and evolution of the mammalian cerebellum. *BioRxiv*.

Sharifnia, T., Wawer, M. J., Chen, T., Huang, Q.-Y., Weir, B. A., Sizemore, A., Lawlor, M. A., Goodale, A., Cowley, G. S., Vazquez, F., Ott, C. J., Francis, J. M., Sassi, S., Cogswell, P., Sheppard, H. E., Zhang, T., Gray, N. S., Clarke, P. A., Blagg, J., … Schreiber, S. L. (2019). Small-molecule targeting of brachyury transcription factor addiction in chordoma. *Nature Medicine*, *25*(2), 292–300. https://doi.org/10.1038/s41591-018-0312-3

Shechter, D., Dormann, H. L., Allis, C. D., & Hake, S. B. (2007). Extraction, purification and analysis of histones. *Nature Protocols*, *2*(6), 1445–1457.

Shen, H., & Laird, P. W. (2013). Interplay between the cancer genome and epigenome. *Cell*, *153*(1), 38–55.

Sheppard, H. E., Dall'Agnese, A., Park, W. D., Shamim, M. H., Dubrulle, J., Johnson, H. L., Stossi, F., Cogswell, P., Sommer, J., Levy, J., Sharifnia, T., Wawer, M. J., Nabet, B., Gray, N. S., Clemons, P. A., Schreiber, S. L., Workman, P., Young, R. A., & Lin, C. Y. (2021). Targeted brachyury degradation disrupts a highly specific autoregulatory program controlling chordoma cell identity. *Cell Reports Medicine*, *2*(1), 100188. https://doi.org/https://doi.org/10.1016/j.xcrm.2020.100188

Siegel, D. A., Richardson, L. C., Henley, S. J., Wilson, R. J., Dowling, N. F., Weir, H. K., Tai, E. W., & Buchanan Lunsford, N. (2020). Pediatric cancer mortality and survival in the United States, 2001-2016. *Cancer*, *126*(19), 4379–4389.

Siegel, R. L., Miller, K. D., Wagle, N. S., & Jemal, A. (2023). Cancer statistics, 2023. *CA: A Cancer Journal for Clinicians*, *73*(1), 17–48. https://doi.org/10.3322/caac.21763

Smith, J., Sen, S., Weeks, R. J., Eccles, M. R., & Chatterjee, A. (2020). Promoter DNA hypermethylation and paradoxical gene activation. *Trends in Cancer*, *6*(5), 392–406.

Smith, K. S., Bihannic, L., Gudenas, B. L., Haldipur, P., Tao, R., Gao, Q., Li, Y., Aldinger, K. A., Iskusnykh, I. Y., Chizhikov, V. V, Scoggins, M., Zhang, S., Edwards, A., Deng, M., Glass, I. A., Overman, L. M., Millman, J., Sjoboen, A. H., Hadley, J., … Northcott, P. A. (2022). Unified rhombic lip origins of group 3 and group 4 medulloblastoma. *Nature*, *609*(7929), 1012–1020. https://doi.org/10.1038/s41586-022-05208-9

Stafford, J. M., Lee, C. H., Voigt, P., Descostes, N., Saldana-Meyer, R., Yu, J. R., Leroy, G., Oksuz, O., Chapman, J. R., Suarez, F., Modrek, A. S., Bayin, N. S., Placantonakis, D. G., Karajannis, M. A., Snuderl, M., Ueberheide, B., & Reinberg, D. (2018). Multiple modes of PRC2 inhibition elicit global chromatin alterations in H3K27M pediatric glioma. *Sci Adv*, *4*(10), eaau5935. https://doi.org/10.1126/sciadv.aau5935

Sturm, D., Witt, H., Hovestadt, V., Khuong-Quang, D.-A., Jones, D. T. W., Konermann, C., Pfaff, E., Tönjes, M., Sill, M., Bender, S., Kool, M., Zapatka, M., Becker, N., Zucknick, M., Hielscher, T., Liu, X.-Y., Fontebasso, A. M., Ryzhova, M., Albrecht, S., … Pfister, S. M. (2012). Hotspot mutations in H3F3A and IDH1 define distinct epigenetic and biological subgroups of glioblastoma. *Cancer Cell*, *22*(4), 425–437. https://doi.org/10.1016/j.ccr.2012.08.024

Sundaresan, N., Rosen, G., & Boriani, S. (2009). Primary malignant tumors of the spine. *Orthopedic Clinics of North America*, *40*(1), 21–36.

Suzuki, A., de la Pompa, J. L., Stambolic, V., Elia, A. J., Sasaki, T., del Barco Barrantes, I., Ho, A., Wakeham, A., Itie, A., Khoo, W., Fukumoto, M., & Mak, T. W. (1998). High cancer susceptibility and embryonic lethality associated with mutation of the PTEN tumor suppressor gene in mice. *Current Biology : CB*, *8*(21), 1169–1178. https://doi.org/10.1016/s0960-9822(07)00488-5

Suzuki, H., Aoki, K., Chiba, K., Sato, Y., Shiozawa, Y., Shiraishi, Y., Shimamura, T., Niida, A., Motomura, K., Ohka, F., Yamamoto, T., Tanahashi, K., Ranjit, M., Wakabayashi, T., Yoshizato, T., Kataoka, K., Yoshida, K., Nagata, Y., Sato-Otsubo, A., … Ogawa, S. (2015). Mutational landscape and clonal architecture in grade II and III gliomas. *Nature Genetics*, *47*(5), 458–468. https://doi.org/10.1038/ng.3273

Sweha, S. R., Chung, C., Natarajan, S. K., Panwalkar, P., Pun, M., Ghali, A., Bayliss, J., Pratt, D., Shankar, A., Ravikumar, V., Rao, A., Cieslik, M., Wilder-Romans, K., Scott, A. J., Wahl, D. R., Jessa, S., Kleinman, C. L., Jabado, N., Mackay, A., … Venneti, S. (2021). Epigenetically defined therapeutic targeting in H3.3G34R/V high-grade gliomas. *Science Translational Medicine*, *13*(615), eabf7860. https://doi.org/10.1126/scitranslmed.abf7860

Tamai, S., Nakano, Y., Kinoshita, M., Sabit, H., Nobusawa, S., Arai, Y., Hama, N., Totoki, Y., Shibata, T., & Ichimura, K. (2021). Ependymoma with C11orf95-MAML2 fusion:

presenting with granular cell and ganglion cell features. *Brain Tumor Pathology*, *38*, 64–70.

Tanaka, K., Imoto, I., Inoue, J., Kozaki, K., Tsuda, H., Shimada, Y., Aiko, S., Yoshizumi, Y., Iwai, T., & Kawano, T. (2007). Frequent methylation-associated silencing of a candidate tumor-suppressor, CRABP1, in esophageal squamous-cell carcinoma. *Oncogene*, *26*(44), 6456–6468.

Tarpey, P. S., Behjati, S., Young, M. D., Martincorena, I., Alexandrov, L. B., Farndon, S. J., Guzzo, C., Hardy, C., Latimer, C., Butler, A. P., Teague, J. W., Shlien, A., Futreal, P. A., Shah, S., Bashashati, A., Jamshidi, F., Nielsen, T. O., Huntsman, D., Baumhoer, D., … Campbell, P. J. (2017). The driver landscape of sporadic chordoma. *Nature Communications*, *8*(1), 890. https://doi.org/10.1038/s41467-017-01026-0

Tauziède-Espariat, A., Siegfried, A., Nicaise, Y., Kergrohen, T., Sievers, P., Vasiljevic, A., Roux, A., Dezamis, E., Benevello, C., Machet, M.-C., Michalak, S., Puiseux, C., Llamas-Gutierrez, F., Leblond, P., Bourdeaut, F., Grill, J., Dufour, C., Guerrini-Rousseau, L., Abbou, S., … the RENOCLIP-LOC Adolescents) consortium, the B. (Biomarkers for E. in C. (2021). Supratentorial non-RELA, ZFTA-fused ependymomas: a comprehensive phenotype genotype correlation highlighting the number of zinc fingers in ZFTA-NCOA1/2 fusions. *Acta Neuropathologica Communications*, *9*(1), 135. https://doi.org/10.1186/s40478-021-01238-y

Tomlinson, I. P. M., Alam, N. A., Rowan, A. J., Barclay, E., Jaeger, E. E. M., Kelsell, D., Leigh, I., Gorman, P., Lamlum, H., Rahman, S., Roylance, R. R., Olpin, S., Bevan, S., Barker, K., Hearle, N., Houlston, R. S., Kiuru, M., Lehtonen, R., Karhu, A., … Aaltonen, L. A. (2002). Germline mutations in FH predispose to dominantly inherited uterine fibroids, skin leiomyomata and papillary renal cell cancer. *Nature Genetics*, *30*(4), 406–410. https://doi.org/10.1038/ng849

Tomomasa, R., Arai, Y., Kawabata-Iwakawa, R., Fukuoka, K., Nakano, Y., Hama, N., Nakata, S., Suzuki, N., Ishi, Y., & Tanaka, S. (2021). Ependymoma-like tumor with mesenchymal differentiation harboring C11orf95-NCOA1/2 or-RELA fusion: A hitherto unclassified tumor related to ependymoma. *Brain Pathology*, *31*(3), e12943.

Turcan, S., Rohle, D., Goenka, A., Walsh, L. A., Fang, F., Yilmaz, E., Campos, C., Fabius, A. W. M., Lu, C., Ward, P. S., Thompson, C. B., Kaufman, A., Guryanova, O., Levine, R., Heguy, A., Viale, A., Morris, L. G. T., Huse, J. T., Mellinghoff, I. K., & Chan, T. A. (2012). IDH1 mutation is sufficient to establish the glioma hypermethylator phenotype. *Nature*, *483*(7390), 479–483. https://doi.org/10.1038/nature10866

Unni, K. K., & Inwards, C. Y. (2010). *Dahlin's bone tumors: general aspects and data on 10,165 cases*. Lippincott Williams & Wilkins.

van Galen, P., Viny, A. D., Ram, O., Ryan, R. J. H., Cotton, M. J., Donohue, L., Sievers, C., Drier, Y., Liau, B. B., Gillespie, S. M., Carroll, K. M., Cross, M. B., Levine, R. L., & Bernstein, B. E. (2016). A Multiplexed System for Quantitative Comparisons of Chromatin Landscapes. *Molecular Cell*, *61*(1), 170–180. https://doi.org/10.1016/j.molcel.2015.11.003

Varela, C., Denis, J. A., Polentes, J., Feyeux, M., Aubert, S., Champon, B., Piétu, G., Peschanski, M., & Lefort, N. (2012). Recurrent genomic instability of chromosome 1q in neural derivatives of human embryonic stem cells. *The Journal of Clinical Investigation*, *122*(2), 569–574. https://doi.org/10.1172/JCI46268

Vaziri-Gohar, A., Cassel, J., Mohammed, F. S., Zarei, M., Hue, J. J., Hajihassani, O., Graor, H. J., Srikanth, Y. V. V, Karim, S. A., & Abbas, A. (2022). Limited nutrient availability in the tumor microenvironment renders pancreatic tumors sensitive to allosteric IDH1 inhibitors. *Nature Cancer*, *3*(7), 852–865.

Vera-Bolanos, E., Aldape, K., Yuan, Y., Wu, J., Wani, K., Necesito-Reyes, M. J., Colman, H., Dhall, G., Lieberman, F. S., Metellus, P., Mikkelsen, T., Omuro, A., Partap, S., Prados, M., Robins, H. I., Soffietti, R., Wu, J., Gilbert, M. R., & Armstrong, T. S. (2015). Clinical course and progression-free survival of adult intracranial and spinal ependymoma patients. *Neuro-Oncology*, *17*(3), 440–447. https://doi.org/10.1093/neuonc/nou162

Vladoiu, M. C., El-Hamamy, I., Donovan, L. K., Farooq, H., Holgado, B. L., Sundaravadanam, Y., Ramaswamy, V., Hendrikse, L. D., Kumar, S., & Mack, S. C. (2019). Childhood cerebellar tumours mirror conserved fetal transcriptional programs. *Nature*, *572*(7767), 67–73.

Voon, H. P. J., Udugama, M., Lin, W., Hii, L., Law, R. H. P., Steer, D. L., Das, P. P., Mann, J. R., & Wong, L. H. (2018). Inhibition of a K9/K36 demethylase by an H3. 3 point mutation found in paediatric glioblastoma. *Nature Communications*, *9*(1), 3142.

Vujovic, S., Henderson, S., Presneau, N., Odell, E., Jacques, T. S., Tirabosco, R., Boshoff, C., & Flanagan, A. M. (2006). Brachyury, a crucial regulator of notochordal development, is a novel biomarker for chordomas. *The Journal of Pathology: A Journal of the Pathological Society of Great Britain and Ireland*, *209*(2), 157–165.

Walcott, B. P., Nahed, B. V, Mohyeldin, A., Coumans, J.-V., Kahle, K. T., & Ferreira, M. J. (2012). Chordoma: current concepts, management, and future directions. *The Lancet. Oncology*, *13*(2), e69-76. https://doi.org/10.1016/S1470-2045(11)70337-0

Wang, J., Huang, T. Y.-T., Hou, Y., Bartom, E., Lu, X., Shilatifard, A., Yue, F., & Saratsis, A. (2021). Epigenomic landscape and 3D genome structure in pediatric high-grade glioma. *Science Advances*, *7*(23). https://doi.org/10.1126/sciadv.abg4126

Wang, L., Zehir, A., Nafa, K., Zhou, N., Berger, M. F., Casanova, J., Sadowska, J., Lu, C., Allis, C. D., Gounder, M., Chandhanayingyong, C., Ladanyi, M., Boland, P. J., & Hameed, M. (2016). Genomic aberrations frequently alter chromatin regulatory genes in chordoma. *Genes, Chromosomes and Cancer*, *55*(7), 591–600. https://doi.org/https://doi.org/10.1002/gcc.22362

Wang, Y., Song, F., Zhang, B., Zhang, L., Xu, J., Kuang, D., Li, D., Choudhary, M. N. K., Li, Y., Hu, M., Hardison, R., Wang, T., & Yue, F. (2018). The 3D Genome Browser: a web-based browser for visualizing 3D genome organization and long-range chromatin interactions. *Genome Biology*, *19*(1), 151. https://doi.org/10.1186/s13059-018-1519-9

Warburg, O., & Negelein, E. (1923). Über den Einfluss der Wellenlänge auf den Energieumsatz bei der Kohlensäureassimilation. *Zeitschrift Für Physikalische Chemie*, *106*(1), 191–218.

Warburg, O., Posener, K., & Negelein, E. (1924). Über den stoffwechsel der carcinomzelle. *Naturwissenschaften*, *12*(50), 1131–1137.

Ward, P. S., Patel, J., Wise, D. R., Abdel-Wahab, O., Bennett, B. D., Coller, H. A., Cross, J. R., Fantin, V. R., Hedvat, C. V, Perl, A. E., Rabinowitz, J. D., Carroll, M., Su, S. M., Sharp, K. A., Levine, R. L., & Thompson, C. B. (2010). The common feature of leukemia-associated IDH1 and IDH2 mutations is a neomorphic enzyme activity converting alpha-ketoglutarate to 2-hydroxyglutarate. *Cancer Cell*, *17*(3), 225–234. https://doi.org/10.1016/j.ccr.2010.01.020

Ward, P. S., & Thompson, C. B. (2012). Metabolic Reprogramming: A Cancer Hallmark Even Warburg Did Not Anticipate. *Cancer Cell*, *21*(3), 297–308. https://doi.org/https://doi.org/10.1016/j.ccr.2012.02.014

Watson, C, & Ullmann, J. (2015). *The Brain Stem* (A. W. B. T.-B. M. Toga (ed.); pp. 251–259). Academic Press. https://doi.org/https://doi.org/10.1016/B978-0-12-397025-1.00219-0

Watson, Charles, Bartholomaeus, C., & Puelles, L. (2019). Time for radical changes in brain stem nomenclature—applying the lessons from developmental gene patterns. *Frontiers in Neuroanatomy*, *13*, 10.

Wedekind, M. F., Widemann, B. C., & Cote, G. (2021). Chordoma: Current status, problems, and future directions. *Current Problems in Cancer*, *45*(4), 100771. https://doi.org/https://doi.org/10.1016/j.currproblcancer.2021.100771

Wei, J., Wu, J., Yin, Z., Li, X., Liu, Y., Wang, Y., Wang, Z., Xu, C., & Fan, L. (2022). Low expression of H3K27me3 is associated with poor prognosis in conventional chordoma. *Frontiers in Oncology*, *12*, 1048482. https://doi.org/10.3389/fonc.2022.1048482

Weintraub, H., Palter, K., & Van Lente, F. (1975). Histones H2a, H2b, H3, and H4 form a tetrameric complex in solutions of high salt. *Cell*, *6*(1), 85–110. https://doi.org/10.1016/0092-8674(75)90077-x

Whelan, J., McTiernan, A., Cooper, N., Wong, Y. K., Francis, M., Vernon, S., & Strauss, S. J. (2012). Incidence and survival of malignant bone sarcomas in England 1979–2007. *International Journal of Cancer*, *131*(4), E508–E517.

Wilson, B. G., Wang, X., Shen, X., McKenna, E. S., Lemieux, M. E., Cho, Y.-J., Koellhoffer, E. C., Pomeroy, S. L., Orkin, S. H., & Roberts, C. W. M. (2010). Epigenetic antagonism between polycomb and SWI/SNF complexes during oncogenic transformation. *Cancer Cell*, *18*(4), 316–328. https://doi.org/10.1016/j.ccr.2010.09.006

Wingett, S. W., & Andrews, S. (2018). FastQ Screen: A tool for multi-genome mapping and quality control. *F1000Research*, *7*, 1338. https://doi.org/10.12688/f1000research.15931.2

Wirbelauer, C., Bell, O., & Schübeler, D. (2005). Variant histone H3. 3 is deposited at sites of nucleosomal displacement throughout transcribed genes while active histone modifications show a promoter-proximal bias. *Genes & Development*, *19*(15), 1761–1766.

Wong, K.-K., Tsang, Y. T. M., Chang, Y.-M., Su, J., Di Francesco, A. M., Meco, D., Riccardi, R., Perlaky, L., Dauser, R. C., & Adesina, A. (2006). Genome-wide allelic imbalance analysis of pediatric gliomas by single nucleotide polymorphic allele array. *Cancer Research*, *66*(23), 11172–11178.

Worcel, A., Han, S., & Wong, M. L. (1978). Assembly of newly replicated chromatin. *Cell*, *15*(3), 969–977. https://doi.org/https://doi.org/10.1016/0092-8674(78)90280-5

Wu, G., Broniscer, A., McEachron, T. A., Lu, C., Paugh, B. S., Becksfort, J., Qu, C., Ding, L., Huether, R., Parker, M., Zhang, J., Gajjar, A., Dyer, M. A., Mullighan, C. G., Gilbertson, R. J., Mardis, E. R., Wilson, R. K., Downing, J. R., Ellison, D. W., … Baker, S. J. (2012). Somatic histone H3 alterations in pediatric diffuse intrinsic pontine gliomas and non-brainstem glioblastomas. *Nature Genetics*, *44*(3), 251–253. https://doi.org/10.1038/ng.1102

Wu, Q., Lothe, R. A., Ahlquist, T., Silins, I., Tropé, C. G., Micci, F., Nesland, J. M., Suo, Z., & Lind, G. E. (2007). DNA methylation profiling of ovarian carcinomas and their in vitro models identifies HOXA9, HOXB5, SCGB3A1, and CRABP1 as novel targets. *Molecular Cancer*, *6*(1), 1–11.

Xiao, L., Parolia, A., Qiao, Y., Bawa, P., Eyunni, S., Mannan, R., Carson, S. E., Chang, Y., Wang, X., & Zhang, Y. (2022). Targeting SWI/SNF ATPases in enhancer-addicted prostate cancer. *Nature*, *601*(7893), 434–439.

Xie, Z., Bailey, A., Kuleshov, M. V, Clarke, D. J. B., Evangelista, J. E., Jenkins, S. L., Lachmann, A., Wojciechowicz, M. L., Kropiwnicki, E., Jagodnik, K. M., Jeon, M., & Ma'ayan, A. (2021). Gene Set Knowledge Discovery with Enrichr. *Current Protocols*, *1*(3), e90. https://doi.org/https://doi.org/10.1002/cpz1.90

Xu, W., Yang, H., Liu, Y., Yang, Y., Wang, P., Kim, S.-H., Ito, S., Yang, C., Wang, P., Xiao, M.-T., Liu, L., Jiang, W., Liu, J., Zhang, J., Wang, B., Frye, S., Zhang, Y., Xu, Y., Lei, Q., … Xiong, Y. (2011). Oncometabolite 2-hydroxyglutarate is a competitive inhibitor of α-ketoglutarate-dependent dioxygenases. *Cancer Cell*, *19*(1), 17–30. https://doi.org/10.1016/j.ccr.2010.12.014

Yang, C., Hornicek, F. J., Wood, K. B., Schwab, J. H., Choy, E., Iafrate, J., Rosenberg, A., Nielsen, G. P., Xavier, R. J., Mankin, H., & Duan, Z. (2010). Characterization and analysis of human chordoma cell lines. *Spine*, *35*(13), 1257–1264. https://doi.org/10.1097/BRS.0b013e3181c2a8b0

Yang, X. R., Ng, D., Alcorta, D. A., Liebsch, N. J., Sheridan, E., Li, S., Goldstein, A. M., Parry, D. M., & Kelley, M. J. (2009). T (brachyury) gene duplication confers major susceptibility to familial chordoma. *Nature Genetics*, *41*(11), 1176–1178. https://doi.org/10.1038/ng.454

Yano, S., Ishiuchi, T., Abe, S., Namekawa, S. H., Huang, G., Ogawa, Y., & Sasaki, H. (2022).

Histone H3K36me2 and H3K36me3 form a chromatin platform essential for DNMT3A-dependent DNA methylation in mouse oocytes. *Nature Communications*, *13*(1), 4440. https://doi.org/10.1038/s41467-022-32141-2

Yeter, H. G., Kosemehmetoglu, K., & Soylemezoglu, F. (2019). Poorly differentiated chordoma: review of 53 cases. *APMIS : Acta Pathologica, Microbiologica, et Immunologica Scandinavica*, *127*(9), 607–615. https://doi.org/10.1111/apm.12978

Yolcu, Y., Wahood, W., Alvi, M. A., Kerezoudis, P., Okuno, S. H., Foote, R. L., & Bydon, M. (2019). Evaluating the Role of Adjuvant Radiotherapy in the Management of Sacral and Vertebral Chordoma: Results from a National Database. *World Neurosurgery*, *127*, e1137–e1144. https://doi.org/https://doi.org/10.1016/j.wneu.2019.04.070

Young, M. D., Willson, T. A., Wakefield, M. J., Trounson, E., Hilton, D. J., Blewitt, M. E., Oshlack, A., & Majewski, I. J. (2011). ChIP-seq analysis reveals distinct H3K27me3 profiles that correlate with transcriptional activity. *Nucleic Acids Research*, *39*(17), 7415–7427. https://doi.org/10.1093/nar/gkr416

Zarei, M., Hajihassani, O., Hue, J. J., Graor, H. J., Loftus, A. W., Rathore, M., Vaziri-Gohar, A., Asara, J. M., Winter, J. M., & Rothermel, L. D. (2022). Wild-type IDH1 inhibition enhances chemotherapy response in melanoma. *Journal of Experimental & Clinical Cancer Research*, *41*(1), 1–18.

Zarei, M., Hue, J. J., Hajihassani, O., Graor, H. J., Katayama, E. S., Loftus, A. W., Bajor, D., Rothermel, L. D., Vaziri-Gohar, A., & Winter, J. M. (2021). Clinical development of IDH1 inhibitors for cancer therapy. *Cancer Treatment Reviews*, 102334.

Zaytseva, M., Papusha, L., Novichkova, G., & Druy, A. (2021). Molecular Stratification of Childhood Ependymomas as a Basis for Personalized Diagnostics and Treatment. In *Cancers* (Vol. 13, Issue 19). https://doi.org/10.3390/cancers13194954

Zhang, J., Fan, J., Venneti, S., Cross, J. R., Takagi, T., Bhinder, B., Djaballah, H., Kanai, M., Cheng, E. H., Judkins, A. R., Pawel, B., Baggs, J., Cherry, S., Rabinowitz, J. D., & Thompson, C. B. (2014). Asparagine plays a critical role in regulating cellular adaptation to glutamine depletion. *Molecular Cell*, *56*(2), 205–218. https://doi.org/10.1016/j.molcel.2014.08.018

Zhang, Y., Dong, W., Zhu, J., Wang, L., Wu, X., & Shan, H. (2017). Combination of EZH2 inhibitor and BET inhibitor for treatment of diffuse intrinsic pontine glioma. *Cell Biosci*, *7*, 56. https://doi.org/10.1186/s13578-017-0184-0

Zheng, T., Ghasemi, D. R., Okonechnikov, K., Korshunov, A., Sill, M., Maass, K. K., Benites Goncalves da Silva, P., Ryzhova, M., Gojo, J., & Stichel, D. (2021). Cross-Species Genomics Reveals Oncogenic Dependencies in ZFTA/C11orf95 Fusion–Positive Supratentorial EpendymomasZFTA Fusion Genes in Supratentorial Ependymomas. *Cancer Discovery*, *11*(9), 2230–2247.

Zoppi, V., Hughes, S. J., Maniaci, C., Testa, A., Gmaschitz, T., Wieshofer, C., Koegl, M.,

Riching, K. M., Daniels, D. L., & Spallarossa, A. (2018). Iterative design and optimization of initially inactive proteolysis targeting chimeras (PROTACs) identify VZ185 as a potent, fast, and selective von Hippel–Lindau (VHL) based dual degrader probe of BRD9 and BRD7. *Journal of Medicinal Chemistry*, *62*(2), 699–726.

Zschernack, V., Jünger, S. T., Mynarek, M., Rutkowski, S., Garre, M. L., Ebinger, M., Neu, M., Faber, J., Erdlenbruch, B., & Claviez, A. (2021). Supratentorial ependymoma in childhood: more than just RELA or YAP. *Acta Neuropathologica*, *141*, 455–466.